

Corrosion Monitoring Research for City of New York Bridges

PUBLICATION NO. FHWA-HRT-14-023

MAY 2014



U.S. Department of Transportation
Federal Highway Administration

Research, Development, and Technology
Turner-Fairbank Highway Research Center
6300 Georgetown Pike
McLean, VA 22101-2296

FOREWORD

Cable suspension bridges are essential components in the transportation networks of large metropolitan areas, such as the City of New York, and their serviceability is extremely important for economic and societal growth. The safety of such structures is closely linked to the safety performance of the cable supported system and, in particular, of their main cables. Currently, all State and local agencies base their maintenance plan mainly on previous experience and on limited visual inspection of the exterior and sometimes the interior of the cable. This report presents the results of a study aimed at developing a corrosion monitoring system for main cables of suspension bridges. Direct and indirect sensing technologies were reviewed, tested, and integrated in a redundant system that is able to monitor quantities like temperature, relative humidity, and corrosion rate. All these technologies were tested on a 20-ft (6.1-m)-long, 20-inch (508-mm)-diameter cable mockup before the field installation on two panels of one of the main cables of the Manhattan Bridge in New York, NY. The sensor system developed for this project recorded measurements of the temperature, relative humidity, and corrosion rate from inside the main cable for a period of almost 1 year, providing valuable information on the internal environment of an in-service main cable. This report will be of interest to highway managers; engineers involved in design, construction, and operations; and researchers.

Jorge E. Pagán-Ortiz
Director, Office of Infrastructure
Research and Development

Notice

This document is disseminated under the sponsorship of the U.S. Department of Transportation in the interest of information exchange. The U.S. Government assumes no liability for the use of the information contained in this document. This report does not constitute a standard, specification, or regulation.

The U.S. Government does not endorse products or manufacturers. Trademarks or manufacturers' names appear in this report only because they are considered essential to the objective of the document.

Quality Assurance Statement

The Federal Highway Administration (FHWA) provides high-quality information to serve Government, industry, and the public in a manner that promotes public understanding. Standards and policies are used to ensure and maximize the quality, objectivity, utility, and integrity of its information. FHWA periodically reviews quality issues and adjusts its programs and processes to ensure continuous quality improvement.

TECHNICAL REPORT DOCUMENTATION PAGE

1. Report No. FHWA-HRT-14-023	2. Government Accession No.	3. Recipient's Catalog No.	
4. Title and Subtitle Corrosion Monitoring Research for City of New York Bridges		5. Report Date May 2014	
		6. Performing Organization Code	
7. Author(s) Raimondo Betti, Dyab Khazem, Mark Carlos, Richard Gostautas, and Y. Paul Virmani		8. Performing Organization Report No.	
9. Performing Organization Name and Address Columbia University Department of Civil Engineering and Engineering Mechanics 500 W. 120th Street, New York, NY 10027 Parsons Transportation Group 100 Broadway, New York, NY 10005 Physical Acoustics Corporation 195 Clarks vill Road, Princeton Junction, NY 08550		10. Work Unit No.	
		11. Contract or Grant No.	
12. Sponsoring Agency Name and Address Office of Infrastructure Research and Development Federal Highway Administration 6300 Georgetown Pike McLean, VA 22101-2296		13. Type of Report and Period Covered Final Report	
		14. Sponsoring Agency Code	
15. Supplementary Notes The Contracting Officer's Technical Representative (COTR) was Y. Paul Virmani, HRDI-60.			
16. Abstract Current inspection procedures for suspension bridge main cables mainly consist of visually inspecting the exterior covering of the cable every 2 years. An indepth inspection is usually scheduled as necessary to assess the condition of the interior wires by wedging the cable at selected locations along the cable. However, such approaches were found to be deficient in uncovering the most deteriorated and weakest regions in the cables of several bridges during their full cable rehabilitation projects. In this study, an integrated methodology was developed that uses state-of-the-art sensing capabilities and non-destructive evaluation (NDE) technologies to assess the cable condition. A smart sensor system integrated with NDE technologies is an approach that shows potential for assessing the condition of suspension bridge cables. NDE technologies for direct detection of the corrosion damage (i.e., main flux method, magnetostrictive technology, and acoustic emission technology) were implemented, validated, and tested for suspension bridge cable applications. In addition, a network of sensors that can monitor the external and internal environment of such cables and provide information that can be used to indirectly assess the cable's deterioration conditions and their evolution over time were assembled and extensively tested. In the selection of the sensors to be used for indirect sensing, special consideration was placed in considering the performance of such sensors in realistic service conditions such as a harsh environment, extreme reversals in cyclic histories (temperature, humidity, strain, electrochemical activity byproducts, etc.), large compaction forces, etc. To recreate conditions as close as possible to real operating conditions, a cable mockup, which was 20 inches (508 mm) in diameter and 20 ft (6.1 m) long and subjected to 1,100 kips (4,893,043.76 N) and fully instrumented, was built at Columbia University and tested in an enclosed accelerated corrosion chamber. The results showed that the selected sensors were able to successfully measure temperature, humidity, and corrosion rate within the cable. The same system was then installed on two panels of the Manhattan Bridge, and measurements of temperature, relative humidity, and corrosion rate in the cable interior were successfully recorded for almost 1 year from November 2010 to September 2011.			
17. Key Words Main cables, Suspension bridges, Corrosion, Monitoring		18. Distribution Statement No restrictions. This document is available to the public through the National Technical Information Service, Springfield, VA 22161	
19. Security Classif. (of this report) Unclassified	20. Security Classif. (of this page) Unclassified	21. No of Pages 200	22. Price

SI* (MODERN METRIC) CONVERSION FACTORS

APPROXIMATE CONVERSIONS TO SI UNITS

Symbol	When You Know	Multiply By	To Find	Symbol
LENGTH				
in	inches	25.4	millimeters	mm
ft	feet	0.305	meters	m
yd	yards	0.914	meters	m
mi	miles	1.61	kilometers	km
AREA				
in ²	square inches	645.2	square millimeters	mm ²
ft ²	square feet	0.093	square meters	m ²
yd ²	square yard	0.836	square meters	m ²
ac	acres	0.405	hectares	ha
mi ²	square miles	2.59	square kilometers	km ²
VOLUME				
fl oz	fluid ounces	29.57	milliliters	mL
gal	gallons	3.785	liters	L
ft ³	cubic feet	0.028	cubic meters	m ³
yd ³	cubic yards	0.765	cubic meters	m ³
NOTE: volumes greater than 1000 L shall be shown in m ³				
MASS				
oz	ounces	28.35	grams	g
lb	pounds	0.454	kilograms	kg
T	short tons (2000 lb)	0.907	megagrams (or "metric ton")	Mg (or "t")
TEMPERATURE (exact degrees)				
°F	Fahrenheit	5 (F-32)/9 or (F-32)/1.8	Celsius	°C
ILLUMINATION				
fc	foot-candles	10.76	lux	lx
fl	foot-Lamberts	3.426	candela/m ²	cd/m ²
FORCE and PRESSURE or STRESS				
lbf	poundforce	4.45	newtons	N
lbf/in ²	poundforce per square inch	6.89	kilopascals	kPa

APPROXIMATE CONVERSIONS FROM SI UNITS

Symbol	When You Know	Multiply By	To Find	Symbol
LENGTH				
mm	millimeters	0.039	inches	in
m	meters	3.28	feet	ft
m	meters	1.09	yards	yd
km	kilometers	0.621	miles	mi
AREA				
mm ²	square millimeters	0.0016	square inches	in ²
m ²	square meters	10.764	square feet	ft ²
m ²	square meters	1.195	square yards	yd ²
ha	hectares	2.47	acres	ac
km ²	square kilometers	0.386	square miles	mi ²
VOLUME				
mL	milliliters	0.034	fluid ounces	fl oz
L	liters	0.264	gallons	gal
m ³	cubic meters	35.314	cubic feet	ft ³
m ³	cubic meters	1.307	cubic yards	yd ³
MASS				
g	grams	0.035	ounces	oz
kg	kilograms	2.202	pounds	lb
Mg (or "t")	megagrams (or "metric ton")	1.103	short tons (2000 lb)	T
TEMPERATURE (exact degrees)				
°C	Celsius	1.8C+32	Fahrenheit	°F
ILLUMINATION				
lx	lux	0.0929	foot-candles	fc
cd/m ²	candela/m ²	0.2919	foot-Lamberts	fl
FORCE and PRESSURE or STRESS				
N	newtons	0.225	poundforce	lbf
kPa	kilopascals	0.145	poundforce per square inch	lbf/in ²

*SI is the symbol for the International System of Units. Appropriate rounding should be made to comply with Section 4 of ASTM E380.
(Revised March 2003)

TABLE OF CONTENTS

CHAPTER 1: INTRODUCTION.....	1
CHAPTER 2: SELECTED TECHNOLOGIES.....	7
LITERATURE REVIEW	7
INDIRECT SENSING TECHNOLOGIES	8
LPR Sensors.....	9
Multiple Array Sensor.....	21
BM or Galvanic Sensors	23
DIRECT SENSING TECHNOLOGIES.....	24
AE and MS Technologies	24
Main Magnetic Flux Method (MMFM).....	57
CHAPTER 3: FULL-SIZE CABLE MOCKUP CONSTRUCTION OF THE CABLE SPECIMEN	63
CHAPTER 4: RESULTS FROM ACCELERATED CYCLIC TESTS	77
GENERAL DESCRIPTION.....	77
Sensor Arrangement.....	77
Cyclic Corrosion Testing Chamber	77
EXPERIMENTAL RESULTS/DISCUSSIONS.....	78
Temperature and Relative Humidity Sensors	78
Corrosion Rate Sensors: LPR Sensors.....	86
Corrosion Rate Sensors: CMAS Sensors.....	89
Other Corrosion Rate Sensors.....	92
CONCLUSIONS	93
Testing the AE System for the Detection of Wire Breaks in the Interior of the Cable	94
CHAPTER 5: CABLE DISSASSEMBLY (AUTOPSY).....	103
CABLE UNLOADING.....	104
Cable Strap/Band Removal.....	105
Strand Removal.....	110
CHAPTER 6: ANALYSIS OF WIRE CONDITIONS.....	113
GENERAL OVERVIEW	113
CORROSION UNDER NEOPRENE PROTECTIVE STRAP.....	113
STAINLESS STEEL STRAPS	115
CABLE BANDS	117
Underside Openings.....	121
INTERIOR OF CABLE.....	122
INTERNAL CABLE STRAPS	124
PRE-CORRODED STRANDS	125
CHAPTER 7: ANALYSIS OF SENSOR CONDITIONS.....	129
PRECON HS2000V TEMPERATURE AND RELATIVE HUMIDITY SENSORS ...	129
LPR CORROSION RATE SENSORS.....	133
CMAS SENSORS.....	137
BM SENSORS.....	138

CHAPTER 8: FIELD INSTALLATION ON A CABLE OF A SUSPENSION BRIDGE.....	141
GENERAL CONSIDERATIONS	141
Phase I: Initial System Installation	141
Phase II: Installation of the Corrosion Monitoring System in the Main Cable	149
CHAPTER 9: CONCLUSIONS	165
APPENDIX A: CALIBRATION OF LPR SENSORS	167
CALIBRATION OF SENSORS	167
DETERMINATION OF B'	169
APPENDIX B: SAMPLE DATA.....	173
REFERENCES.....	185

LIST OF FIGURES

Figure 1. Graph. Number of broken wires along the south cable of an 80-year-old bridge during rehabilitation.....	3
Figure 2. Graph. Number of broken wires along the north cable of an 80-year-old bridge during rehabilitation.....	3
Figure 3. Illustration. Layout of the LPR sensor	10
Figure 4. Photo. Q-fog cyclic corrosion tester.....	11
Figure 5. Photo. Wire bundles to be placed in corrosion chamber.....	12
Figure 6. Photo. Onset of corrosion in an LPR sensor.....	12
Figure 7. Graph. Close-up of a humidity step.....	13
Figure 8. Graph. Corrosion rate versus time in cyclic humidity testing of a sensor.....	14
Figure 9. Photo. Corroded LPR sensor after 1 week test.....	14
Figure 10. Photo. Specimens placed in the Q-fog cyclic corrosion tester	17
Figure 11. Graph. Proportionality constant for 0.006-inch (150- μm) sensors.....	19
Figure 12. Graph. Proportionality constant for 0.012-inch (300- μm) sensors.....	20
Figure 13. Graph. Proportionality constant for 0.048-inch (1,200- μm) sensors.....	21
Figure 14. Illustration. Schematic description of CMAS probe	22
Figure 15. Illustration. Electrons flow from anodic areas to cathodic areas inside a metal (top) and through a CMAS probe (bottom)	22
Figure 16. Photo. Close-up of a CMAS.....	23
Figure 17. Illustration. Schematic diagram of a galvanic probe.....	23
Figure 18. Photo. Precon HS2000V temperature/relative humidity sensor.....	24
Figure 19. Illustration. AE technology principle	25
Figure 20. Illustration. MS instrument.....	26
Figure 21. Graph. Acoustic signals recorded on a single wire by the R3I sensor—baseline	28
Figure 22. Graph. Acoustic signals recorded on a single wire by the R3I sensor—stage 1	28
Figure 23. Graph. Acoustic signals recorded on a single wire by the R3I sensor—stage 2	28
Figure 24. Graph. Acoustic signals recorded on a single wire by the R3I sensor—stage 3	29
Figure 25. Graph. Maximum amplitude of the acoustic signals propagating along a single wire as function of the reduction in cross sectional area for the R3I AE and MS sensors.....	29
Figure 26. Graph. Acoustic signals recorded on the strand of five wires by the R1.5I sensor—baseline	30
Figure 27. Graph. Acoustic signals recorded on the strand of five wires by the R1.5I sensor—after wire break	31
Figure 28. Graph. Acoustic signals recorded on the strand of five wires by the R3I sensor—baseline	31
Figure 29. Graph. Acoustic signals recorded on the strand of five wires by the R3I sensor—after wire break	32
Figure 30. Graph. Acoustic signals recorded on the strand of five wires by the MS sensor—baseline	32
Figure 31. Graph. Acoustic signals recorded on the strand of five wires by the MS sensor—after wire break	33
Figure 32. Graph. Maximum amplitude of the acoustic signals propagating along the five-wire strand as function of the reduction in cross section area in a single wire for R1.5I and R3I sensors.....	34

Figure 33. Graph. Maximum amplitude of the acoustic signals propagating along the five-wire strand as function of the reduction in cross section area in a single wire for MS located in one of the outside wires and in the center wire	34
Figure 34. Photo. Location of the wire cuts and sensors on the strand.....	35
Figure 35. Graph. Acoustic signals recorded on the strand with the R1.5I sensor— (a) no damage, (b) 1 wire cut, (c) 2 wires cut, (d) 3 wires cut, (e) 4 wires cut, and (f) 5 wires cut.....	36
Figure 36. Graph. Maximum amplitude of the signals detected by the MS-AE technique— sensors located before the wire cut location	37
Figure 37. Graph. Maximum amplitude of the signals detected by the MS-AE technique— sensors located after the wire cut location	37
Figure 38. Illustration. Position of the AE sensors along the strand.....	38
Figure 39. Illustration. Notch locations along the wire strand.....	39
Figure 40. Illustration. Cross section of the wire strand showing position and depth of the notches along the strand length.....	39
Figure 41. Photo. Wire strand mounted on the tensile machine and instrumented with AE and MS sensors	40
Figure 42. Graph. AE activity as a function of time during the tensile test of the wire strand	41
Figure 43. Graph. Cumulative AE absolute energy as a function of load	42
Figure 44. Graph. Events located around notches B, C, and D located by sensor groups 1, 3, 5, and 7.....	43
Figure 45. Graph. Events located around notches B and D located by sensor groups 2, 4, 6, and 8.....	43
Figure 46. Graph. Events located around notches A and E located by sensor groups 1, 3, 5, and 7 (unfiltered data).....	45
Figure 47. Graph. Events located around notches A and E located by sensor groups 2, 4, 6, and 8 (unfiltered data).....	45
Figure 48. Photo. Failure of the epoxy filler inside the sockets	45
Figure 49. Illustration. AE signals from a potential wire break at notch A.....	46
Figure 50. Graph. Events located around notches A and E by sensor groups 1, 3, 5, and 7 (filtered data).....	46
Figure 51. Graph. Events located around notches A and E located by sensor groups 2, 4, 6, and 8 (filtered data).....	47
Figure 52. Graph. Baseline acoustic signals detected by the AE sensors along the strand	49
Figure 53. Graph. Acoustic signals detected by the AE sensors 2, 3, 6, and 7 during the hold at 34,000 lb (15,436 kg) (no damage).....	51
Figure 54. Graph. Acoustic signals detected by the AE sensors 2, 3, 6, and 7 during the hold at 142,000 lb (64,468 kg) (severe damage)	51
Figure 55. Graph. Signal strength as function of load for sensors 2, 3, 6, and 7.....	52
Figure 56. Graph. Signal strength versus cross section reduction for sensors 2, 3, 6, and 7.....	53
Figure 57. Illustration. MS and AE sensors.....	54
Figure 58. Illustration. MS and AE strand configurations.....	54
Figure 59. Illustration. Multibundle configurations for MS and AE testing—test 5-1.....	55
Figure 60. Illustration. Multibundle configurations for MS and AE testing—test 5-2.....	55
Figure 61. Illustration. Multibundle configurations for MS and AE testing—test 5-3.....	55
Figure 62. Photo. Seven-strand wire bundle with outside MS magnet.....	55
Figure 63. Photo. Compaction of strand bundle	56

Figure 64. Photo. Mounted AE sensors	56
Figure 65. Illustration. Flow of magnetic flux in a wire rope.....	58
Figure 66. Illustration. MMFM measurement system	58
Figure 67. Photo. MMFM bobbin mounted on a cable mockup.....	59
Figure 68. Illustration. Schematic of the MMFM measurement system used in this study	59
Figure 69. Illustration. Magnetic flux versus magnetic field plot for an MMFM test.....	60
Figure 70. Graph. Increase in magnetic flux versus increase in the number of wires.....	61
Figure 71. Illustration. Drawing of the cable mockup and corrosion chamber—plan and elevation.....	65
Figure 72. Photo. Wire coils to be used for the construction of the cable mockup (first row of coils)	66
Figure 73. Photo. Strand under construction	67
Figure 74. Photo. Final straight strand from coiled wire	67
Figure 75. Illustration. Cable cross section and strand details.....	68
Figure 76. Photo. Long strand made of original coiled wires.....	69
Figure 77. Photo. Lower strand assemblage.....	69
Figure 78. Photo. Central strand assemblage.....	70
Figure 79. Photo. Intermediate cable construction phase	70
Figure 80. Illustration. Schematic locations of sensors in cable mockup cross section	72
Figure 81. Photo. Placement of sensors inside the cable mockup	72
Figure 82. Photo. Cable compaction.....	73
Figure 83. Photo. Jacking the first strand	73
Figure 84. Photo. Cable mockup representative of a full-scale section of a suspension bridge cable.....	74
Figure 85. Photo. Cable specimen with environmental chamber	75
Figure 86. Graph. Test 1 AT2 chamber temperature recordings	79
Figure 87. Graph. Test 1 upper cable temperature distributions along diameter at -60°	80
Figure 88. Graph. Test 1 upper cable temperature distributions along diameter at 0°	81
Figure 89. Graph. Test 1 upper cable temperature distributions along diameter at 60°	81
Figure 90. Graph. Test 1 Precon HS2000V ARH2 chamber relative humidity recordings.....	82
Figure 91. Graph. Test 1 upper cable relative humidity distributions along diameter at -60°	83
Figure 92. Graph. Test 1 upper cable relative humidity distributions along diameter at 0°	84
Figure 93. Graph. Test 1 upper cable relative humidity distributions along diameter at 60°	84
Figure 94. Illustration. Mapping of maximum and minimum temperature and relative humidity distribution during cycle 1 over the entire cable’s cross section.....	85
Figure 95. Illustration. Mapping of maximum and minimum temperature and relative humidity distribution during the final cycle over the entire cable’s cross section.....	85
Figure 96. Graph. Test 1 LPR3 versus RH13	87
Figure 97. Graph. Test 1 LPR3 versus T13	87
Figure 98. Graph. Test 1 LPR4 versus RH15	88
Figure 99. Graph. Test 1 LPR4 versus T15	88
Figure 100. Graph. Test 4 CMAS CS with sensor 5 readings for relative humidity	90
Figure 101. Graph. Test 4 CMAS CS with sensor 5 readings for temperature	90
Figure 102. Graph. Test 2 CMAS CS with sensor 5 readings for relative humidity	91
Figure 103. Graph. Test 2 CMAS CS with sensor 5 readings for temperature	91

Figure 104. Illustration. Test 2 corrosion rate for CS and zinc obtained by sensor BM5 in test 2	93
Figure 105. Illustration. Sensor locations	94
Figure 106. Photo. Mechanism to apply load to the prenotched wires.....	95
Figure 107. Graph. ASL (green), absolute energy (red), and load (blue) versus time during the third wire break attempt	96
Figure 108. Photo. Broken wire pulled out from the edge of the cable before breaking.....	97
Figure 109. Illustration. Low- and high-energy events during the wire break from R0.45I sensors.....	98
Figure 110. Illustration. Low- and high-energy events during the wire break from R1.5I sensors.....	99
Figure 111. Illustration. Location of the wire break with the R0.45I sensor on the surface of the cable mockup	100
Figure 112. Illustration. Location of the wire break with the R1.5I sensor on the surface of the cable mockup.....	100
Figure 113. Graph. Planar localization of the wire break using the R0.45I sensor	101
Figure 114. Graph. Planar localization of the wire break using the R1.5I sensor	101
Figure 115. Photo. Disassembled environmental chamber with cable mockup specimen	103
Figure 116. Illustration. Strand labeling	104
Figure 117. Photo. Jacking beam with hydraulic jacks secured into position	104
Figure 118. Photo. Strain gauge setup on strands 4 and 7	105
Figure 119. Photo. North end of cable mockup with stainless steel straps.....	106
Figure 120. Photo. Removal of south-side strap.....	106
Figure 121. Photo. Stainless steel straps removed from north side of cable mockup specimen	107
Figure 122. Photo. Stainless steel straps removed from north central side of cable mockup specimen	107
Figure 123. Photo. Stainless steel straps removed from south central side of cable mockup specimen	108
Figure 124. Photo. Stainless steel straps removed from south side of cable mockup specimen	108
Figure 125. Photo. North side prior to cable band removal.....	109
Figure 126. Photo. North side cable end following cable band removal.....	109
Figure 127. Photo. Cable specimen during disassembly	110
Figure 128. Photo. Removed strands.....	110
Figure 129. Photo. Completed cable deconstruction	111
Figure 130. Photo. Corroded area under neoprene wrapping.....	113
Figure 131. Photo. Close-up view of corroded area under neoprene wrapping	114
Figure 132. Photo. Wires with stage 4 corrosion on the top of the cable surface.....	114
Figure 133. Photo. Close-up view of corroded wire.....	115
Figure 134. Photo. Salt build-up and zinc/ferrous corrosion product.....	116
Figure 135. Photo. Pitting corrosion under stainless steel strap	117
Figure 136. Photo. Close-up view of pit.....	117
Figure 137. Photo. North end of cable with band removed.....	118
Figure 138. Photo. Wires at north end of cable with stage 3 corrosion.....	118
Figure 139. Photo. South end of cable with band removed.....	119

Figure 140. Photo. Wires at south end of cable with large percentage of stage 3 corrosion	119
Figure 141. Photo. South end of cable highlighting teeth of cable band	120
Figure 142. Photo. Interior of top of south side of cable band	120
Figure 143. Photo. Mockup cable specimen within environmental chamber and location of both holes	121
Figure 144. Photo. Image of one of the 11.89-by-11.89-inch (30.5-by-30.5-cm) holes placed in the aluminum cable cover	121
Figure 145. Photo. Product that formed where the 11.89-by-11.89-inch (30.5-by-30.5-cm) hole was placed in the aluminum cable cover	122
Figure 146. Photo. Close-up view of the product formed on the high-strength steel wires	122
Figure 147. Photo. Inner core of the specimen during disassembly	123
Figure 148. Photo. Orange nylon strap embedded within cable	124
Figure 149. Photo. Corrosion formation at nylon strip location	124
Figure 150. Photo. Close-up view of the wires with stage 4 corrosion	125
Figure 151. Photo. North end of cable—pre-corroded strand 9R (bottom) and adjacent side of strand 16R	126
Figure 152. Photo. North end of cable close-up of 16R showing stage 3 corrosion	126
Figure 153. Photo. South end of cable pre-corroded strand 9R (bottom)	127
Figure 154. Photo. South end of cable adjacent side of strand 16R	127
Figure 155. Photo. South end of cable close-up of 16R showing stage 4 corrosion	127
Figure 156. Photo. Sensors T1, BM1, and CMAS CS1	129
Figure 157. Photo. Precon HS2000V sensor 3 during cable disassembly	130
Figure 158. Photo. Close-up view of Precon HS2000V sensor 3 electrode	130
Figure 159. Photo. Precon HS2000V sensor 13 during cable dissection	131
Figure 160. Photo. Close-up view of Precon HS2000V sensor 13 electrode	131
Figure 161. Photo. Precon HS2000V sensor 7 close-up of electrode during cable dissection	132
Figure 162. Photo. Precon HS2000V sensor 7 wires exposed	132
Figure 163. Photo. Precon HS2000V sensor 10 during cable dissection	133
Figure 164. Photo. LPR sensor 4 during cable disassembly	133
Figure 165. Photo. Close-up view of LPR sensor 4	134
Figure 166. Photo. LPR sensor 6 during cable disassembly	134
Figure 167. Photo. Close-up view of LPR sensor 6	135
Figure 168. Photo. Corroded LPR sensor 5	135
Figure 169. Photo. Corroded and disfigured LPR sensor 7	136
Figure 170. Photo. LPR sensor 8 during cable dissection	136
Figure 171. Photo. LPR sensor 8 close-up of corroded sensor electrodes	136
Figure 172. Photo. CMAS CS 2 intact	137
Figure 173. Photo. Crushed CMAS Zn 2 sensor	138
Figure 174. Photo. Heavy corrosion on BM sensor 7	139
Figure 175. Photo. Minimal corrosion on BM sensor 3	139
Figure 176. Illustration. Cable sketch and dimensions of field installation phase 1	142
Figure 177. Photo. Panel point 2 of Manhattan Bridge	142
Figure 178. Photo. Sensor Highway II System	143
Figure 179. Illustration. Block diagram of the Sensor Highway II System	143
Figure 180. Photo. Vaisala WXT510 weather transmitter	144
Figure 181. Photo. Weather station installed on the Manhattan Bridge	144

Figure 182. Screenshot. Graph of temperature and humidity inside the cable anchorage remotely reported via a secure Web portal	145
Figure 183. Illustration. Mounted SOFO sensors	146
Figure 184. Photo. Actual locations of mounted SOFO and MuST fiber-optic sensors	147
Figure 185. Photo. Strands at the anchorage with mounted fiber-optic strain sensors	147
Figure 186. Photo. Strain gauges mounted on the eyebar.....	148
Figure 187. Photo. Typical NEMA-4 enclosure housing fiber-optic reading unit, DSL router, and modem	149
Figure 188. Screenshot. Web portal for secure remote data collection	149
Figure 189. Illustration. Field installation location of sensor prototype on Manhattan Bridge north cable D.....	150
Figure 190. Photo. Suspended platform between panel points 13 and 15	151
Figure 191. Photo. Walkway where the DAQ was installed	151
Figure 192. Photo. Cable preparation by unwrapping and wedging.....	152
Figure 193. Illustration. Sensor distribution diagram within the cross section of the main cable (grooves A–D).....	153
Figure 194. Photo. Sensor array used in each groove opening consisting of temperature/humidity sensors and LPR, CMAS, and BM corrosion sensors	154
Figure 195. Photo. Set of sensors ready for installation	154
Figure 196. Photo. Sensor lead wires exiting from the cable after installation	154
Figure 197. Photo. Cable temporary wrapping with neoprene and main conduit exiting at the bottom of cable leading to the main DAQ box at roadway level.....	155
Figure 198. Photo. Final stage of the installation of the neoprene wrapping	155
Figure 199. Photo. DAQ system/subsystem layout	156
Figure 200. Photo. Installation of the central DAQ system.....	156
Figure 201. Illustration. Schematic representation of DAQ system	156
Figure 202. Graph. Temperature and relative humidity over a 24-h period.....	157
Figure 203. Graph. Temperature and relative humidity over a 24-h period showing variations from winter to summer.....	158
Figure 204. Illustration. Temperature and relative humidity relationship/distribution throughout the cable cross section during winter, spring, and summer.....	159
Figure 205. Graph. Relative humidity versus corrosion rate measurement for LPR sensor	160
Figure 206. Graph. Relative humidity versus corrosion rate measurement for BM sensor.....	160
Figure 207. Graph. Increases in zinc corrosion recorded by BM sensor	161
Figure 208. Graph. Increases in steel corrosion recorded by BM sensor	161
Figure 209. Graph. Increase in corrosion rate recorded by LPR sensors	161
Figure 210. Photo. Damaged neoprene wrapping due to construction activity on the bridge....	162
Figure 211. Photo. Decommissioning of the monitoring system by wedging the cable and pulling the sensors out	162
Figure 212. Photo. Wires from sensors prior to removal.....	163
Figure 213. Photo. Close-up view of cable wires at the same location where the sensors were installed showing no damage to the main cable wire.....	163
Figure 214. Equation. Equivalent weight	167
Figure 215. Equation. Relationship between the charge from the corrosion reaction with the number of lost electron and the moles of metal	167
Figure 216. Equation. Amount of mass loss	167

Figure 217. Equation. Relationship between the amount of mass loss with the equivalent weight and the charge	167
Figure 218. Equation. Mass loss related to density of the material and volume of the lost material	168
Figure 219. Equation. Charge as the product of the corrosion current and time	168
Figure 220. Equation. Mass loss from geometric considerations to the mass loss from equivalent weight and charge.....	168
Figure 221. Equation. Rate of change of thickness	168
Figure 222. Equation. Corrosion rate of the metal.....	168
Figure 223. Equation. Alternative expression of the corrosion rate	168
Figure 224. Equation. Simplified expression of the corrosion rate	169
Figure 225. Equation. Estimated thickness loss in 1 min	169
Figure 226. Equation. Alternative expression of the estimated thickness loss in 1 min.....	169
Figure 227. Equation. Expression of the estimate of the total thickness loss.....	169
Figure 228. Equation. Proportionality constant as function of the thickness loss and of the polarization resistance.....	170
Figure 229. Graph. Inverse of R_p versus time.....	170
Figure 230. Graph. Integration of inverse of R_p	171
Figure 231. Equation. Estimation of constant of proportionality from experiment 1.....	171
Figure 232. Graph. Instantaneous corrosion rates versus time	172
Figure 233. Graph. Temperature-relative humidity measurements for sensor A4 on Brooklyn side in March 2011	173
Figure 234. Graph. Temperature-relative humidity measurements for sensor A5 on Brooklyn side in March 2011	173
Figure 235. Graph. Temperature-relative humidity measurements for sensor B4 on Brooklyn side in March 2011	174
Figure 236. Graph. Temperature-relative humidity measurements for sensor A4 on Manhattan side in March 2011	174
Figure 237. Graph. Temperature-relative humidity measurements for sensor B4 on Manhattan side in March 2011	175
Figure 238. Graph. Temperature-relative humidity measurements for sensor C6 on Manhattan side in March 2011	175
Figure 239. Graph. Corrosion rate measurements for CMAS CS sensor in March 2011.....	176
Figure 240. Graph. Corrosion rate measurements for CMAS Zn sensor in March 2011	176
Figure 241. Graph. Corrosion rate measurements for BM CS sensor in March 2011.....	177
Figure 242. Graph. Corrosion rate measurements for BM Zn sensor in March 2011	177
Figure 243. Graph. Temperature-relative humidity measurements for sensor A4 on Brooklyn side in April 2011	178
Figure 244. Graph. Temperature-relative humidity measurements for sensor A5 on Brooklyn side in April 2011	178
Figure 245. Graph. Temperature-relative humidity measurements for sensor B1 on Brooklyn side in April 2011	179
Figure 246. Graph. Temperature-relative humidity measurements for sensor B4 on Brooklyn side in April 2011	179
Figure 247. Graph. Temperature-relative humidity measurements for sensor B1 on Manhattan side in April 2011	180

Figure 248. Graph. Temperature-relative humidity measurements for sensor B4 on Manhattan side in April 2011	180
Figure 249. Graph. Temperature-relative humidity measurements for sensor C6 on Manhattan side in April 2011	181
Figure 250. Graph. Corrosion rate measurements for CMAS CS sensor in April 2011.....	181
Figure 251. Graph. Corrosion rate measurements for CMAS Zn sensor in April 2011	182
Figure 252. Graph. Corrosion rate measurements for BM CS sensor in April 2011.....	182
Figure 253. Graph. Corrosion rate measurements for BM Zn sensor in April 2011	183

LIST OF TABLES

Table 1. List of City of New York cable suspension bridges with corresponding indepth inspection and cable rehabilitation.....	4
Table 2. Chemical compositions of AISI 1080 steel and standard bridge wire.....	10
Table 3. Experimental program	16
Table 4. Average weight loss and equivalent corrosion depth for wire specimens.....	18
Table 5. Type and number of LPR sensors used in experiments.....	18
Table 6. Damage induced in a single wire.....	27
Table 7. Average signal amplitudes from PLB at sensor locations	40
Table 8. Sensor groups and corresponding coverage area.....	42
Table 9. Events located by the AE system at notches B, C, and D.....	44
Table 10. Events located by the AE system at Notch sites A and E.....	48
Table 11. Amplitude and peak frequency of acoustic signals produced by the MS device and detected with AE sensors.....	50
Table 12. AE sensor positions for MS-AE tests	54
Table 13. Environmental chamber cyclic corrosion test descriptions	78
Table 14. Positions and types of AE sensors.....	94
Table 15. Stress levels during cable de-tensioning.....	105

CHAPTER 1: INTRODUCTION

Currently, all State and local agencies responsible for the maintenance of suspension bridge cables base their maintenance plans primarily on previous experiences and on information from limited inspections. Usually, the exterior covering of a cable is visually inspected biannually. If such inspections reveal deterioration problems, the cable undergoes an indepth inspection if the maintenance budget allows for such undertaking. The cable is then unwrapped at a few locations along the cable length and is wedged into its center. Next, a visual inspection of the wires' conditions is performed, and in some cases, a few wires are cut and removed for laboratory testing. As a result of NCHRP Project 10-57, guidelines for inspections have been developed so as to standardize such cable inspections.⁽¹⁾

Indepth inspections of cable systems in aging suspension bridges in the City of New York area and the broader Midatlantic region have often shown that there are many broken wires inside the cables and at the anchorages, indicating brittle fractures and extensive corrosion. These alarming findings are inexplicable, and the reason for the presence of such broken wires must be found in the complex deterioration process with a main cable. While the effects of corrosion on ordinary structural steel are mainly due to a loss of material and the ensuing reduction of the cross sectional areas of members, the failure of high-strength bridge wires manifests itself, in addition to the loss of material, in a number of related phenomena referred to as stress corrosion, corrosion cracking, corrosion fatigue, and hydrogen embrittlement. These phenomena appear to have a much more detrimental effect on the strength of wires than just the reduction of the wires' cross section area.

All these interacting and complex deterioration mechanisms play a fundamental role in determining the actual strength of bridge cables. The current methodologies do not account for the actual deteriorated conditions of the wires; the use of a ductile model for the estimation of the residual cable strength has been proven to be valid only for new bridges and overestimates the actual cable strength in existing bridges. In addition, there are overwhelming problems related to the uncertainties in the current inspections' data since these indepth inspections are conducted only at a few selected locations along the bridge length, usually at locations that appear to be in the worst conditions from a visual point of view.

The effectiveness of all these methodologies for estimating the remaining cable strength, however, depends on the reliability and completeness of the information that is extracted during inspections. Unfortunately, current visual inspections do not provide an adequate amount or sufficiently reliable data, highlighting the need for innovative non-destructive testing (NDT) and sensing technologies that can provide an immediate, comprehensive, and reliable assessment of cable conditions and their evolution with time either directly or through measuring related variables (i.e., temperature, acidity, humidity, etc.).

The goal of this research project was to develop an integrated system that uses state-of-the-art sensing capabilities and non-destructive evaluation (NDE) technologies to assess cable conditions. Based on this study, it is reasonable to say that a smart sensor system integrated with global NDE technologies and that would map the entire length of the cable is an accurate tool for reliably assessing the condition of suspension bridge cables.

Current inspection procedures of suspension bridge main cables mainly consist of visually inspecting the exterior covering of the cable every 2 years. A team of inspectors observe the surface of the cable protection materials and report the findings regarding cracks and chipping of materials (neoprene wrapping or paint), signs of water and residue leaking from the cable (mainly at cable band locations), and other indications and levels of deterioration of the wrapping/painting materials. An indepth inspection is usually scheduled as necessary to assess the condition of the interior wires by wedging the cable at radial groove positions at selected locations along the cable. These locations are usually limited to about eight or less, and the evaluation is based on a combination of heuristics and statistical considerations. However, such approaches were discovered to be deficient in uncovering the most deteriorated and weakest regions in the cables of several bridges during their full cable rehabilitation projects.

In figure 1 and figure 2, the number of broken wires along the south and north cables of an 80-year-old bridge is plotted as a function of the location along the cable length. For each panel, the length of the cable between two consecutive cable bands was defined. Each cable was divided into two segments indicated by “W” or “E,” where “W” indicates the part of the cable west of the central point, and “E” indicates the east part of the cable. Two panels (77E-78E and 76E-77E) on the north cable have a number of broken wires (307 and 119 out of 18,666 wires, respectively) that are off the charts. It is clear that locations of breaks within the main cable and the number of broken wires cannot be characterized with any specific pattern, and such data cannot be accurately predicted by inspecting some selected locations along the cable. Even when the cable is wedged open, the total number of visible wires that are exposed is limited to about 2 percent of the total number of wires in a cable cross section.

Traditionally, during the indepth inspection procedure, the wires are classified in four stages of wire deterioration, which are characterized by the presence of the following (NCHRP Report 534):⁽¹⁾

- **Stage 1:** Spots of zinc oxidation on the surface of the wire.
- **Stage 2:** Zinc oxidation on the entire surface of the wire.
- **Stage 3:** Areas of brown rust covering up to 30 percent of the surface of the wire.
- **Stage 4:** Brown rust covering more than 30 percent of the surface of the wire.⁽²⁾

The following conclusions were made based on a 1998 comprehensive analysis of the suspension bridge inspections in the City of New York metropolitan area:⁽³⁾

- Water penetrated into the interior of the cable, with water pH values as low as 4.
- There was corrosion of the zinc coating, evidenced by the presence of zinc hydroxide (white rust) as well as corrosion of steel with discernible pitting and loss of wire cross section.
- There were broken wires inside the cables.

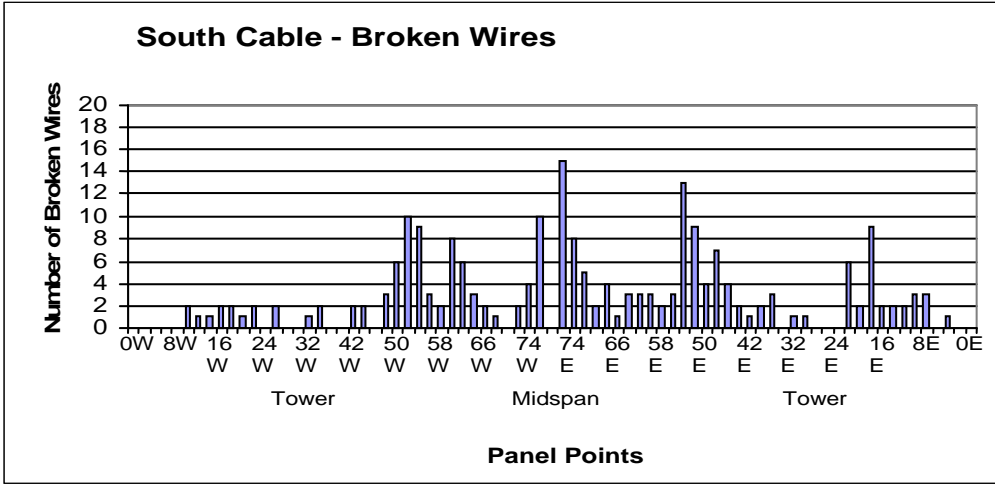


Figure 1. Graph. Number of broken wires along the south cable of an 80-year-old bridge during rehabilitation.

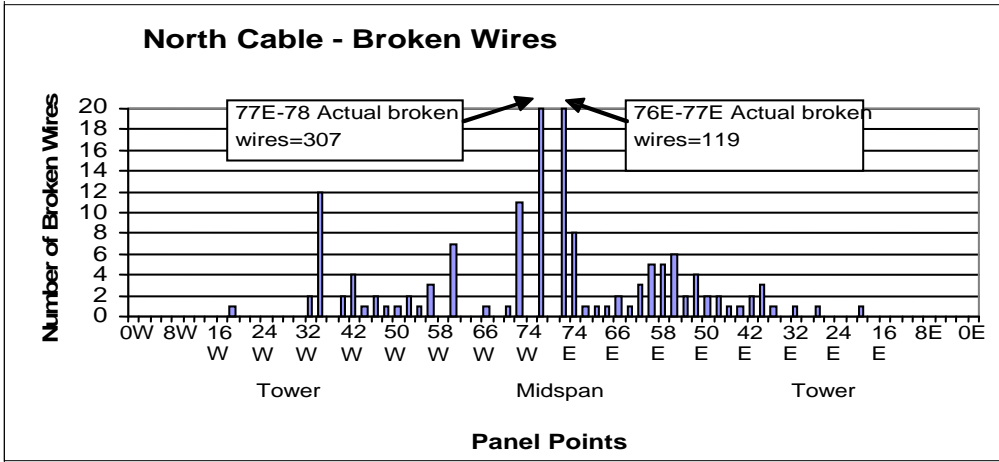


Figure 2. Graph. Number of broken wires along the north cable of an 80-year-old bridge during rehabilitation.

A listing of the bridges, from which the previous conclusions were drawn, and the status of their inspection and/or rehabilitation are provided in table 1.⁽³⁾ In this study, more than 100 inspection reports for the main cables of the 10 suspension bridges in the New York metropolitan area were reviewed and analyzed. Most of these bridges underwent various cable inspections over their life time, with unwrapping, wedging and, in some cases, oiling of the cables.

Table 1. List of City of New York cable suspension bridges with corresponding indepth inspection and cable rehabilitation.

Bridge Name	Year Built	Number of Cables	Cable Diameter (inch)	Indepth Inspection (Y/N)	Cable Rehabilitation (Y/N)
Brooklyn	1883	4	15.75	Y	Y
Williamsburg	1903	4	18.75	Y	Y
Manhattan	1909	4	20.5	Y	Y
Triboro	1936	2	21	Y	Y
George Washington	1931	4	36	Y	N
Throgs Neck	1961	2	21	N	N
Whitestone	1939	2	21	Y	Y
Bear Mountain	1924	2	22	Y	Y
Mid Hudson	1930	2	16.75	Y	Y
Verrazano	1964	4	36	Y	N

1 inch = 25.4 mm

The pattern of cable deterioration at various locations depends on many factors such as stresses, geometry, exposure to acid rain, sun and wind, construction details, etc. Usually, the outer wire layers show a higher degree of degradation and a larger number of broken wires, especially in the lower portion of the cable's cross section, while wire conditions improve toward the inner layers. However, depending on the procedures used at the time of the bridge's construction, the deterioration pattern may be reversed, and the inner wires may be in much worse conditions than those in the outer layers.

The environmental deterioration of bridge wires is a result of electrochemical processes and their interaction with mechanical stresses. Although atmospheric air is the most common in the environment, aqueous solutions, including natural water, atmospheric moisture, and rain as well as man-made adverse chemical solutions are the conditions most frequently associated with degradation problems. In bridge wires, various forms of material deterioration have been associated with the word "corrosion," including surface corrosion, corrosion pitting, intergranular and crevice corrosion, stress corrosion, and corrosion fatigue. Another important process in wire degradation is represented by hydrogen embrittlement. In contrast to most forms of corrosion, hydrogen embrittlement generally occurs in service when the part is being protected for corrosion or when corrosion on the part is absent, that is, when a high-strength steel is cathodically protected. The corrosion is usually taking place elsewhere (at the anode), but atomic hydrogen is generated at the surface of the steel (cathode) by the dissolution of water. The hydrogen atoms diffuse in the interior of the wire and weaken the interatomic bond of the wire metal. The penetration and movement of hydrogen with the wire are towards zones of high tensile stress (e.g., at crack tip in wires under tension).

Corrosion involves the interaction (reaction) between a metal or alloy and its environment. The initiation of the corrosion process and its rate of development are affected by the properties of both the metal or alloy and the environment. A measurement of the environment inside and outside the cable, the changes in electrochemical processes, and the existence of corrosion products can provide valuable information in corrosion monitoring programs. For example, the measurement of pH, conductivity, dissolved oxygen, metallic and other ion concentrations,

inhibitor concentrations and other indices (e.g., relative humidity) can all be correlated to the existence of ongoing corrosion. In addition, complex interrelationships and interactions can exist among these variables which can enhance or reduce corrosion activity. Conversely, a NDE technique that can diagnose changes in the effective cross sectional area of the cable is needed to determine the impacts of corrosion on the mechanical characteristics.

The objective of this research project was twofold: (1) to explore the most recent and promising NDE technologies for direct detection of the corrosion damage inside the main cables of suspension bridges and to select the most promising ones for further development and customizing for main cable applications (direct sensing method) and (2) to install a network of sensors that can monitor the external and internal environment of these cables and provide information that can be used to indirectly assess the cable's deterioration conditions and their evolution over time (indirect sensing method). With regard to direct sensing methods, it was important to consider NDE technologies that could be realistically applied in the field on an existing suspension bridge, considering the limitations imposed by working few hundred feet above the roadway, with limited or no traffic disruption, in harsh environments, with limited power sources, etc. In the selection of the sensors to be used as indirect sensing methods, special consideration was given to the performance of such sensors in realistic conditions similar to those in service such as a harsh environment, extreme reversals in cyclic histories (temperature, humidity, wind, strain, etc.), large compaction forces, a lack of easy access from the exterior of the cables, and the necessity of extracting clear and accurate information. The integration of indirect multimode sensing technologies and direct NDE technologies has allowed researchers to develop a global monitoring system for main cables of suspension bridges that can provide valuable information to bridge engineers and owners so to make reasonable, better informed, and cost effective maintenance decisions.

CHAPTER 2: SELECTED TECHNOLOGIES

LITERATURE REVIEW

A complete literature review of the available corrosion monitoring techniques and sensors was conducted. The goal was to find out about the state of the art of the currently available sensor technologies, especially corrosion monitoring techniques, and to see whether these sensors/technologies could be applied to monitor main cables in suspension bridges. The literature review remained open for the entire duration of the project to consider any new developments that may have had potential for detecting and monitoring corrosion damage inside a suspension bridge cable.

Technologies were classified into two categories: (1) indirect sensing technologies and (2) direct sensing technologies. Indirect sensing technologies include all sensors and technologies that measure quantities that can be either directly (e.g., corrosion rate) or indirectly (e.g., temperature) related to corrosion of the wires. Direct sensing technologies include technologies that can directly measure the effect of corrosion (e.g., magnetic flux measurements can be directly correlated to the cross section of the specimen).

After an extensive literature review, the following technologies were considered worthy of further investigation:

- Acoustic emission (AE).
- Magnetostrictive (MS)
- Fiber optics (pH, humidity, chloride content, strain, etc.).
- Electromagnetic (magnetic flux leakage).
- Linear polarization resistance (LPR).
- Electrochemical impedance spectroscopy.

The main lesson learned from the literature review phase was that no single means of corrosion detection (sensors or technologies) is either ideal or suitable for assessing all possible forms of corrosion-induced damage. The key point is the peculiarity of the structural element (in this case, the cable) under consideration. There are many sensors available on the market that can measure temperature, pH, relative humidity, etc., but only a few of those can be used in a bundle of over 10,000 steel wires subjected to strong compaction forces with difficult accessibility to the core. The proposed corrosion monitoring system will be an integrated system of sensors and technologies that will provide complementary (and sometimes redundant) information for the assessment of the cable's internal conditions.

INDIRECT SENSING TECHNOLOGIES

In order to select the most appropriate sensors, a series of evaluation criteria was identified. The main criteria include the following:

- **Size:** Small enough to be embedded inside the cable.
- **Ruggedness:** Ability to handle installation process.
- **Depth of scan/in situ loss of section (direct):** Ability of the device to probe to the center of the cable cross section and/or ability to determine material loss.
- **Reliability/accuracy:** Sensors must be reliable and provide accurate readings of environmental/mechanical changes
- **Life span:** Ability for continued operation with reliable and accurate results.
- **Coupling/installment:** Easy installation and coupling with other sensors/elements within the cable.
- **Mobility (direct):** Ease in conducting measurements along the axis of the cable and special requirements for moving between cable panels over the cable band.
- **Sensitivity:** Expected sensitivity for a given parameter (pH, relative humidity, chloride content, strain, temperature, etc.).
- **Power:** Power consumption is critical, and power management is necessary (i.e., low power).
- **Environment:** Ability of the sensor to function in a liquid or in air.
- **Performance history:** How well the sensor systems and/or components work as designed for other projects.

Based on those criteria, the following sensors were selected for installation in the cable mockup specimen:

- Analatom LRP sensors.
- Corr Instrument bimetallic (BM) sensors.
- Corr Instrument multiple array carbon steel (CS) sensors.
- Corr Instrument multiple array zinc sensors.
- Temperature and humidity Precon HS2000V sensors.
- BM sensors provided by Florida Atlantic University.

- Temperature, pH, and moisture fiber optic sensors provided by Polytechnic/New York University.
- Fiber optics strain gauges provided by the University of Illinois–Chicago.

Some of these sensors were extensively tested in a series of accelerated corrosion tests prior to their installation in the cable mockup specimen. Others had already been tested and calibrated by the manufacturers.

LPR Sensors

Evaluation

Linear polarization is an electrochemical technique where a potential scan is applied to a freely corroding sensor element, and the resulting current response is measured. This small perturbation is applied step-wise, starting below the free corrosion potential (the open circuit potential) and terminating above the free corrosion potential. The LPR sensor used in this study has two electrodes: a working electrode and a counter/reference electrode (see figure 3). The potential between the two electrodes is measured directly, eliminating the need for a third reference electrode typical of three electrode procedures. In the sensor in figure 3, the 0.006-inch (150- μm)-wide fingers of the working electrode are aligned with the 0.017-inch (450- μm)-wide fingers of the counter/reference electrode in an interlocking configuration, leaving an interdigitation gap between the two electrodes. The interdigitation distance, indicating the distance between the electrode fingers, determines the sensitivity of the sensors. A narrower gap allows an easier charge exchange and leads to more sensitive readings. In this study, three kinds of sensors with different interdigitation distances were tested. They will be referred to as 0.006-, 0.012-, and 0.048-inch (150-, 300-, and 1,200- μm) sensors, indicating the interdigitation gap between the electrodes. A smaller interdigitation gap results in a larger number of electrodes. The electrodes are 0.78 inch (20 mm) long and 0.37 inch (9.5 mm) wide and are made from standard shim stock of American Iron and Steel Institute (AISI) 1080 steel, which has a chemical composition similar to that of the bridge wires (see table 2). In this manner, the effect of sensor sensitivity stemming from material property fluctuation could be minimized. The electrodes are mounted on a Kapton[®] film, a non-conducting polymer not susceptible to corrosion.

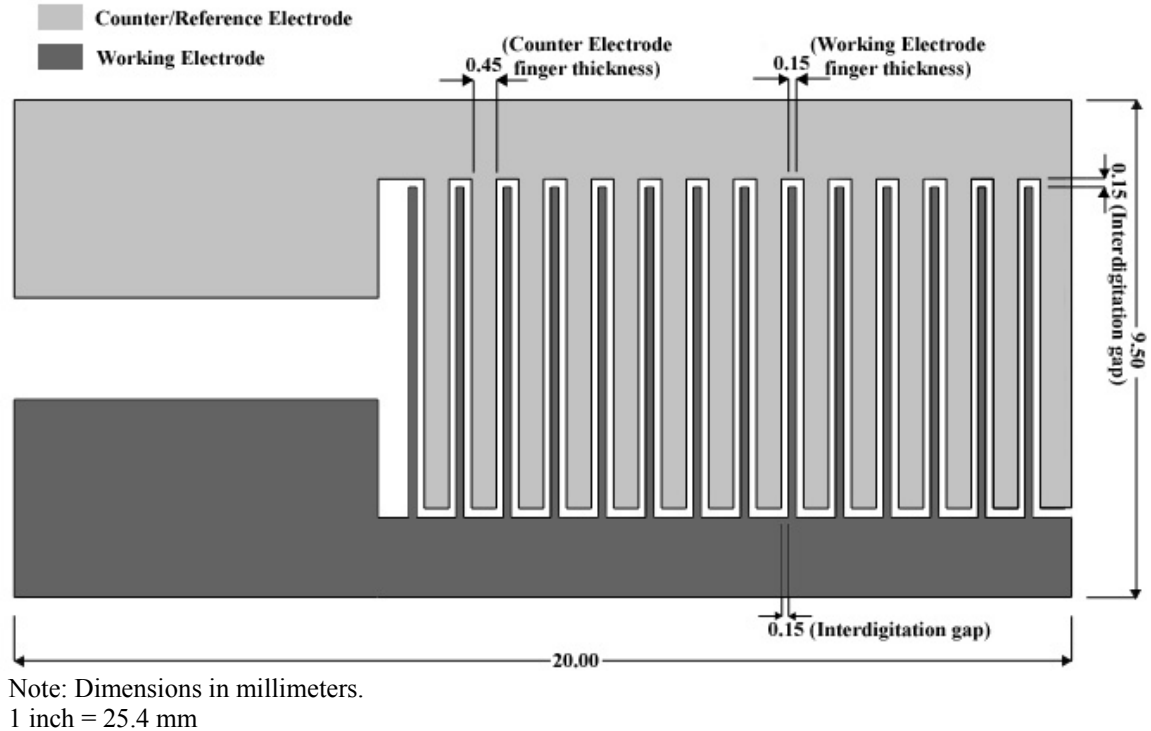


Figure 3. Illustration. Layout of the LPR sensor.

Table 2. Chemical compositions of AISI 1080 steel and standard bridge wire.

Chemical Composition	AISI 1080 Steel	Standard Bridge Wire
Carbon	0.75–0.88 percent	0.75–0.85 percent
Manganese	0.60–0.90 percent	0.55–0.75 percent
Phosphorus	0.04 percent max	0.04 percent max
Sulfur	0.05 percent max	0.04 percent max

An LPR sensor can be considered an array of counter and working electrodes (a network of 14 sensors). A data acquisition unit performs a voltage sweep about the open circuit potential of the LPR sensor through a circuit that uses two operational amplifiers. The input voltage to the circuit is provided by the analog-to-digital (A/D) converter of the micro-controller, which can provide a voltage range of 0 to 1.5 V. The output voltage is proportional to the current through the LPR sensor. From the operational amplifier circuit, this voltage is measured by the micro-controller's A/D converter, which can sense voltages in the same voltage range. The slope of the input voltage versus output voltage curve is proportional to the polarization resistance (R_p) and is calculated from a least-squares data fit on the data collected from the voltage sweep. R_p data from the sensors are then recorded and converted into corrosion rate values.

Cyclic Corrosion Testing

Cyclic corrosion tests were developed in the 1960s and 1970s to test industrial maintenance coatings.^(4,5) Cyclic corrosion tests expose specimens to a series of different environments in a repetitive cycle. This cyclic approach enables simulating environments that naturally oscillate due to atmospheric conditions. Cyclic corrosion testing has been shown to be a more realistic

way of evaluating corrosion performance compared to traditional steady state exposures.⁽⁶⁾ Relative corrosion rates, corrosion structure, and morphology observed in cyclic corrosion tests are excellent predictors of corrosion performance in real service environments. This has been particularly shown for zinc and steel corrosion.^(7,8)

Cyclic cabinet testing simulates the changing outdoor environment such as corrosive ions, temperature, and humidity.⁽⁹⁾ Most previous studies performed on the corrosion testing of suspension cable bridges had employed a version of cyclic testing. Eiselstein and Caligiuri used an immersion dry cycle to estimate the rate of corrosion-induced damage.⁽¹⁰⁾ Their corrosive solution was prepared to match the chemical composition of acid rain that was collected from the Williamsburg Bridge in the City of New York. Betti and Vermaas et al. used solutions of higher acidity and salinity, applied as fog sprays, in order to further increase the corrosion rate. (See references 9 and 11–14.) Suzumura et al. employed wet-dry cycles by wetting gauzes wrapped around bridge wires through periodic water sprays. (See references 15–18.) Instead of preparing saline solutions, a method of depositing salt particles on the surface of test specimens prior to cyclic testing was selected.

In this study, an array of solutions ranging from mild to high corrosiveness were used as fog sprays. Cyclic tests were also run at different temperatures to investigate the impact of temperature on the corrosion rate.

Preliminary Testing:

The 290.4-gal (1,100-L) capacity Q-fog cyclic corrosion tester shown in figure 4 was used to run the cyclic tests. The corrosion tester is capable of running different cycles (fog, dry-off, and humidity) repetitively to reproduce outdoor cyclic conditions.



Figure 4. Photo. Q-fog cyclic corrosion tester.

The sensors were first tested for their durability and ability to function under cyclic variation of relative humidity. A two-step cycle consisting of a high and a low humidity step was repeated continuously. At the start of the high humidity step, relative humidity within the chamber rose to 100 percent and remained constant for the rest of the phase. In the low humidity phase, the moist air inside the chamber was purged, and the relative humidity dropped to approximately 30 percent.

Figure 5 shows 2 of the 49-wire bundles used in this test. LPR sensors were placed in various locations on the surface and inside the bundles. The sensors showed high sensitivity to humid environments and were successful in capturing the start of corrosion reactions. Figure 6 illustrates an LPR sensor showing the onset of corrosion.

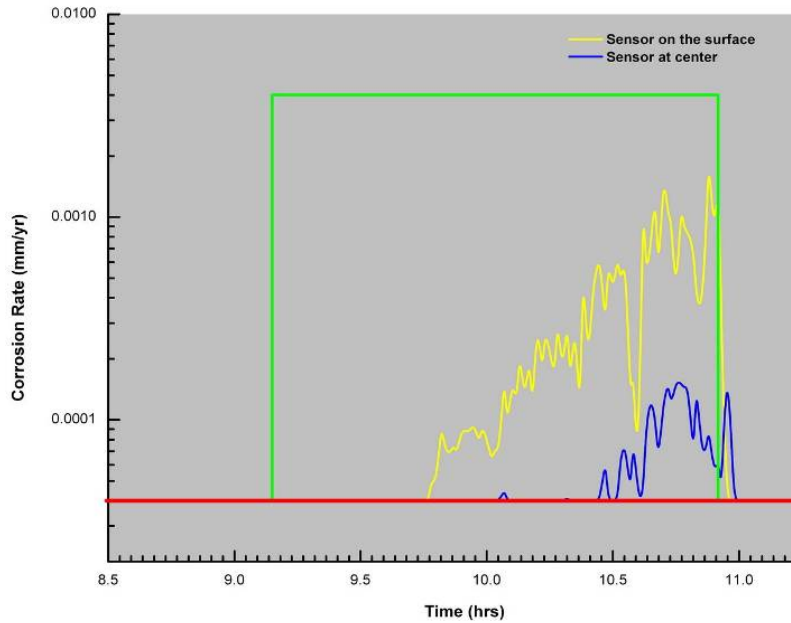


Figure 5. Photo. Wire bundles to be placed in corrosion chamber.



Figure 6. Photo. Onset of corrosion in an LPR sensor.

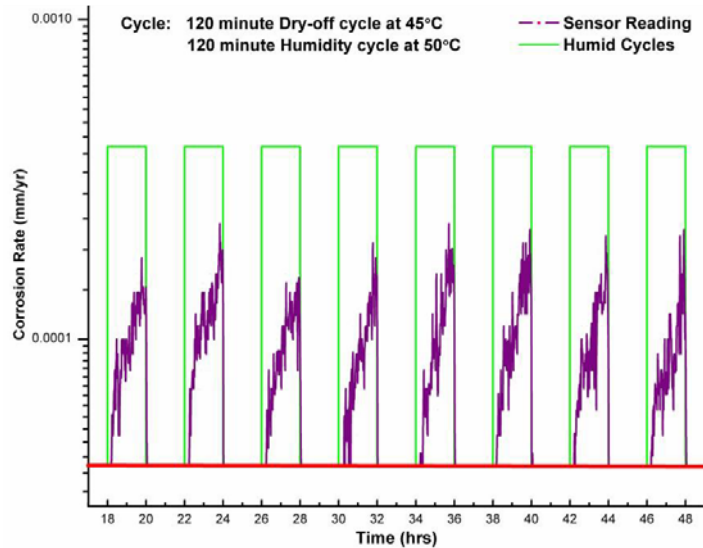
Figure 7 shows corrosion rate readings from two LPR sensors, one located on the surface (yellow line) and the other located at the center of a bundle (blue line) during a single high humidity step. The green ramp function indicates the start and the end of this humidity step. With the start of the humidity phase, relative humidity inside the chamber increased gradually and reached 100 percent. From the figure, it can be observed that the sensor mounted on the surface of the bundle detected corrosive activity earlier and at a higher rate than the sensor inside the bundle. This was expected since the wire bundle acts as a barrier against moisture.



1 inch = 25.4 mm

Figure 7. Graph. Close-up of a humidity step.

The next step of the testing was aimed at examining the consistency of the sensors when subjected to the same humidity cycle for an extended duration of time. Figure 8 shows corrosion rate readings from an LPR sensor subject to repetitive cycles. Each cycle lasted 4 h and consisted of 120 min of humid environment at 122 °F (50 °C) and 120 min of dry cycle at 842 °F (450 °C). Since the goal of this testing program was to calibrate the sensor readings to the wire corrosion rate, it was important to keep the sensor away from saturation, which is why the corrosion rate readings were low. In addition, this was the actual corrosion rate of the sensor and not that of the bridge wire. To determine this correlation, it is important to prevent saturation in the sensor. Corrosion rate readings obtained from sets of sensors with the same interdigitation distance and in the same environmental conditions were found to be consistent over time and in agreement with each other.



1 inch = 25.4 mm
1 °C = (°F - 32)/1.8

Figure 8. Graph. Corrosion rate versus time in cyclic humidity testing of a sensor.

Several tests consisting of humidity, dry-off, and fog cycles were run to test the survival of sensors in harsh environments. During the fog cycles, aggressive solutions of low pH and high chloride content were sprayed on the sensors in fine mist form. Figure 9 shows an LPR sensor after a week of testing with a solution of pH = 2.5 and 3.5 percent sodium chloride in weight. Most of the sensors ceased to function after a week of cyclic testing under these severe conditions. The LPR sensors performed better in milder tests of humid dry cycles in the 77 to 140 °F (25 to 60 °C) range and fog sprays of pH = 3.5 and higher. Almost all of the sensors were functional after a month of cyclic testing with only a few sensor failures.



Figure 9. Photo. Corroded LPR sensor after 1 week test.

Experimental Program:

After evaluating the performance and establishing the soundness of LPR sensors, cyclic tests were run to collect calibration data for the LPR sensors. A series of tests were conducted in which LPR sensors and bridge wires with the zinc coating removed were placed in the cyclic corrosion chamber at the same time and subjected to the same environment. Corrosion rate

readings from the sensors were recorded and integrated over time, while the mass loss from before and after the testing was measured for the wires. By correlating the sensors' reading with the wires' mass loss, it was possible to obtain the proportionality constant that allows to adjust the sensors' reading to the wires.

An array of LPR sensors (up to 6 sensors for experiment) were mounted on a Plexiglas® board and placed in the vicinity of the bridge wire samples (10 for each experiment). The sensors were connected to a data acquisition unit supplied by Analatom Inc., which communicated with a computer via a serial port. This unit was capable of recording R_p readings from up to eight channels at specified intervals. During each test, R_p data from the LPR sensors were recorded at 1-min intervals for the duration of the test. These readings were used for calibrating the sensors against the measured mass loss for bridge wires undergoing the same tests.

The corrosion cycle used in this study is similar to the cyclic acidified salt fog test A2 outlined in ASTM G85-02.⁽¹⁹⁾ The 3-h three-step cycle consisted of the following:

- 10 min of salt fog.
- 120 min of high humidity.
- 50 min of low humidity.

In the salt fog step, a fog solution was sprayed on the specimens through a nozzle in fine mist form. Distribution of the fog spray was homogeneous within the corrosion chamber. As the high humidity step began, relative humidity in the chamber increased to 100 percent and remained constant throughout the phase. During the following low humidity phase, the moist air inside the chamber was purged out, and relative humidity dropped to a constant ambient laboratory level of approximately 30 percent.

For each experiment, 48 cycles were performed. A total of 18 experiments were carried out to study the effects of temperature, pH, and chloride concentration on the corrosion rate of bridge wires. In six of these experiments (1, 2, and 4–7), wires were placed together with sensors to obtain recordings needed for sensor calibration. Chloride content and pH of fog solutions were varied, along with the temperature at which each test was run. Table 3 lists the test conditions for each experiment. The pH of the fog solutions were adjusted with acetic acid to attain pH values of 3.0, 4.0, and 6.0. Chloride content was regulated by sodium chloride to achieve 100 and 500 ppm chlorine ion solutions. For 100 ppm, 0.02 oz (0.62 g) of sodium chloride per gallon of water were used, while 0.11 oz (3.115 g) were used for the 500 ppm condition.

Table 3. Experimental program.

Experiment Number	Temperature (°C)	pH	Chlorides (ppm)
1	30	6	100
2	35	6	100
3	45	6	100
4	30	4	100
5	35	4	100
6	45	4	100
7	30	3	100
8	35	3	100
9	45	3	100
10	30	6	500
11	35	6	500
12	45	6	500
13	30	4	500
14	35	4	500
15	45	4	500
16	30	3	500
17	35	3	500
18	45	3	500

$$1\text{ }^{\circ}\text{C} = (\text{ }^{\circ}\text{F} - 32)/1.8$$

Wires used in the tests were typical high-strength bridge wires of 0.196-inch (4.95-mm) nominal diameter including the protective zinc coating and 0.192-inch (4.88-mm) diameter without the coating. The samples were prepared by cutting long, straight bridge wires into 10-inch (254-mm) segments. For each experiment, 10 samples were prepared. Since the purpose of testing was to investigate the corrosion of steel, the zinc coating layer was removed by immersing the wires in hydrochloric acid until all the zinc was dissolved. The wires were then rinsed thoroughly and hot air dried in a desiccator. The clean, dry specimens were weighed to the sixth significant figure.

The 10 samples were placed in the corrosion chamber as shown in figure 10. Wires were held in place using two racks made out of acrylic. The only points of contact between the wires and the acrylic racks were at the wire ends where the wires were supported. These contact points were confined to thin strips of less than $\frac{1}{8}$ inch (3.18 mm). Wires were hanging freely in between the support racks. This setup ensured that the corrosion reactions were only between the wires and the atmosphere within the chamber. At the end of each test, samples were hot air dried in a desiccator for 24 h. To measure the corrosion loss for each specimen, corrosion products were removed from the surface of each wire. First, extraneous deposits and bulky corrosion products were removed by brushing. Special care was given to the cleaning so that the uncorroded metal was not removed along with the corrosion products. A chemical cleaning procedure given in ASTM G1-03 was followed to remove the remaining corrosion products.⁽²⁰⁾ The following solution was prepared at room temperature:

- 34 fl oz (1,000 mL) of hydrochloric acid.
- 0.7 oz (20 g) of antimony trioxide.
- 1.75 oz (50 g) of stannous chloride.

Wires were immersed in this solution until all remaining corrosion products were removed. The solution was vigorously stirred by a magnetic stirrer during this phase. Wires were removed from the solution every 5 min, wiped with a cloth, and inspected for remaining corrosion products. If rust was still present on a wire, the wire was returned to the cleaning solution; otherwise it was dried and weighed. The difference between this final sample weight after cleaning and the initial weight gives the total corrosion loss in terms of mass. This loss was then converted to uniform thickness loss using the known geometric properties of the bridge wires.

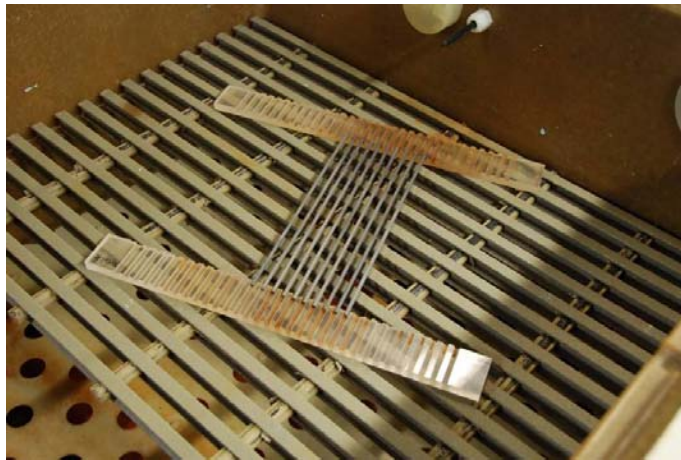


Figure 10. Photo. Specimens placed in the Q-fog cyclic corrosion tester.

Table 4 presents the average weight loss and an equivalent value of the corrosion depth for all wires used in the 18 experiments.

Table 4. Average weight loss and equivalent corrosion depth for wire specimens.

Experiment Number	Weight Loss (g)	Corrosion Depth (μm)
1	0.2696	14.87
2	0.3020	16.67
3	0.3249	17.93
4	0.3204	17.68
5	0.3543	19.56
6	0.3838	21.19
7	0.3539	19.56
8	0.3760	20.76
9	0.4409	24.35
10	0.2829	15.61
11	0.3147	17.37
12	0.4025	22.23
13	0.3398	18.76
14	0.3840	21.20
15	0.4382	24.20
16	0.3746	20.68
17	0.4292	23.70
18	0.5068	28.00

1 oz = 28.35 g

1 inch = 25,400 μm

Calibration of LPR Sensors:

Table 5 presents a list of the experiments where the sensors were tested for calibration and the type of sensors used. In experiment 3, there were power problems with the data acquisition system (DAQ), so the measurements obtained by the three sensors in the test were not considered in the analysis. On the contrary, experiment 3 appears in the list of the experiments for the determination of the corrosion rate of the wires (see table 4) since the wires were not affected by the malfunctioning of the DAQ.

Table 5. Type and number of LPR sensors used in experiments.

Sensor Type	Number of Sensors per Experiment Number						
	1	2	4	5	6	7	
150 μm	1	1	—	2	2	2	
300 μm	—	—	—	2	2	2	
1,200 μm	—	—	1	2	1	2	

— Indicates that there were no sensors of that type.

1 inch = 25,400 μm

In order to obtain the bridge wire corrosion rate from the measurements of the LPR sensors, a relationship between corrosion rate of the wire and the R_p readings from the sensors was needed. The corrosion rate was calculated from measured R_p and from mass loss measurements on the corroding metal using the concept of equivalent weight and Faraday's Law (see appendix A for details on how to obtain the proportionality constant to convert the corrosion rate measurements from the sensor reading to the corrosion rate of the bridge wires). Figure 11 through figure 13 show the calculated overall proportionality constants from the experiments for 0.006-, 0.012-, and 0.048-inch (150-, 300-, and 1,200- μm) sensors, respectively. The mean values of the constants are also displayed. The constants for the 0.006- and 0.012-inch (150- and 300- μm) sensors are virtually identical. However, the constant calculated for the 0.048-inch (1,200- μm) sensor is two orders of magnitude smaller. This cannot be explained by the decreased sensitivity due to the larger interdigtation gaps of the 0.048-inch (1,200- μm) sensor. Stemming from this, higher R_p values would be expected for the 0.048-inch (1,200- μm) sensor compared to the 0.006- and 0.012-inch (150- and 300- μm) sensors. Consequently, the 0.048-inch (1,200- μm) sensor should have had higher constants than the rest of the sensors. Apart from this peculiarity with the order of magnitude of the constants calculated for the 0.048-inch (1,200- μm) sensor, the variance in constants calculated for the three sensor types are all reasonably low, suggesting a consistency of the results. This suggests that the proportionality constants obtained for LPR sensors were accurate, and so these LPR sensors could be considered as a valuable means for measuring corrosion rate of bridge wires.

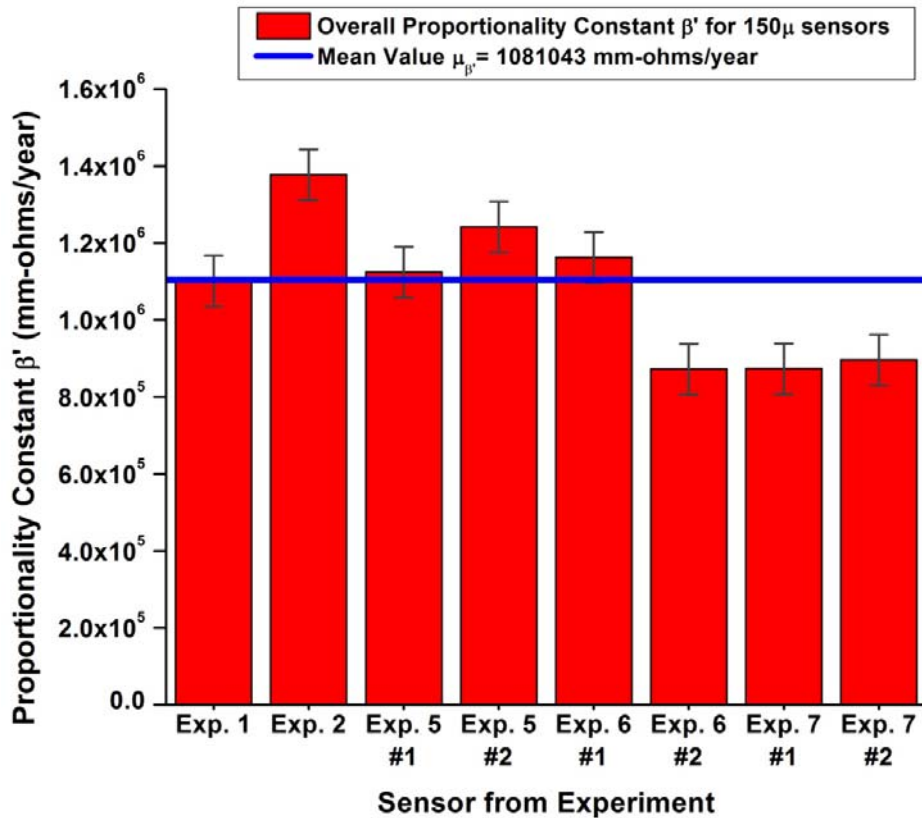
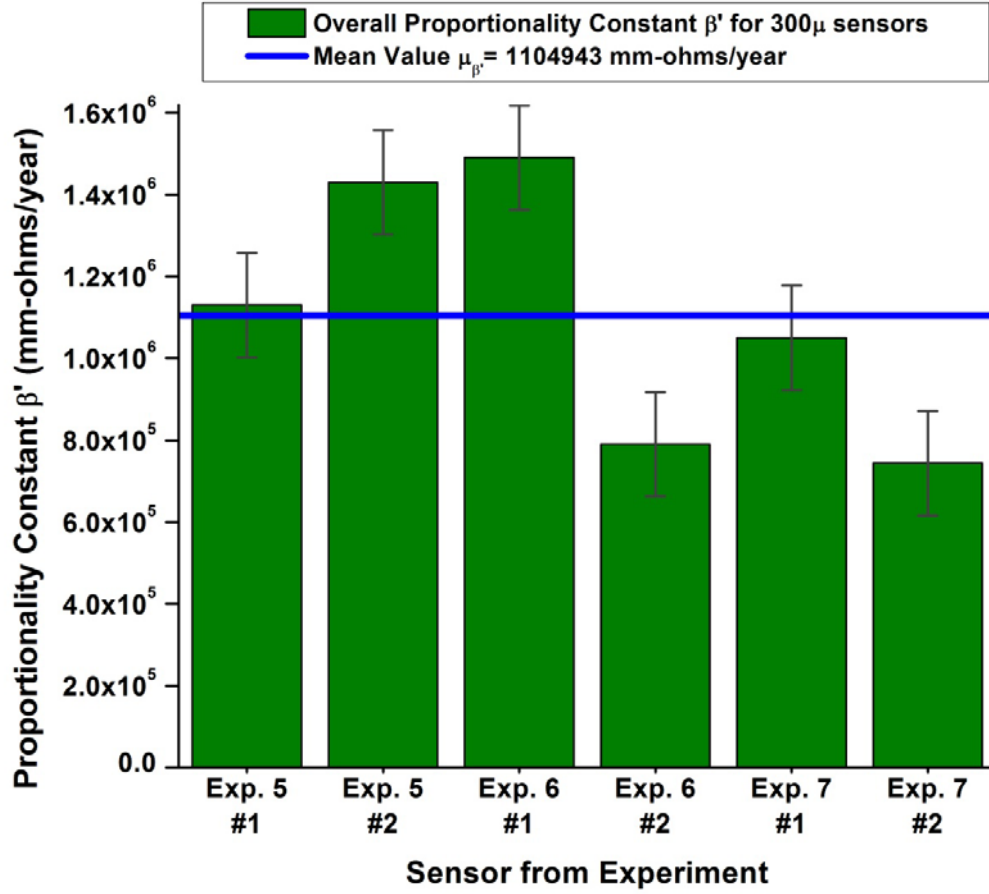
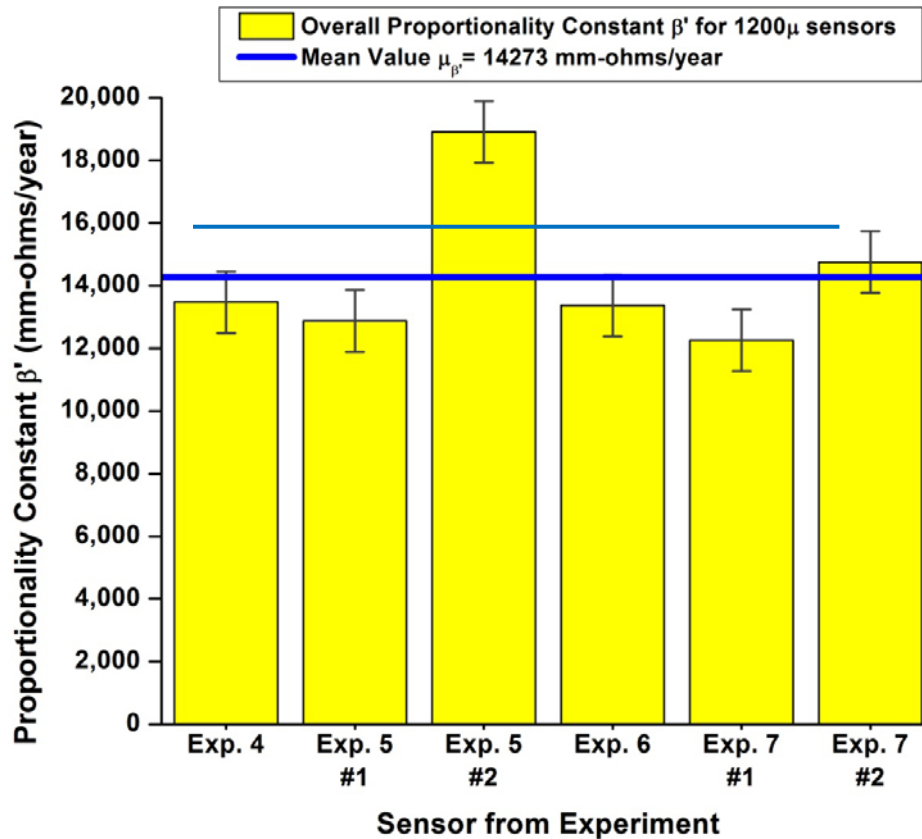


Figure 11. Graph. Proportionality constant for 0.006-inch (150- μm) sensors.



1 inch = 25.4 mm
 1 inch = 25,400 μ m

Figure 12. Graph. Proportionality constant for 0.012-inch (300- μ m) sensors.



1 inch = 25.4 mm
 1 inch = 25,400 μm

Figure 13. Graph. Proportionality constant for 0.048-inch (1,200- μm) sensors.

Multiple Array Sensor

The multiple array sensor produced by Corr Instruments, Inc., was chosen as a corrosion rate monitoring sensor because of its geometry (a cylinder of similar diameter as a bridge wire fits perfectly inside the wire bundle) (see figure 14). These sensors were built specifically for this project and utilized electrodes of the same materials (steel and zinc) that are used in the bridge wires.

Figure 14 and figure 15 show the principle of a coupled multi-electrode corrosion sensor (CMAS). When a metal is covered by a corrosive electrolyte such as seawater or a thin film of brine formed by the deliquescence of salt deposits on the metal, corrosion may take place.⁽²¹⁾ The corrosion may be localized or nonuniform even in most cases of general corrosion. Some areas of the metal corrode more, while other areas corrode less. The areas that corrode more are considered as the anodic areas, and the areas that corrode less are referred as the less anodic or the cathodic areas. Electrons released at the anodic areas flow to the cathodic areas (see top section of figure 15). Such electron flows represent the unevenness of the corrosion taking place on the metal surface. If the metal is divided into many small pieces, with some of them mainly covered by the anodic areas and other areas mainly covered by the less corroded or not corroded areas, and these small pieces are electrically connected together through an instrument externally, the electrons produced at the anodic areas would flow through the instrument.

Thus, the electron flows can be measured by the instrument and converted to nonuniform corrosion rate using Faraday's Law. This is the principle on which the multiple array sensor is based on, with the anodic pieces being called the anodic electrodes and the cathodic pieces the cathodic electrodes.

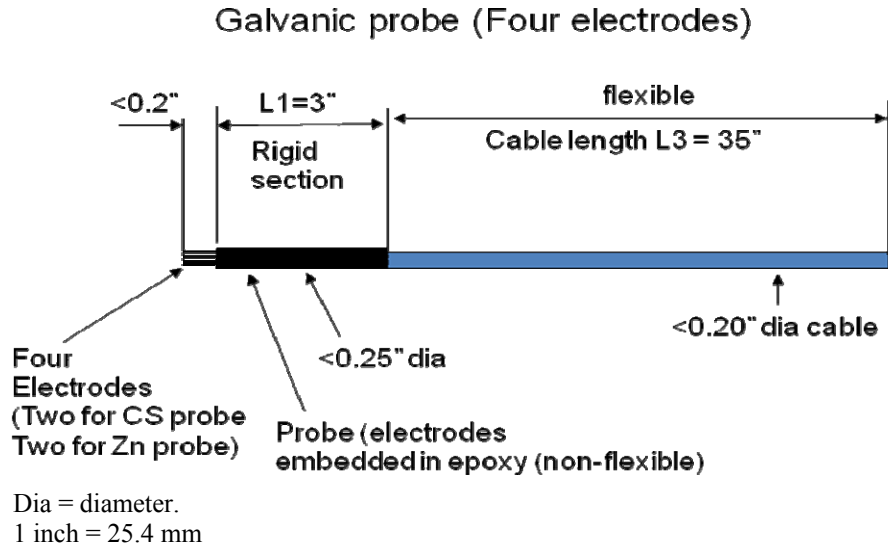
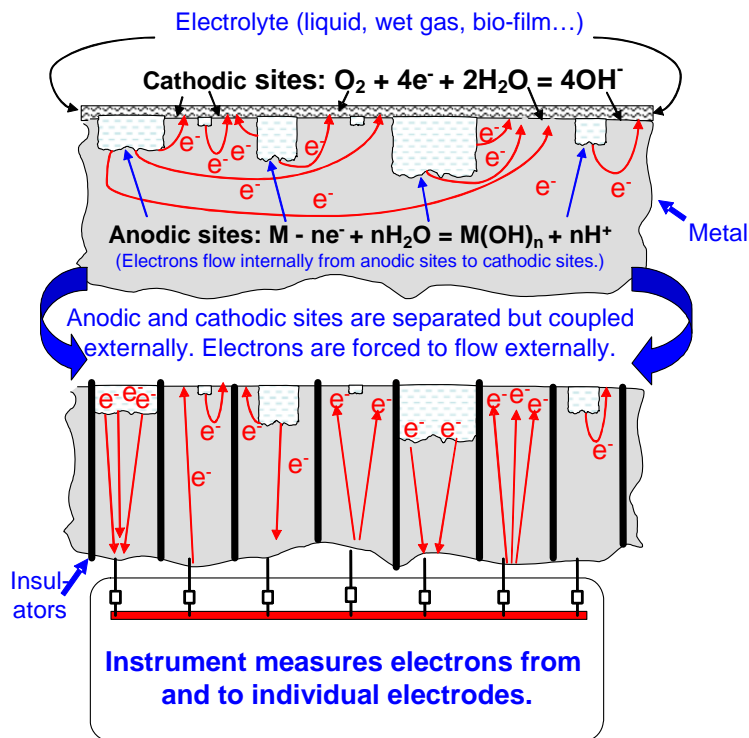


Figure 14. Illustration. Schematic description of CMAS probe.



H = hydrogen; O = oxygen; M = metal, E = electron, and n = integer.

Figure 15. Illustration. Electrons flow from anodic areas to cathodic areas inside a metal (top) and through a CMAS probe (bottom).

For this study, two types of CMAS were provided. One type was developed using a probe approximately 0.19 inch (5 mm) in diameter with eight high-strength steel filaments isolated with rubber (figure 16). The other type of CMAS sensors had the steel filaments replaced by zinc filaments in order to obtain measurements of the corrosion rates both of the steel core of the wire (once the wire coating has been depleted) and of the zinc coating itself.



Figure 16. Photo. Close-up of a CMAS.

BM or Galvanic Sensors

Figure 17 shows the schematic diagram of a galvanic probe for corrosion monitoring.⁽²²⁾ A sensing electrode made of a material whose corrosion rate is of interest is connected to a cathodic electrode via an ammeter, usually a zero-resistance ammeter. The cathodic electrode is made of a metal that has a higher corrosion potential than the sensing electrode. For instance, if the sensing electrode is made of CS and has a corrosion potential (open circuit potential) around -0.6 versus silver/silver chloride in seawater, the cathodic electrode is usually made of copper or stainless steel which has a corrosion potential near zero in seawater. The current from the ammeter is an indication of how much the sensing electrode is corroding under the polarized condition.

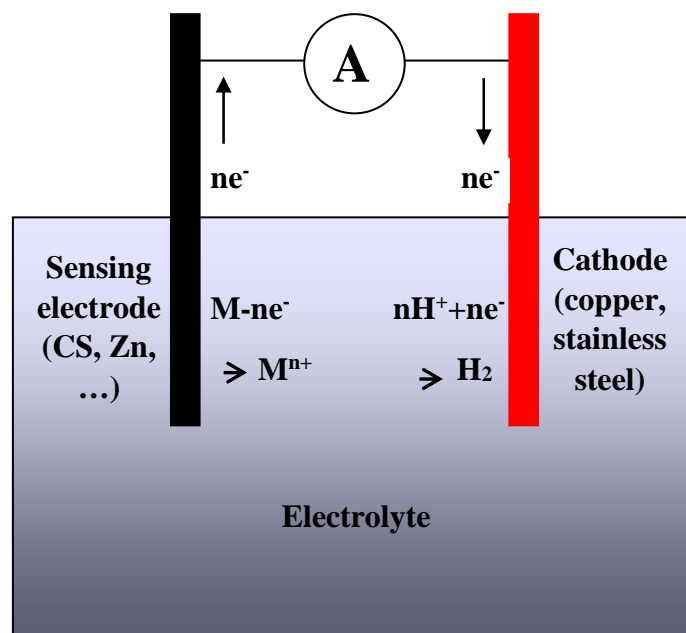


Figure 17. Illustration. Schematic diagram of a galvanic probe.

Because the sensing electrode is at a potential that is higher than the normal natural corrosion potential, such current is not the corrosion current under natural conditions and is usually higher than the true corrosion current. However, if many such identical galvanic probes are used and installed at different places, these may provide good indications for the relative corrosivity of the environment at the different places. If the corrosion rate at certain locations is measured using a quantitative probe (such as a CMAS probe), the corrosion rate at the different locations may be estimated using the results from the galvanic probes.

Temperature-Relative Humidity Precon HS2000V Sensors

The Precon HS2000V humidity sensors combine capacitive polymer sensing technology with a novel measurement method, eliminating the need for temperature correction and calibration by the user. The sensor, calibrated by the manufacturer, includes a thermistor and circuitry to correct for temperature and calculate the true relative humidity. The sensor provides both humidity and temperature outputs and is accurate to ± 2 percent. The sensor covers a standard temperature range of -22 to 185 °F (-30 to 85 °C) and can operate within a humidity range from 0 to 100 percent.

The dimensions of the sensor are 0.89 inch (22.61 mm) long, 0.47 inch (11.94 mm) wide, and 0.365 inch (9.27 mm) tall (see figure 18). Since the goal was to install these sensors inside the cable, special protection was needed to protect the sensor from crushing because of the surrounding wire pressure. The performance of this sensor was tested through a series of laboratory tests.

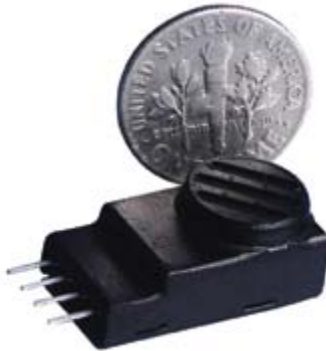


Figure 18. Photo. Precon HS2000V temperature/relative humidity sensor.

DIRECT SENSING TECHNOLOGIES

AE and MS Technologies

AE

AE testing is a powerful method for examining the behavior of materials deforming under stress. AE may be defined as a transient elastic wave generated by the rapid release of energy within a material, as shown in figure 19. Materials produce AE when the local stresses around a discontinuity reach levels close to yielding. The high level of stresses can result in growing cracks and breaking fibers as well as many other modes of active damage in the stressed material.

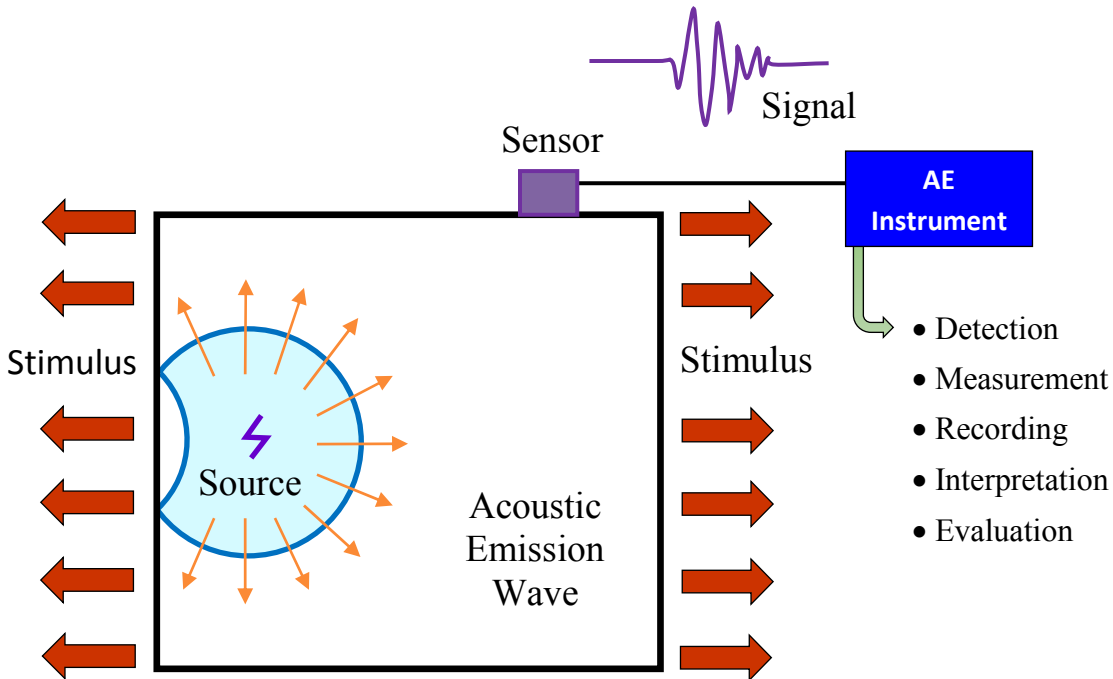


Figure 19. Illustration. AE technology principle.

Small-scale damage is detectable long before failure, so AE can be used as a non-destructive technique to find defects during structural proof tests and high load periods in civil structures.

A typical AE system consists of the following:

- A piezoelectric sensor that detects the acoustic wave traveling through the material being tested and converts it into an electric signal.
- A preamplifier that adds gain to the electric signal.
- An A/D converter board where the signal is digitized and analyzed in both the time and frequency domains.

By using several sensors distributed on the material under test or along a suspension bridge cable, the sources of AE, such as wire breaks, can be identified, detected, and located even in the mist of background noise caused by bridge movement and traffic.

MS

The phenomenon known as the MS effect consists of a small change in the physical dimensions of ferromagnetic materials by the presence of a magnetic field and, conversely, a physical deformation or strain producing a change of magnetization in the material.

Figure 20 shows the arrangement and instrumentation used for active inspection of structures using MS technology. The MS system consists of two parts: a means for applying a time varying magnetic field or detecting a magnetization change in the material (this is most conveniently

achieved by using an inductive coil that encircles a component under inspection) and a means for providing direct current (DC) bias magnetic fields to the component (this is achieved by using a permanent magnet). The DC bias magnetic fields are used to enhance the efficiency of the energy transduction between electric and mechanical energies and to make the frequency of the elastic wave follow that of the electrical signals and vice versa. When a pulse of electrical current is applied to the coil in the transmitting MS, a time-varying magnetic field is applied to the component under inspection. This field in turn generates a pulse of elastic waves in the component which propagate in both directions along the length of the component. When the propagating elastic pulse reaches the coil in the receiving MS, it causes a change in the magnetic induction of the material via the inverse-MS effect. This change induces an electric voltage in the receiving coil that is subsequently amplified, conditioned, and processed.

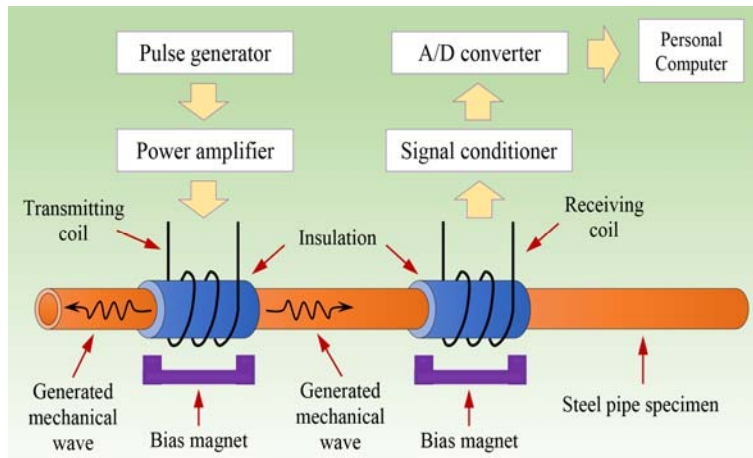


Figure 20. Illustration. MS instrument.

Combination of AE and MS Technologies

As part of the development of a corrosion condition detection system for suspension cable bridges, a study on the potential combination of the AE and MS technologies to detect wire breaks and consequent reduction of the cable's cross section was performed. The principal idea behind AE-MS is that a baseline measurement of the state of the cable can first be established and then, by interrogating the system periodically, any variation of the wave propagation characteristics of the system can be related to a certain type of damage. In this type of measurement, the MS generates an acoustic wave that propagates along the cable, and its propagation characteristics are established by analyzing the response of the AE sensors to the propagating acoustic wave. If damage appears in the cable, the propagation characteristics of the cable change in the vicinity of the damaged area and thus the characteristics of the acoustic signal propagating along the cable. In this way, an array of AE passive sensors serves as continuous online monitoring detectors of wire brakes or other type of damage, and help evaluating the damage in combination with MS.

In this project, an attempt was made to merge these two technologies, and an extensive experimental phase was planned to test such a technique in applications related to suspension bridge cables. The following series of experiments were performed using a combination of AE and MS technologies and are described in the following subsections:

1. Detection of simulated corrosion-induced damage in a single wire.
2. Detection of simulated corrosion-induced damage on a single wire inside a five-wire strand.
3. Detection of wire breaks in a strand mockup.
4. Detection, localization, and evaluation of simulated corrosion-induced damage in a wire strand under tension.
5. Detection, localization, and evaluation of simulated corrosion-induced damage in a bundle of seven strands.

1. Detection of Simulated Corrosion-Induced Damage in a Single Wire:

A series of experiments were performed to determine the sensitivity of the MS generation and AE detection (MS-AE) combined technology to the progressive loss of wire cross section due to corrosion on a single wire. For this experiment, a single steel wire that was 179 inches (4,546.6 mm) long was instrumented with three receiving sensors: R1.5I with a resonant frequency of 15 kHz, R3I with a resonant frequency of 30 kHz (both AE sensors), and an MS sensor. Another MS sensor was used to generate propagating signals in the wire. The receiving and pulsing sensors were installed at the opposite ends of the wire. The AE sensors were connected to a Physical Acoustics Corporation (PAC) eight-channel AE system, while the MS sensor, consisting of a coil and a bias magnet, was connected to an MS NDT system. The experiments consisted in sending tone burst pulses of 32 kHz using the pulsing MS.

A baseline reading was taken with the wire in good conditions without any simulated corrosion-induced damage. Then, an area of simulated corrosion-induced damage was introduced in the wire by mechanically removing part of the cross section for a short segment of the wire. This area was located in the middle point between the sensors approximately 8 inches (203.2 mm) from the wire edge. Once the corrosion damage was simulated, then measurements were taken again. The area of simulated defect was progressively increased to occupy a larger percentage of the cross section in three stages, as indicated in table 6.

Table 6. Damage induced in a single wire.

Stage	Approximate Wire Diameter Reduction
Baseline	0.196 inches
1	0.028 inches
2	0.043 inches
3	0.052 inches

1 inch = 25.4 mm

As an example of how the signals propagating in the wire change as the simulated corrosion area increased, figure 21 through figure 24 show the waveforms recorded with the R3I sensor at different stages of damage on the wire. These waveforms represent a total of six times the signal traveling back and forth along the wire. Each one of the echoes represents a reflection of the signals from the back end of the wire. In figure 21, the time elapsed between each of the echoes

can be used to estimate the propagation velocity of the wave along the wire, which in this case was calculated as 50,000 inches/s (1.27 mm/ μ s).

The waveform in figure 22 shows that as soon as the cross section of the wire was reduced by the introduction of damage, additional echoes appeared between the signals corresponding to the full wire length. These new echoes correspond to reflections produced by the damaged area.

As seen in figure 23, as the cross section area of the wire is further reduced in stage 2, the amplitude of the echoes corresponding to the damaged area decreased significantly. Finally, in stage 3, the whole signal was severely affected by a notorious loss in amplitude and by a widening of the echoes corresponding to the edge of the wire and to the corrosion area (see figure 24).

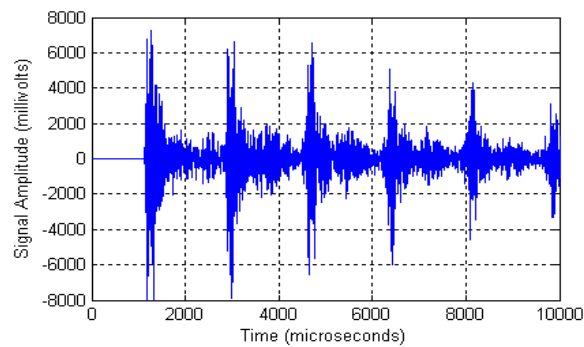


Figure 21. Graph. Acoustic signals recorded on a single wire by the R3I sensor—baseline.

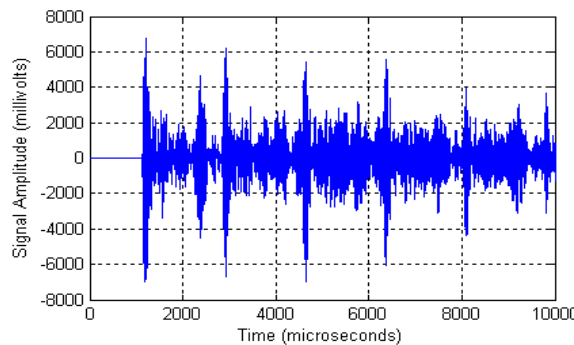


Figure 22. Graph. Acoustic signals recorded on a single wire by the R3I sensor—stage 1.

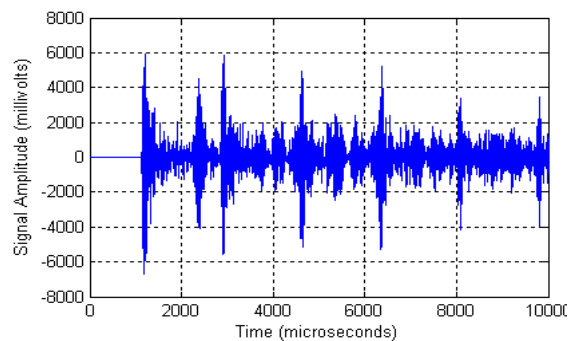


Figure 23. Graph. Acoustic signals recorded on a single wire by the R3I sensor—stage 2.

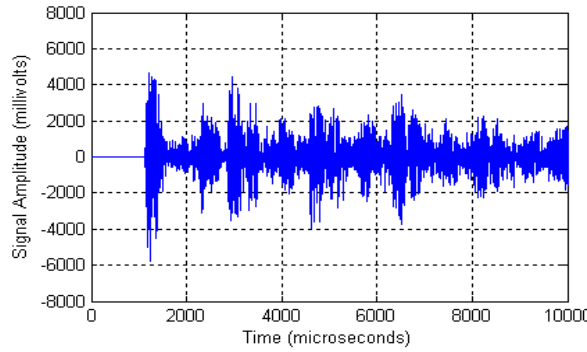


Figure 24. Graph. Acoustic signals recorded on a single wire by the R3I sensor—stage 3.

A plot of the change in maximum amplitude detected in the wire as a function of the reduction in cross section area as indicated in table 6 for the R3I and MS sensors is shown in figure 25. The results for sensor R1.5I were very inconsistent and are thus not included in this report.

The curves in figure 25 show that there is a clear reduction on the maximum amplitude of the signals traveling along the wire as the damaged area increases for both the R3I and the MS sensors. The amplitude drop for the R3I is approximately 11 percent and approximately 31 percent for the MS sensor. The drop is monotonic for the R3I with incremental drops as the damage increases, while the MS sensor dropped quickly for stage 1, increased slightly for stage 2, and dropped again for the last stage. Most likely this is a result of constructive and destructive interference in the wire, since the wavelength is approximately six times larger than the wire diameter.

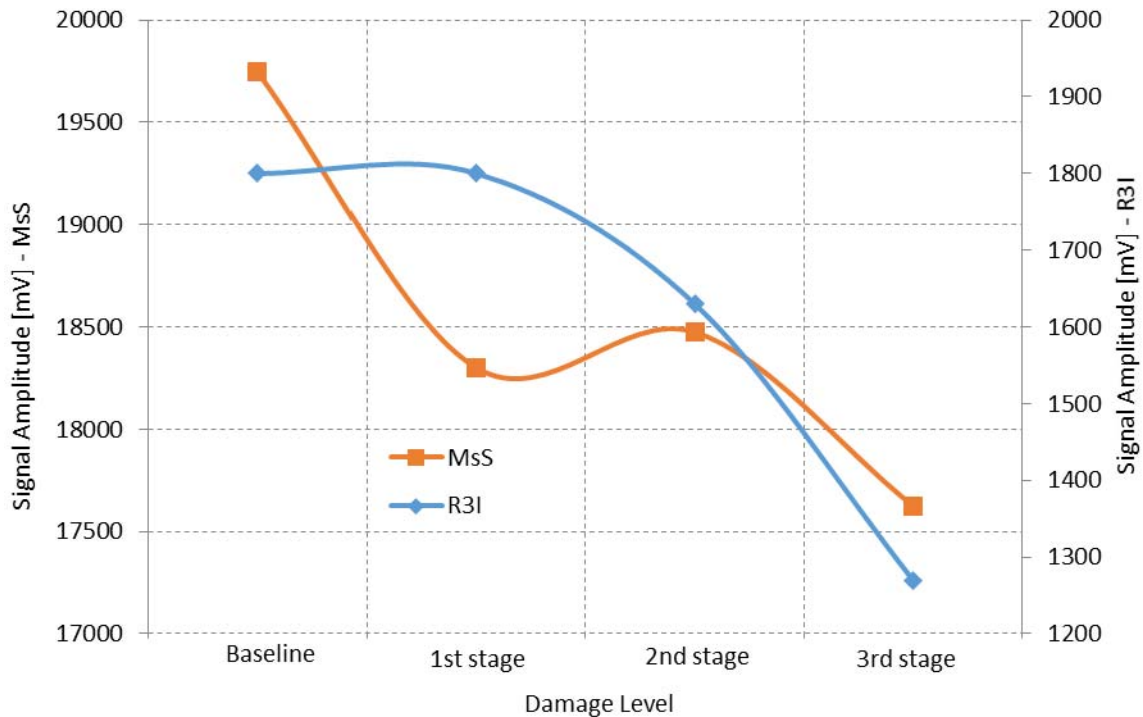


Figure 25. Graph. Maximum amplitude of the acoustic signals propagating along a single wire as function of the reduction in cross sectional area for the R3I AE and MS sensors.

In summary, the R3I sensor and the MS are more sensitive to changes in the cross section area of a single wire than the R1.5I sensor.

2. Detection of Simulated Corrosion-Induced Damage on a Single Wire Inside a Five-Wire Strand:

After demonstrating that the MS-AE technique sensitivity is enough to detect damage in a single wire, the next step was to evaluate the possibility of detecting the same type of damage in a single wire as part of a strand. For this test, five wires 170 inches (4,318 mm) long and 0.196 inch (4.98 mm) in diameter were assembled together in a strand. The R1.5I, R3I, and MS sensors were installed at the far end of the strand as receivers, while a MS device acting as a pulser was installed at the near end of the strand first on one of the outside wires and then in the center wire.

Signals with a frequency of 32 kHz were coupled into the strand, and a baseline measurement was performed. Next, an area of damage was introduced in one of the wires by mechanically removing part of the cross section. It was progressively enlarged in three stages until the wire was broken. The reduction in the wire cross section was similar as in the previous experiment (see table 6). As an example of the change in the acoustic signals propagating in the five wire strand, figure 26 through figure 31 show the waveforms detected by the three different sensors before and after the wire was broken.

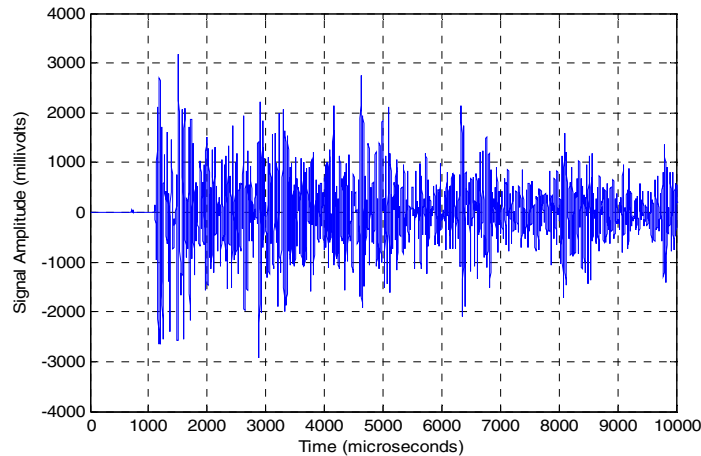


Figure 26. Graph. Acoustic signals recorded on the strand of five wires by the R1.5I sensor—baseline.

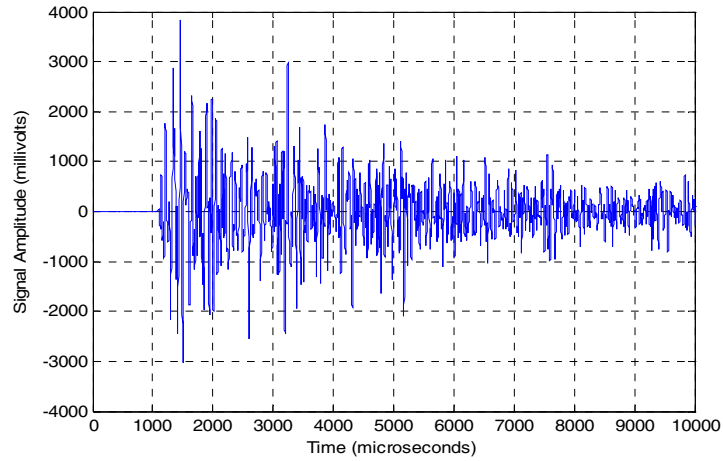


Figure 27. Graph. Acoustic signals recorded on the strand of five wires by the R1.5I sensor—after wire break.

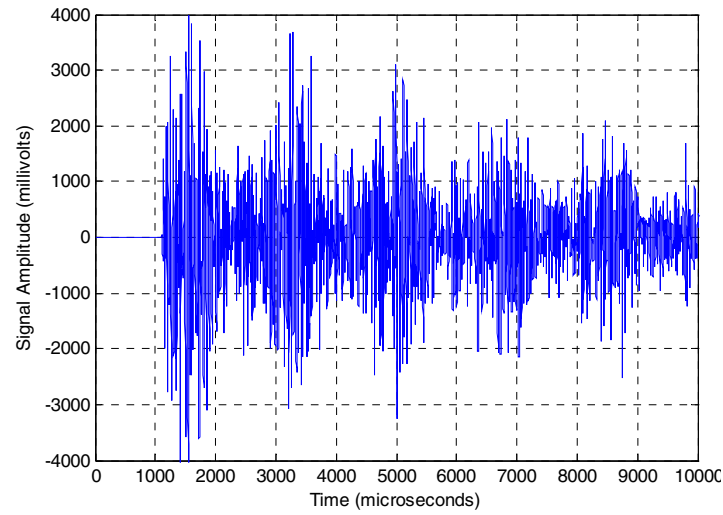


Figure 28. Graph. Acoustic signals recorded on the strand of five wires by the R3I sensor—baseline.

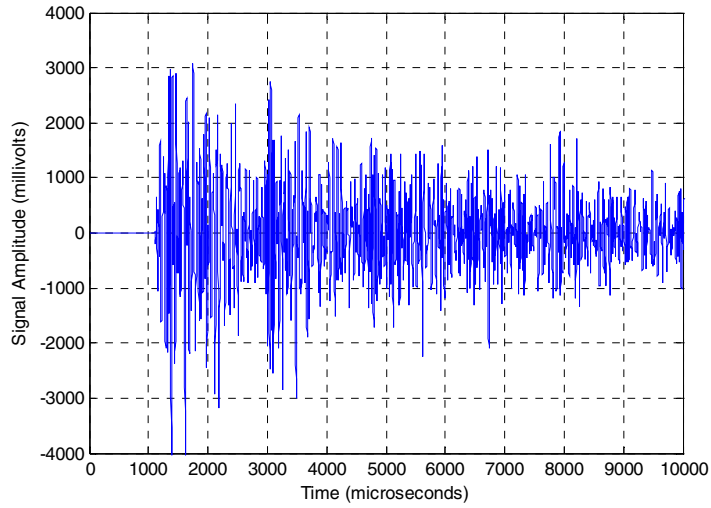


Figure 29. Graph. Acoustic signals recorded on the strand of five wires by the R3I sensor—after wire break.

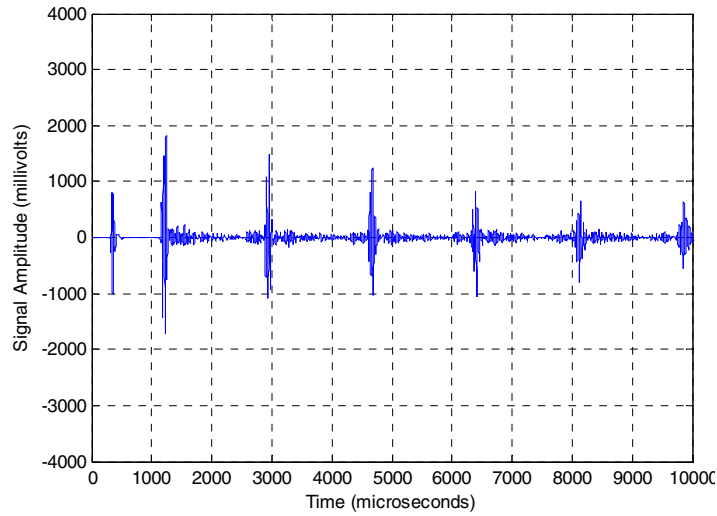


Figure 30. Graph. Acoustic signals recorded on the strand of five wires by the MS sensor—baseline.

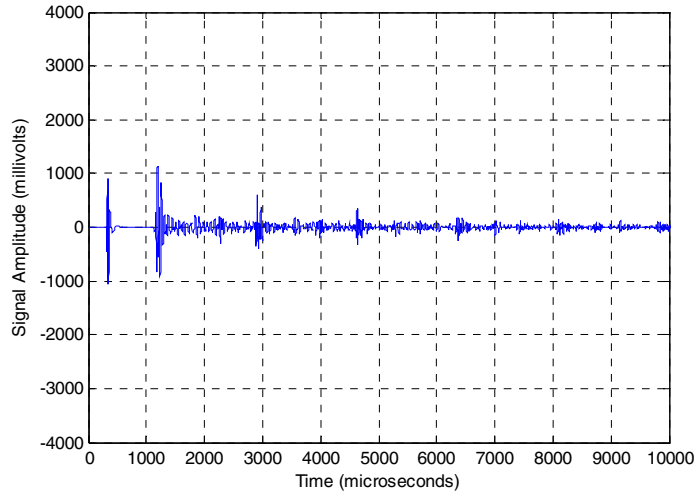


Figure 31. Graph. Acoustic signals recorded on the strand of five wires by the MS sensor—after wire break.

Using the same type of analysis discussed in the previous section, the signal’s maximum amplitude was measured for each of the sensors at every stage during the damage simulation. The results of this analysis are presented in figure 32 and figure 33.

The R1.5I sensor detected a steady drop in signal amplitude, down to 50 percent of the baseline value at the transition third stage of damage, and then increased after the wire was broken. This increase could be related to constructive interference caused by signals reflected from the damaged area and the edge of the broken wire. Taking into account this increase, the total drop in amplitude between the baseline and the broken wire was approximately 34 percent. The R3I sensor showed a small increase in amplitude at the first stage of damage and then decreased steadily to 43 percent of the baseline value.

Finally, the data from figure 32 and figure 33 show that the total drop in amplitude between the baseline and the broken wire is almost 50 percent for the MS mounted in the outside wire and almost 90 percent for the inside wire.

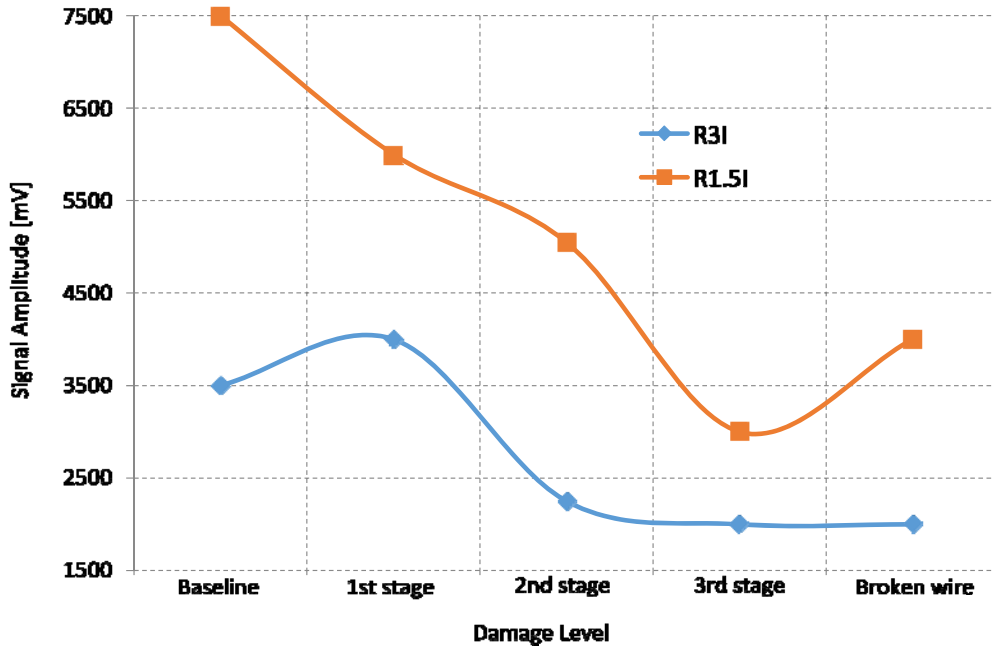


Figure 32. Graph. Maximum amplitude of the acoustic signals propagating along the five-wire strand as function of the reduction in cross section area in a single wire for R1.5I and R3I sensors.

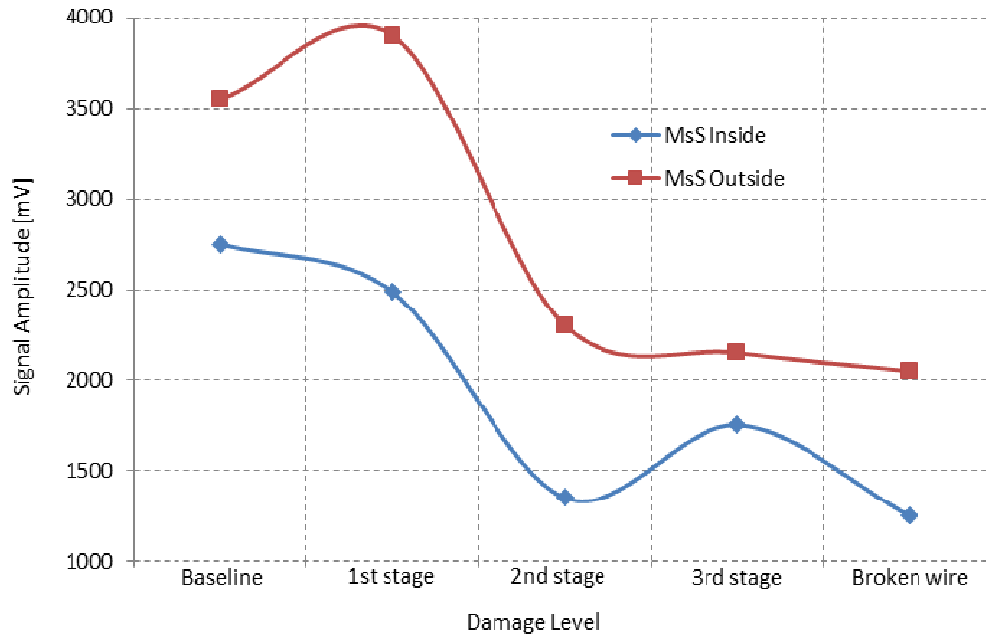


Figure 33. Graph. Maximum amplitude of the acoustic signals propagating along the five-wire strand as function of the reduction in cross section area in a single wire for MS located in one of the outside wires and in the center wire.

In summary, both AE sensors and MS in the outside and center wire show a net decrease in amplitude as the damage progresses in the five-wire strand.

3. Detection of Wire Breaks in a Strand Mockup:

In this series of tests, a strand consisting of 127 wires 0.196 inch (4.98 mm) in diameter and arranged in a hexagonal pattern was monitored as 5 wires in the strand were cut. The length of the strand was 19 ft (5.78 m). For this test, the R1.5I and R3I sensors were used as receivers, and the MS sensor was used as a pulser. The strand was monitored before any of the wires were cut to create a baseline as well as every time after a wire was cut. The R1.5I sensors were located 5 and 17 ft (1.53 and 5.16 m) from the MS, while the R3I sensors were located at 5, 10, and 17 ft (1.53, 3.05, and 5.16 m) from the MS system. The wire cuts were located 13 ft (3.97 m) from the MS position. Figure 34 shows the location of the sensors and the wire cuts.

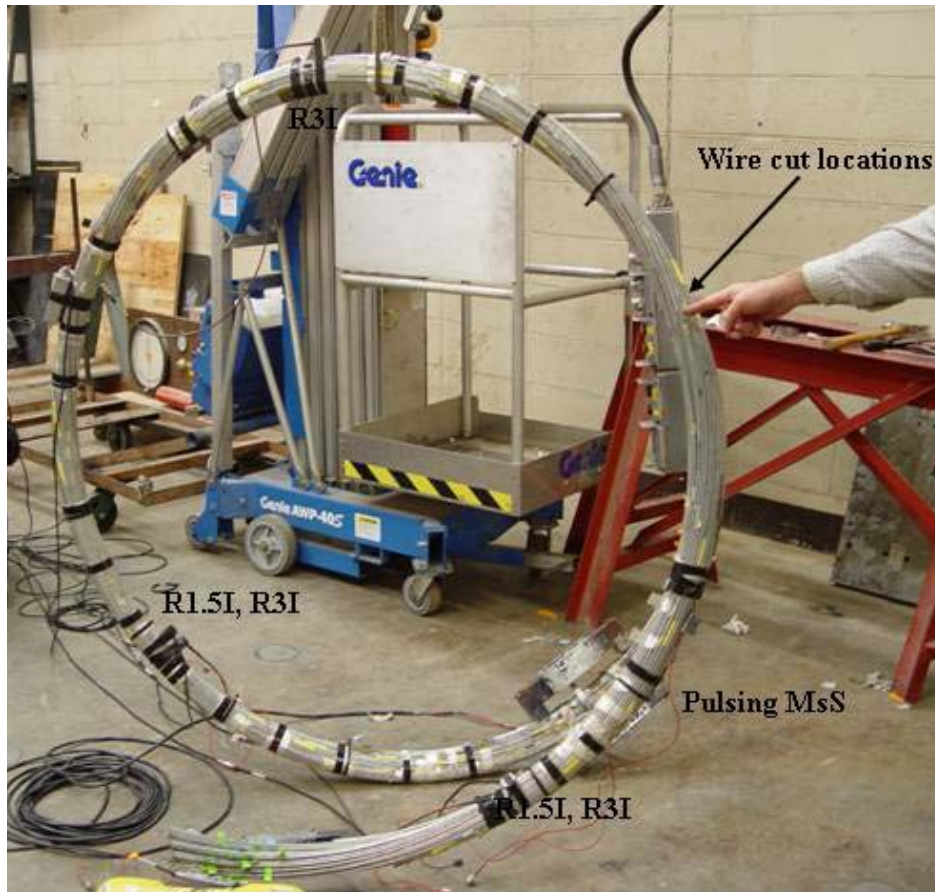


Figure 34. Photo. Location of the wire cuts and sensors on the strand.

As an example of changes in the waveforms observed in this test, figure 35 shows the signals recorded with the R1.5I sensor at the 17-ft (5.16-m) location beyond the point of the wire cuts. There was no drop in amplitude from the baseline value (see figure 35a) as well as for the first three wire cuts (figure 35b, c, and d). There was a clear drop for the last two wire cuts (see figure 35e and f). Results for the R3I sensors in the same position showed similar results.

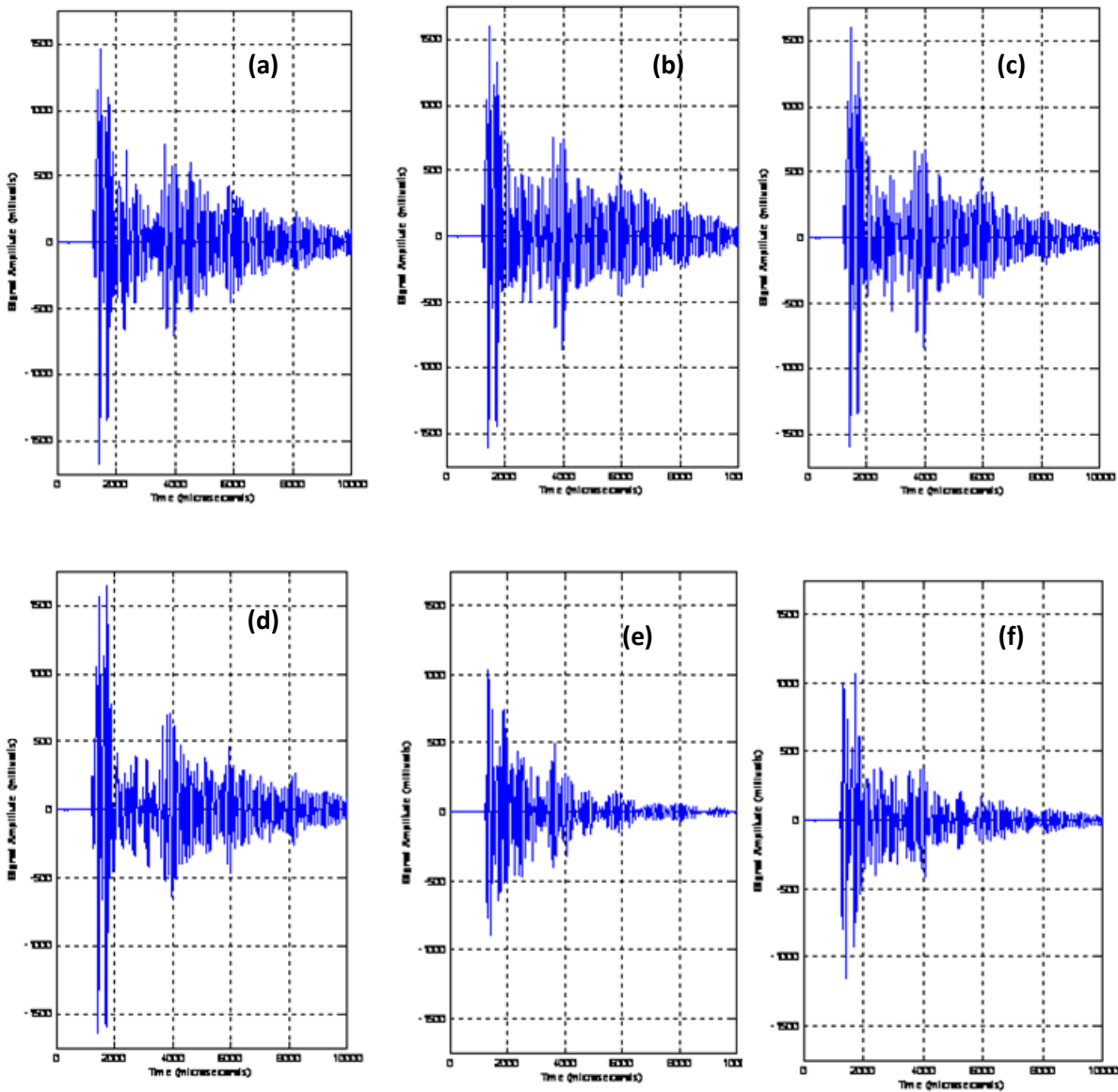


Figure 35. Graph. Acoustic signals recorded on the strand with the R1.5I sensor— (a) no damage, (b) 1 wire cut, (c) 2 wires cut, (d) 3 wires cut, (e) 4 wires cut, and (f) 5 wires cut.

Figure 36 and figure 37 show the maximum amplitude detected by the sensors located before and beyond the wire cut locations (see figure 34). It is clear that the sensors located closer to the MS were affected in a different way by the wire cuts, as shown in figure 36. Either the amplitude values fluctuated around the baseline as for the R1.5I sensor or increased as for the R3I sensor. For the sensors beyond the wire cut location, the signal dropped suddenly after the fourth wire was cut. The drop in amplitude is approximately 30 percent of the baseline value for both the R1.5I and the R3I sensors. In terms of the cross section area of the strand, this means that the MS-AE technique is sensitive to losses in the cross section area larger than 3 percent.

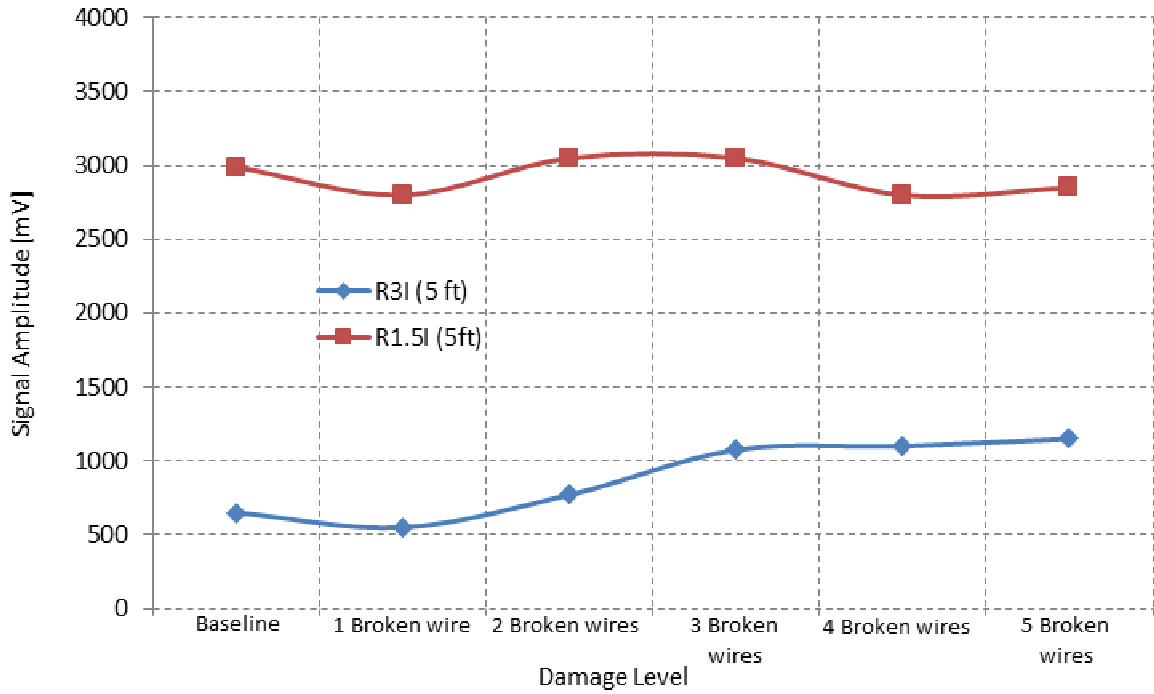


Figure 36. Graph. Maximum amplitude of the signals detected by the MS-AE technique—sensors located before the wire cut location.

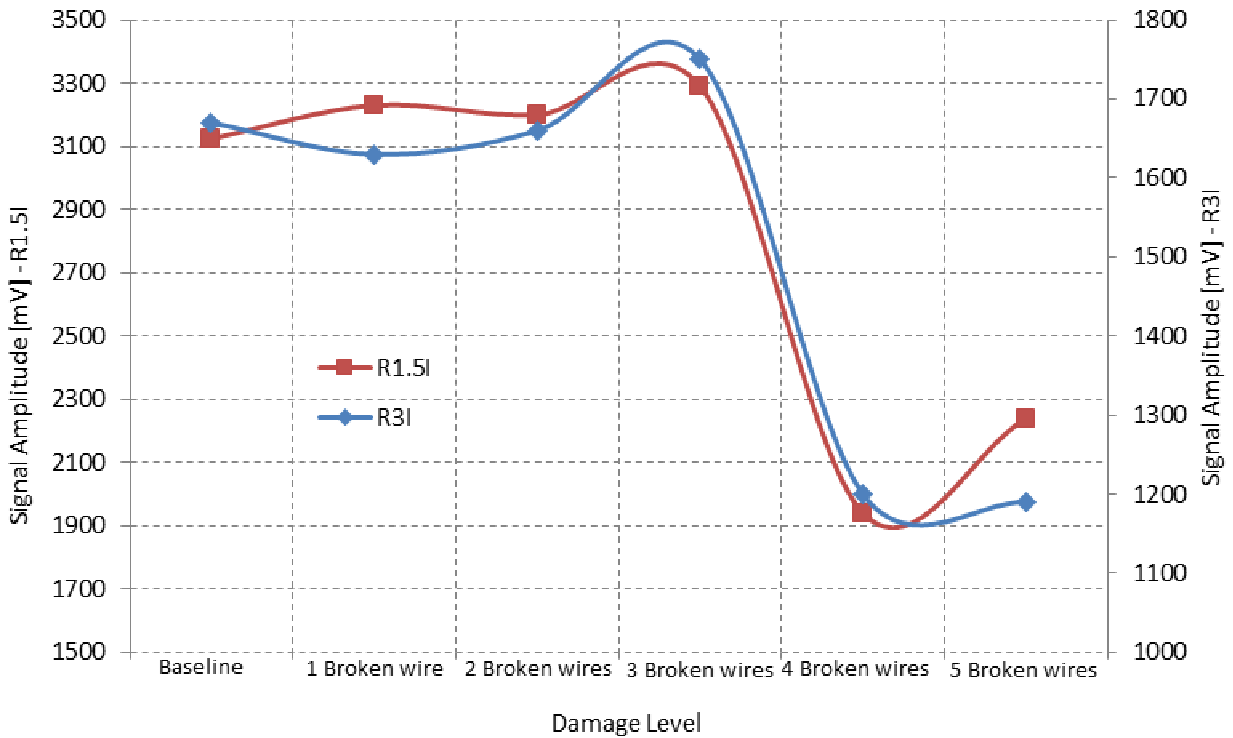


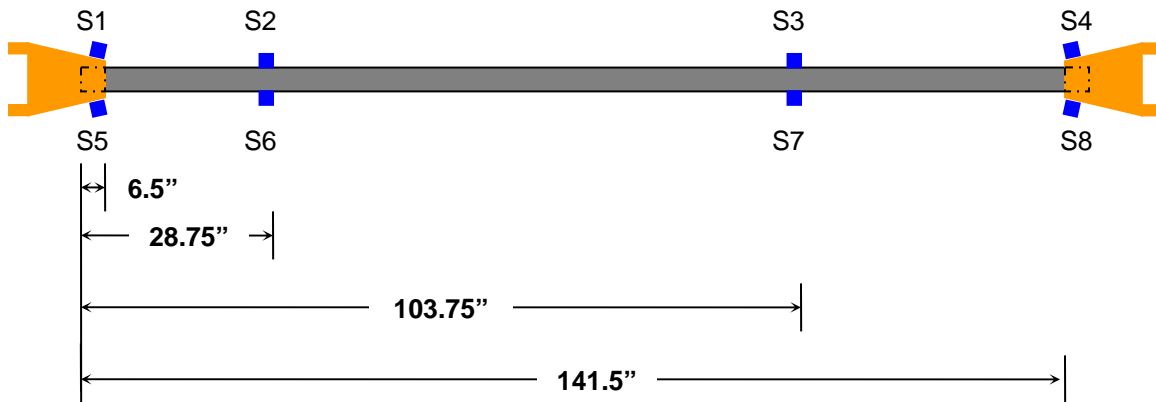
Figure 37. Graph. Maximum amplitude of the signals detected by the MS-AE technique—sensors located after the wire cut location.

4. Detection, Localization, and Evaluation of Simulated Corrosion-Induced Damage in a Wire Strand Under Tension:

The idea behind this test was that the AE system, operating in a passive mode during the increasing tension periods, would detect and locate wire breaks in real time, while the MS system, operating in active mode during the holding tension periods, would be able to evaluate the damage in the strand created by the wire breaks. During the holding tension periods, the AE sensors would be synchronized with the MS sensor to function as detectors of the acoustic signal propagating along the strand. If there is any damage caused by wire breaks, the characteristics of the propagating signal produced by the MS would change. By comparing the signals after damage has occurred with baseline data, the extent of the damage could be assessed. In this way, the MS and AE sensors would function as an active-passive system for detection and location of wire break damage in the strand.

Strand Construction and Instrumentation:

The steel wire strand used in these experiments had a length of 148 inches (3,759.2 mm) and was made of 61 wires with a diameter of 0.196 inch (4.98 mm) arranged in a hexagonal pattern and mounted on two steel sockets. The strand was instrumented with eight R3I PAC AE sensors distributed on the sockets and at two locations along the strand. The position of the sensors is shown in figure 38.



S = Sensor.
1 inch = 25.4 mm

Figure 38. Illustration. Position of the AE sensors along the strand.

Out of the 61 wires in the strand, 54 were notched, with the notches distributed along the cable at 5 different positions. The positions of the notches, labeled A to E, are shown in figure 39. A schematic of the strand cross section showing the 54 notched wires and the position and depth of each notch is shown in figure 40.

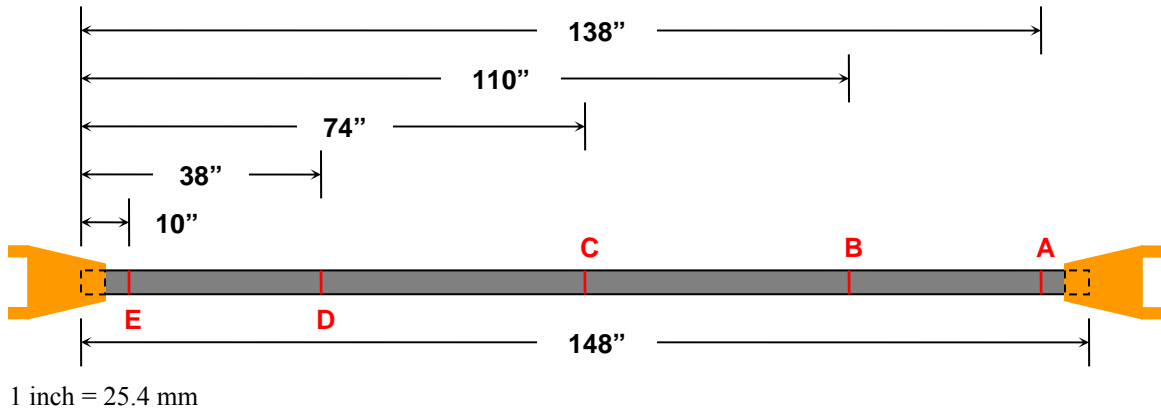


Figure 39. Illustration. Notch locations along the wire strand.

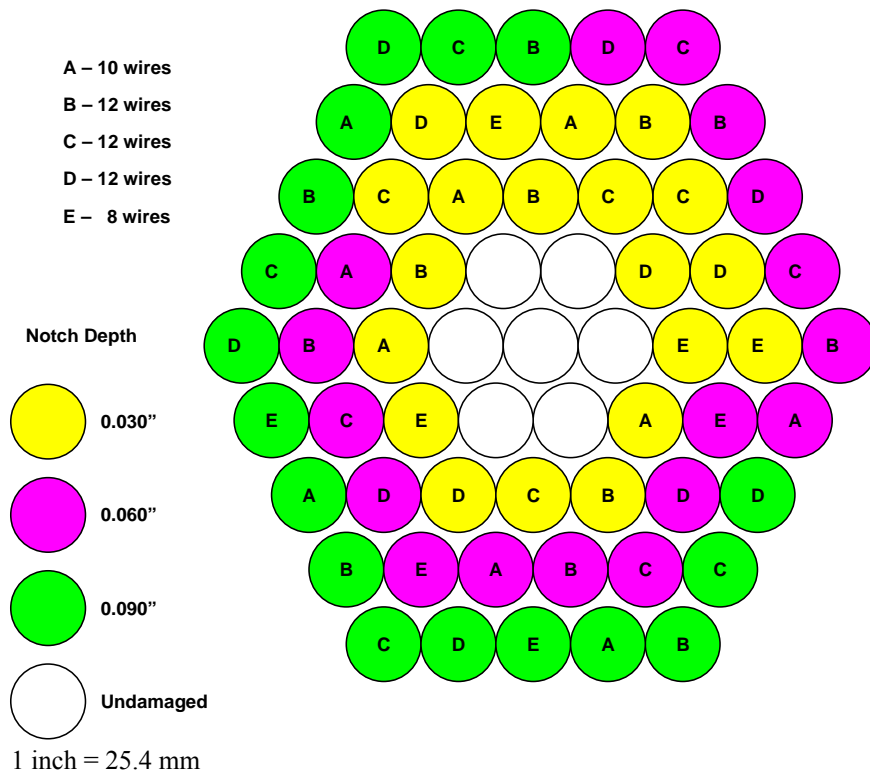


Figure 40. Illustration. Cross section of the wire strand showing position and depth of the notches along the strand length.

The instrumented strand was mounted on the tensile machine. The top end of the strand corresponds to the end where sensor 1 was mounted, according to figure 36 and figure 37. Once the strand was mounted in the tensile machine, the MS sensor was installed 116 inches (2,946.4 mm) from the top end of the strand. The AE sensors were connected to a PAC AE eight-channel Samos system, and the MS was connected to a computer controlled system. Figure 41 shows the strand mounted in the tensile machine as well as the position of the AE and MS sensors.

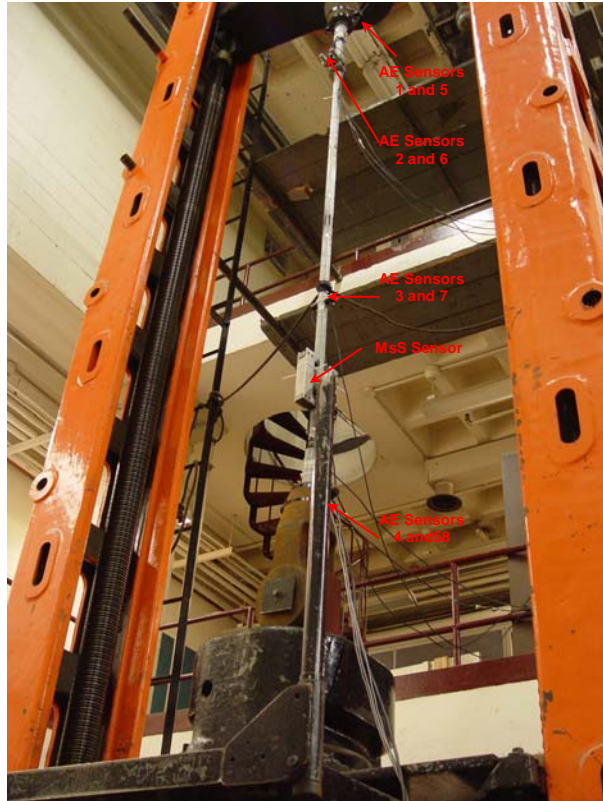


Figure 41. Photo. Wire strand mounted on the tensile machine and instrumented with AE and MS sensors.

Before applying any load, a series of pencil lead breaks (PLBs) were performed on the strand in order to verify the coupling of the AE sensors to the strand. Three PLBs were performed on the strand 4 inches (101.6 mm) from each of the sensors. The average amplitude for each sensor is shown in table 7.

These results show that the transmission of the acoustic waves from the bundle to the sensors is better for the sensors mounted on the upper socket and on the clamp than for those mounted directly on the strand and on the lower socket. These results suggest that the best location for mounting sensors in a real cable may be the cable band and not necessarily directly on the cable.

Table 7. Average signal amplitudes from PLB at sensor locations.

Sensor	Amplitude PLB (dB)	Position Along the Cable (inches)
1	80	6.5 (upper socket)
2	75	28.75 (on clamp)
3	66	103.75 (on strand)
4	66	141.5 (lower socket)
5	78	6.5 (upper socket)
6	77	28.75 (on clamp)
7	64	103.75 (on strand)
8	69	141.5 (lower socket)

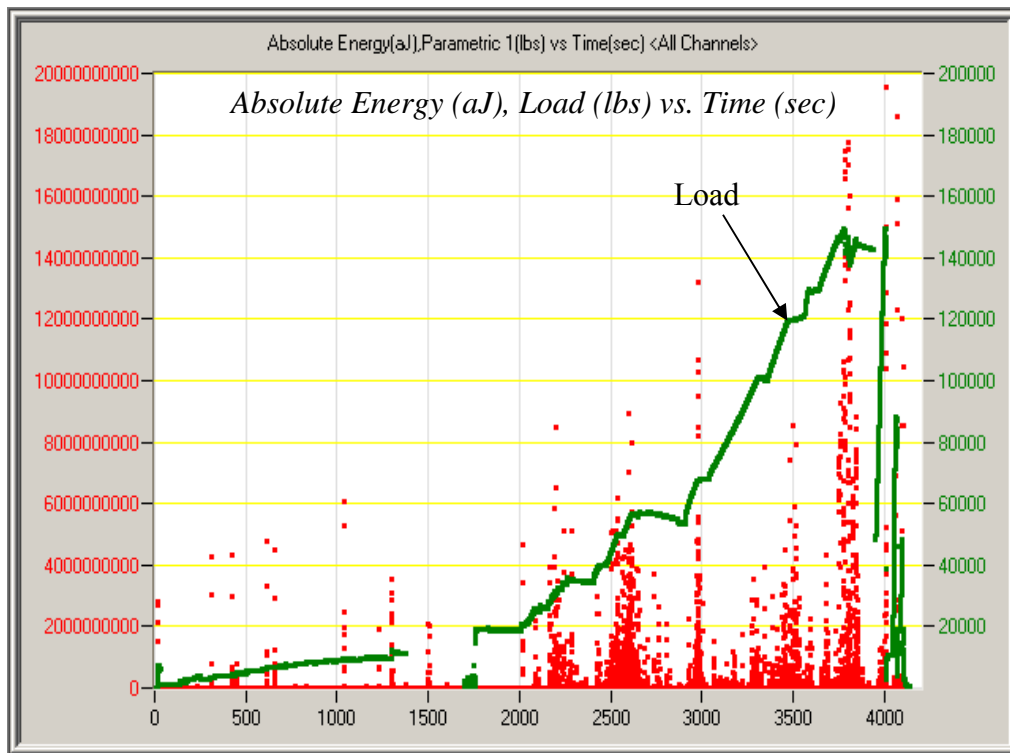
1 inch = 25.4 mm

Detection of Wire Breaks During the Tensile Test of the Strand Using AE Sensors:

Once the wire strand was mounted on the tensile machine and instrumented with the MS and AE sensors, it was subjected to an increasing tensile load until catastrophic failure occurred at an ultimate load of approximately 150,000 lb (68,100 kg). During the loading period, the AE sensors recorded all the acoustic activity that was above the threshold of 40 dB (1 mV in terms of voltage amplitude). This activity included friction between the sockets and the tensile machine, cracking on the epoxy used to join the strand to the sockets, adjustments of the strand under tension, friction between the wires in the strand, wires pulling out of the sockets, and failure of the wires.

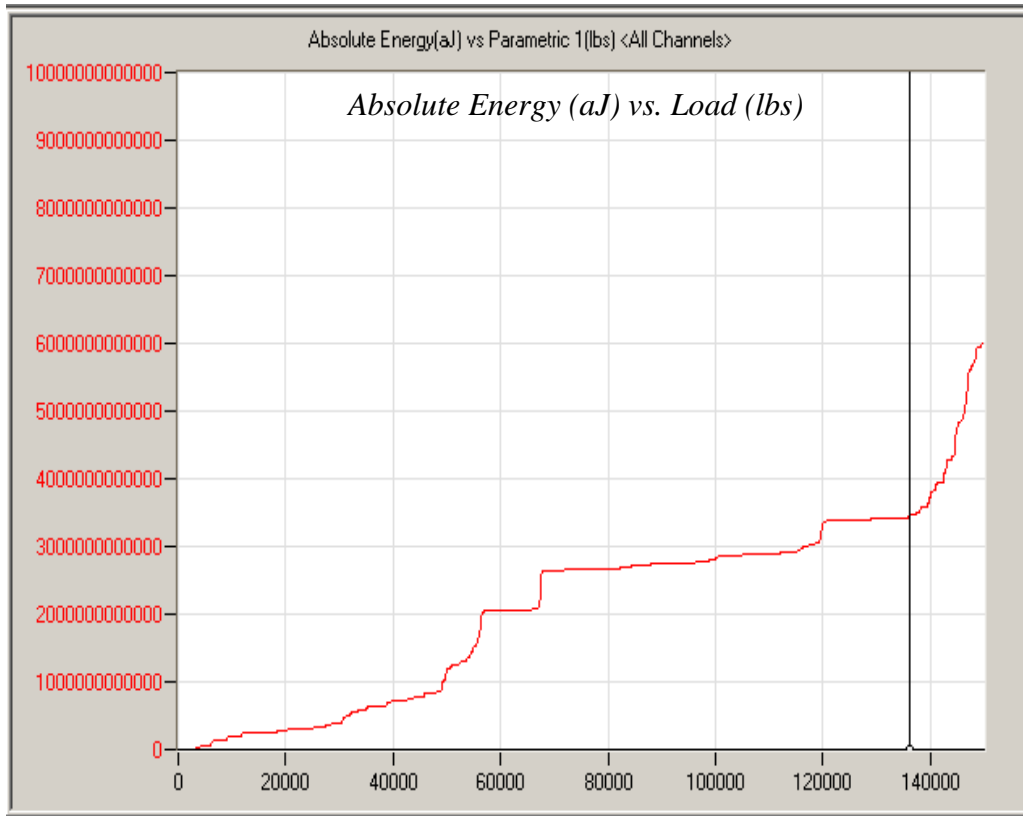
Figure 42 shows the AE activity detected during the active load periods of the test in terms of the absolute energy released in the form of acoustic waves as a function of time. Superimposed with this AE data (red dots), the green trace represents the actual load being applied to the strand and read directly from the load cell. The load was monitored by the AE system at a rate of 10 times/s (10Hz) regardless of the amount of AE activity being detected by the AE sensors.

As it is observed in figure 43 in which the cumulative AE absolute energy is displayed as function of the load, there is very little AE activity below 30,000 lb (13,620 kg), and it increases steadily up to 136,000 lb (61,744 kg). At this point, the AE activity began to increase exponentially, an indication of impending catastrophic failure, which occurs at 150,000 lb (68,100 kg).



1 lb = 0.454 kg

Figure 42. Graph. AE activity as a function of time during the tensile test of the wire strand.



1 lb = 0.454 kg

Figure 43. Graph. Cumulative AE absolute energy as a function of load.

It was assumed that most of the activity below 30,000 lb (13,620 kg) was due to sources other than legitimate AE produced by wire breaks in the strand. After filtering the data to eliminate signals with very low energy and duration, different sensor groups were used to locate potential wire brakes in different notch positions. Table 8 shows the sensor groups with the corresponding area of coverage.

Table 8. Sensor groups and corresponding coverage area.

Group Number	Sensor Number	Coverage Area
1	S1 and S4	Notches A–E
2	S5 and S6	Notch A
3	S2 and S3	Notches B and C
4	S6 and S7	Notches B and C
5	S3 and S4	Notches D and E
6	S5 and S8	Notches A–E
7	S1 and S2	Notch A
8	S7 and S8	Notches D and E

Figure 44 and figure 45 show histogram plots of the AE events located by these sensor groups. For reference, the positions of the sensors are indicated on top of the plots. The y-axis shows the number of AE events, and the x-axis shows the location along the length of the strand. Figure 44

shows the event located by sensor groups 1, 3, 5, and 7, and figure 45 shows the events located by sensor groups 2, 4, 6, and 8. The events observed at the locations of the notches B, C, and D, which were 38, 74, and 110 inches (965.2, 1,879.6, and 2794 mm), respectively. These events all happened at loads higher than 30,000 lb (13,620 kg) and within ± 2 inches (50.4 mm) of the nominal position of the notch site, as indicated in table 9.

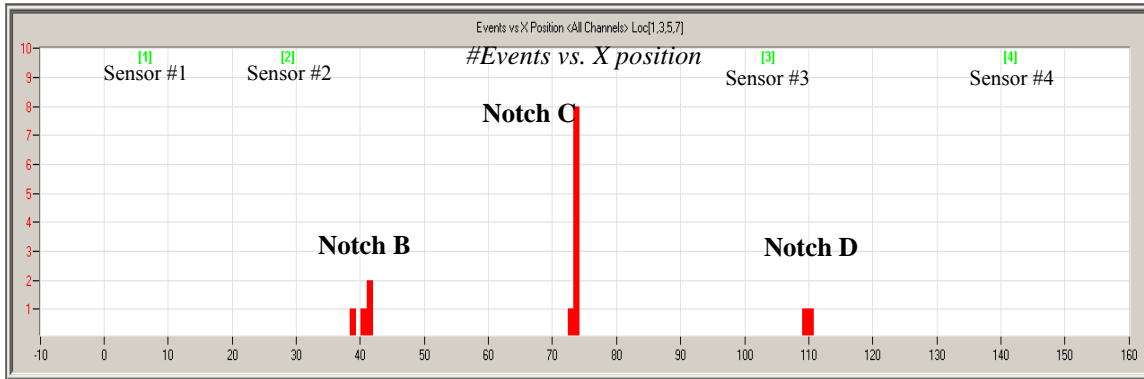


Figure 44. Graph. Events located around notches B, C, and D located by sensor groups 1, 3, 5, and 7.

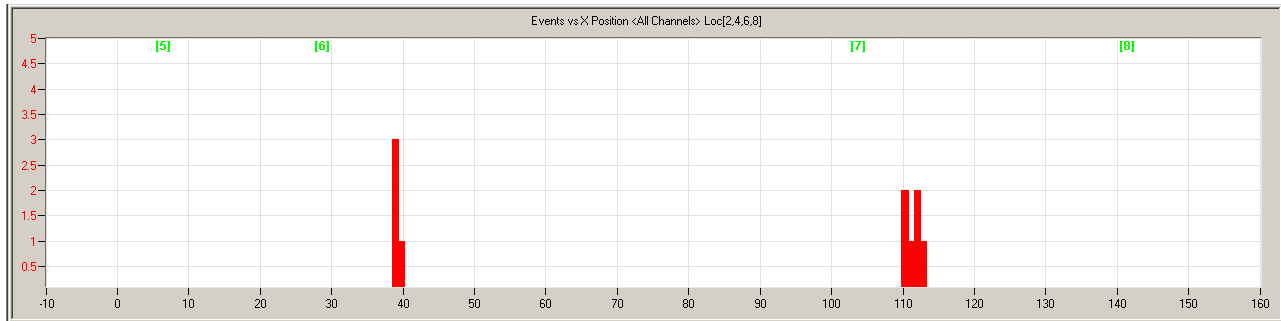


Figure 45. Graph. Events located around notches B and D located by sensor groups 2, 4, 6, and 8.

Table 9. Events located by the AE system at notches B, C, and D.

Event Number	Load (lb)	Nominal Position (inches)	Detected Position (inches)	Difference in Position (Percent)	Absolute Energy (aJ)
1	39,259	40 (Notch B)	39.0	-2.5	2.29E+09
2	39,702	40 (Notch B)	38.6	-3.5	7.85E+05
3	45,259	40 (Notch B)	38.5	-3.7	3.02E+05
4	56,475	40 (Notch B)	39.2	-2.0	8.01E+05
5	56,584	40 (Notch B)	41.2	3.0	5.02E+05
6	63,552	40 (Notch B)	41.6	4.0	5.75E+05
7	109,934	40 (Notch B)	40.5	1.2	7.00E+08
8	145,613	40 (Notch B)	40.0	0.0	3.14E+05
1	46,312	74 (Notch C)	74.0	0.0	8.29E+03
2	100,970	74 (Notch C)	74.0	0.0	3.41E+05
3	118,879	74 (Notch C)	73.2	1.0	6.34E+03
4	119,730	74 (Notch C)	74.0	0.0	2.01E+03
5	143,013	74 (Notch C)	74.0	0.0	9.96E+03
6	143,086	74 (Notch C)	74.0	0.0	4.67E+03
7	143,141	74 (Notch C)	74.0	0.0	6.58E+03
8	146,666	74 (Notch C)	74.0	0.0	7.10E+04
9	148,616	74 (Notch C)	74.0	0.0	3.41E+03
1	56,621	110 (Notch D)	112.2	2.0	9.30E+05
2	139,232	110 (Notch D)	111.2	1.1	3.13E+07
3	143,260	110 (Notch D)	109.1	0.08	1.71E+06
4	144,322	110 (Notch D)	110.3	0.03	2.96E+08
5	144,716	110 (Notch D)	112.5	2.3	3.33E+09
6	147,737	110 (Notch D)	110.1	0.01	3.85E+05
7	147,884	110 (Notch D)	111.7	1.5	6.44E+05
8	149,037	110 (Notch D)	110.4	0.04	6.00E+04

1 lb = 0.454 kg
1 inch = 25.4 mm

According to figure 44, figure 45, and table 9, there were a total of 25 events: 8 at notch B, 9 at notch C, and 8 at notch D. Figure 45 shows that 12 wires were notched at each one of these sites. If it is assumed that each one of the events corresponds to a notch wired breaking, then four, three, and four notched wires must have remained unbroken at the notch sites, respectively. A postmortem analysis of the failed strand corroborated that four unbroken notched wires remained at notches B and D and three remained at notch C. All these 11 notched unbroken wires have shallow notches 0.03 inch (0.76 mm) deep marked in yellow in figure 40. The events located by the AE sensors in notches B, C, and D were confirmed as wire breaks.

The AE system detected hundreds of events around notches A and E at 10 and 138 inches (254 and 3,505.2 mm) respectively, from the reference end of the strand, as shown in figure 46 and figure 47. In the figures, the y-axis shows the number of AE events, while the x-axis shows the location along the length of the strand.

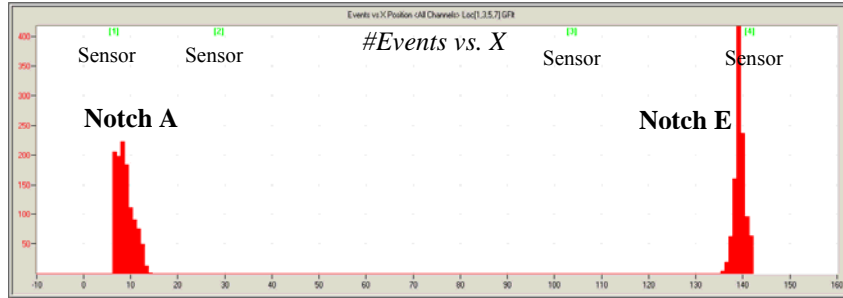


Figure 46. Graph. Events located around notches A and E located by sensor groups 1, 3, 5, and 7 (unfiltered data).

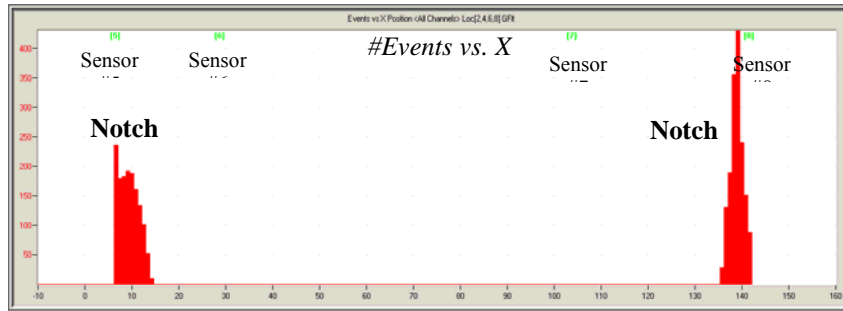


Figure 47. Graph. Events located around notches A and E located by sensor groups 2, 4, 6, and 8 (unfiltered data).

According to figure 39 and figure 40, there were only 10 wires at notch A and 8 at notch E, so the massive amount of activity observed could not be the result of potential wire breaks alone. This event accumulation was most likely produced not only by wire breaks, but also by potential pullout of wires from the epoxy filler and by cracking of the epoxy inside the sockets. An example of this type of failure in the lower socket is shown in figure 48.



Figure 48. Photo. Failure of the epoxy filler inside the sockets.

In order to better discriminate the potential wire breaks from the epoxy failure and wire pullouts, a series of filters were applied to the data in figure 46 and figure 47. It was expected that the wire breaks would happen at relatively high loads, and since the sensors were in close proximity to

the potential wire break site, it was also expected that a signal from an actual wire break would have in fact saturated the AE channel, as shown in figure 49.

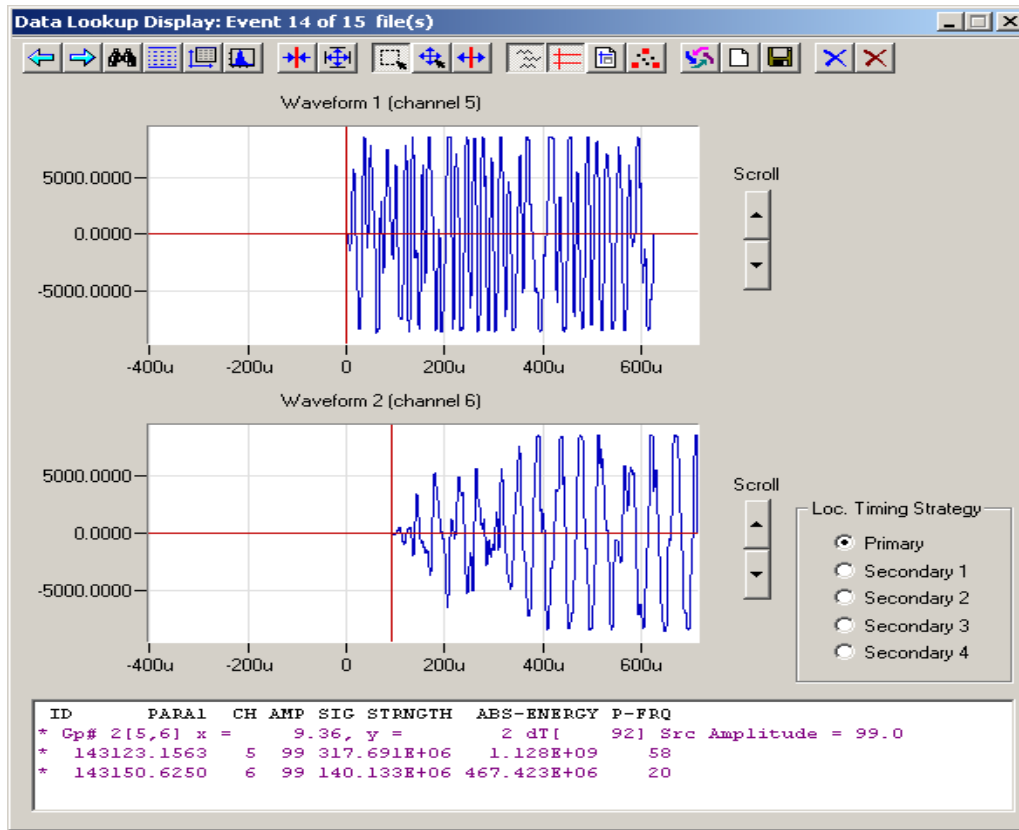


Figure 49. Illustration. AE signals from a potential wire break at notch A.

A simple analysis of this type in conjunction with the requirement that the event was detected at a load 30,000 lb (13,620 kg) or higher led to the elimination of a massive number of events, leaving only 7 events for the notch A and 19 for notch E. Figure 50 and figure 51 show the location plot for these 26 events. In the figures, the y-axis shows the number of AE events, and the x-axis shows the location along the length of the strand.

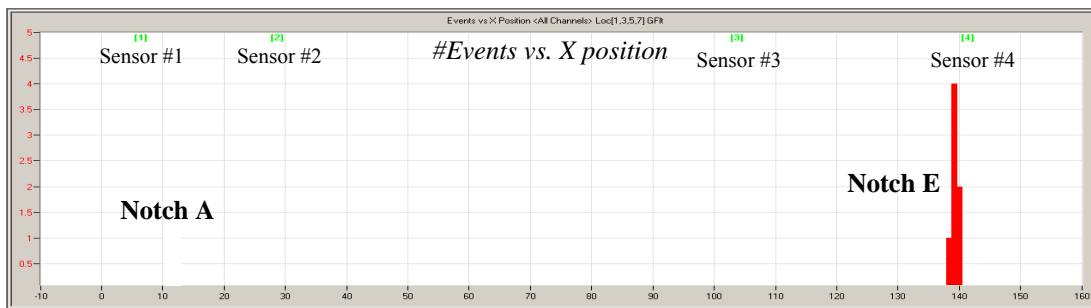


Figure 50. Graph. Events located around notches A and E by sensor groups 1, 3, 5, and 7 (filtered data).

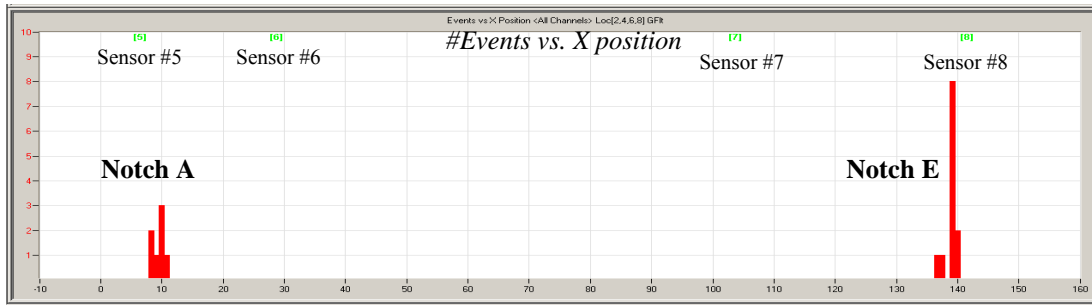


Figure 51. Graph. Events located around notches A and E located by sensor groups 2, 4, 6, and 8 (filtered data).

The postmortem analysis of the strand indicated that four notched wires were broken at notch A, and two wires pulled out of the epoxy filler in the socket. No wire breaks were found at notch E. However, 19 wires pulled out from the epoxy filler in the socket. Analyzing the absolute energy characteristics of the seven events from notch A, it was found that there were four events with energies larger than 5×10^9 aJ. These events were most likely produced by the wire breaks. The next two in terms of energy could be produced by the wire pullout and the one with the lowest energy could have been produced by epoxy cracking. If the same absolute energy threshold that was used for the notch A is applied to the events from notch E, only 1 event out of the 19 detected could correspond to a wire break. However, as mentioned before, no wire breaks occurred at this location. So it can be concluded that all the events in notch E were created by wires pulling out of the epoxy filler.

Table 10 summarizes the absolute energy characteristics of the events located at notches A and E, their calculated position, the load at which they occurred, and the likely source (wire break (WB), pullout (PO), or epoxy cracking (EC)).

Table 10. Events located by the AE system at Notch sites A and E.

Event Number	Load (lb)	Position (inches)		Likely Source	Absolute Energy (aJ)
		Nominal	Detected		
Notch A					
1	25,272	10	10.0	PO	7.45E+08
2	35,069	10	10.3	PO	1.21E+09
3	35,087	10	9.0	WB	6.74E+09
4	35,087	10	10.7	WB	6.74E+09
5	49,187	10	8.6	WB	5.56E+09
6	84,893	10	10.6	EC	2.37E+08
7	144,716	10	8.3	WB	6.02E+09
Notch E					
1	41,148	138	138.6	PO	3.14E+05
2	42,375	138	139.8	PO	4.16E+06
3	43,510	138	137.9	PO	2.88E+07
4	44,902	138	139.9	PO	3.73E+08
5	67,388	138	139.3	PO	3.29E+07
6	67,452	138	137.0	PO	1.91E+07
7	67,901	138	139.2	PO	8.16E+09
8	75,152	138	138.8	PO	9.23E+06
9	86,349	138	139.3	PO	1.71E+08
10	87,896	138	139.6	PO	7.37E+06
11	96,283	138	139.5	PO	4.53E+07
12	113,431	138	139.4	PO	3.03E+06
13	113,431	138	139.2	PO	4.20E+07
14	116,526	138	139.4	PO	1.33E+08
15	129,096	138	139.5	PO	1.19E+09
16	137,437	138	139.9	PO	2.85E+09
17	137,437	138	139.5	PO	3.70E+09
18	145,750	138	139.4	PO	2.40E+09
19	145,750	138	139.0	PO	1.03E+07

1 lb = 0.454 kg

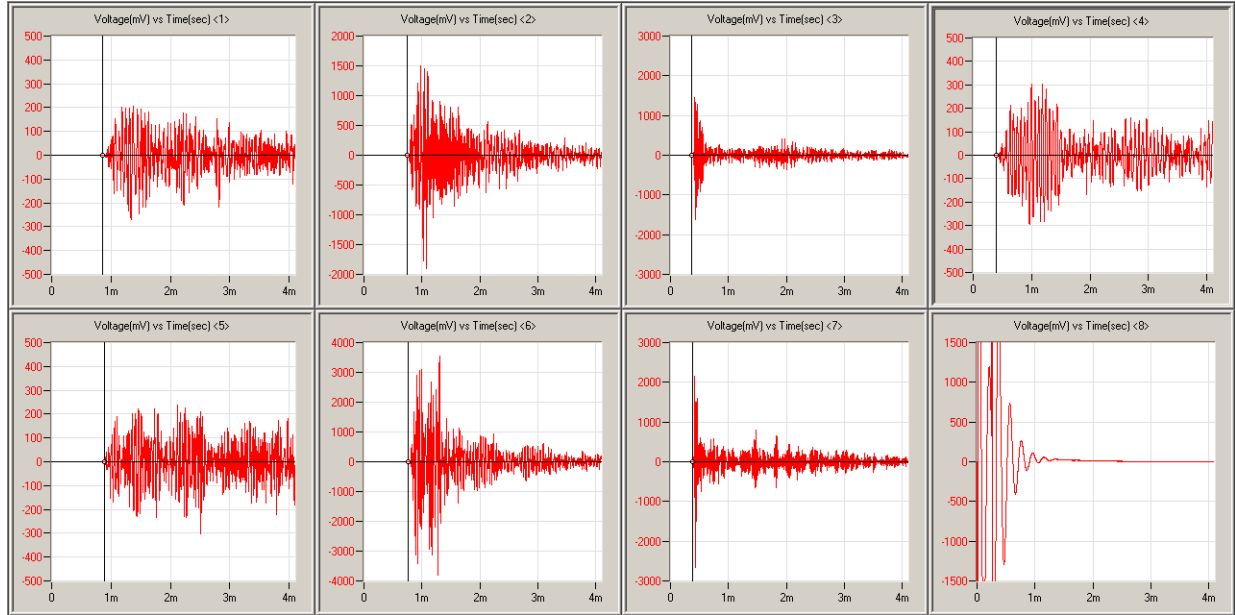
1 inch = 25.4 mm

Detection and Localization of Corrosion-Induced Damage by MS-AE Combined Techniques:

As mentioned in the introductory section, the potential combination of AE and MS techniques was also investigated during the tensile test of the strand. The principle is that the MS actively generates an acoustic signal that travels along the wire, strand, or cable and is detected by the AE sensors. If there are changes in the cable caused by damage, the signals generated by the MS system and received by the AE sensors will change depending on the damage level and location. This combined technique requires a baseline measurement from which the comparison for subsequent measurements will be established. It is important to mention that this baseline measurement will not offer any information about pre-existing damage; it will only provide a platform for evaluation of new damage.

Baseline Measurements on the Strand:

In order to establish a common reference point for measurements with no load applied to the strand, the MS was pulsed using a tone burst signal with central frequency of 64 kHz at a rate of 10 Hz. This acoustic wave propagated along the strand and was detected by the AE sensors located at different positions. Figure 52 shows the baseline recorded waveforms detected by sensors 1 to 7, whose locations are provided figure 38. Only seven sensors were used in this operation because channel 8 was used to synchronize the AE system with the MS system, as can be seen in the waveform corresponding to channel 8 in figure 52.



1 ft = 0.305 m

Figure 52. Graph. Baseline acoustic signals detected by the AE sensors along the strand.

The increasing delay in the arrival of the signals corresponds to the increasing distance between the MS and the position of the AE sensor along the strand. This delay was used to calculate the average propagation velocity of the elastic wave along the wires, which resulted in an average value of 193,800 inches/s (4.92 mm/ μ s). The waveforms can also provide valuable information about the loss of different frequency components as the signal travels along the strand. For this purpose, the power spectra of the signals from figure 52 were extracted and analyzed. The results indicate that the peak frequency of the signals shifts to lower frequencies as the acoustic wave propagates along the strand away from the MS (see table 11).

Sensors 3 and 7, located directly on the cable and closer to the MS magnet, showed the highest peak frequencies of 59.5 and 50.1 kHz, respectively. Sensors 2 and 6 showed a decrease in peak frequency down to 49.8 and 48.8 kHz, respectively, while sensors 1 and 5 showed a severe decrease to 15.6 and 18.5 kHz, respectively. It is important to note that the decrease in peak frequency value of the last two sensors, as the decrease in sensor 4 (decreased to 15.6 kHz), was amplified by the fact that sensors 1, 5, and 4 are mounted on the steel sockets, which introduces an extra interface that the signal has to go through in order to reach the sensors, therefore increasing the attenuation of the high frequency components of the signal. This fact has to be

taken into account when selecting the frequency of the AE sensors and their locations for installation on a real suspension bridge cable.

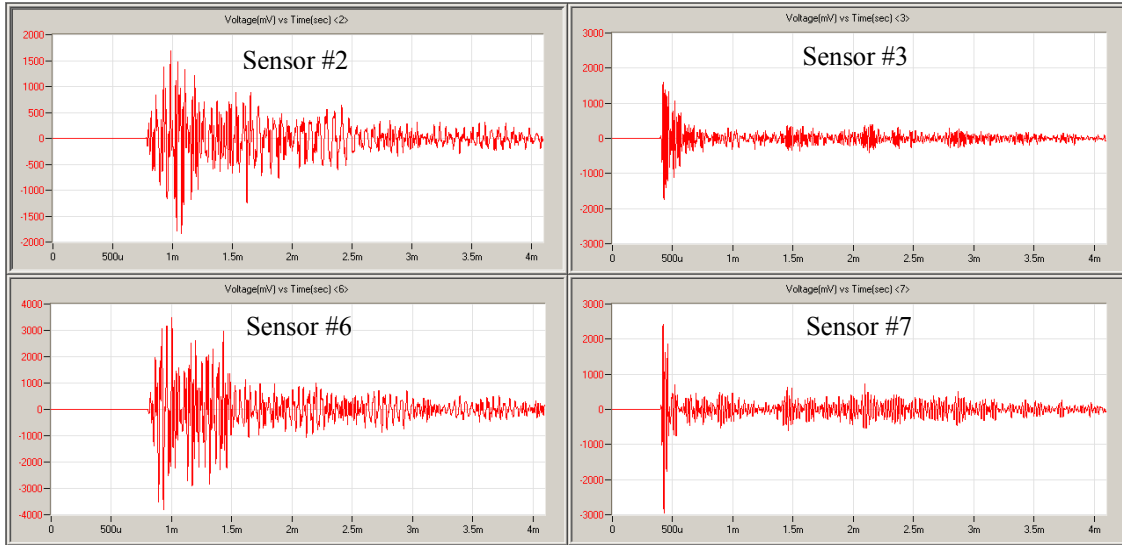
Table 11. Amplitude and peak frequency of acoustic signals produced by the MS device and detected with AE sensors.

Sensor Number	Amplitude (V)	Peak Frequency (kHz)
1	0.205	15.6
2	1.493	49.8
3	1.475	59.5
4	0.303	15.6
5	0.240	18.5
6	3.575	48.8
7	2.128	50.0

Measurements During Strand Loading:

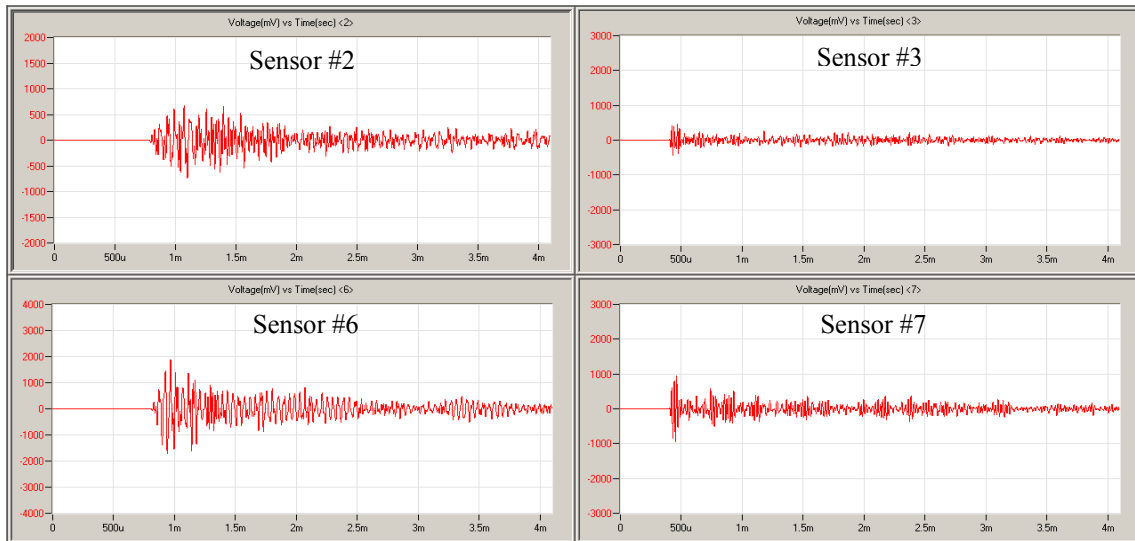
MS-AE measurements were performed at several points during the tensile test. During the measurements, the load was held constant at different levels, and the MS was pulsed for a period of approximately 20 s, during which the AE sensors recorded the acoustic signals propagating along the cable. As an example of the changes in the signal characteristics, figure 52 shows the signals detected by sensors 2, 3, 6, and 7 during the load holds at 34,000 and 142,000 lb (15,436 and 64,468 kg), respectively. These sensors covered the area between the MS and notches B, C, and D. According to the previous results, most of the damage that led to failure of the strand happened at these three positions.

The data in table 10 indicate that no wire break had occurred at 34,000 lb (15,436 kg) in notches B, C, or D. Thus, the signals in figure 53 can be considered representative of the strand with full cross section. The signals detected by the same sensors during the hold at 142,000 lb (64,468 kg) are shown in figure 54. According to the previous results, at the tensile load of 142,000 lb (64,468 kg), 13 wire breaks had occurred at this point in the test, which is reflected in the clear reduction in amplitude of the signals in all the sensors. This reduction in amplitude is approximately 50 percent across the four sensors. Ideally, these changes in signal characteristics could be related to a known damage level, in this case a known reduction in the strand’s cross section. An extensive analysis was performed in the different features of the signals detected at different levels of damage produced in the strand during the tensile test.



1 ft = 0.305 m

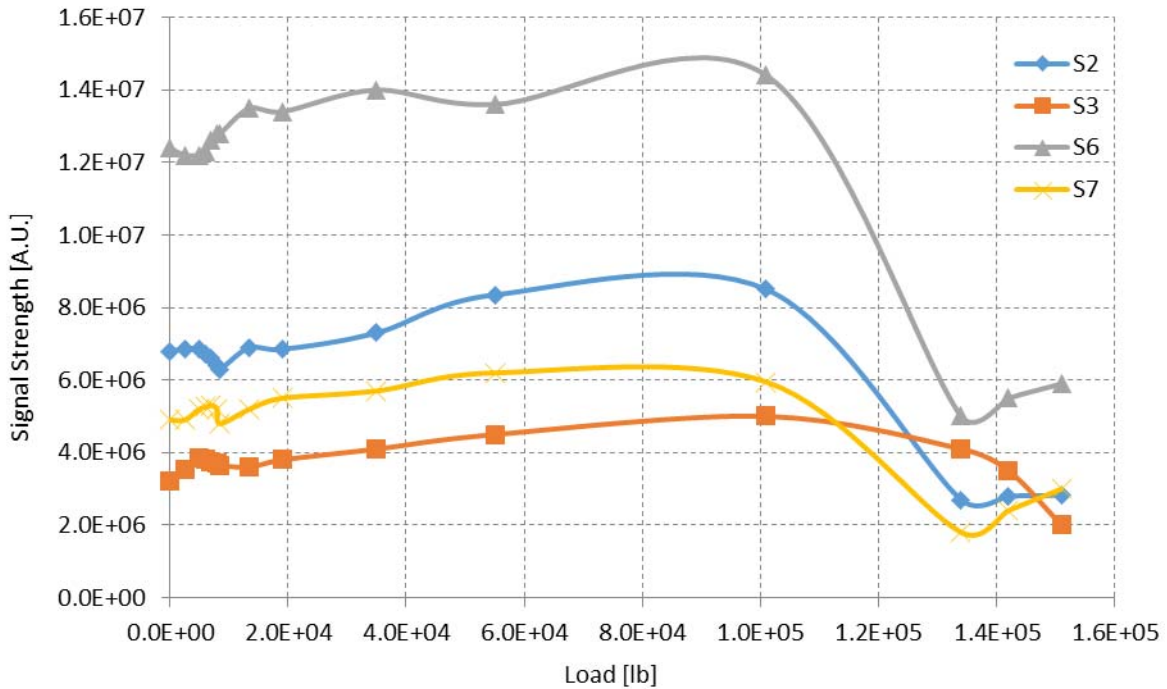
Figure 53. Graph. Acoustic signals detected by the AE sensors 2, 3, 6, and 7 during the hold at 34,000 lb (15,436 kg) (no damage).



1 ft = 0.305 m

Figure 54. Graph. Acoustic signals detected by the AE sensors 2, 3, 6, and 7 during the hold at 142,000 lb (64,468 kg) (severe damage).

This analysis revealed that the signal feature that correlated better with the progression of damage in the strand is the signal strength. Figure 55 shows a plot of signal strength versus load on the strand for sensors 2, 3, 6, and 7. It is clear from these plots that there is an increase in the signal strength with load on the strand up to approximately 100,000 lb (45,400 kg). This increase is caused by changes in the strand as the wires get tensioned and by the fact that the attenuation of the signal in the strand decreases due to a better consolidation of the wires. However, according to figure 42 and figure 43, at 100,000 lb (45,400 kg), there is significant damage in the strand. It is at this point where the signal strength starts to drop substantially, with increasing load and more damage being produced in the strand.



1 lb = 0.454 kg

Figure 55. Graph. Signal strength as function of load for sensors 2, 3, 6, and 7.

In order to decouple the effect of load and correlate the change in signal strength directly to damage, the changes measured by sensors 2, 3, 6, and 7 were plotted against the actual loss in strand cross section according to the sequence of wire breaks shown in table 10. The results are shown in figure 56.

Sensors 3 and 7 covered the area between the MS sensor and notch D. The results indicate that the signal strength decreases sharply after the damage accumulation reached 10 percent. The plots for sensors 2 and 6 showed a decrease in the signal strength after the damage accumulation reached 13 percent. This slight decrease in sensitivity may be the result of sensors 2 and 6 being mounted in a clamp, which causes the loss of high frequency components, as previously discussed in this section.

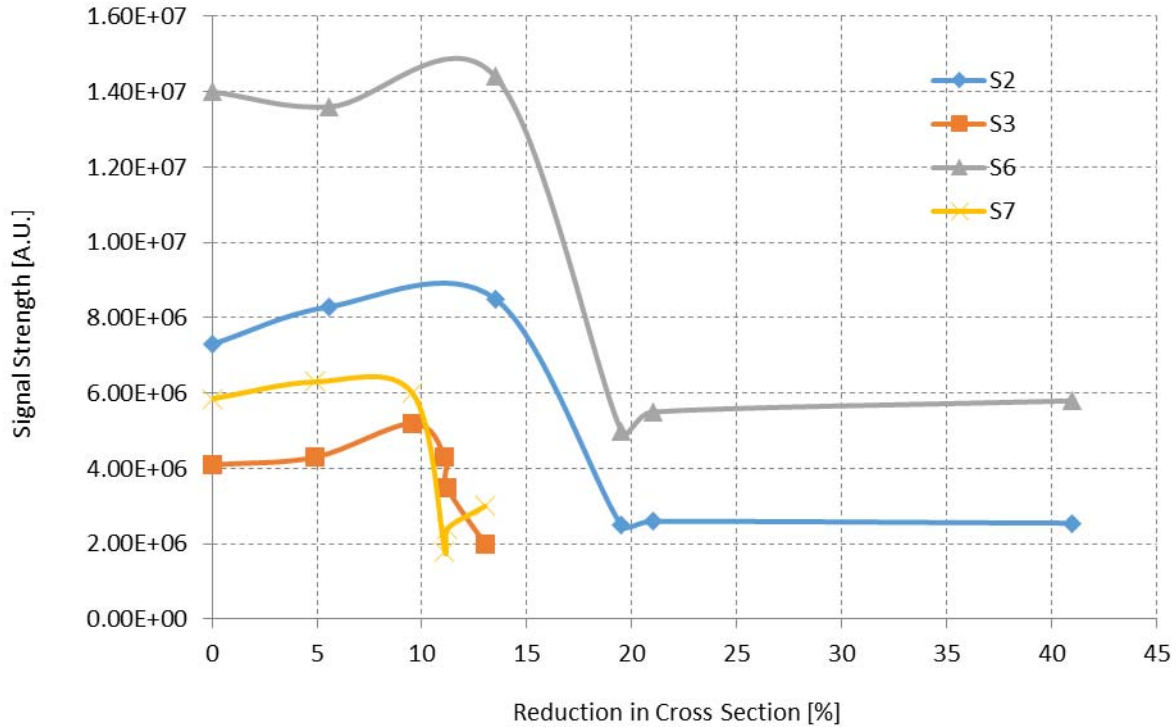


Figure 56. Graph. Signal strength versus cross section reduction for sensors 2, 3, 6, and 7.

At the end of this test, it was shown that the AE-MS system detected and located 25 wire breaks in notches B, C, and D in the main body of the strand. The detection and location of these wire breaks was confirmed by a postmortem analysis of the strand. It is clear that the failure of the strand under tension was due not only to wire breaks but also failure of the epoxy resin in the socket. To that effect, AE sensors located a multitude of events at the two socket locations generated precisely by the pullout of wires from the epoxy resin. From the analysis, it was clear that those events carried acoustic energy lower than those events generated by wire breaks. This difference in energy levels allowed researchers to establish a good criterion to distinguish potential wire breaks from other types of failure mechanisms. To this effect, a threshold value of 5.0×10^9 AJ was established to separate the two different types of events at the socket locations.

As a conclusion of this experiment of a strand under tensile load, it was determined that the results obtained by the combined MS-AE techniques showed that the signal strength feature correlated well with the damage progression and that cross section losses in the strand cross section larger than 10 percent could be detected.

5. Detection, Localization, and Evaluation of Simulated Corrosion-Induced Damage in a Bundle of Seven Strands:

In this series of tests, 7 127-wire strands were assembled (labeled A through G) as shown in figure 57, figure 58, and table 12. In these tests, AE sensors (R61 with a resonant frequency of 60 KHz, R1.5I, and R3I) were used together. To simulate corrosion-induced damage, seven wires on one face of one of the strands were cut (strand is labeled “CT” in figure 58) at approximately half of the strand’s length (between positions D and E). The MS receiver was placed 12 inches (304.8 mm) to the left of position A. The coil was placed either around this

single strand or around the seven-strand bundle and was positioned with the pulser at the far end of the cable along with the magnet. Similarly to previous tests, when just a single strand was considered, the MS sensor, either alone or together with the AE system, was able to accurately locate the cut wires at the top of the bundle. Using an 8- or 16-kHz pulse, only sensor A (low frequency 15-kHz sensor) was able to detect the pulse. For the 32-kHz pulse, all sensors were able to detect the pulse, but the overall responses for the 30- and 60-kHz sensors were weak as compared to the previous testing.

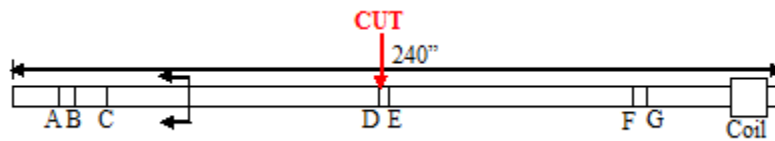


Figure 57. Illustration. MS and AE sensors.

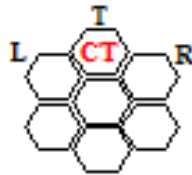


Figure 58. Illustration. MS and AE strand configurations.

Table 12. AE sensor positions for MS-AE tests.

Position (Horizontal)	Position (Cross Section)	AE Sensor	Distance (Inches)
A	T	R1.5I	24
B	T	R6I	26
C	R	R3I	38.25
D	T	R3I	119.25
E	T	R6I	121
F	T	R6I	189.25
G	L	R3I	192.75

1 inch = 25.4 mm

To test the effectiveness of the system on cables with a larger number of wires, the strand with the seven cut wires was placed in the center with an additional six strands surrounding it. Three tests were conducted by changing the position of the electric coil. For test 5-1, the coil was wrapped around the entire bundle of wires. In test 5-2, the coil was moved to the center strand, while in test 5-3, coils were placed on the center strand as well as around the entire bundle of wires. The coil configurations are shown in figure 59 through figure 62. The AE sensors instead were placed along the same line and positions as shown in figure 57 and figure 58.



Figure 59. Illustration. Multibundle configurations for MS and AE testing—test 5-1.

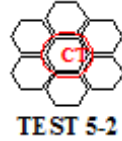


Figure 60. Illustration. Multibundle configurations for MS and AE testing—test 5-2.



Figure 61. Illustration. Multibundle configurations for MS and AE testing—test 5-3.

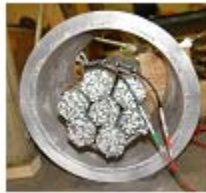


Figure 62. Photo. Seven-strand wire bundle with outside MS magnet.

In the first test, the strand with cut wires was moved to the center of the bundle, and then the seven strands were strapped together at three locations, as shown by the yellow straps in figure 63, to enhance their contact and the transmissibility of the traveling elastic waves. The MS coil was then placed around the entire bundle of strands to generate a magnetic field within the bundle. The AE sensors were placed on the outer surfaces of the strands (see figure 64). For this test, as well as for tests 5-2 and 5-3, the excitation of the pulse was performed at 8, 16, 32, and 64 kHz.



Figure 63. Photo. Compaction of strand bundle.



Figure 64. Photo. Mounted AE sensors.

With the coil wrapped around the entire bundle, the MS pulse could not detect the cut wires located in the center strand at all four excitation levels. However, the AE sensors located along the outer strand (see figure 64) were able to detect the MS pulse. To understand why the MS pulse could not detect the broken wires, sensor A (the 15-kHz R1.5I sensor) was moved and mounted to the center strand where the cut wires were. This is the low frequency sensor, and it is more sensitive to the lower frequency guided waves generated by the MS system. After moving this sensor to the center strand, it was determined that the MS pulse was not reaching the center strand. It was found that while the MS pulse could reach the opposite end of the strand setup, it could only be detected along the portion of the strand that was in contact with the MS coil. Two possible reasons for such lack of signal in the central strands were identified: lack of penetration of the magnetic field and lack of contact force between the strands. To better understand the effect of the compaction force on the signal transmission through the strands in test 5-2, the strands were tightened further to increase contact force between all the wires, and the coil was then moved to the center strand.

For test 5-2, the MS coil was moved to the center strand, while the AE sensors were left mounted on the outer circumference of the entire setup. In this configuration, the MS sensor was now able to detect the cut wires within the strand, while the AE sensors, still placed on the outer strands, were not able to detect the MS signal from the center strand despite the increase in compaction force. Again, the R1.5 low-frequency sensor was moved to various positions along the length and circumference of the cable. As previously observed in test 5-1, the AE sensor could only detect the MS pulse when it was mounted to the center strand that was in contact with the coil.

In the third and final test of this series, two MS coils were used: coil 1 was wrapped around the center strand, while coil 2 was wrapped around the entire seven-strand setup. Again, it was observed that for the AE sensors, the pulse was only detected if the sensor was mounted to the same surface that the coil was in contact with. Starting from the surface of the strand that was in contact with the coil, the MS pulse was detected on the outer layer but, already at the second layer below the surface, there was almost a 60 percent loss in the signal. At the third layer, the MS signal was lost. Based on the results from this test as well as previous tests, it was determined that the pulse from the coil was not strong enough to penetrate more than two layers into a strand and that the magnetic field was not strong enough to provide a complete saturation of the seven-strand setup. Additionally, it could be concluded that the increase in attenuation and loss of the signal was due to transmission of the wave energy into the adjacent wire bundles, which resulted in energy loss from the main pulse. Hence, by identifying potential limitations of this combined MS-AE technique, it is possible that a larger coil and a stronger magnetic field could overcome some of these effects which were limited by the existing hardware.

From this series of tests, the results showed that the combination of AE and MS technologies can provide complimentary information in the detection of existing wire breaks and corrosion-induced cross section loss, with the added benefit that AE can also help detect future wire breaks as they occur. However, the use of MS for locating existing wire breaks is limited to smaller bundles. In these series of tests, the maximum bundle size in which existing wire breaks could be detected was 127 wires, which is nothing compared to the thousands of wires that make a main cable of a suspension bridge. This makes the technique ideal for testing of suspender ropes (already being done) as well as in the anchorage where the main cable is divided into smaller bundles at the anchor/shoe. However, an increase in the bundle size (or in a multibundle configuration) greatly attenuates the pulse energy as it gets transmitted into the adjacent strands due to physical contact.

Main Magnetic Flux Method (MMFM)

Another interesting technology that can be considered as a direct sensing technology is represented by a modified version of the MMFM system. This type of technology is currently available to assess suspenders and has never been applied to a main cable of a suspension bridge before this project.

The fundamental principle of this technology is that when a steel wire, rope, or cable is longitudinally saturated by a strong magnetic field, the magnetic flux in the wire, rope, or cable is proportional to the wire's, rope's, or cable's cross sectional area, as shown in figure 65. When a magnetic field moves along the length of the cable, then the measured variation of the magnetic flux at a given location may be correlated to the change in cross sectional area at that location.

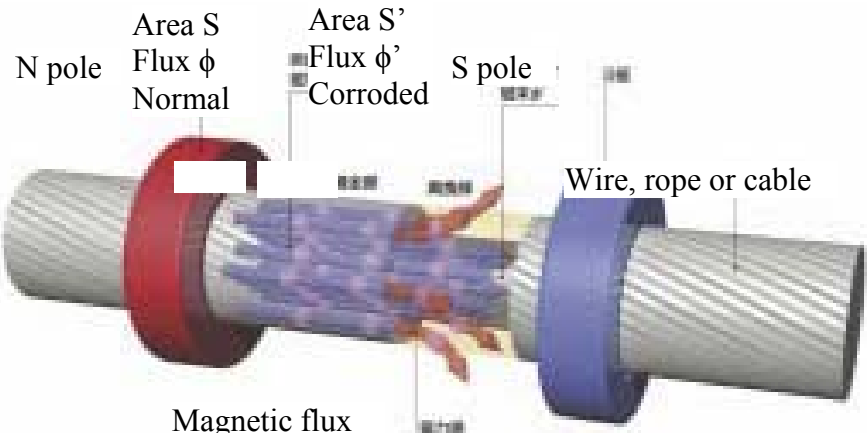


Figure 65. Illustration. Flow of magnetic flux in a wire rope.

The MMFM system consists of a magnetizing unit, sensor units, and a computer (see figure 66). The magnetizing units consist of an electromagnet, a variable DC power supply, and a switch of polarity. The sensor units are comprised of the search coil, flux meter, Hall-sensors, and Gauss-meter. A computer controls the magnetizing current and records and analyses the measurement data. Figure 67 and figure 68 show the electromagnet, mounted on the cable mockup, and the MMFM system developed for this specific test.

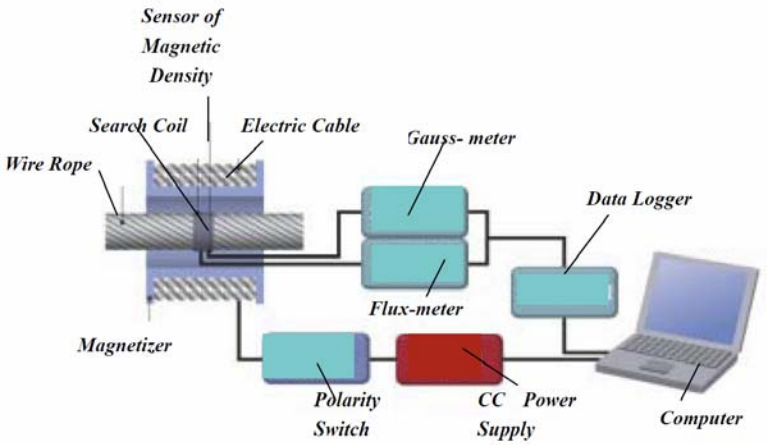


Figure 66. Illustration. MMFM measurement system.



Figure 67. Photo. MMFM bobbin mounted on a cable mockup.

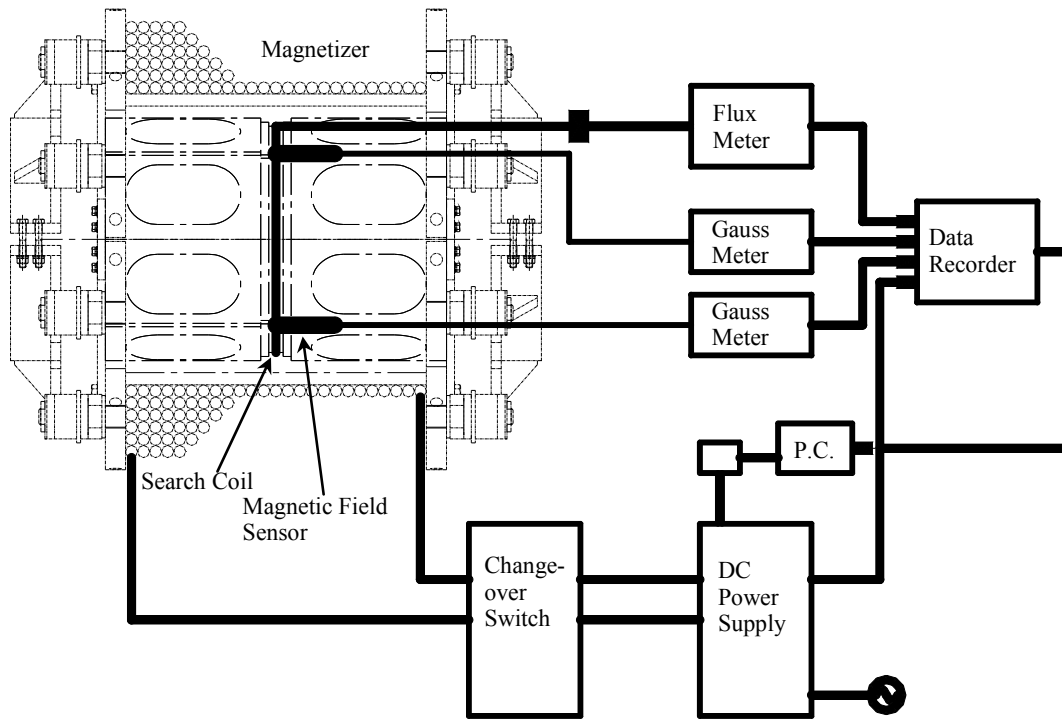


Figure 68. Illustration. Schematic of the MMFM measurement system used in this study.

Tests were conducted at two different stages: before the accelerated environmental test started and after the accelerated environmental test was completed. The idea was to see the capability of the MMFM technology in dealing with cables of such large dimensions and its accuracy in detecting changes in cross sectional area. Since this was a validation test for such new technology, tests were conducted at two stationary positions along the length of the cable without moving the magnet from these two positions. These two positions were located 4.15 ft (1.265 m) from the south side of the cable mockup and 3.49 ft (1.065 m) from the north side of the cable mockup.

Tests Conducted Before Accelerated Environmental Test

In this test, since the cable was made of new wires, damage was simulated by adding wires on the surface of the cable and then removing a few of them at a time to test MMFM sensitivity. For each test condition, the test was repeated three times, and averages were obtained.

During each test, the cable mockup was saturated with a magnetic field of 55 kA/m, and measurements of the maximum magnetic flux were recorded. In figure 69, the results from a single test (location B, 45 additional wires added to the cable) are presented.

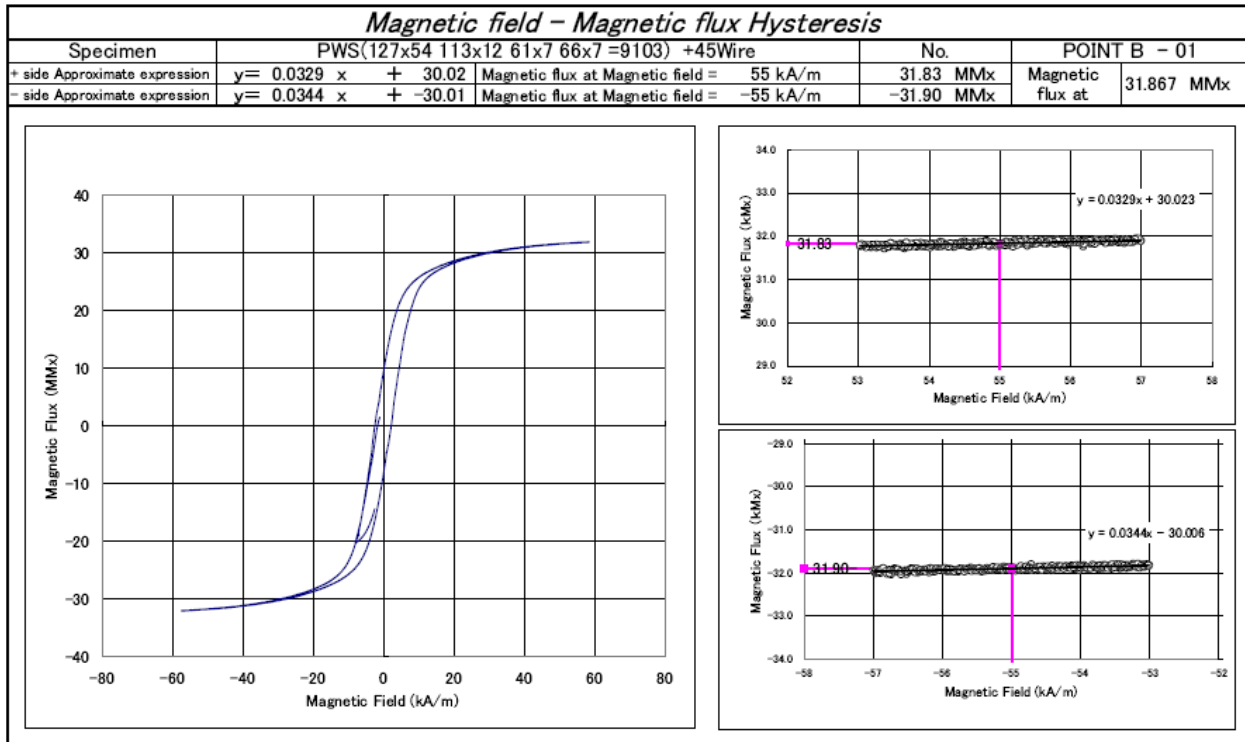


Figure 69. Illustration. Magnetic flux versus magnetic field plot for an MMFM test.

The baseline (no wires added) showed a magnetic flux value of 31.842 and 31.688 MMx for locations A and B, respectively. This small difference (0.5 percent) between the magnetic fluxes at the two locations is within the measurement error range of the method (1 percent).

When wires were added to the surface of the cable, then the magnetic flux corresponding to a magnetic field of 55k A/m increased, reaching values up to 31.970 MMx at location A and 31.868 MMx at location B. Plotting the changes in magnetic flux with the increased number of wires, it is possible to see a linear relation between these two quantities (see figure 70).

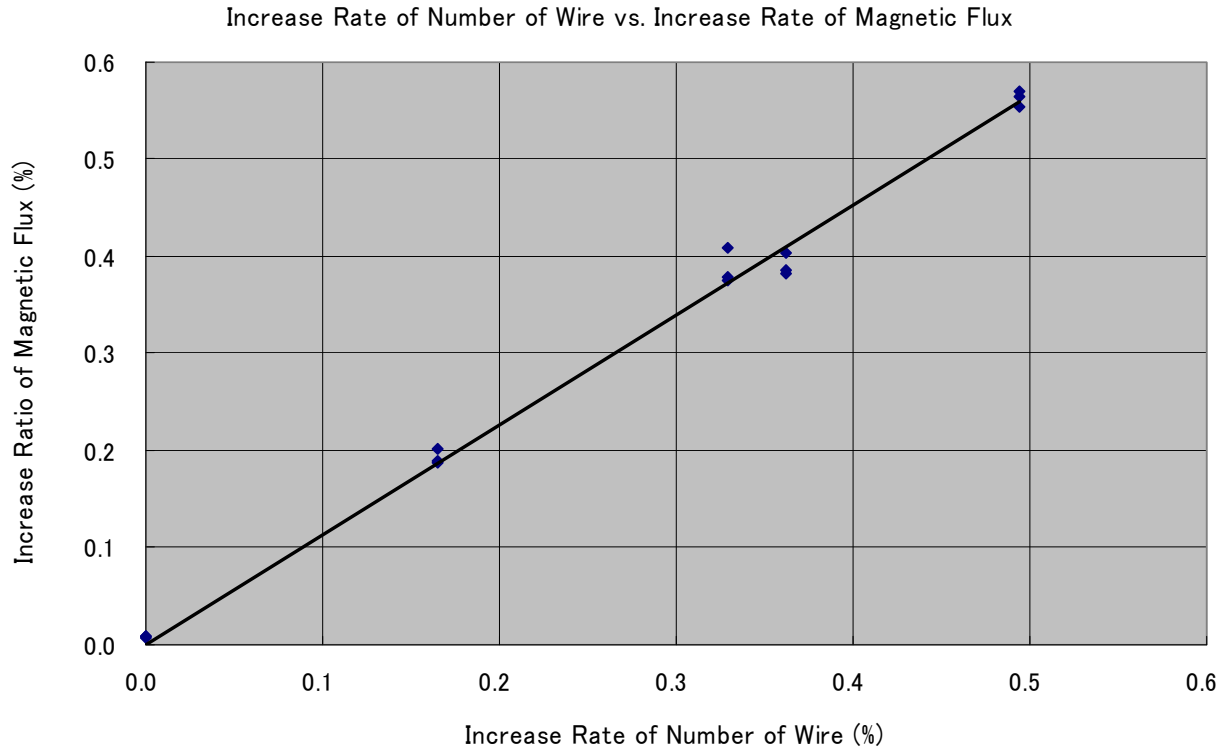


Figure 70. Graph. Increase in magnetic flux versus increase in the number of wires.

This graph presents a very interesting result. In real-life applications, this graph should be read from right to left, considering that the number of “good” wires decreases. In any case, the results show that there is a linear relation between the number of wires that deteriorate and the reduction of magnetic flux. This could be quite useful in real bridge applications for an accurate estimate of the number of broken wires.

Tests Conducted After Accelerated Environmental Test

A second set of MMFM tests was conducted on the cable specimen after completion of the aggressive environmental test. The same locations, A and B, were considered, but no additional wires were added this time. The purpose was to determine whether a year-long experiment had induced reduction of the cable’s cross section. The measurements of the magnetic flux at the two locations showed values slightly lower than the ones previously recorded. At location A, the average magnetic flux measured was about 31.682 MMx, slightly lower than 31.842 MMx previously measured. At location B, the new reading of the average magnetic flux was 31.652 MMx versus the original 31.688 MMx.

By looking at these measurements, it is clear that not much can be said about the reduction of the cable’s cross section. The differences between the magnetic fluxes before the first and second test (0.5 and 0.11 percent) fall within the margins of errors of the measurements. As shown in the section related to the cable autopsy, in the two locations tested in the MMFM tests, the effects of the aggressive environmental tests resulted in extensive zinc corrosion with large amount of salt deposits. No substantial ferrous corrosion was measured at these two locations. More evident changes of the magnetic flux probably would have been recorded if the bobbin would have been

moved along the entire length of the cable, where more extensive corrosion was induced; however, the technology is not ready for such a kind of applications. Nonetheless, the readings provided by the MMFM were consistent (not an increase of magnetic flux), and this is promising for future applications of such technology. It is recommended to test such a technology on more deteriorated cables.

CHAPTER 3: FULL-SIZE CABLE MOCKUP CONSTRUCTION OF THE CABLE SPECIMEN

One of the main tasks of the original study was to evaluate the selected monitoring systems, sensors, and technologies on a cable mockup specimen that recreated as closely as possible the in-service conditions. To accomplish this objective, a 20-inch (508-mm)-diameter, 20-ft (6.1-m)-long cable specimen was fabricated in the laboratory at Columbia University. It was made up of 73 127-wire hexagonal strands for a total of more than 9,000 0.196-inch (4.98-mm)-diameter steel wires. The reason for building hexagonal shape strands was to optimize/minimize the void ratio inside the cable and to improve the final compaction of the cable. Of the 73 hexagonal strands, 7 were 35 ft (10.68 m) long and were subjected to tension, while the remaining 66 strands, which were 20 ft (6.1 m) long, were unloaded. This cable specimen was placed in a loading frame properly designed for this particular action, and some of the strands were subjected to a load so to induce stresses up to 100 ksi (689.48 MPa) (so to include the effects induced by stress corrosion cracking). The total length of the experimental setup was over 35 ft (10.68 m). An environmental chamber was built around it, and the cable was subjected to harsh environmental conditions.

The construction of such a cable was a challenging task because this is the longest cable of such diameter ever built in the world subjected to some external loading. Additionally, original bridge wires were used in the construction of the cable so to simulate as closely as possible the real conditions and to improve the fidelity of the experiment. Its design and construction presented many difficulties that required a lot of trial and error attempts. Figure 71 shows the side and plan views of the cable mockup and the cable cross section.

The steel wires have a diameter of 0.196 inch (4.98 mm) and are coated with class A zinc coating. The ultimate strength is approximately 246.56 ksi (1,700 MPa), while the yield strength is around 203.05 ksi (1,400 MPa). The chemical composition is made of the following components, with iron as the remaining percentage:

- 0.8 to 0.81 percent carbon.
- 0.81 to 0.82 percent manganese.
- 0.23 to 0.27 percent silicon.
- 0.07 to 0.08 percent chromium.
- 0.06 percent nickel.
- 0.006 percent sulfur.
- 0.003 percent phosphorus.

The actual production of bridge wires starts with reheating the steel billets to about 2,012 °F (1,100 °C) and rolling them in one continuous operation into a rod of about 0.39 inch (1 cm) in diameter. The coiled rods are then transferred to the wire mill. There, the rods are heat treated at

a temperature of 1,652 °F (900 °C) and quenched to about 1,004 °F (540 °C) in a molten lead bath. After being air cooled so as to obtain the desired ductility and strength, the coiled rod is immersed in a series of tanks containing acid, water, and a coating solution. This coating solution eliminates any remaining traces of acid and acts as a lubricant in the subsequent cold drawing operations. The rods are then placed in annealing ovens to dry the coating and soften the steel in preparation for the drawing operation.

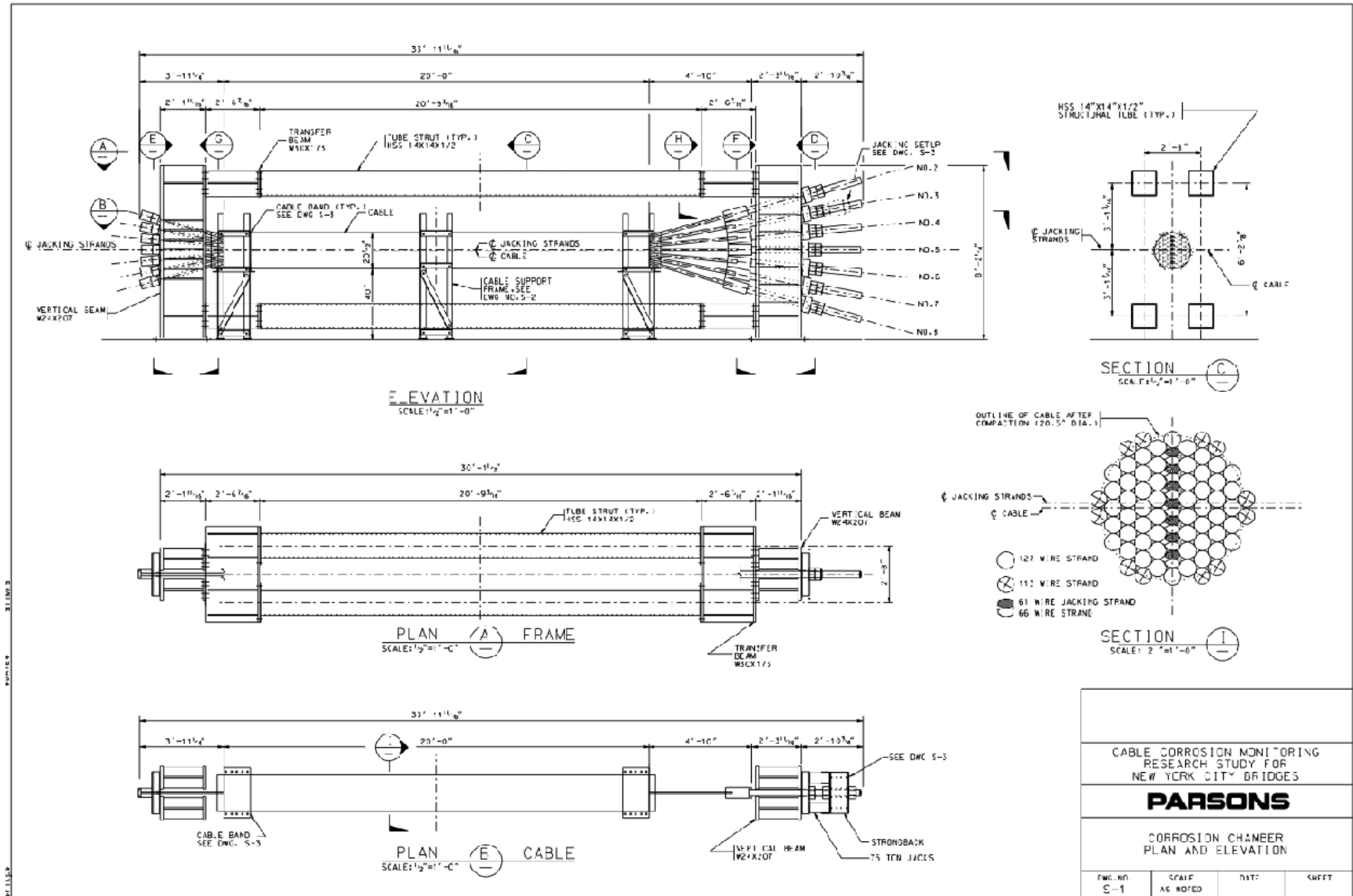


Figure 71. Illustration. Drawing of the cable mockup and corrosion chamber—plan and elevation.

The typical manufacturing process of a bridge wire involves the wires being sent through a set of dices made of tungsten carbide steel in order to reach the final diameter of the desired cross section. This process is driven by a set of power-activated drums, each one 36 inches (91.44 cm) in diameter. Cold working alters the wire microstructure. The grains are squashed, and their dislocation density is raised dramatically, producing tangles and residual stresses. Because of the small diameter of the pulling drum, the wires are subjected to large plastic strains, which induce a plastic distribution of stresses inside the wires. The effect of cold drawing increases the strength of the metal but also reduces its ductility. After being removed from the pulling drum, the wire coil experiences an increase in diameter (up to 50 to 60 inches (1,270 to 1,524 mm)) due to the fact that no pulling action is applied to the wire. This change in curvature induces an additional distribution of internal stresses which are then added to the original plastic stress distribution (currently unknown). The final wire coil is then chemically and thermally processed before being dipped in a hot zinc bath for galvanizing. Heating the cold-worked metal (annealing) reverses the effects produced by the cold drawing process. With the supplied thermal energy, dislocations will move to accommodate the stored residual stresses, forming a polygonized subgrain structure that concentrates the lattice disruption in just a small part of the grain volume. Recrystallization of the steel will begin with nucleation and growth of new grains, improving the ductility but reducing the wire strength. The galvanized wire is then wrapped on a reel of 60 inches (152.4 cm) in diameter and taken to the construction site. Figure 84 shows the entire amount of bridge wires used for the construction of the cable mockup.



Figure 72. Photo. Wire coils to be used for the construction of the cable mockup (first row of coils).

One of the major challenges has been the study of a procedure to build by hand straight strands from coiled steel wires. This has never been attempted before and requires a lot of trial and error. A complex procedure was finally developed that allowed researchers to build a straight strand out of coiled wires, as shown in figure 73. This required passing the wire in a series of combs and distributing the ends in a proper order of directions so that the curvature effects were minimized.

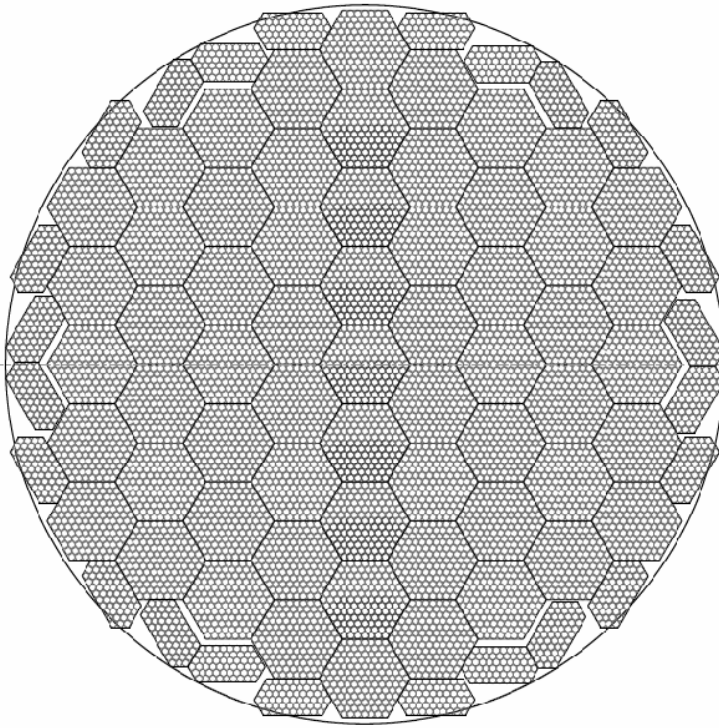
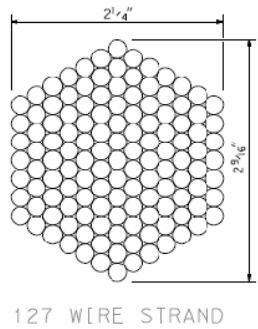


Figure 73. Photo. Strand under construction.

This methodology was used for the construction of the 7 35-ft (10.68-m) strands that were subjected to loading. The other 66 strands, all 20 ft (6.1 m) in length, were built using the same methodology and the same steel wires from the initial coils but straightened (see figure 74). The straightening of the wires was necessary; otherwise, it would have not been possible to build such short strands. In fact, these strands were not socketed, and this would have made it impossible to build them from the original wires. The arrangement and details of the various strands are presented in figure 75.



Figure 74. Photo. Final straight strand from coiled wire.



CABLE CORROSION MONITORING RESEARCH STUDY FOR NEW YORK CITY BRIDGES			
PARSONS			
CORROSION CHAMBER CABLE SUPPORT FRAME			
DWG. NO. 5-4	SCALE	DATE	SHEET 2 of 2

Figure 75. Illustration. Cable cross section and strand details.

Once all the strands were completed, they were assembled following the arrangement presented in figure 75. Stacking of the strands started from the bottom of the cable moving upward, first placing the long strands and then the surrounding straight strands. Because of their tendency to curl as a result of the initial state of stress in the wires, the long strands needed to be pretensioned. First, a long strand was placed within the form and pretensioned, and then the surrounding straight strands were positioned so to restrain the long one. This procedure is shown in figure 76 through figure 78.



Figure 76. Photo. Long strand made of original coiled wires.



Figure 77. Photo. Lower strand assemblage.



Figure 78. Photo. Central strand assemblage.

Figure 79 shows an intermediate phase of the construction of the cable mockup.

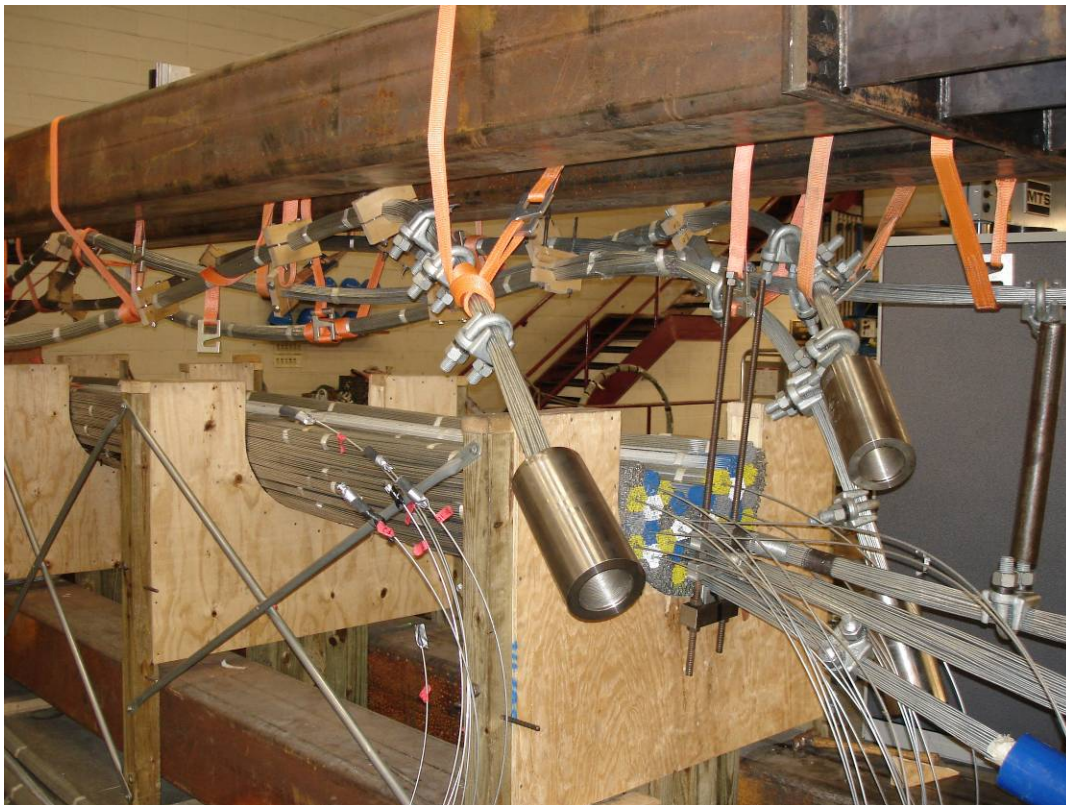


Figure 79. Photo. Intermediate cable construction phase.

It is interesting to see the long strands with the end sockets hanging from the top beams of the loading frame. These strands were socketed at both ends and placed in tension through tensioning rods.

In figure 79, long wires are visible coming out of the shorter strands. Twenty-five long wires were prenotched at three locations along their length and inserted into various strands. Three of these wires were pulled to failure, and the results were used to test the AE system in detecting wire breaks occurring in the interior of a cable. The knowledge of the breaking locations allowed researchers to record and study different wire breaking signatures based on the breaking location along the cable length and along its diameter and on the sensor location relative to the breaking.

In addition, two strands were precorroded before being placed inside the cable. The two strands were placed for a month in a properly designed container and covered with acidic solution. The purpose of these two corroded strands was to generate interior conditions that were not uniform from the beginning of the experiment so that when direct sensing methods were tested for assessing the initial cable condition, a verification of their accuracy could have been available even before beginning the testing program.

In total, 72 sensors were installed in the cross section of the cable. Figure 80 provides a schematic representation of the locations where sensors that successfully performed during the tests were placed. Sensors were placed along three diameters, inclined at 60° with respect to each other. Such distributions allows for measurements that are distributed along the radial direction in order to have a three-dimensional distribution of the various parameters (e.g., temperature, humidity, etc.). The 16 temperature/relative humidity sensors were evenly spaced along the three diameters in order to have measurements for the temperature and humidity variations inside the entire cross section. Figure 81 shows a phase of the sensor placement inside the cable mockup. Special attention had to be made in protecting the sensors from being squished during the cable compaction. As shown in figure 81, sensors were protected using stainless steel pipes that were 3 inches (76.2 mm) long and covered with heat shrinking moisture-resistant coating. The heat shrink coating was used to prevent stainless steel pipes to act as cathode (since the chemical composition of the stainless steel pipe was unknown) and thus induce accelerating corrosion on the wires. The sensors were hard wired, and the electrical wires were run out of the center of the cable at two vertical locations.

Once all the strands had been placed in the right position, the cable was compacted using a 20.75-inch (527.05-mm)-diameter compactor (see figure 82). It is estimated that the compaction force produced inside the cable a pressure of approximately 2,000 psi (13,780 kPa). After the cable was compacted, the temporary wood forms were removed, and the cable was pulled to approximately 1,100 kip (4,893.04 kN) of tension. This cable tensioning was obtained by pulling each strand in increments of 25 kip (111.21 kN) each up to the maximum load of 145 kip (644.99 kN) for the central and lower three strands and 175 kip (778.44 kN) for the upper three strands. The tensioning of each strand was done using two 100-kip (444.82-kN) hydraulic jacks, as shown in (see figure 83).

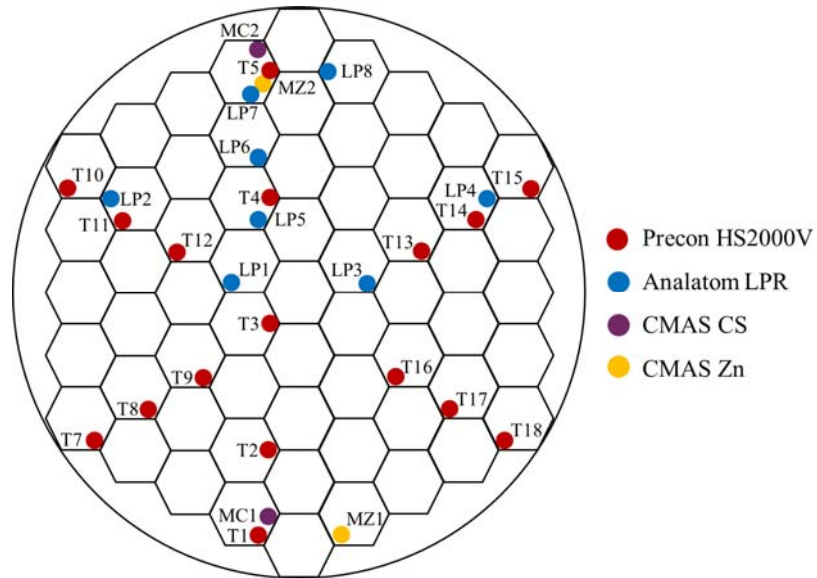


Figure 80. Illustration. Schematic locations of sensors in cable mockup cross section.



Figure 81. Photo. Placement of sensors inside the cable mockup.



Figure 82. Photo. Cable compaction.



Figure 83. Photo. Jacking the first strand.

The cable mockup in its final configuration prior to wrapping and to the construction of the environmental chamber is shown in figure 84.

The exterior protective wrapping of the cable mockup was performed by wrapping the cable with aluminum tape. It is important to observe that in these tests, the function of the wrapping was different from in a real bridge. In this test, since the sensor network had to be tested, the function of the wrapping coating was to keep as much humidity as possible inside the specimen so that the humidity sensors could be successfully tested. In real cables, instead, the function of the external wrapping is exactly the opposite (to prevent water to enter the cable). A neoprene strap

was placed under the aluminum wrapping in correspondence of the exit location of the electric wires from the interior of the cable. This strap was needed to protect the electric wires from the intense heat of the heating lamps.



Figure 84. Photo. Cable mockup representative of a full-scale section of a suspension bridge cable.

An environmental chamber was built around the mockup cable specimen. The chamber was designed to expose the cable to controlled environmental conditions (i.e., simulated rain, heating, and cooling) to accelerate corrosion of the cable specimen, thereby assessing the functionality of the sensor network. Moisture was introduced into the system via water pumps and elevated punctured polyvinyl chloride (PVC) piping to simulate rainfall. Midway through the test program, openings were made in the cable wrapping coating to facilitate the influx of moisture to the inside of the cable mockup. Temperature increases were controlled with heat lamps located at the top of the chamber with a cut-off temperature of 125 °F (51.67 °C), while an air conditioning unit promoted temperature stabilization and rapid chamber/cable cooling. A ventilation system

allowed for increased control of the relative humidity levels within the chamber environment. The final cable mockup with the environmental chamber ready for testing is shown in figure 85.



Figure 85. Photo. Cable specimen with environmental chamber.

CHAPTER 4: RESULTS FROM ACCELERATED CYCLIC TESTS

GENERAL DESCRIPTION

After the cable mockup was built, a long series of cyclic corrosion tests were planned to test the sensors that were part of the proposed corrosion monitoring system. These tests consisted of subjecting the cable specimen to cycles of rain, heat, and cooling of different duration; each experiment lasted for days, and at the end of each test, measurement data were analyzed, and changes of the test conditions were made if necessary. The total duration of this experimental phase lasted approximately 1 year.

Sensor Arrangement

Of the total 72 sensors initially installed in the cable, only 50 sensors provided data worthy of analysis (see figure 80). Those sensors measured temperature, relative humidity, and corrosion rate. Being distributed across the cross section of the cable, they provided an experimental image of the distributions of temperature, relative humidity, and corrosion activity within the cable. The sensors were hard wired, and the electrical wires were run out of the cable center and connected to a DAQ.

The sensor numbering displayed corresponded to the numbering used during data collection. A total of 17 Precon HS2000V temperature/relative humidity sensors (labeled “T” in figure 80 to represent temperature; referred to as “RH” to represent relative humidity) were evenly distributed according to depth and angle of incline. Sensor T6 was discarded from use (not referenced in figure 80) because of early installation malfunctions, while sensors T7 and T18 had some malfunctioning problems during the early tests. Both temperature and relative humidity data was collected at 300-s intervals for the duration of each test.

Eight LPR sensors (labeled “LP” in figure 80) were distributed in the upper half of the mockup cable specimen’s cross section. Four sensors were placed along the upper vertical radius, while two were placed on each of the radii oriented at $\pm 60^\circ$ (see figure 3). A complete cross sectional distribution of corrosion rate sensors was desirable; however, laboratory construction operation forced the placement of LPR sensors to the upper half of the cable’s cross section. LPR sensors collected corrosion rate data every 60 s.

Four CMAS sensors (one CMAS CS and one zinc sensor (CMAS Zn)) were present: one each at the top of the cable and one each at the bottom of the cable, recording corrosion rate every 300 s.

The remaining 22 sensors (not displayed in figure 80) measured pH and corrosion rate levels (using different methods). However, their measurements were erratic and considered unreliable and consequently discarded.

Cyclic Corrosion Testing Chamber

In the environmental chamber built around the cable specimen, moisture was introduced into the system via water pumps and elevated punctured PVC piping so to simulate rainfall. A 300 ppm sodium chloride solution was used to enhance corrosion activity. Midway through the test

program at points approximately 3.94 ft (1.2 m) from either end of the cable mockup, four holes were placed in the cable wrapping. Two 11.89-by-11.89-inch (30.5-by-30.5-cm) openings were made in the underside of the wrapping and at a location on the topside of the cable. At 3.94 ft (1.2 m) from the jacking end, two 0.99-by-0.99-inch (2.54-by-2.54-cm) openings were made to facilitate the influx of moisture to the inside of the cable mockup. Temperature increases were controlled with heat lamps located at the top of the chamber with a cut-off temperature of 125 °F (51.67 °C), while an air conditioning unit promoted temperature stabilization and rapid chamber/cable cooling. A ventilation system allowed for increased control of the relative humidity level within the chamber environment.

The cable mockup specimen was exposed to a variety of cyclic environmental conditions consisting of different combinations of rain, heat, air conditioning, and ambient conditions. These tests provided results that were representative of all the other tests and contained all the important characteristics to understand the environmental conditions inside the cable mockup. The composition and duration of such tests is presented in table 13.

Table 13. Environmental chamber cyclic corrosion test descriptions.

Test Composition/Duration		Test 1	Test 2	Test 3	Test 4
Total cycle length (h)		4	6	6	4
Cycle phase	Rain (h)	0.5	1	1	1
	Heat (h)	1	3	3	1
	Heat-air condit. (h)	1	—	—	1
	Air conditioning (h)	1.5	—	—	1
	Ambient (h)	—	2	2	—
Ventilation		Open	Closed	Open	Closed
Cable		None	4	4	4

— Indicates there was no such phase.

EXPERIMENTAL RESULTS/DISCUSSIONS

Temperature and Relative Humidity Sensors

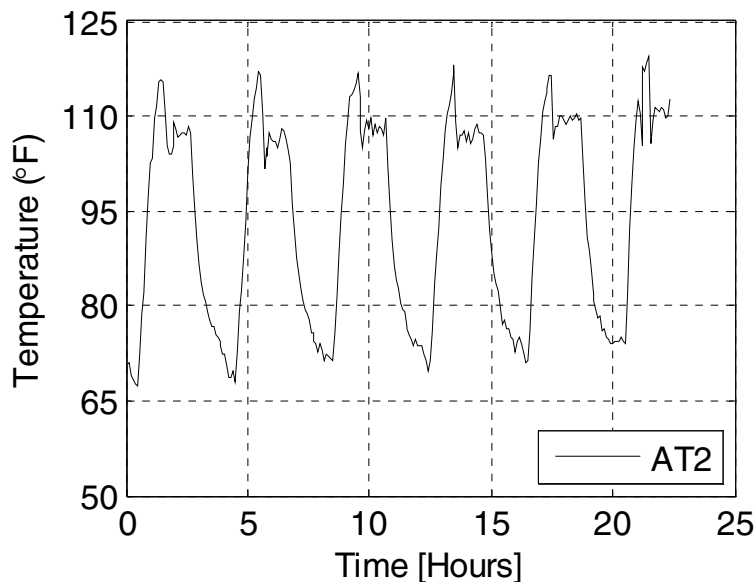
In this section, general temperature and relative humidity trends are discussed using the measurements from test 1. This test was chosen because a Precon HS2000V sensor (AT2) was placed inside the chamber, making it possible to relate the chamber environment to the environment within the cable specimen. Additionally, from the measurements, relative humidity levels within the cable varied significantly, allowing for a better understanding of the relative humidity distributions across the cable’s cross section. Finally, since initial temperature levels were recorded at approximately room temperature throughout the cross section, it was possible to clearly highlight the effects that the proximity to the heat source and the cable surface had on the temperature distribution inside the cable specimen.

In the data analysis, initial data recordings were smoothed using a local regression scheme with weighted linear least squares and a second-degree polynomial model in which outlier data points received a lower weighting than others. Once smoothed, cyclic maxima and minima were identified, and temperature gradients were found for different locations within the cable cross

section. Gradients were compared to highlight the effects of distance from the heat source and of the atmospheric conditions on temperature variation within the cable.

With regard to the distribution of the temperature inside the cable, particular attention was given to the analysis of the temperature distribution inside the upper part of the cable (closer to the heat source). However, similar conclusions can be drawn for the lower portion of the cable. Due to significant differences in temperature values and variations, the analysis of the upper section was subdivided based on three levels (inner, middle and outer) of the sensor distance from the center of the cable's cross section. Following the notation in figure 80, in the upper portion of the cable cross section, the inner level consists of sensors T12, T4, and T13, while the middle and outer levels consist of sensors T11 and T14 and T5 and T15, respectively (the temperature component of sensor 10 did not function). For the lower portion of the cable's cross section, the inner, middle, and outer levels consisted of sensors T9, T16, and T2; T8 and T17; and T1, respectively (sensors T7 and T18 did not function following installation).

Figure 86 clearly shows the temperature pattern inside the chamber. After an initial drop associated with the 30 min of rain, there was a constant increase of temperature in correspondence to the heat phase of the cycle, after which the temperature stabilized around a value of approximately 105 to 110 °F (40.56 to 43.33 °C). Such a temperature remains approximately constant until the heating lamps are shut off and the air conditioning only phase starts. This induces a cooling of the air inside the chamber and a corresponding decrease in temperature. In general, only minor increases of chamber temperature minima were recorded with each cycle in the tests progression.



$$1\text{ }^{\circ}\text{C} = (\text{ }^{\circ}\text{F} - 32)/1.8$$

Figure 86. Graph. Test 1 AT2 chamber temperature recordings.

As far as the temperature distribution inside the cable, sensor T3, which was centrally located within the cable's cross section, was taken as the baseline, and its recordings are shown in figure 87 through figure 89 for comparative purposes. It recorded temperature values between 72 and 85 °F (22.22 and 29.44 °C), showing no distinct cyclic minima and maxima. Although

slight fluctuations appear, a linear regression analysis provided an R^2 value of 0.9606 for the temperature increases recorded by T3 (see figure 87), stating that the temperature at the cable center appears to monotonically increase with a rate of approximately $1^\circ\text{F}/\text{h}$ ($0.56^\circ\text{C}/\text{h}$).

As expected, the greatest temperature increases and fluctuations were recorded in the outer level of the cable's upper section (T5 and T15 (see figure 88 and figure 89)) because of the proximity of the sensors to the heat sources. Sensor T5, which was the closest to the heat lamp, shows sharper cycles than T15. Similar temperature cyclic variations were recorded by the middle and inner layer sensors (T11, T14, T12, T4, and T13 in figure 87 through figure 89) even though the range of such fluctuations decreased when moving toward the center of the cable. The measurements confirm that the left part of the cable shows a temperature distribution that is the mirror image of the temperature distribution in the right half, as expected because of the position of the heat lamps. At the inner level, temperature minima were recorded approximately 20 min after those recorded in the chamber. The time interval between minimum and maximum temperature at the inner level is the same as those recorded at both the middle and outer levels; however, there is a time lag of 10 to 15 min between these minimum and maximum temperatures and the corresponding temperatures at the other outer levels. This lag is a result of the thermal diffusivity properties of the cable.

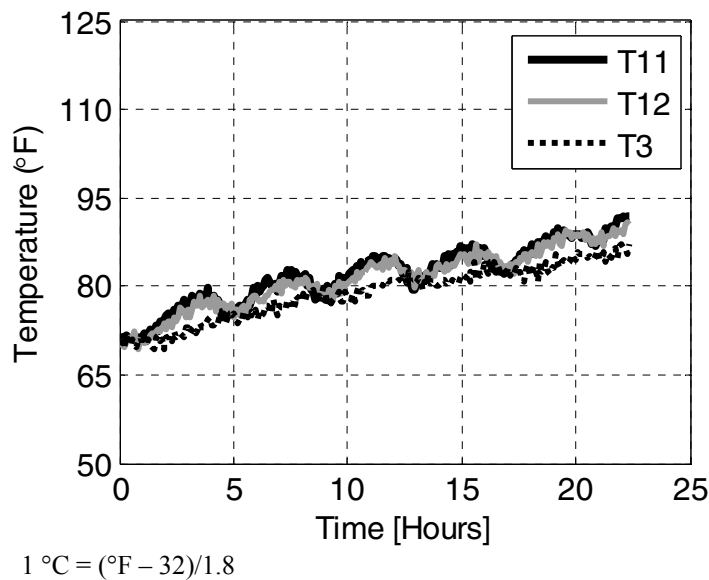
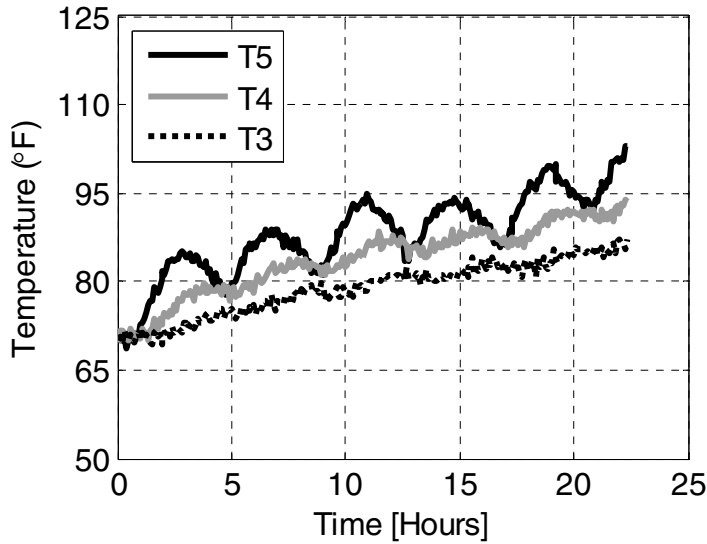
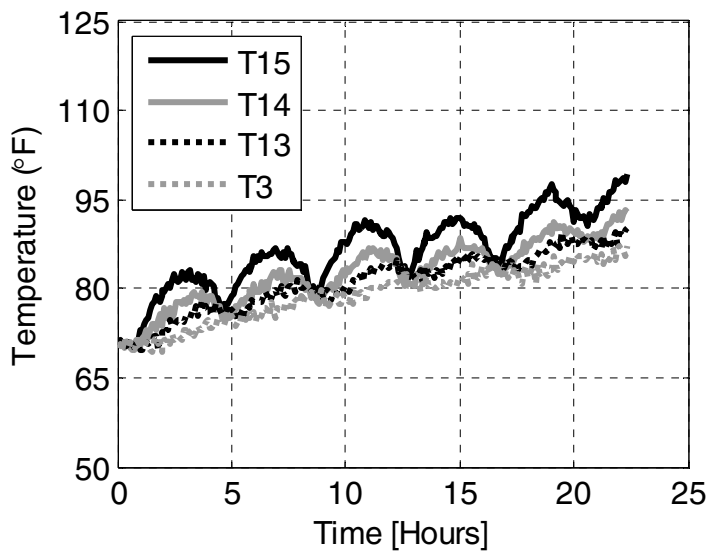


Figure 87. Graph. Test 1 upper cable temperature distributions along diameter at -60° .



$$1\text{ }^{\circ}\text{C} = (\text{ }^{\circ}\text{F} - 32)/1.8$$

Figure 88. Graph. Test 1 upper cable temperature distributions along diameter at 0°.



$$1\text{ }^{\circ}\text{C} = (\text{ }^{\circ}\text{F} - 32)/1.8$$

Figure 89. Graph. Test 1 upper cable temperature distributions along diameter at 60°.

From these measurements, it can be concluded that with greater distance from the heat source, the temperature variations within the cable's cross section diminished with respect to the outside temperature. Maximum temperatures within the cable did not reach levels as high as those recorded in the chamber, and temperature fluctuations decreased with increased distance from the heat source. The upper outer region showed substantial temperature fluctuations, whereas near monotonic increases in temperature occurred in the center of the cable. Average temperature gradients found during the heating phase of each cycle prove that the cable heated evenly with maximum heating rates obtained at central vertical locations. Last, the time to which the cable interior was affected by temperature fluctuations increased with greater cable depth.

The interpretation of the relative humidity data is much more complex because while the temperature data lend itself to a collective analysis, general trends are not as identifiable in the relative humidity data. This is because water can penetrate inside the cable from many different locations and can find many different paths to spread in between the many wires and reach the sensors at different times. However, some general trends can still be found and provide useful information on the functioning of certain sensors. In figure 90, the recordings of the Precon sensor labeled “ARH2” are presented and display the effects of the various phases of the cycle on the relative humidity levels within the testing chamber. Starting from an average level of 55 percent relative humidity in the chamber, the onset of the rain phase caused the chamber relative humidity to increase from 55 to 99 percent. After the rain phase was over, ARH2 recorded relative humidity values of approximately 15 to 20 percent during the heat and heat plus air conditioning phases and increased to the initial 55 percent value at the end of the cycle. This type of fluctuation was as expected and showed the good functioning of the sensor placed in the environmental chamber.

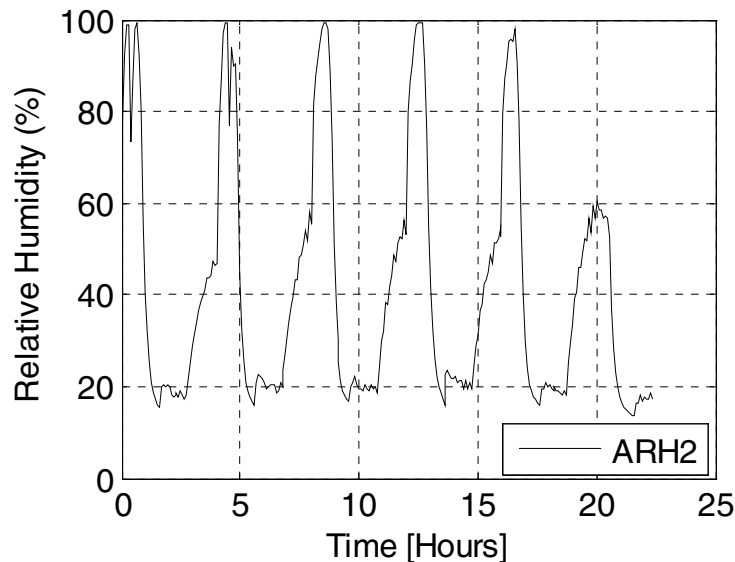


Figure 90. Graph. Test 1 Precon HS2000V ARH2 chamber relative humidity recordings.

As in the temperature analysis, the relative humidity recordings of Precon sensor 3 (RH3), referring to the center of the cable, was used for comparative purposes. The sensor recorded initial relative humidity levels of 40 percent, while the reading within the chamber was at 55 percent. Over the course of testing, despite the external fluctuations in relative humidity levels, the center of the mockup cable experienced an approximate cyclic decline in relative humidity of 2 percent. A linear regression analysis returned an R^2 value of 0.9701, suggesting a nearly linear decline of the relative humidity in the cable center. This is consistent with the linear increase of the temperature at the center, as shown in figure 87 through figure 89.

Sensors within the outer level (RH10, RH5, and RH15) of the upper portion of the cable mockup specimen recorded substantial variations in relative humidity levels (see figure 91 through figure 93). RH10 recorded the highest initial relative humidity levels at 88 percent (see figure 91). This occurred due to three possibilities: some local trapped water, the sensor was near complete saturation, and/or a possible sensor malfunction (the temperature component

of sensor 10 (T10) was not functioning, thus the relative humidity readings may also have been inaccurate).

Inner sensors located on the diagonals in the upper section of the cable's cross section (RH12 and RH13) recorded near steady declines over the course of test. This agrees with the fact that the internal temperature of the cable steadily increased.

In general, the relative humidity levels varied significantly across the mockup cable cross section, especially in the outer layers. As previously mentioned, this was expected because of the different ways water infiltrates inside the cable. Sensors located closer to the cable surface (e.g., RH15 and RH10) recorded elevated relative humidity levels, while those closer to the cable center recorded substantially lower levels. Additionally, close to the cable's core, sensors recorded near linear monotonic decreases in relative humidity of approximately 2 percent per cycle corresponding to nearly linear increases in temperature of approximately 5 °F (-15 °C) . Conversely, over the course of testing, sensors closer to the surface displayed greater cyclic fluctuations.

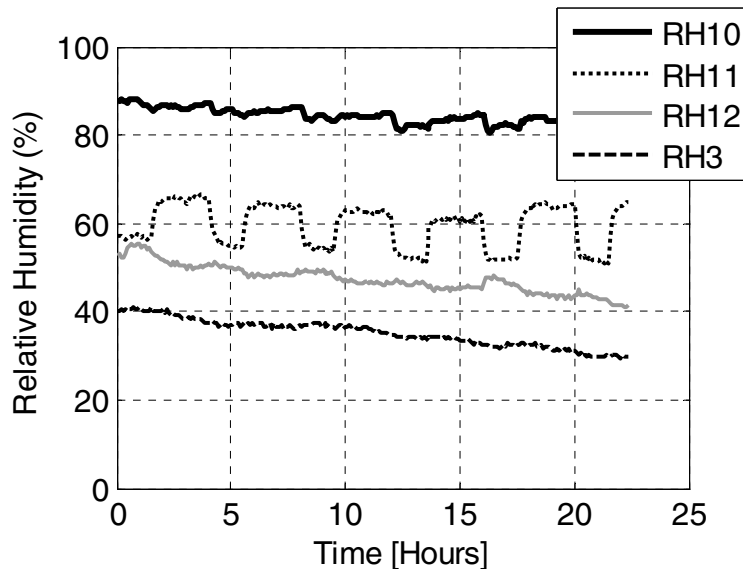


Figure 91. Graph. Test 1 upper cable relative humidity distributions along diameter at -60°.

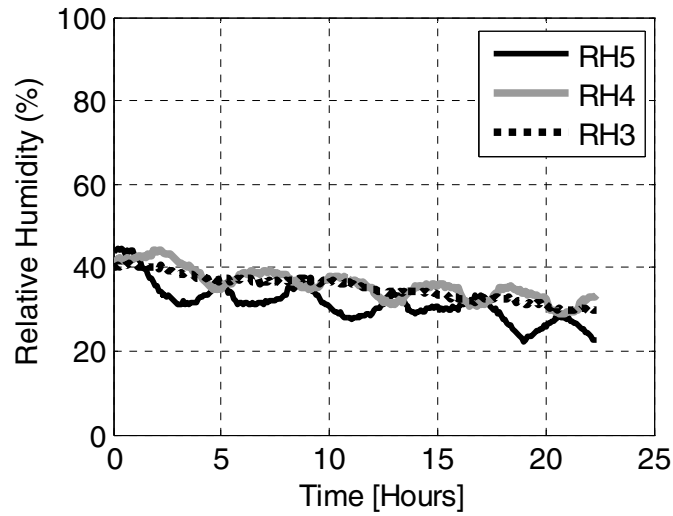


Figure 92. Graph. Test 1 upper cable relative humidity distributions along diameter at 0°.

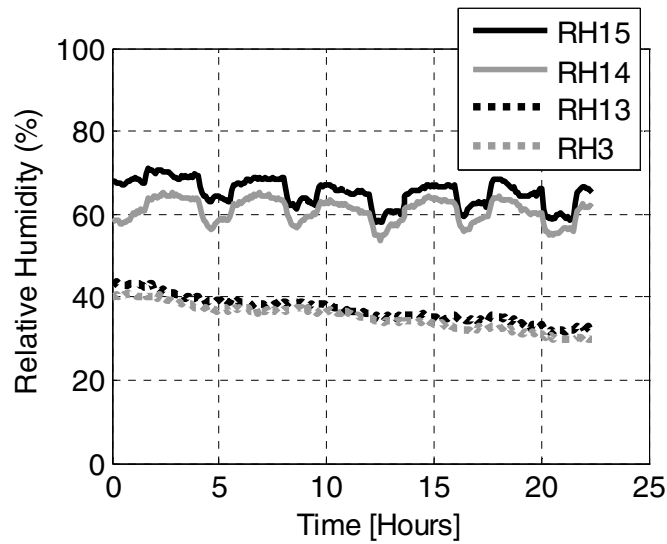
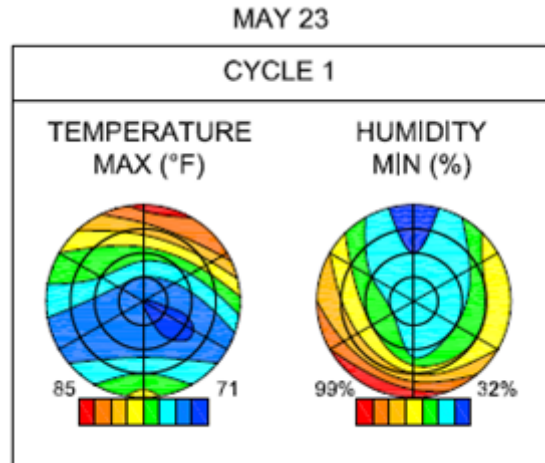


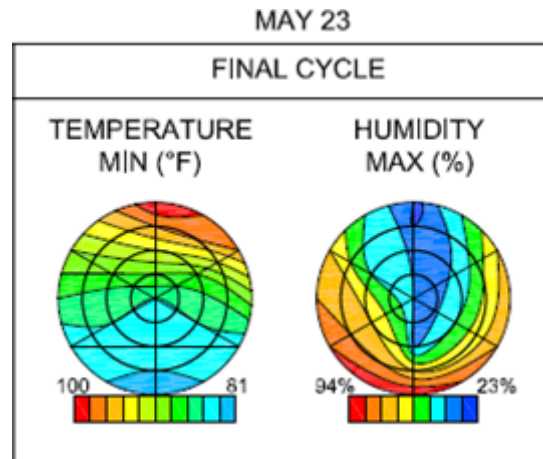
Figure 93. Graph. Test 1 upper cable relative humidity distributions along diameter at 60°.

Figure 94 and figure 95 provide a visual mapping of the variation of the maximum and minimum temperatures and relative humidity over the entire cable's cross section.



$$1\text{ }^{\circ}\text{C} = (\text{ }^{\circ}\text{F} - 32)/1.8$$

Figure 94. Illustration. Mapping of maximum and minimum temperature and relative humidity distribution during cycle 1 over the entire cable’s cross section.



$$1\text{ }^{\circ}\text{C} = (\text{ }^{\circ}\text{F} - 32)/1.8$$

Figure 95. Illustration. Mapping of maximum and minimum temperature and relative humidity distribution during the final cycle over the entire cable’s cross section.

Although increased levels of relative humidity seem to correspond well with increased distances from the cable core (i.e., closer proximity to the cable surface), levels of cyclic relative humidity fluctuations do not. This could be linked to the different infiltration paths, especially in the outer layers. In general, relative humidity sensors recorded increased levels 1.5 h after the onset of cyclic rain phases.

The role of temperature and sensor saturation must be considered, as areas of the cable may be prone to collect or expunge water, resulting in inexplicable levels and fluctuations of relative humidity. Many sensors recorded prolonged periods of elevated relative humidity, suggesting that water introduced into the cable during the rain phase could not evaporate during the cyclic heat phases. The entrapment of moisture within the mockup cable represents a serious problem in the deterioration of suspension bridge main cables. Specifically, the inability for evaporation

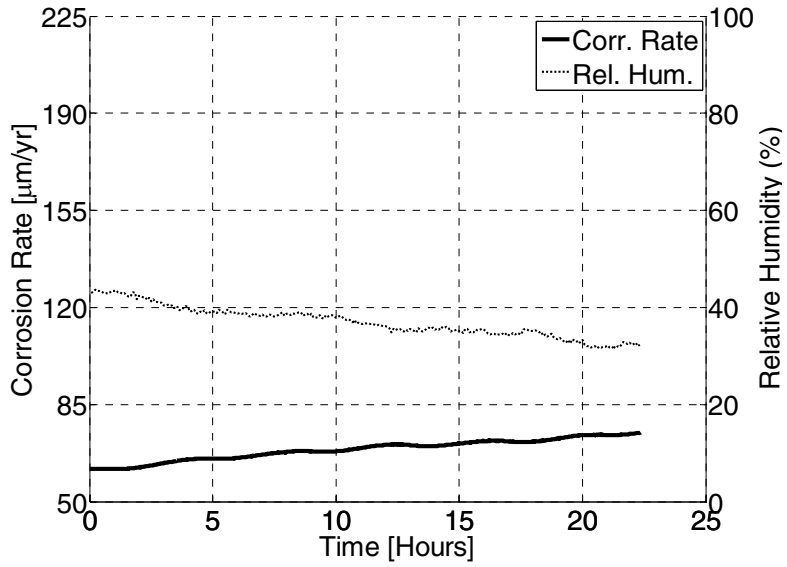
to occur results in an aggressive environment in which corrosion may occur at elevated rates, and sensing technology may be negatively affected.

This conclusion is further bolstered by a consideration of the RH5 sensor recordings. Relative humidity levels recorded by RH5 peaked with the onset of the rain phase. Peak levels proceeded to decline during the heat phase, eventually increasing with the onset of air-conditioning. The lowering of relative humidity with increased temperature was expected, as increasing temperature promotes the evaporation of the water molecules from the electrode surface. The position of sensor 5 at the top of the cable and its proximity to the cable surface may allow for the excess water/moisture to both drain and/or evaporate from the sensor surface. Furthermore, condensation and an increase of relative humidity with decreasing temperature were both expected and seen in the recordings of sensor 5 during test 1. The distribution of the relative humidity recorded by the sensors over the cross section further validates the 2004 findings of Suzumura and Nakamura in which decreased levels of relative humidity were identified in the upper portion while higher levels of relative humidity were found in the sides and lower portion of the cross section.⁽¹⁸⁾

Temperature and relative humidity recordings from this test confirm the expectation of an inversely proportional relationship between these two environmental variables. A statistical analysis of the temperature and relative humidity levels recorded by sensors 3, 5, 12, and 13 returned correlation coefficient values of less than -0.95, showing an extremely strong inversely linear relationship between the respective temperature and relative humidity recordings. Unfortunately, due to the potential presence of pockets of water, moisture, and sensor saturation, not all correlations were as strong. Thus, relative humidity levels cannot be strictly explained with temperature recordings; rather, they must be considered individually.

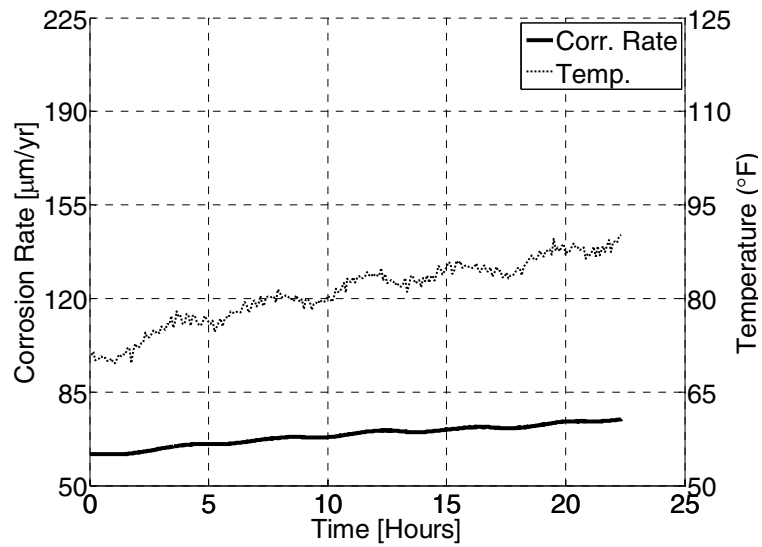
Corrosion Rate Sensors: LPR Sensors

Of the eight LPR sensors placed in the cable, only LPR3 and LPR4 recorded corrosion rates above noise values. The analysis of the corrosion rate sensors was twofold. Corrosion rate recordings from each sensor were compared and related to local temperature and relative humidity recordings as well as other corrosion rate sensor recordings. The effect of both the environmental conditions and the location within the cable cross section on corrosion was addressed by considering the correlation between atmospheric variables and corrosion rate fluctuation. For a better understanding of the interaction between temperature/relative humidity and corrosion rate, the recordings of LPR3 and LPR4 are presented against RH13 (figure 96), T13 (figure 97), RH15 (figure 98), and T15 (figure 99) for tests 1 and 3 (table 13). These tests were selected because while temperature ranges were similar, the relative humidity values differed enough between tests to permit an analysis of the effects of both environmental variables. Corrosion rate values recorded by LPR sensors appeared to follow distinct cyclic trends associated with temperature, while initial rate levels were affected by relative humidity.



1 inch = 25,400 µm

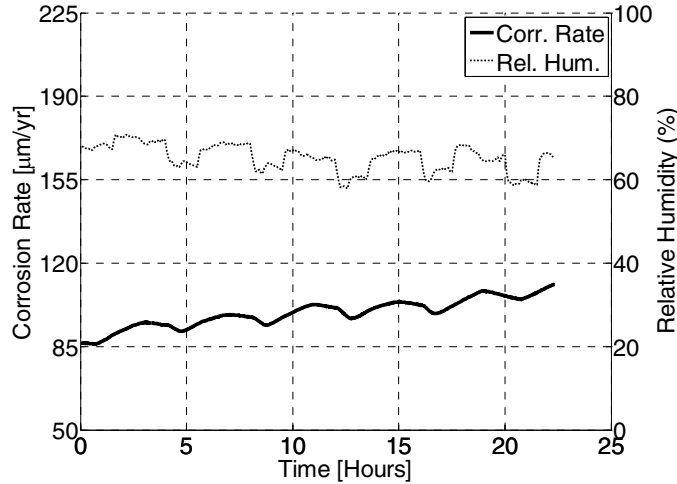
Figure 96. Graph. Test 1 LPR3 versus RH13.



1 inch = 25,400 µm

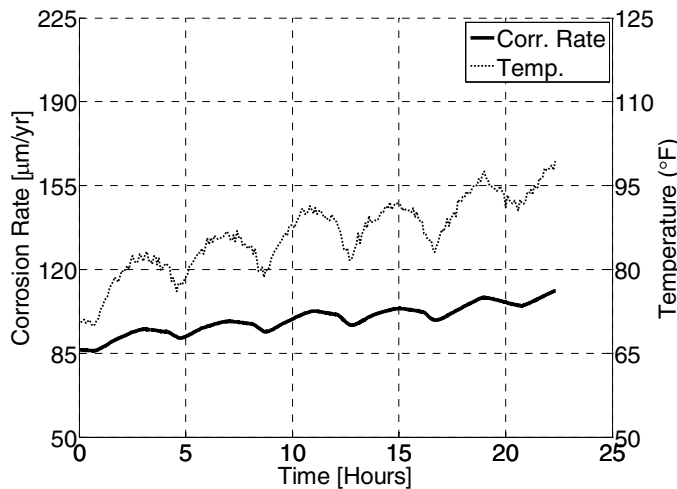
1 °C = (°F - 32)/1.8

Figure 97. Graph. Test 1 LPR3 versus T13.



1 inch = 25,400 µm

Figure 98. Graph. Test 1 LPR4 versus RH15.



1 inch = 25,400 µm

1 °C = (°F - 32)/1.8

Figure 99. Graph. Test 1 LPR4 versus T15.

A statistical analysis of the data presented in figure 96 and figure 97 revealed that in test 1, the LPR3 recordings had strong linear (positive and negative) relationships with temperature and relative humidity levels, respectively. A correlation coefficient of 0.9855 existed between the data recorded for LPR3 and T13, while a correlation coefficient of -0.9844 existed between the recordings for LPR3 and RH13.

Conversely, for the correlation between LPR4 and RH15, it was found that the correlation coefficient dropped to -0.3192, losing the inverse proportionality seen in LPR3 and RH13. With regard to the T15 temperatures, the correlation coefficient for the LPR4 data was 0.9841, thus confirming the strong linear relationship between corrosion rate and temperature readings. For each ± 1.5 °F (0.83 °C) increase in temperature, there was a $\pm 3.93 \times 10^{-5}$ inch/year (1 µm/year) increase in corrosion rate. Comparing the measurements from RH13 and RH15, a difference in relative humidity levels of 25 percent appears to have induced an increase in baseline corrosion

rates of 0.00094 inch/year (24 $\mu\text{m}/\text{year}$) between LPR3 and LPR4. For the overall test, temperature increases of 23 °F (-5 °C) recorded by T13 led to increases in corrosion rate recordings by LPR3 of 0.00047 inch/year (12 $\mu\text{m}/\text{year}$), whereas temperature increases recorded by T15 of approximately 30 °F (-1.11 °C) resulted in corrosion rate increases of 0.00094 inch/year (24 $\mu\text{m}/\text{year}$) by LPR4, maintaining almost identical increase and decrease rates within cycles. Similar conclusions were reached in test 3, with a strong linear relationship between corrosion rate and temperature (correlation coefficients of 0.9899 for LPR3 and 0.9928 for LPR4), respectively. As seen in test 1, the test 3 corrosion rate fluctuations did not strongly relate to relative humidity fluctuations.

From the analysis of the recorded data, it appears that relative humidity controls the overall (average) levels of corrosion rate fluctuations, while temperature changes affect the more localized and cyclic corrosion rates. The effects of relative humidity were shown in the readings of LPR3 and RH13 compared to those of LPR4 and RH15. At increased levels of relative humidity (test 3), a shift in temperature of approximately 1 °F (0.56 °C) resulted in a shift of approximately 3.93×10^{-5} inch/year (1 $\mu\text{m}/\text{year}$) in corrosion rate. At lower humidity levels, the ratio changes as a 1 °F (0.56 °C) shift in temperature led to a shift in corrosion rate that is less than 3.93×10^{-5} inch/year (1 $\mu\text{m}/\text{year}$) (test 1). Thus, depending on the relative humidity levels and the corresponding initial corrosion rates, it may be possible to determine a proportionality constant between temperature and corrosion rate and use temperature data to predict and verify corrosion rates within the mockup cable's cross section.

Corrosion Rate Sensors: CMAS Sensors

Corrosion rate readings from the CMAS CS sensors were analyzed in conjunction with temperature and relative humidity levels as recorded by T5. In similar fashion to the LPR analysis, the CMAS sensor analysis identified cyclic fluctuations in corrosion rate readings as well as the fluctuations of the surrounding environmental variables. The sensors being considered were located at the top of the cable cross section 0° from the vertical axis (MC2 and T5 in figure 80). Because of different characteristics, measured corrosion rates are presented for two different conditions: for relative humidity below 50 percent (test 4 in figure 100 and figure 101) and between 80 and 90 percent (test 2 in figure 102 and figure 103).

When humidity levels were consistently below 50 percent (see figure 100) and the temperature varied between 70 and 110 °F (21.11 and 43.33 °C) (see figure 101), the CMAS CS sensors recorded low yet viable corrosion rates. However, the overall level of relative humidity within the cable was sufficiently low so as to not induce much corrosion activity. Only at times when the relative humidity showed some non-negligible gradients did the CMAS CS sensor record slight activity.

The introduction of two openings on the top and two openings on the bottom in the wrapping of the mockup cable specimen as well as closing the chamber ventilation resulted in a substantial increase of relative humidity both within the chamber and within the cable (80 to 90 percent) at 92 to 119 °F (33.33 to 48.33 °C), respectively (see figure 102 and figure 103). The corrosion rate measurements showed a similar pattern as those from the previous test, but the values are much higher: an average value of 0.00098 inch/year (25 $\mu\text{m}/\text{year}$) in the stable part of the test versus a value below 0.00015 inch/year (4 $\mu\text{m}/\text{year}$) in the previous test.

From the analysis of these results, it can be concluded that the CMAS corrosion rate sensors showed a similar performance as the LPR sensors. Increases in chamber relative humidity levels led to general increases in CS corrosion rate values.

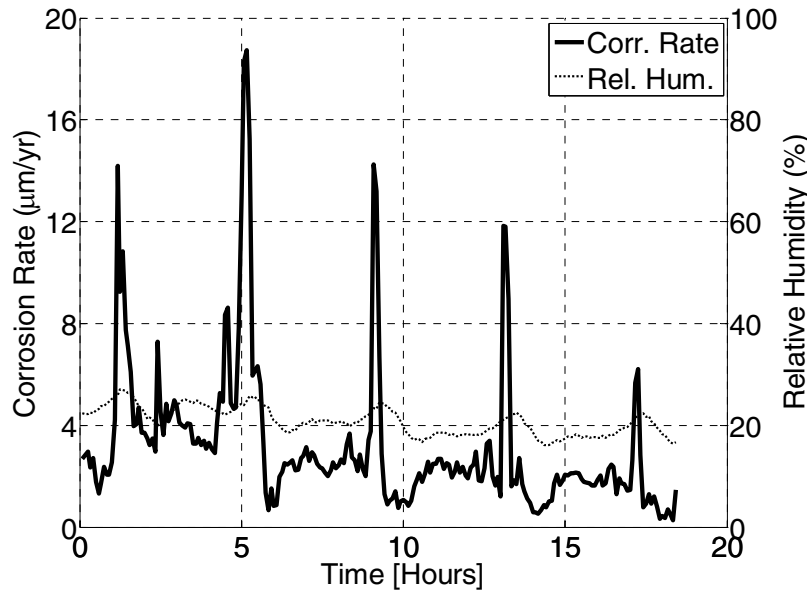


Figure 100. Graph. Test 4 CMAS CS with sensor 5 readings for relative humidity.

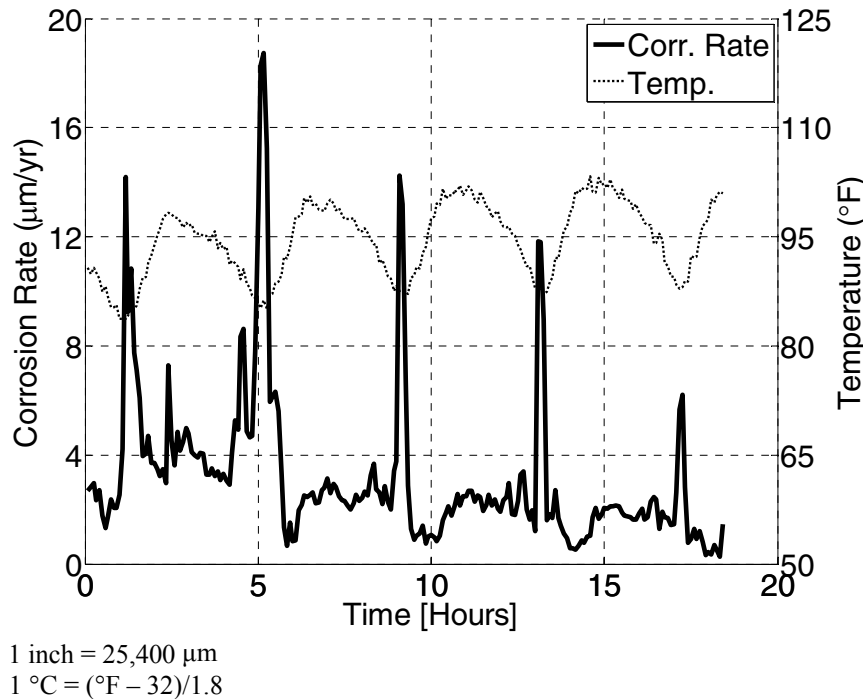
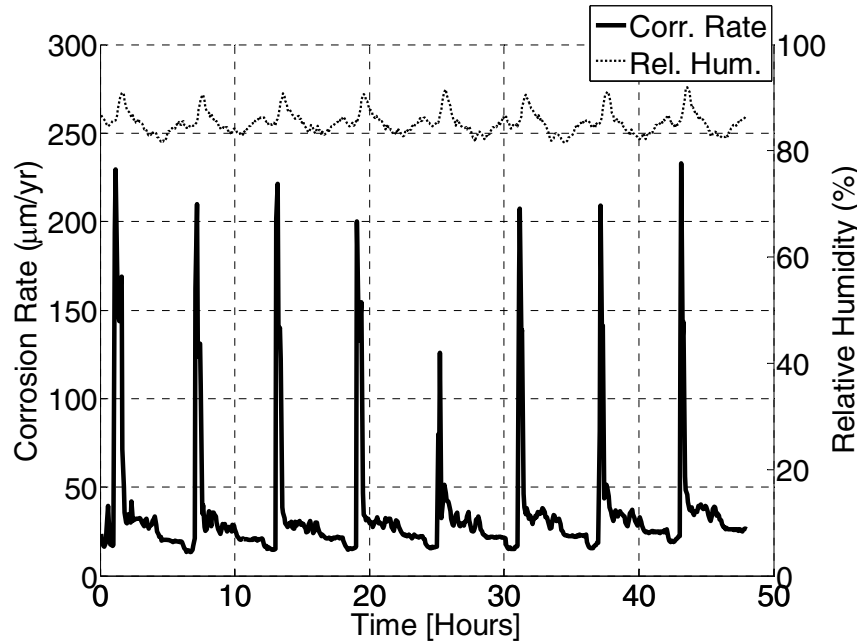
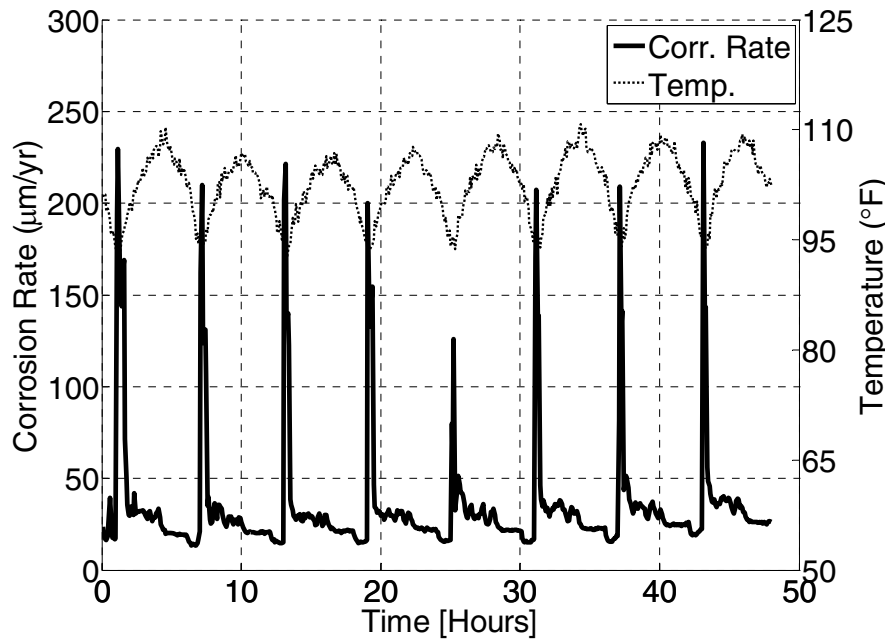


Figure 101. Graph. Test 4 CMAS CS with sensor 5 readings for temperature.



1 inch = 25,400 µm

Figure 102. Graph. Test 2 CMAS CS with sensor 5 readings for relative humidity.



1 inch = 25,400 µm

1 °C = (°F - 32)/1.8

Figure 103. Graph. Test 2 CMAS CS with sensor 5 readings for temperature.

With relative humidity levels of 80 to 90 percent, both CS corrosion rate peaks and baseline values increased by approximately 15 to 20 times those recorded at low levels of relative humidity (< 50 percent). At high levels of relative humidity (> 80 percent), temperature effects were more pronounced and identifiable. Increases in corrosion rate minimum values from

one cycle to the next for test 2 revealed that relative humidity levels affected the baseline values of CS corrosion rates. Temperature shifts, however, contributed to minor shifts in corrosion rates both cyclically and over the total course of testing. High levels of relative humidity created the aqueous environment to cause the onset of CS corrosion, while elevated temperatures increased the kinetics of the chemical reactions and the corresponding corrosion rates.

The large decreases in corrosion rate of 0.0063 to 0.0075 inch/year (160 to 190 $\mu\text{m}/\text{year}$) during test 2 corresponding to minor relative humidity drops of 4 to 6 percent are inexplicable. Extremely elevated levels of corrosion activity may be misleading. Due to the proximity of the CMAS CS sensor to the cable surface, it is possible that with the presence of water in the cable (due to holes in the cable wrapping), the sensor became saturated at points corresponding to peak values.

Other Corrosion Rate Sensors

The other sensors considered in this testing phase did not show the same sensitivity as the LPR and CMAS sensors. The recorded measurements were consistently below the noise threshold in any of the tests conducted. This could be due to either a reduced sensitivity of the sensor or to the lack of corrosion activity in the proximity of the sensor itself. However, as seen in the next section, extensive water penetration and salt deposition occurred inside the cable, which should have activated some of the sensors.

As an example, the BM corrosion sensors recorded some activity, but the levels of the measured corrosion rate were well below those recorded by other corrosion rate sensors. Figure 104 shows the measurements of the corrosion rate recorded by sensor BM5, which is in the proximity of the T4 and RH4. Even with high temperature levels (between 70 and 100 °F (21.11 and 37.78 °C)) and relative humidity (between 86 and 92 percent), the recorded corrosion rates for CS and zinc were low (1.97×10^{-5} to 0.00014 inch/year (0.5 to 3.5 $\mu\text{m}/\text{year}$) for steel and 3.93×10^{-5} to 0.00027 inch/year (1 to 7 $\mu\text{m}/\text{year}$) for the zinc). Also these BM sensors showed a clear dependence of the corrosion rate with the temperature; at high relative humidity levels (between 87 and 92 percent), the corrosion rate measurements for both the CS and zinc presents a strong correlation with the temperature (see figure 104).

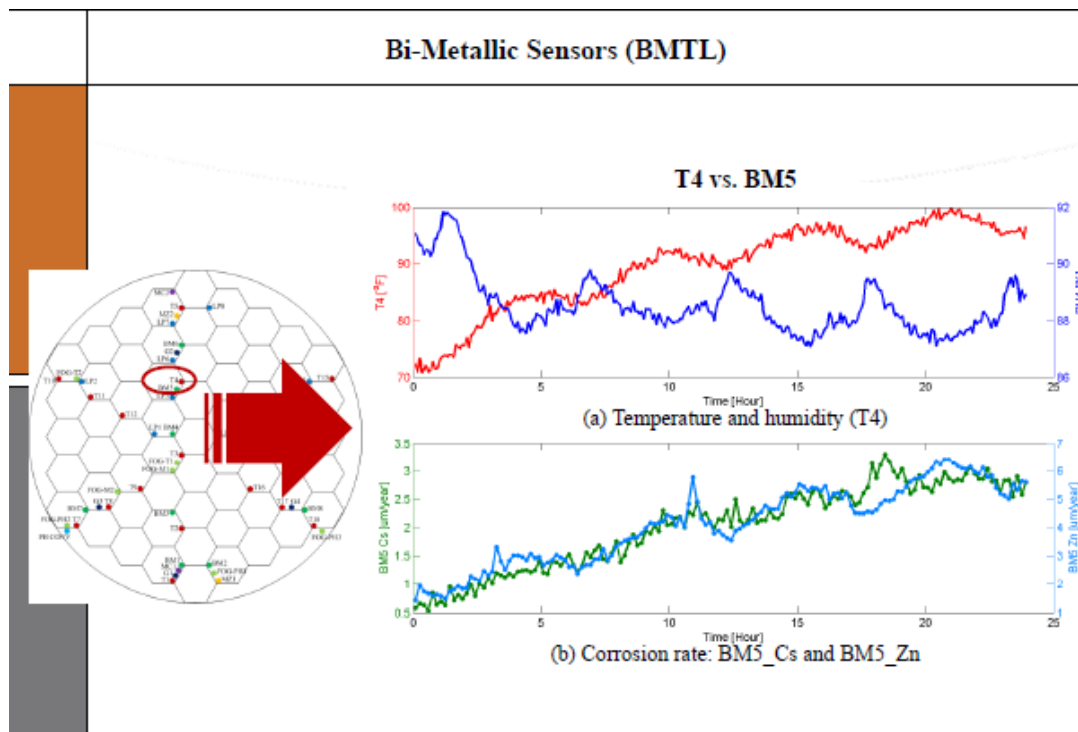


Figure 104. Illustration. Test 2 corrosion rate for CS and zinc obtained by sensor BM5 in test 2.

CONCLUSIONS

The laboratory testing phase of this project served to test a set of selected sensors in a cable specimen that closely resemble real-life conditions. The construction of an environmental testing chamber permitted the testing of various environments affecting the temperature, relative humidity, and corrosion rate distributions within the mockup cable. As compared with the external chamber environment, cyclic environmental fluctuations were reflected in outer sensor recordings of temperature and relative humidity, while sensors in the core of the cable recorded near constant increases in temperature and decreases in relative humidity. Temperature levels and fluctuations proved to vary according to depth within the cable.

Although they did not follow consistent trends across the cable's cross section, relative humidity values were strong indicators of corrosion rate levels, as validated by those recorded by LPR, CMAS, and BM corrosion rate sensors.

Increased levels of relative humidity resulted in increased levels of corrosion activity recorded by both types of sensors. Furthermore, statistical analyses showed that the experimental dependence of corrosion rate values, as recorded by LPR sensors, on temperature was strongly linear. In addition, while temperature values varied with cable depth and followed distinct trends in cyclic fluctuations, relative humidity did not.

While the LPR, CMAS, and BM sensors showed good sensitivity in measuring corrosion activities inside the cable, other sensors did not record values beyond the noise threshold. Fiber-optic sensors did not show any reliable measurement data, with most of them broken during

operation. This information was then used in preparing the sensor system that was installed on the main cable of the Manhattan Bridge.

Testing the AE System for the Detection of Wire Breaks in the Interior of the Cable

Having a full-scale mockup of a main cable of a suspension bridge with prenotched wires in the interior allowed for the possibility to test and tune the AE system to detect wire breaks occurring in the interior of the cable. By pulling interior wires that were originally notched at specific locations along the cable’s length until they failed, it allowed for the opportunity to record the signal signature of an interior wire breaks in a lab environment (without any unexpected environmental interferences) and to test the sensitivity of such an AE system in detecting this type of wire failure.

In order to accomplish this objective, two different types of AE sensors were mounted on the mockup cable: eight AE sensors R0.45I (4.5 kHz) and eight AE sensors R1.5I (15 kHz) were installed on the two cable bands at the ends of the cable specimen (see table 14). Data were collected using the PAC 16-channel sensor highway II installed as part of the permanent equipment designed for monitoring and control of the environmental chamber of the cable mockup. The sensor locations on the cable bands of the mockup are shown in figure 105.

Table 14. Positions and types of AE sensors.

Channel Number	Type of Sensor	Position
1, 4, 5, and 8	R1.5I	South end
2, 3, 6, and 7	R0.45I	South end
9, 12, 13, and 15	R1.5I	North end
10, 11, 16, and 14	R0.45I	North end

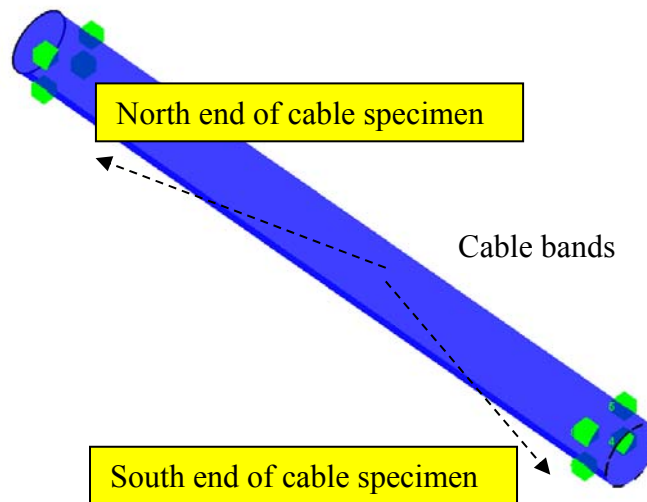


Figure 105. Illustration. Sensor locations.

The sensors were used in three different location setups to determine the position of the wire breaks: linear location, two-dimensional planar location, and cylindrical location. On each test, a strain gauge was mounted on the prenotched wire being loaded, and its signal was recorded as an external parameter to monitor the load applied to the pre-notched wire. Also, average signal level

(ASL), absolute energy, and root mean square voltage of the acoustic signals were monitored at a frequency of 10 Hz as time-driven data. The threshold for the AE system was set to 45 dB.

The objective of the test was to attempt to break three prenotched wires. The difficulties in pulling wires until they failed were created by the presence of the massive steel frame supporting the cable specimen (see figure 106), and this limited the number of pulled wires to three. Figure 106 shows the setup used to load the prenotched wires. In the first two wires, the prenotched wires broke at the junction with the grip used to applied load, so the results were not considered.



Figure 106. Photo. Mechanism to apply load to the prenotched wires.

In the third attempt, the wire broke as expected. Figure 107 shows plots of acoustic ASL, absolute energy ($\text{Joules} \times 10^{-18}$), and load (kips) versus time during the third wire break attempt. In the figure, ASL is depicted in green, absolute energy is depicted in red, and load is depicted in blue.

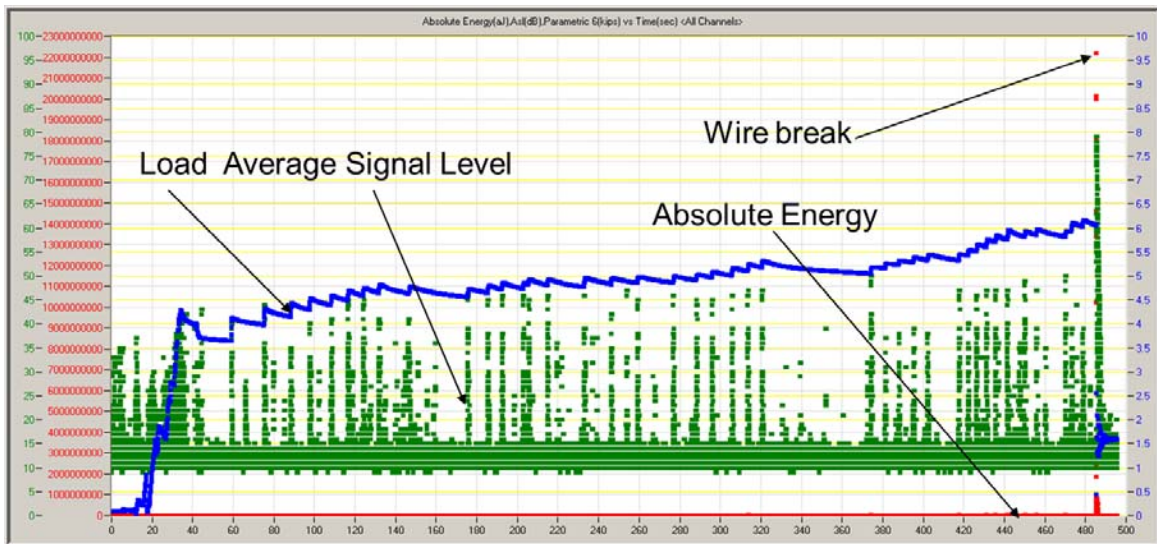


Figure 107. Graph. ASL (green), absolute energy (red), and load (blue) versus time during the third wire break attempt.

The green line represents the average signal level (a measurement of the AE signals over time that reach a channel) and is measured in dB units. The red line indicates the absolute energy, representing the area under the curve of the rectified waveform, and is measured in aJ, while the blue line indicates the load applied to the wire in kips. Figure 107 indicates that bursts of AE produced by friction were detected every time the load was increased.

However, the absolute energy of these AE bursts was insignificant compared to the absolute energy generated by the wire break. This means that a wire break could be clearly set apart from regular AE caused by movement or load changes in the cable.

After the wire was broken, the wire was pulled out about 5 inches (127 mm) from the edge of the cable before it broke, as can be seen in figure 108.



Figure 108. Photo. Broken wire pulled out from the edge of the cable before breaking.

During the wire break, the R0.45I array sensors located many low energy events during the loading process, in addition to the actual high energy wire break, as shown in figure 109. In this figure, the cylindrical surface of the mockup cable is shown open, with the horizontal axis (in inches) representing the length of the mockup, and the vertical axis representing the perimetral distance. In addition, the locations, with related channel number corresponding to the sensors, are presented on their actual locations on the cable bands.

The low-energy events generated by friction and movement of the cable, shown in green, are located all along and around the cable, while the high-energy data, generated by the wire failure, are shown in blue, yellow, and red. A quick review of the waveforms corresponding to the low- and high-energy events show a clear difference when comparing the amplitude of the signals with the threshold values represented by the red horizontal lines. The wire break signals show a large amplitude and sharp rise time, while the noise signals are barely above the threshold. The difference in energy between these two types of signals is of two orders of magnitude or about 40 dB.

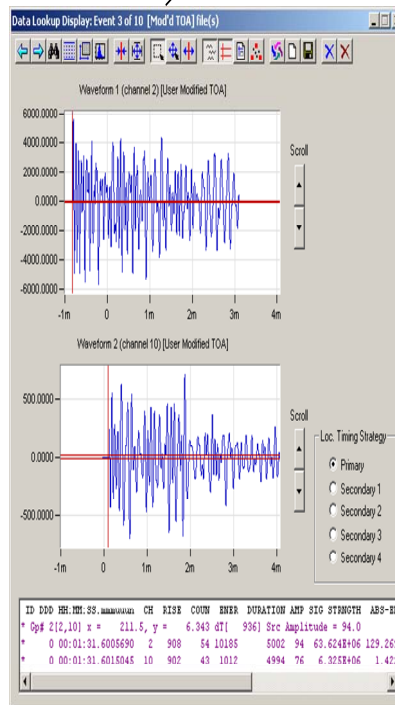
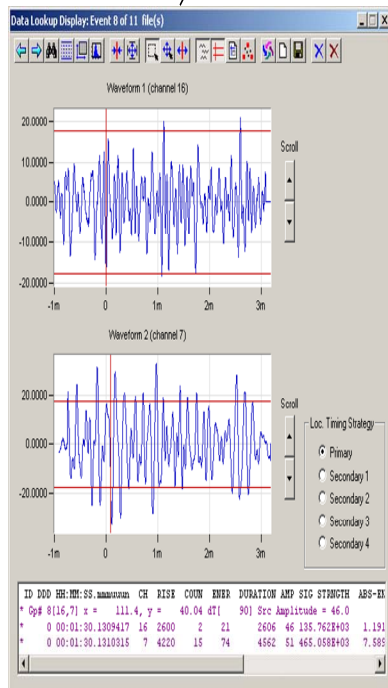
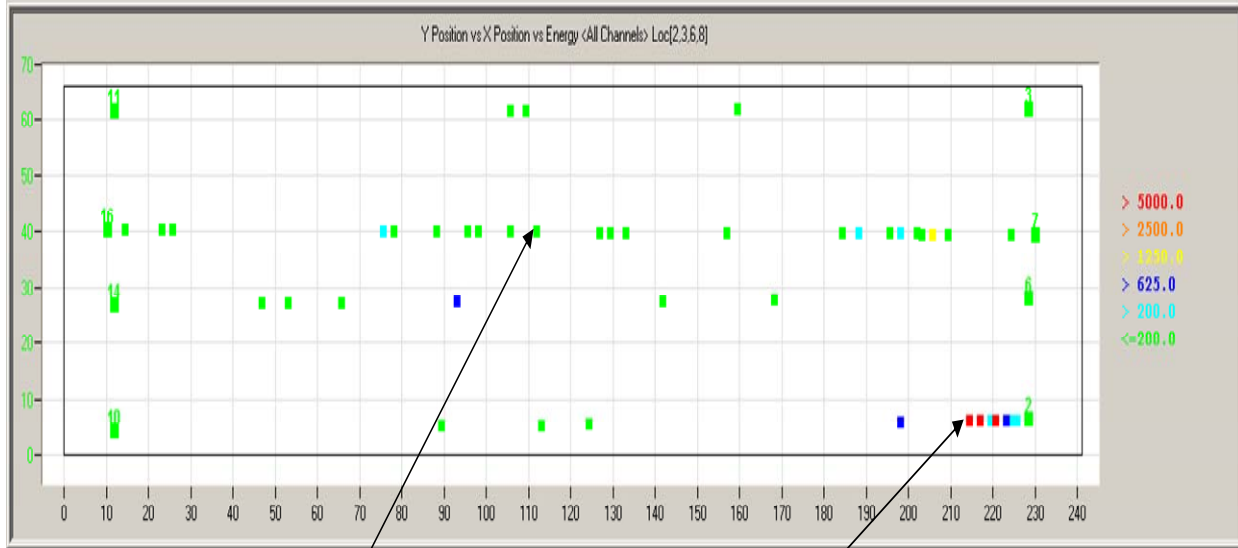


Figure 109. Illustration. Low- and high-energy events during the wire break from R0.45I sensors.

By comparison, the results obtaining with the R1.5I sensors shown in figure 110 present only one event with low energy and two events related to the wire break. This indicates that the R1.5I sensor is less susceptible to detect the noise signals, traditionally containing lower frequency. It is important to mention that the two set of sensors correctly located the position of the wire break.

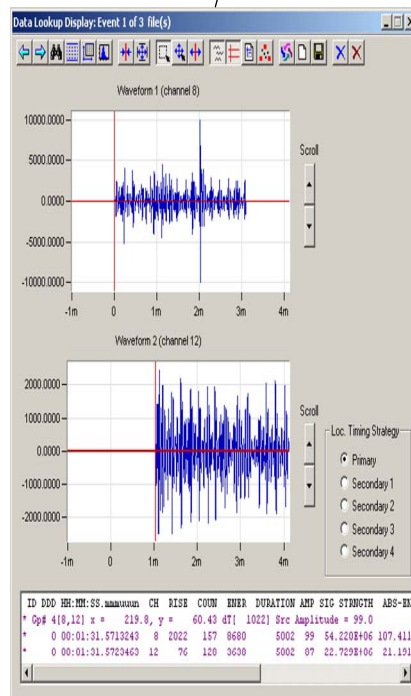
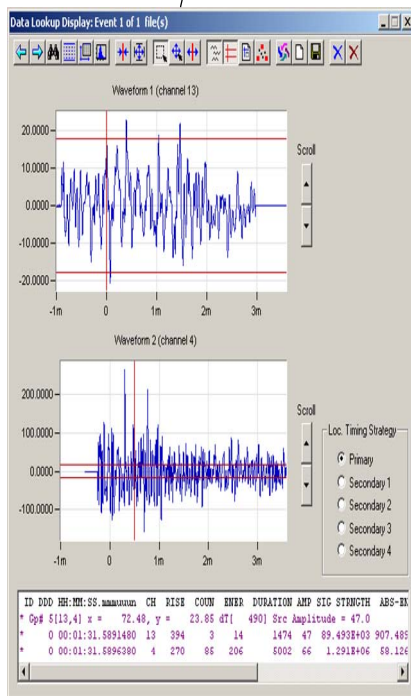


Figure 110. Illustration. Low- and high-energy events during the wire break from R1.5I sensors.

The array of R0.45I sensors detected and located the wire break longitudinal position with good accuracy—217.9 inches (5,534.66 mm) from the edge of the cable versus 223 inches (5,664.2 mm) of the actual wire break. The circumferential position calculated was 18 inches (457.2 mm) away from the actual position at 61 inches (1,549.4 mm) along the circumference of the cable. The R1.5I sensors detected and located the wire break longitudinal position with excellent accuracy—222.9 inches (5,661.66 mm) from the edge of the cable versus 223 inches (5,664.2 mm) of the actual wire break. The circumferential position calculated was 57.9 inches (1,470.66 mm) versus 61 inches (1,549.4 mm) for the actual position. The position of the wire break on the cylindrical surface of the cable is shown in figure 111 and figure 112.

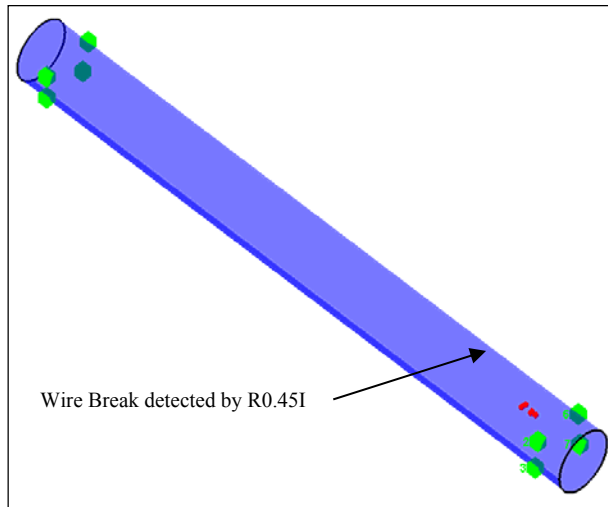


Figure 111. Illustration. Location of the wire break with the R0.45I sensor on the surface of the cable mockup.

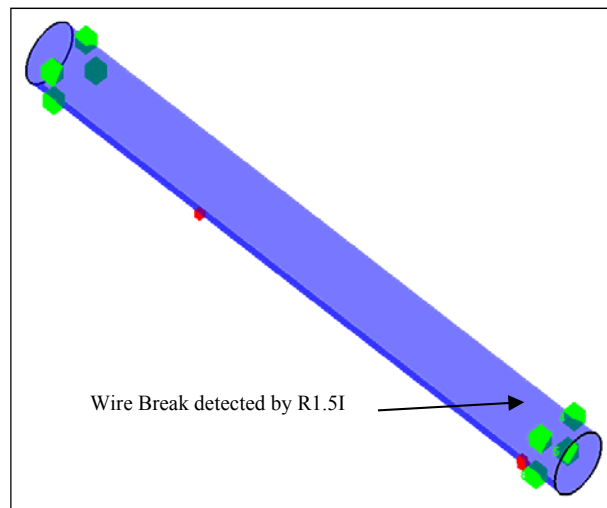
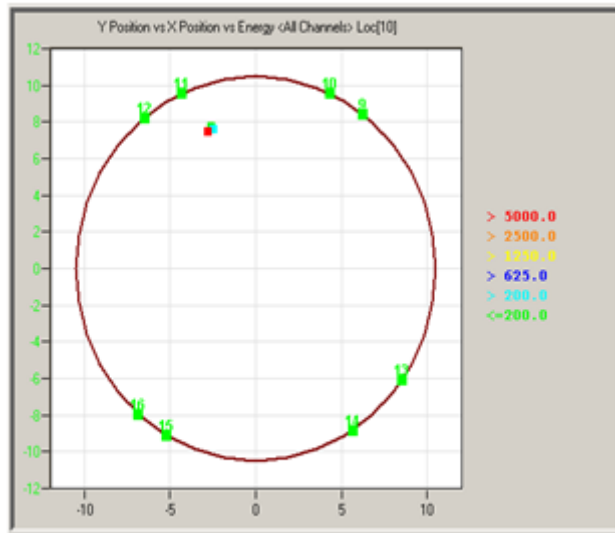


Figure 112. Illustration. Location of the wire break with the R1.5I sensor on the surface of the cable mockup.

Looking at the localization of the wire break in the cable cross section, both sets of AE sensors, R0.45I and 4 R1.5I, provided accurate estimation of the wire break position. The calculated position of the wire break was approximately 2.5 inches (63.5 mm) from the surface of the cable (figure 113 and figure 114), which was very close to the position of the broken prenotched wire. In the figures, the x- and y-axes represent the Cartesian coordinates that indicate the wire locations. The circle represents the cable cross section with the corresponding sensor locations. The recorded AEE vents are indicated by colored dots.

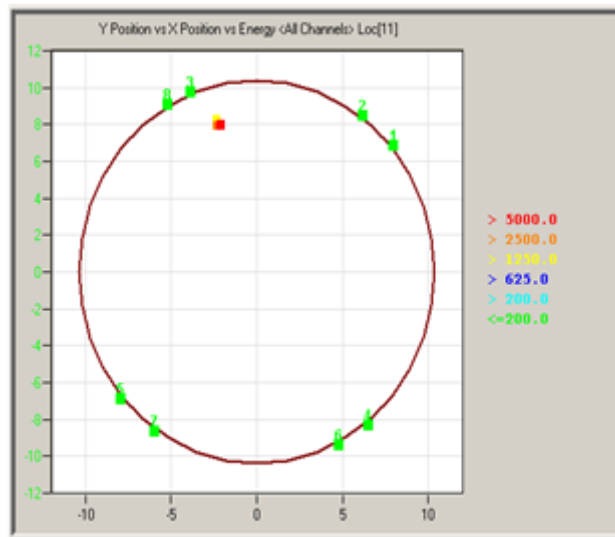
From these preliminary results (only one wire pulled to failure), it is possible to infer that the AE system used in this study, with both R0.45I and R1.5I sensors, showed potential for assessing the location of wire failure in interior wires. Looking at the different energy content, it is possible to segregate the characteristics of a wire break signal from background noise. Also, by observing the minimum instrumentation required, the results demonstrate that at least three AE sensors per

cable band are needed for an accurate estimation of the wire break location (within 1 inch (25.4 mm)) while even only one AE sensor is sufficient along the cable length. However, these conclusions are based on a successful experiment, and more tests are needed.



Fixed End Cable Band

Figure 113. Graph. Planar localization of the wire break using the R0.45I sensor.



Loaded End Cable Band

Figure 114. Graph. Planar localization of the wire break using the R1.5I sensor.

CHAPTER 5: CABLE DISSASSEMBLY (AUTOPSY)

In an effort to directly determine the effects of cyclic corrosion testing, the cable mockup specimen was deconstructed. Following the completion of cyclic testing, both the aluminum wrapping and centrally located neoprene strap were removed from the cable, the environmental chamber was disassembled, and form work was placed around the cable (see figure 115).



Figure 115. Photo. Disassembled environmental chamber with cable mockup specimen.

The tension in the seven jacked strands was released prior to the removal of the cable bands, stainless steel straps, and the subsequent dissection of the mockup cable specimen. It was predetermined that the hexagonal strands of 127 parallel, high-strength steel wires would be removed individually, and each strand's hexagonal shape would be maintained and/or reassumed.

Prior to dissection, the ends of the individual strands were color coded. Both the color-coded left side and the numbering system cable mockup's cross section are shown in figure 115 and figure 116. The wire strands on the surface of the cable (not marked in figure 116) were shaped so as to fill in any voids thereby ensuring a compact circular cross section.

In figure 116, the 20-ft (6.1-m) straightened strands were labeled with a number and a letter indicating the placement and side of the mockup cable when viewed from the jacking end (e.g., 09L). The 35-ft (10.68-m)-long tensioned strands were labeled from bottom to top with numbers 1 through 7. The top and bottom centrally located strands were 20 ft (6.1 m) long and were labeled "T" and "B," respectively.

To differentiate the two ends of the cable specimen, the end where jacking of the strands occurred was called the "South End" while the opposite end was called the "North End." This was done in reference to the geographical orientation of the cable.

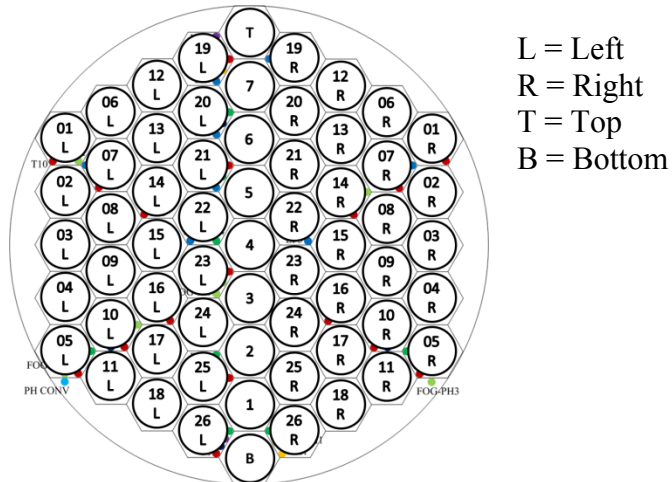


Figure 116. Illustration. Strand labeling.

Three wires separated at 120° angles from one another on the surface of each of the 20-ft (6.1-m)-long straight strands as well as individual wires from the cable surface separated at 30° angles were marked for removal and future strength testing.

CABLE UNLOADING

Once all strands were identified and labeled, the stresses in the tensioned strands were determined and released. In order to de-tension a strand, a jacking beam and two hydraulic jacks that were 6.5 inches (165.1 mm) long and 100,000 lb (45,400 kg) were used (see figure 117). The stress required to completely separate the nut from the framework was recorded by considering the tensile force in the strands using the hydraulic jack's conversion factor of 39 lb/psi (0.689 N/cm²).



Figure 117. Photo. Jacking beam with hydraulic jacks secured into position.

Although the goal was to completely free the cable from all tensile stresses, the stress levels in each strand were not immediately brought to zero, but the unloading was carried out in four steps. The levels of stress in each of the four rounds of de-tensioning are presented in table 15.

Table 15. Stress levels during cable de-tensioning.

Strand Number	Remaining Stress (psi)	~75 Percent Stress (psi)	Near Zero Stress (psi)	~Zero Stress (psi)
1	3,230	2,460	0	0
2	4,600	3,450	0	0
3	3,940	2,970	35	0
4	3,800	2,740	20	0
5	3,875	2,920	40	0
6	4,620	3,460	35	0
7	4,700	3,532	30	0

1 psi = 6.89 kPa

During the de-tensioning process, strain levels in two wires of strands 4 and 7, and visual observations of the cable reactions were recorded. Figure 118 shows an image of the setup of the strain gauges attached to the cable on strands 4 and 7.

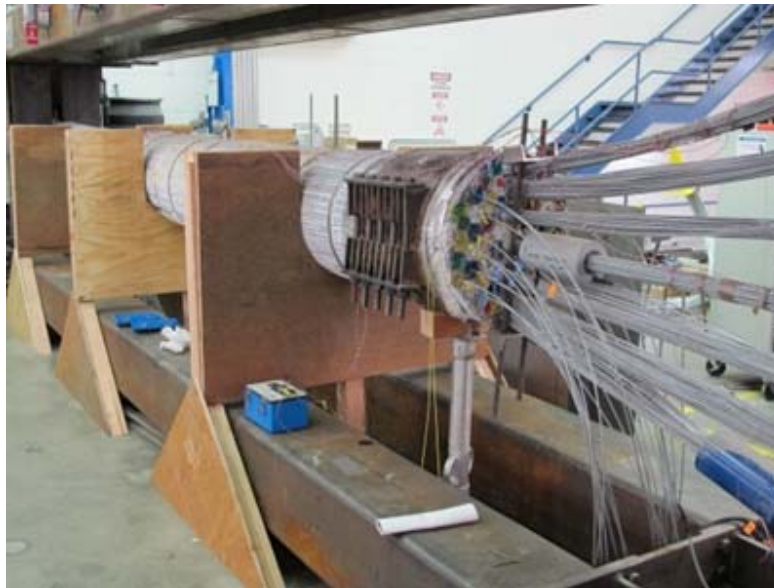


Figure 118. Photo. Strain gauge setup on strands 4 and 7.

Cable Strap/Band Removal

As stated earlier, the neoprene wrapping used to cover the area at which the wires connected to the sensors exit the cable's cross section was removed prior to the unloading process. Following the unloading, the stainless steel straps (see figure 119) were removed from the cable. The straps were removed from the outside to the inside. The first stainless steel strap was removed at the south end of the cable near the threaded rods. The clamps were unhooked using a screwdriver and then loosened with a hammer until the strap released. This process (see figure 120) was subsequently performed on the north side of the cable and then repeated until all the straps were removed.



Figure 119. Photo. North end of cable mockup with stainless steel straps.



Figure 120. Photo. Removal of south-side strap.

Following strap removal, images were taken over the entire length of the cable to document its condition. Several images of the cable from north to south (looking eastward) are presented in figure 121 through figure 124.

Areas of high ferrous corrosion occurring underneath the stainless steel straps were easily identifiable in the south central location shown in figure 123, whereas the north side of the cable experienced little to no ferrous corrosion under the stainless steel straps (see figure 121). This observation can be related to the fact that the cable specimen was slightly inclined toward the south end. The water that penetrated into the inside of the wrapping was able to move toward the south end, favoring the accumulation of water, and consequently the beginning of corrosion, at this end.

Next, both the south and north side cable bands were removed. The bolts and exterior of the cable bands experienced large amounts of corrosion. Wires underneath the cable band remained intact and experienced various amounts of corrosion (addressed in the subsequent section). A before and after image of the area under the north side cable band is shown in figure 125 and figure 126.



Figure 121. Photo. Stainless steel straps removed from north side of cable mockup specimen.



Figure 122. Photo. Stainless steel straps removed from north central side of cable mockup specimen.



Figure 123. Photo. Stainless steel straps removed from south central side of cable mockup specimen.



Figure 124. Photo. Stainless steel straps removed from south side of cable mockup specimen.



Figure 125. Photo. North side prior to cable band removal.



Figure 126. Photo. North side cable end following cable band removal.

Strand Removal

Removal of the strands started with the removal of the top strands and proceeded toward the bottom of the cable mockup. Because of the difficulties in mounting the long central strands, it was decided to keep the long strands in the loading frame with no tension in them. Upon removal, each strand was first labeled and photographed. Then, a careful visual inspection was carried out for each strand, and pertinent details were reported. Figure 127 and figure 128 show some stage of the cable disassembly. Figure 129 shows the long strands in the loading frame.



Figure 127. Photo. Cable specimen during disassembly.



Figure 128. Photo. Removed strands.



Figure 129. Photo. Completed cable deconstruction.

CHAPTER 6: ANALYSIS OF WIRE CONDITIONS

GENERAL OVERVIEW

Once the wrapping was removed, a general inspection of the cable was performed. It appeared that the cable was heavily covered by a white powder, which was a mix of salt residue and zinc oxide. In a couple of spots along the length of the cable, small pockets of water were found on the side portion of the cable cross section. Heavy corrosion appeared at the location where the sensors' wires exited the cable. Apparently, the neoprene strap that served as a protection for the electric wires functioned as a moisture trap and kept the wires in a wet environment for a long time. In addition, areas of high ferrous corrosion occurring underneath the stainless steel straps were easily identifiable in the south part of the cable, as shown figure 123, whereas the north side of the cable seemed to have experienced little to no ferrous corrosion (see figure 121).

CORROSION UNDER NEOPRENE PROTECTIVE STRAP

Upon removal of the neoprene strap, it was found that large amounts of what appeared to be uniform corrosion occurred under the neoprene wrapping. Furthermore, the strap was still moist when removed from the cable surface. The area where the neoprene strap was is shown in figure 126. Figure 130 and figure 131 show progressively closer views of the corroded area. It is interesting to note that the highest density of corrosion appears to have occurred on the top side of the cable directly in line with the water and heat sources.



Figure 130. Photo. Corroded area under neoprene wrapping.



Figure 131. Photo. Close-up view of corroded area under neoprene wrapping.

A close-up investigation of the top of the cable revealed stage 4 uniform corrosion for the wires on the outer layers in which close to 90 percent of the high-strength steel wires had undergone ferrous corrosion (see figure 132 and figure 133). This area was the one most exposed to higher temperatures (directly below the central heating lamp) and rain. The presence of the neoprene strap helped maintain high levels of humidity that, with high temperature levels, created ideal conditions for the progress of corrosion.

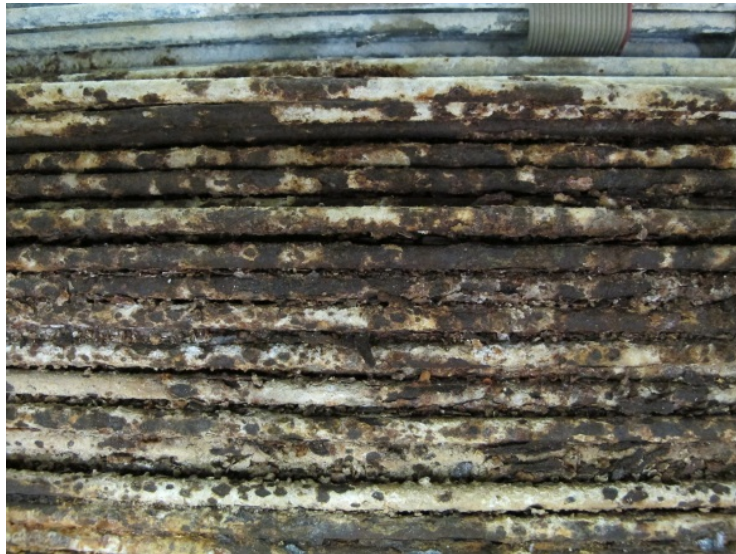


Figure 132. Photo. Wires with stage 4 corrosion on the top of the cable surface.



Figure 133. Photo. Close-up view of corroded wire.

STAINLESS STEEL STRAPS

Galvanic as well as crevice and pitting corrosion in areas of moisture build-up occurred in this cable. The build-up of salt and/or zinc oxide as well as ferrous oxide below the stainless straps was easily identifiable, as shown in figure 122 and figure 123. These straps were made of unknown chemical composition, so they may have facilitated the onset of corrosion at their location. In addition, the small gaps between the strap and the outer wires ended up trapping rain water and moisture for a long time, initiating crevice and pitting corrosion. The corrosion of the wires under the stainless steel straps tended to increase toward the south side of the cable. As previously mentioned, the cable was constructed on a slight angle for drainage purposes, thus the increase of ferrous oxide was directly a result of the increased moisture content at the south side of the cable. Mild salt build-up, zinc oxide, and ferrous oxide may be seen under the stainless steel straps, as shown in figure 134.



Figure 134. Photo. Salt build-up and zinc/ferrous corrosion product.

At points closer to the south side of the cable, more critical forms of corrosion formed. The presence of high moisture, the potential difference between the stainless steel of the strap and the zinc-coated high-strength steel wires, and the presence of crevices created by the voids between the straps and the wires initiated heavy pitting corrosion (see figure 135 and figure 136). From this result, it is noteworthy that the use of stainless steel straps, which are commonly used in practice, should be carefully considered in environments with aggressive conditions.



Figure 135. Photo. Pitting corrosion under stainless steel strap.



Figure 136. Photo. Close-up view of pit.

CABLE BANDS

The cable bands on either end of the cable mockup specimen presented another place for moisture entrapment. Similar to the stainless steel straps, the corrosion of the high-strength steel wires was greater at the south side of the cable. Looking eastward at the north side of the cable, it is possible to identify what may be assumed to be stage 2 corrosion (near complete zinc oxidation) and definite signs of stage 3 corrosion (ferrous corrosion is identifiable at approximately 20 to 30 percent coverage) (see figure 137 and figure 138).



Figure 137. Photo. North end of cable with band removed.

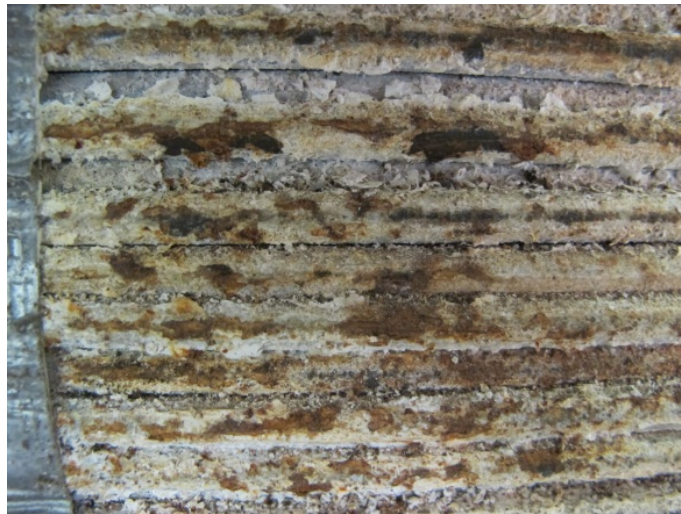


Figure 138. Photo. Wires at north end of cable with stage 3 corrosion.

The corrosion under the cable band at the south end of the cable was more severe than that at the north end, as both the percentage of area covered by stage 3 corrosion (see figure 139), and the degree/depth of corrosion was greater at the south end (see figure 140).



Figure 139. Photo. South end of cable with band removed.



Figure 140. Photo. Wires at south end of cable with large percentage of stage 3 corrosion.

The corrosion at the south end cable band was most heavily concentrated to the left portion of the outer surface. This was the result of an irregular (uncontrollable) path of water penetration. The ferrous oxide was found where the cable band began, suggesting an interaction between the galvanized wires, the steel cable band, and the surrounding environment.

The cable bands themselves also experienced significant amounts of corrosion. A high concentration of ferrous corrosion product was found on the cable band at the location where the cable band began on the south side of the cable. On the surface, the greatest amount of corrosion was seen on the teeth where the top and bottom cable bands met, which is an area directly in contact with air (see figure 141).



Figure 141. Photo. South end of cable highlighting teeth of cable band.

On the underside of the cable band, a substantial amount of salt and/or zinc oxide and ferrous oxide was found (see figure 142). The concentration of ferrous corrosion was observed on the left side of the cable band.



Figure 142. Photo. Interior of top of south side of cable band.

Underside Openings

Midway through the test program at points approximately 3.94 ft (1.2 m) from either end of the cable mockup, four holes were placed in the cable wrapping (see figure 143). Two 11.89-by-11.89-inch (30.5-by-30.5-cm) openings were made in the underside of the wrapping and at a location on the topside of the cable, and two 0.99-by-0.99-inch (2.54-by-2.54-cm) openings were made 3.94 ft (1.2 m) from the jacking end to facilitate the influx of moisture to the inside of the cable mockup and accelerate corrosion of the wires (see figure 144).

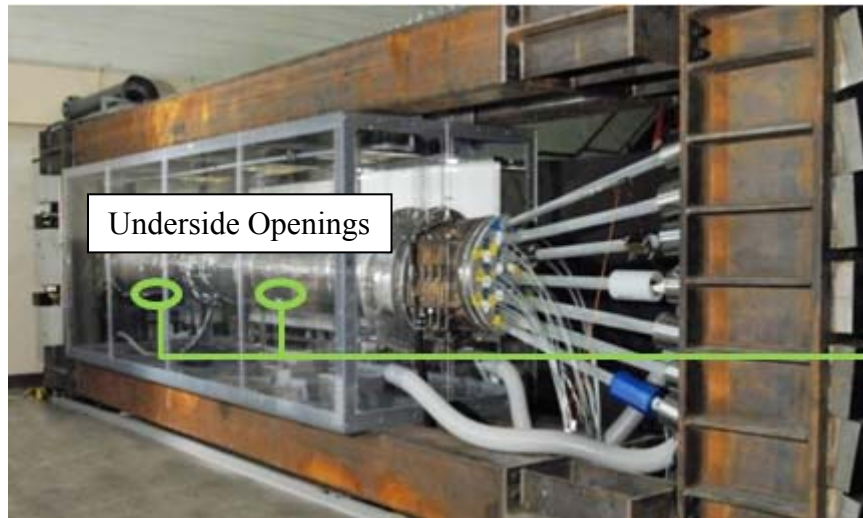


Figure 143. Photo. Mockup cable specimen within environmental chamber and location of both holes.

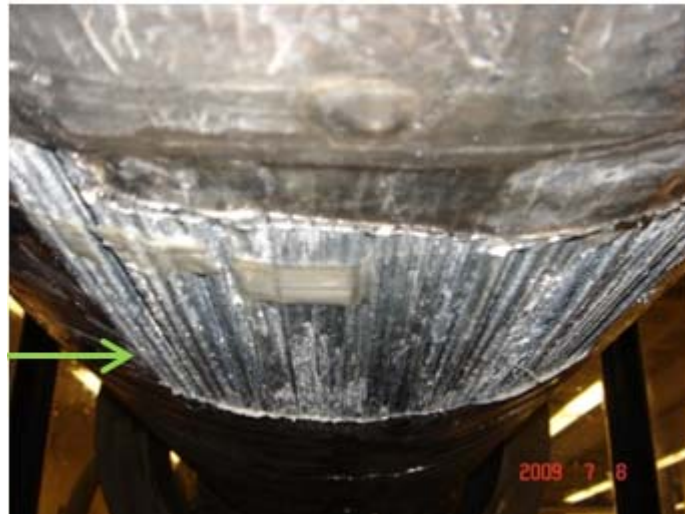


Figure 144. Photo. Image of one of the 11.89-by-11.89-inch (30.5-by-30.5-cm) holes placed in the aluminum cable cover.

During cable disassembly, the area highlighted in figure 144 was analyzed and documented. A solid white coating developed and enveloped the exposed wires (see figure 145 and figure 146). It is evident that ferrous corrosion was not present; the wires were covered by a thick layer of a white substance mainly composed of salt but also with the presence of zinc oxide (see

figure 146). The presence of such a high concentration of salt in the test solution was justified by the fact that test conditions were supposed to create harsh conditions for the sensor system.



Figure 145. Photo. Product that formed where the 11.89-by-11.89-inch (30.5-by-30.5-cm) hole was placed in the aluminum cable cover.



Figure 146. Photo. Close-up view of the product formed on the high-strength steel wires.

INTERIOR OF CABLE

With respect to the inner strands, the general observations were as follows:

- The majority of wires showed substantial salt deposits accompanied by deterioration of the zinc coating.

- Substantial corrosion was developed in the vicinity of the internal straps placed in correspondence of the electrical wires' exit.
- The two pre-corroded stands showed substantial ferrous corrosion.
- Substantial corrosion developed in the sides of the strands that were in contact with the two pre-corroded stands.

The interior of the cable showed areas where heavy salt deposition occurred. These areas showed no particular pattern, following more the potential path of the water that penetrated inside the wrapping. Such areas were more frequent in the south end of the cable because of the specimen inclination. In addition to these areas of salt deposition, it appeared that extensive zinc coating corrosion occurred. Almost the totality of the inside wires were coated with a white dust, and once this dust was removed, the wires had a non-shiny zinc surface. Figure 147 shows the inner core of the specimen.



Figure 147. Photo. Inner core of the specimen during disassembly.

INTERNAL CABLE STRAPS

Areas that were highly subjected to corrosion activity were those located adjacent to the nylon straps embedded within the cable (see figure 148). These straps were placed only at one location along the length of the cable to protect the electrical wires from the sensors during compaction operations. The gaps next to the straps were not sealed before the wrapping, with the intention that water could easily penetrate the interior of the cable to activate the sensors. In real-life applications, it is strongly recommended to seal these openings to avoid water penetration inside the cable.



Figure 148. Photo. Orange nylon strap embedded within cable.

Basically, these straps acted similarly to the neoprene wrapping. That is to say, the nylon straps held any moisture present within the cable for extended periods of time, keeping the solution necessary for the electrochemical corrosion reaction. The corrosion product formed in the distinct shape of the overlapping strap (see figure 149).



Figure 149. Photo. Corrosion formation at nylon strip location.

As was seen with the corrosion associated with the neoprene wrapping, the corrosion around the nylon straps was fairly uniform. Heavy stage 4 corrosion was seen on the bottom of a strand in contact with a nylon strap (see figure 150).



Figure 150. Photo. Close-up view of the wires with stage 4 corrosion.

PRE-CORRODED STRANDS

New strands within the cable mockup specimen that were adjacent to the two pre-corroded strands also experienced heavy amounts of corrosion on the contact surface between the strands. As was commonplace with the other corrosion documented, corrosion of strands adjacent to pre-corroded strands was heaviest in the central and southern sections of the cable due to the slight inclination of the cable specimen toward the jacking end. Following the nomenclature introduced in figure 116, strands 8R and 9R were pre-corroded with the intent of generating some hidden corrosion damage for the direct sensing technologies. Looking at the surface of strand 16R in contact with strand 9R, it was evident the presence of ferrous corrosion in stage 3, approaching stage 4, was seen in the area adjacent to strand 9R even on the north side of strand 16R (see figure 151). In fact, several sections displayed stage 4 corrosion and black oxides (see figure 152).

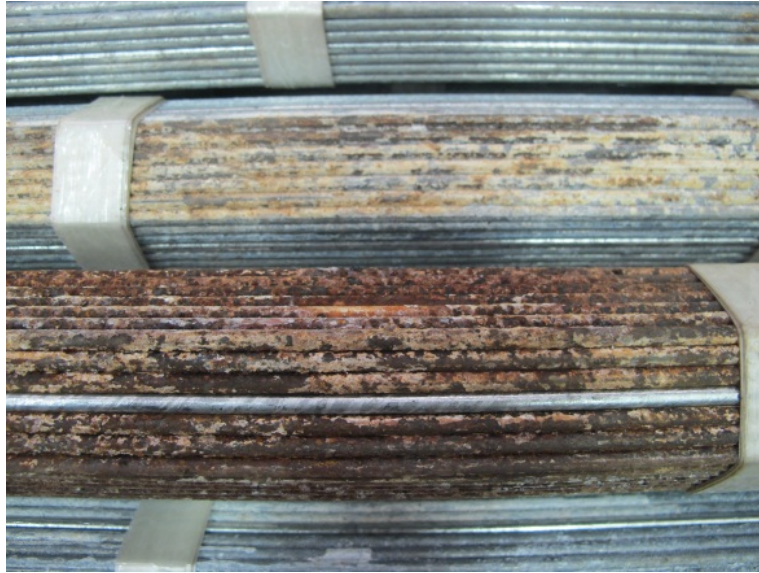


Figure 151. Photo. North end of cable—pre-corroded strand 9R (bottom) and adjacent side of strand 16R.



Figure 152. Photo. North end of cable close-up of 16R showing stage 3 corrosion.

The effect of the contact between the corroded strand and the initially uncorroded strand was evident. Even greater amounts of ferrous corrosion were seen on the southern end of strand 16R (see figure 153). At the southern end, nearly the entire adjacent face had undergone stage 4 corrosion (see figure 154 and figure 155). Once again, it appears that the slight angle at which the cable sat caused a greater amount of moisture build-up in the southern end of the cable; however, unlike the corrosion under the stainless steel straps, the extent of the corrosion caused by the pre-corroded strands did not differ drastically from one end to the next. The corroded surface of the pre-corroded strand provided more surface area for water particles to adhere to, thereby increasing the time of wetness of the material, the time of wetness on the adjacent strand face, and the length of the corrosive electrochemical reaction.

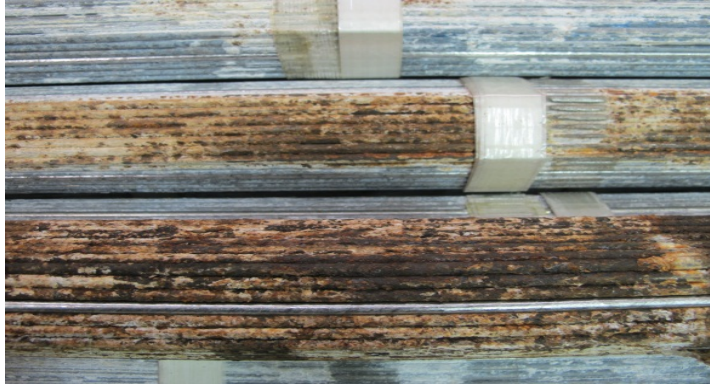


Figure 153. Photo. South end of cable pre-corroded strand 9R (bottom).



Figure 154. Photo. South end of cable adjacent side of strand 16R.



Figure 155. Photo. South end of cable close-up of 16R showing stage 4 corrosion.

CHAPTER 7: ANALYSIS OF SENSOR CONDITIONS

The purpose of this project was to develop a robust NDT sensing system for corrosion monitoring. Following the placement of the sensors into the mockup cable specimen, the status of the sensors and the damage they sustained were only assumed based on the data recordings ascertained. The effects of the cable compaction and the environmental variables are of extreme importance in determining the durability and real-world functionality of the sensing system. Precon HS2000V temperature and relative humidity sensors, Analatom LPR sensors, and Corr Instrument CMAS sensors provided the most discernable and understandable data. While some of these sensors have malfunctioned, others have proven to detect strong signals. The conditions of various sensors were then evaluated and displayed to further determine any reasons for their functioning/malfunctioning.

On the surface, mostly all of the sensors appeared to not have been crushed by the cable compactions. Figure 156 shows the conditions of the exterior of the Precon sensor 1, BM sensor 1, and CMAS CS 1. They were placed in the lowest point of the cable cross section. The surrounding wires were not damaged by galvanic corrosion resulting from the potential difference between the wires and the stainless steel protective piping. The general state of the sensors and the surrounding wires shown in figure 156 is applicable to almost all the sensors throughout the cable.



Figure 156. Photo. Sensors T1, BM1, and CMAS CS1.

PRECON HS2000V TEMPERATURE AND RELATIVE HUMIDITY SENSORS

With the exception of a few, nearly all of the Precon sensors performed satisfactorily during testing. For example, sensor 3, located at the center of the cable, recorded consistent temperature and relative humidity values. The consistency of these recordings provided a sense of reliability in the functionality of this sensor, shown in figure 157 and figure 158. Figure 157 shows that the stainless steel piping with heat shrinking coating appears to have worked in protecting the sensor from crushing. Figure 158 indicates that no visual damage could be seen on the electrode itself.



Figure 157. Photo. Precon HS2000V sensor 3 during cable disassembly.



Figure 158. Photo. Close-up view of Precon HS2000V sensor 3 electrode.

Similarly, sensor 13 provided reliable data that recorded large amounts of temperature and relative humidity fluctuations during testing. Figure 159 and figure 160 reflect the image of Precon sensor 3 with no visual damage being recognizable. Almost all the Precon temperature and relative humidity sensors look similar to sensors 3 and 13.



Figure 159. Photo. Precon HS2000V sensor 13 during cable dissection.



Figure 160. Photo. Close-up view of Precon HS2000V sensor 13 electrode.

On the contrary, since the beginning of testing, sensor 7, located close to the surface on one of the diagonal diameters, malfunctioned, and no significant data were ever ascertained. The opening of the cable revealed the status of the sensor (see figure 161 and figure 162). During the cable autopsy, sensor 7 was discovered hanging from a piece of masking tape, as shown in figure 161, with the internal wires exposed (see figure 162). Short circuiting of the electrode and exposure problems may have led to the sensor malfunction.



Figure 161. Photo. Precon HS2000V sensor 7 close-up of electrode during cable dissection.

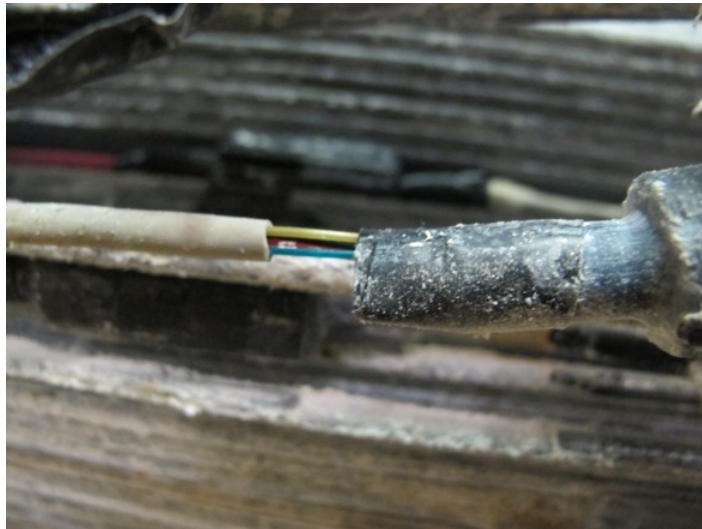


Figure 162. Photo. Precon HS2000V sensor 7 wires exposed.

Unfortunately, not all sensors that malfunctioned showed problems that were as easily identifiable as those of sensor 7. For example, sensor 10, which was located close to the outer surface along one of the diagonal diameters, consistently recorded extremely elevated relative humidity levels. The analysis of sensor 10 (see figure 163) showed that the sensor suffered no damage, suggesting that sensor saturation during testing may have been the cause of the high levels recorded.



Figure 163. Photo. Precon HS2000V sensor 10 during cable dissection.

LPR CORROSION RATE SENSORS

As shown in the data analysis section, eight LPR sensors were placed in the cable cross section. From data analyses, it was found that only LPR sensors 3 and 4 provided consistent data that extended beyond noise level threshold, while the remaining six did not record any significant activity, posing the question of whether or not all the sensors were functioning correctly. Upon disassembly of the specimen, LPR sensor 4 was found to be in good condition. The protective casing had remained intact, leaving the sensor unscathed (see figure 164), and the sensor probe itself had not corroded nor did it appear to have been damaged in any other way (see figure 165). LPR sensor 3 was found to be in similar condition as LPR sensor 4. These two sensors were placed along the upper part of the inclined diameter in the right half of the cable cross section.



Figure 164. Photo. LPR sensor 4 during cable disassembly.



Figure 165. Photo. Close-up view of LPR sensor 4.

Some of the remaining LPR sensors suffered extensive corrosion damage that, most probably, compromised their functioning. For example, LPR sensor 6 recorded fluctuations beyond noise at times; however, the data were too erratic and inconsistent to be deemed usable. LPR sensor 6 was located in its original place on the vertical diameter halfway from the center and the surface of the cable. This sensor was placed together with other corrosion rate sensors (see figure 166), and it appeared to have been severely corroded (see figure 167). The corrosion of the sensor electrodes of LPR sensor 6 provides an explanation for the erratic data recordings.



Figure 166. Photo. LPR sensor 6 during cable disassembly.



Figure 167. Photo. Close-up view of LPR sensor 6.

As shown figure 166 and figure 167, LPR sensor 6 appeared to be in an area of heavy salt deposit, indicating that the area must have been subjected to aggressive corrosive action and justifying the presence of extensive corrosion products on the sensor.

Upon further inspection, however, all of the sensors were either corroded or the electrodes were disfigured. LPR sensor 5 was found to be corroded (see figure 168), while LPR sensor 7 was found to be both crushed and corroded (see figure 169).



Figure 168. Photo. Corroded LPR sensor 5.



Figure 169. Photo. Corroded and disfigured LPR sensor 7.

At first glance, it appeared that the sensors closer to the surface (e.g., LPR 7) were more likely to fail due to crushing; however, LPR sensor 8, which was located in a position analogous to LPR 7, did not get crushed from compaction forces (see figure 170). Rather, it seemed to have malfunctioned due to corrosion (see figure 171).



Figure 170. Photo. LPR sensor 8 during cable dissection.

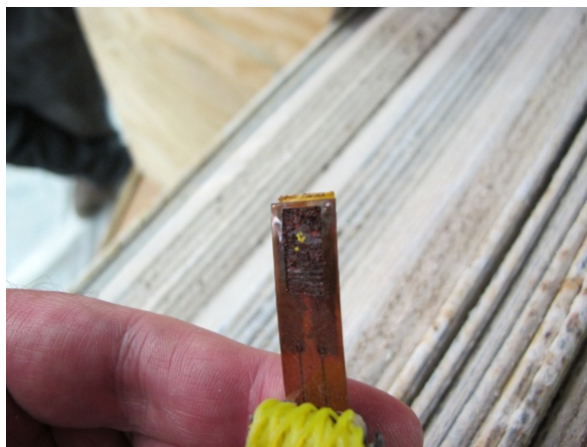


Figure 171. Photo. LPR sensor 8 close-up of corroded sensor electrodes.

Similar corrosion and disfiguration of LPR sensors 1 and 2 were found. The difference in noise data based on crushing as opposed to electrode corrosion is currently unknown.

In conclusion, LPR sensors can provide accurate readings of the corrosion rate inside the cable even though the ones used in this series of tests showed substantial corrosion that could impair their functioning. However, in real applications, it is rare to find conditions so aggressive and sustained for such a long time as the one the cable specimen was subjected to. As a result, it is reasonable to expect a service life longer than the test duration. However, better protection from crushing should be provided.

CMAS SENSORS

Looking at the data collected during the experimental analyses, the measurement of the corrosion rate obtained from the CMAS CS sensor appeared to be promising, while the recorded data for zinc corrosion rates (CMAS Zn 2) did not. During the cable autopsy, it was found that the CMAS CS sensor 2 (located at the top of the cable cross section) (see figure 172) was not affected by the cable compaction and appeared to have resisted severe corrosion deterioration. Conversely, CMAS Zn sensor 2, located next to CMAS CS sensor 2, was crushed during cable compaction (see figure 173), which explained the lack of measurement data from it.



Figure 172. Photo. CMAS CS 2 intact.



Figure 173. Photo. Crushed CMAS Zn 2 sensor.

The recordings of these sensors were analyzed and have been previously presented. The noise signal recorded by the CMAS Zn sensor 2 was a result of the sensor malfunctioning due to crushing during cable compaction.

In conclusion, the CMAS sensors obtained reliable measurements of the corrosion rate for the steel, while no data were obtained from the CMAS Zn 2 sensor because it was crushed during compaction. Of the four CMAS sensors used in this study, two of them were badly crushed during compaction. However, it was decided to keep these sensors among those which would be tested in the field during the last phase of this project, with the recommendation of providing a stronger protection.

BM SENSORS

Most of the BM sensors did not record much corrosion activity beyond the noise level. During the cable autopsy, BM electrodes were found to have various amounts of corrosion, from heavy (sensor 7 in figure 174) to minimal (sensor 3 in figure 175).



Figure 174. Photo. Heavy corrosion on BM sensor 7.

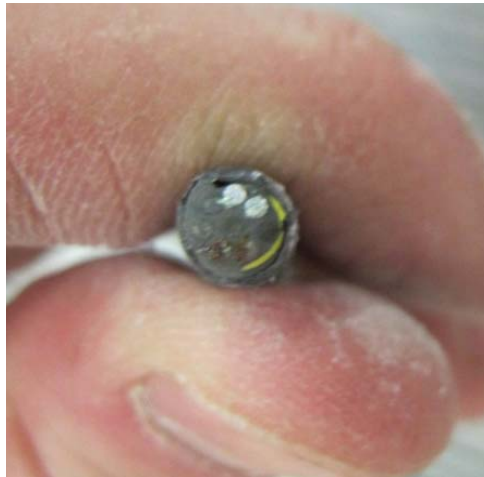


Figure 175. Photo. Minimal corrosion on BM sensor 3.

Although these sensors did not record any reasonable level of corrosion in the accelerated corrosion tests, they were included in the final list of sensors to be tested in the field. Because of their almost identical resemblance to the CMAS sensors, it was considered appropriate to test the BM sensors in real-life conditions, paired with the CMAS sensors, using better care in protecting the sensing probe and the electronic encasement.

In conclusion, the indirect sensing system proposed for installation on a main cable of a suspension bridge in the City of New York comprised of the following sensors:

- Precon HS2000V temperature and relative humidity sensors.
- Analatom LPR sensors.
- Corr Instruments CMAS.
- Corr Instruments BM sensors.

CHAPTER 8: FIELD INSTALLATION ON A CABLE OF A SUSPENSION BRIDGE

GENERAL CONSIDERATIONS

The last phase of the project called for the installation of the developed integrated system of sensors and technologies on a real cable of a suspension bridge in the City of New York. In agreement with the New York City Department of Transportation (NYCDOT), cable D of the Manhattan Bridge was chosen. This bridge was going through an extensive cable evaluation operation, so it would have made the installation and the removal of the sensors at the end of the test period easy. Built in 1912, this suspension bridge is one of the main traffic arteries between Manhattan and Brooklyn. Spanning over a length of 6,851.92 ft (2,089 m) with a central span of 1,469.77 ft (448.1 m), this bridge carries a daily traffic flow of over 72,000 vehicles per day. There are 4 main cables, each made of 37 strands of 256 wires each, for a total of 9,472 wires bundled in a cable with a 21-inch (533.4-mm) diameter. The number of wires and the corresponding cable diameter of one of the Manhattan Bridge cables are close to the number of wires and cable diameter of the cable mockup tested in this study.

The field installation was divided into two phases. The first phase was conducted at an early stage of the problem to look at the problems associated with the logistics of installing a network of sensors that had to provide measurements in real time. Hence, problems related to the wireless and wired transmission of data from the cable panel remote locations to the DAQ installed in the cable anchorage, to data transfer through the internet, to power requirement, to safety, etc., were addressed. In this phase, the sensor system was represented by fiber-optic strain gauges among cable bands, electromechanical strain gauges on the eyebars, temperature and humidity sensors for the anchorage chamber, and a weather station. Having addressed all these logistics issues saved time and resources in the second (and final) phase of the field testing when the final sensor system, selected after the laboratory phase, was installed.

Phase I: Initial System Installation

A first set of sensors (fiber-optic strain gauges) was installed between panel point 1 and panel point 2 of cable D, as shown in figure 176 and figure 177, a location that is relatively close to anchorage D and where there were no obstructions for sensors mounting. Access to the main cable was coordinated with the appropriate bridge authorities.

With regard to the technologies used in this initial test, the monitoring system installed on the cable consisted of the following:

- Sensor Highway II System.
- Eight AE sensors.
- Two accelerometers.
- One weather station.
- Temperature/humidity sensors.

- Fiber-optic strain gauges.
- Wireless parametric sensor interface.

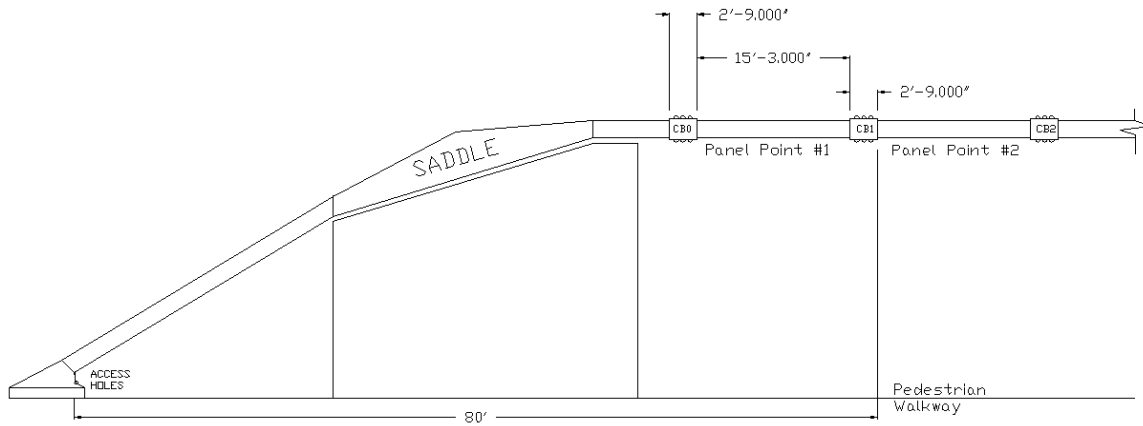


Figure 176. Illustration. Cable sketch and dimensions of field installation phase 1.

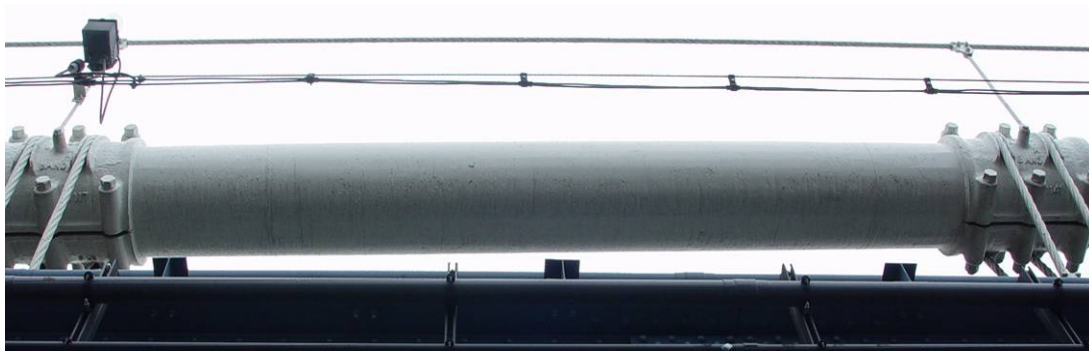


Figure 177. Photo. Panel point 2 of Manhattan Bridge.

Figure 178 shows the PAC Sensor Highway II system developed for this study. One key aspect in the final monitoring system was that all the sensors and technologies had to be integrated together into the sensor highway. A prototype of this system was developed and installed on the Manhattan Bridge, utilizing up to eight AE sensors/channels, an internal (and external) temperature sensor, two accelerometers, a weather station, and a wireless parametric adapter for monitoring suspension cable environmental parameters including temperature, humidity, and corrosion rate. The Sensor Highway II System was located inside the chamber of anchorage D (north cable on the Brooklyn side). The current block diagram for the integration of the various sensors and sensing systems that are being utilized in this project is shown in figure 179.



Figure 178. Photo. Sensor Highway II System.

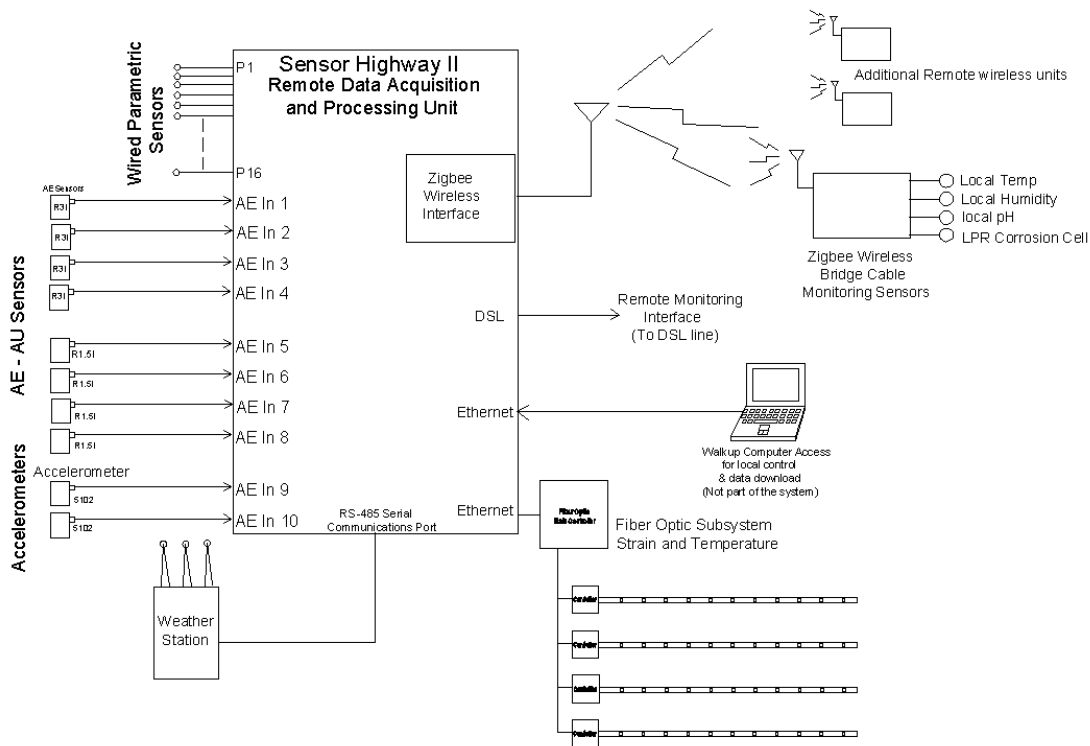


Figure 179. Illustration. Block diagram of the Sensor Highway II System.

Four PAC R1.51C auto sensor test (AST) and four PAC R31C AST AE (environmentally coated) sensors were mounted directly on each cable band using epoxy. Cable band locations were selected rather than locations on the external wire coating because there was a better transmissibility of the AE signal from the wire through the cast iron of the band. The wrapping wire coating, which was not directly in contact with the wires and resting on a layer of lead/zinc paste, functioned as a filter for the signal transmission to the AE sensor, altering the amplitude and frequency content of the recorded signal. This information was used in the laboratory test on

the cable mockup. The AST feature in the selected AE sensors allowed researchers to verify sensor coupling and performance at any time throughout the monitoring period.

Two model 5102 accelerometers were mounted to the bridge to monitor vibration and bridge movement for analysis correlation of any detected AE activity with respect to bridge movement.

A Vaisala WXT510 weather transmitter was selected to measure external temperature, relative humidity, rainfall, wind speed and direction, barometric pressure, etc. (see figure 180 and figure 181). This model was chosen because of it is entirely solid state; it is completely electronic without any moving parts. Mounted on the parapet above the arch over the pedestrian walkway approximately 50 ft (15.25 m) from panel point 2, this weather station used the RS-485 interface and was connected to the Sensor Highway II system (via cable) in anchorage D, which also provided the required 12-V power for operation.



Figure 180. Photo. Vaisala WXT510 weather transmitter.



Figure 181. Photo. Weather station installed on the Manhattan Bridge.

A temperature/humidity sensor was connected to the wireless parametric interface box. The size of the integrated sensor was 0.9-by-0.5-by-0.365 inch (22.86-by-12.7-by-9.27 mm) and required low power and minimal external conditioning circuitry. This sensor was used to monitor any changes of the environmental conditions inside anchorage D (e.g., shut down of dehumidification system). The wireless parametric sensor interface was installed to create a wireless link between the parametric readings of temperature and humidity in the anchorage and the Sensor Highway II System installed in the same location. The initial data collection was configured for collection on an hourly basis to maximize battery life. This system was tested by shutting down the anchorage dehumidification system. As shown in figure 182, the system immediately recorded a decrease in temperature and a consequent increase in humidity. As soon as the anchorage dehumidification system was reactivated, the temperature and the humidity inside the anchorage chamber returned to normal values.

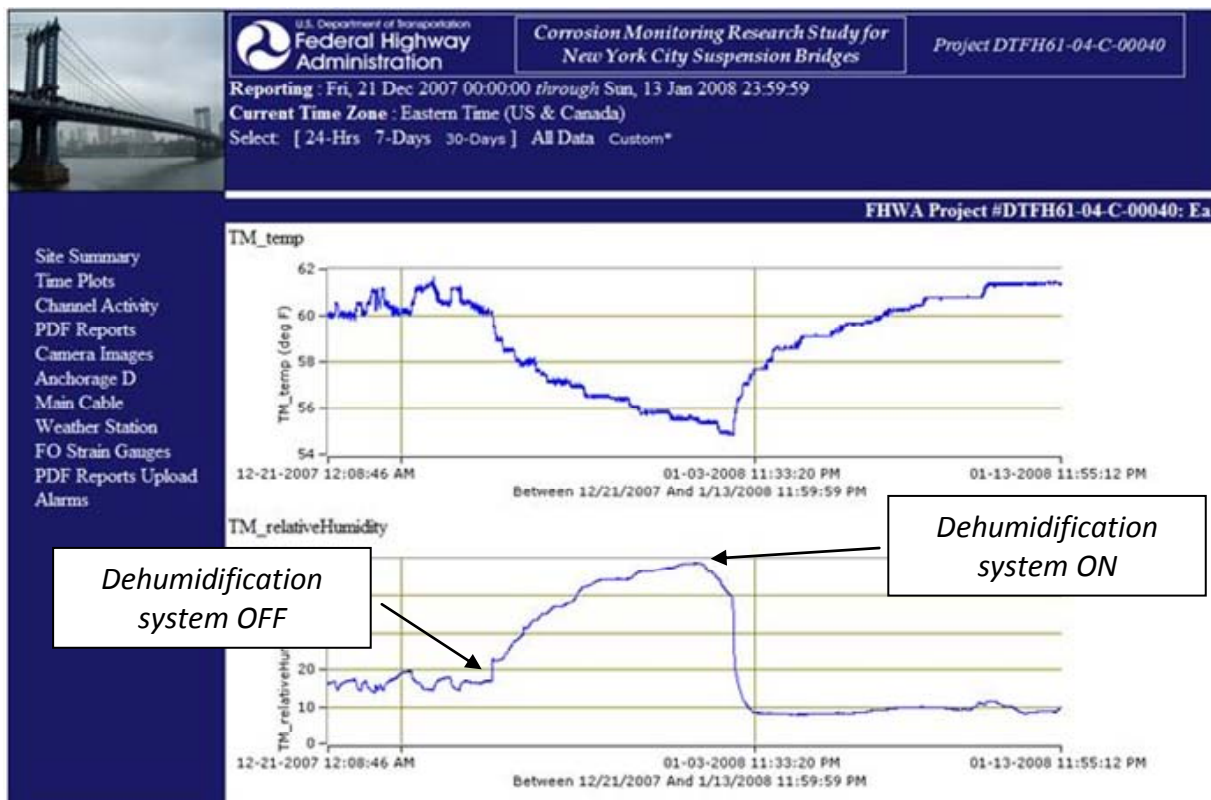


Figure 182. Screenshot. Graph of temperature and humidity inside the cable anchorage remotely reported via a secure Web portal.

The fiber-optic strain gauge system was installed on panel point 2 as well on the eyebars at the anchorage, as shown in figure 183 through figure 186. It consisted of three Surveillance d’Ouvrages par Fiber Optiques (SOFO) sensors placed along the suspension cable and two multiplexed strain and temperature (MuST) deformation sensors mounted on the eyebars in the anchorage. Mounting of these sensors on the cable and eyebars has been coordinated with NYCDOT.

The SOFO system is a fiber-optic displacement sensor with a resolution in the micrometer range. It is based on the principle of low-coherence interferometry. The infrared emission of a light-

emitting diode is launched into a standard single mode fiber and directed, through a coupler, toward two optical fibers mounted on or embedded in the structure to be monitored. The measurement fiber is in contact with the structure itself and follows the elongations and contractions of the structure. The second fiber, called the reference fiber, is installed free next to the measurement fiber. Mirrors placed at the end of both fibers reflect the light back to the coupler that recombines the two beams and directs them towards the analyzer which, in turn, transforms a change in the path unbalance between two optical fibers into a distance variation and consequently into strains. Hence, it is possible to say that this type of sensor has both an active and passive part. The active part contains the reference and the measurement fibers and measures the deformations between its two ends, while the passive part is insensitive to deformations and serves as a reference. The MuST system is based on a fiber Bragg grating (FBG) design that transforms a static or dynamic distance variation into a change in reflected wavelength of a prestressed FBG. The main interest in using Bragg gratings is in their multiplexing potential. Many gratings can be written in the same fiber at different locations and tuned to reflect at different wavelengths. This allows the measurement of strain at different locations along a fiber using a single cable.

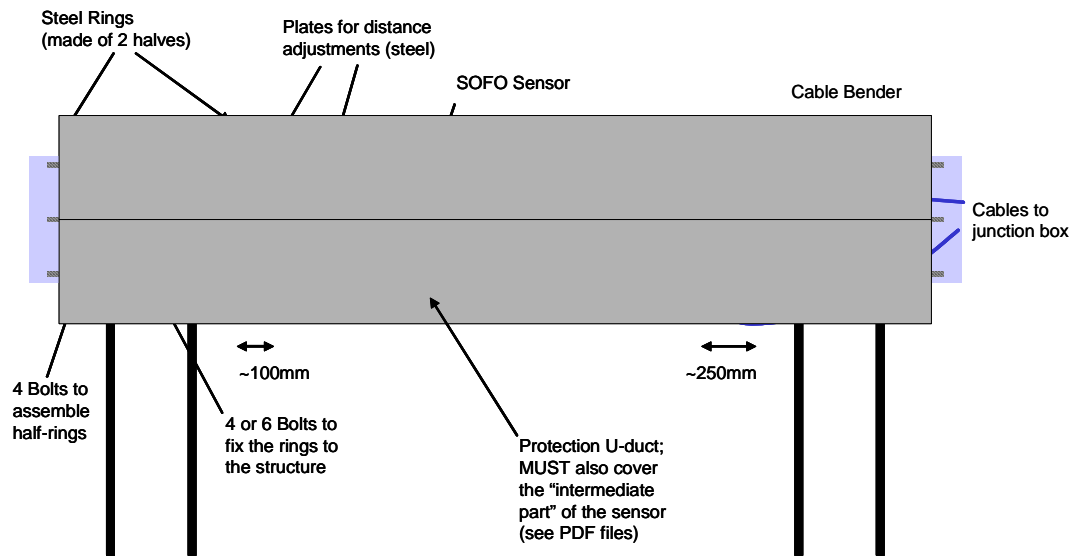


Figure 183. Illustration. Mounted SOFO sensors.

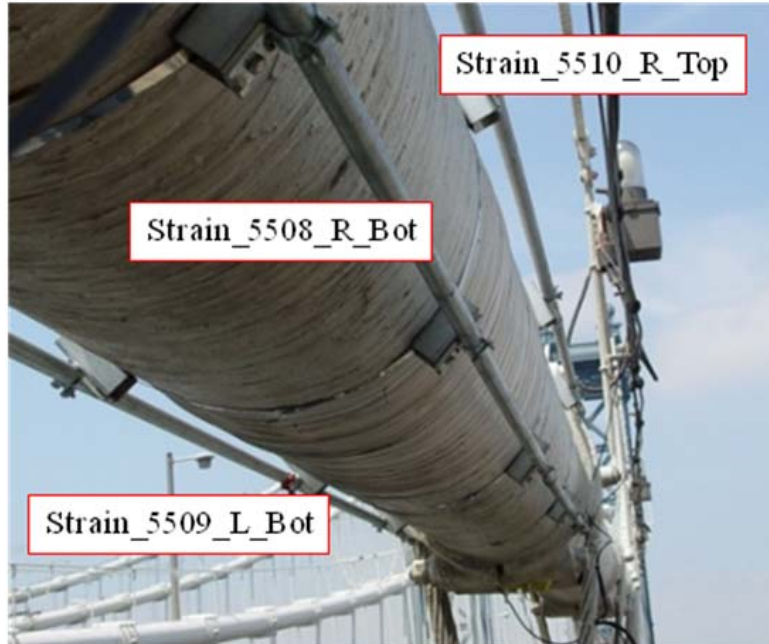


Figure 184. Photo. Actual locations of mounted SOFO and MuST fiber-optic sensors.

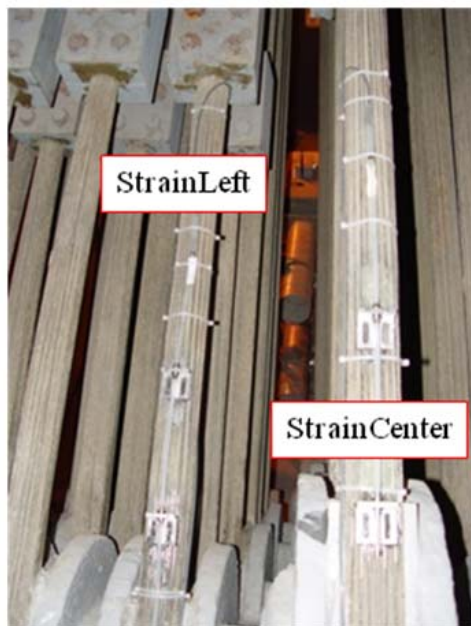


Figure 185. Photo. Strands at the anchorage with mounted fiber-optic strain sensors.



Figure 186. Photo. Strain gauges mounted on the eyebar.

All DAQs were housed in a standard National Electrical Manufacturers Association (NEMA-4) enclosure (see figure 187). The “4” rating means that the enclosure is intended for indoor or outdoor use primarily for providing a degree of protection against windblown dust, rain splashing, and hose-directed water. Communication and data collection between the Sensor Highway II system and the fiber optic system was through a digital subscriber line (DSL) connection at the bridge with a cable/DSL router connected to the DSL modem to allow the connection and remote access of the two DAQs (see figure 187). The cable/DSL router had a built-in firewall capability that was configured for security to protect the systems from unauthorized access. A Web portal (see figure 188) for secure remote data collection was created.

During phase I, data regarding temperature, humidity, and strains in the cable as well as in the eyebars were recorded and periodically analyzed. Since the goal of this phase was to address all the logistic problems related to the installation of the data acquisition and transmission infrastructure, the reliability of the system was extensively tested. For example, various tests were conducted changing the sampling rate of the sensors or looking at different combinations of different parameters (i.e., temperature versus relative humidity or temperature versus strains). At the end, it was concluded that the reliability of the system was quite good. As a result, the overall sensor highway system was considered to be ready for the corrosion monitoring sensors that had to be installed on the interior of the main cable during phase II.

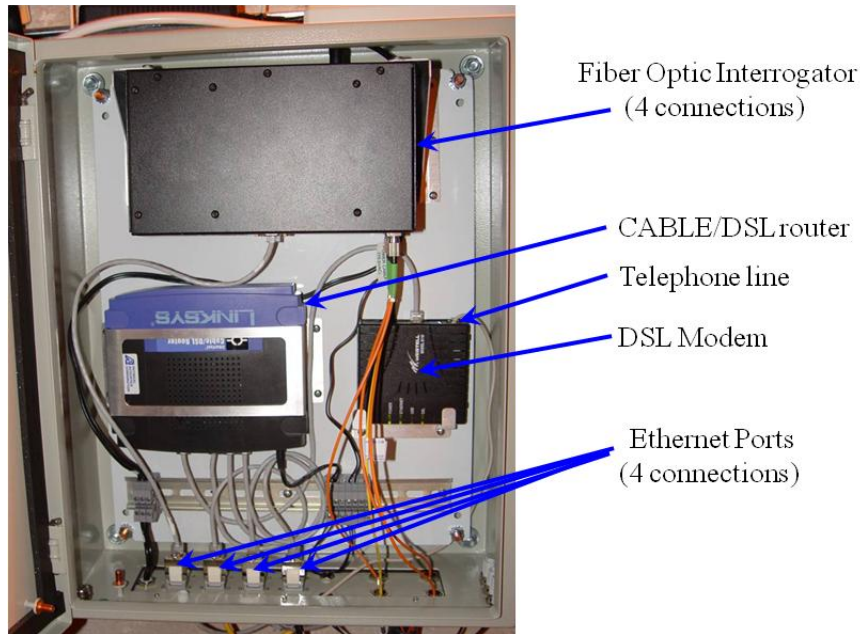


Figure 187. Photo. Typical NEMA-4 enclosure housing fiber-optic reading unit, DSL router, and modem.

U.S. Department of Transportation
Federal Highway Administration
Corrosion Monitoring Research Study for New York City Suspension Bridges
Project DTFH61-04-C-00040

Reporting: Mon, 23 Feb 2009 10:37:23 through Mon, 02 Mar 2009 10:37:23
Current Time Zone: Eastern Time (US & Canada)

Select: [24-Hrs 7-Days* 30-Days] All Data Custom

Summary Statistics	Cumulative waveforms	Cumulative Events	Cumulative ABS Energy	Cumulative counts
Most Recent Data Acquisition	1	0	65,547	14
Summed Over Reporting Period	81	0	8,686,786	4,958

Manhattan Bridge Information

Type:	Suspension
Construction:	October 1, 1901 to December 31, 1909
Total length:	6855 feet
Length of main span:	1470 feet
Length of side spans:	725 feet
Length, anchorage to anchorage:	2,920 feet
Total length of bridge and approaches:	6,855 feet
Length of each of the (4) cables:	3224 feet
Diameter of each of the (4) cables:	21.1/4 inch
Number of decks:	2 decks
Number of traffic lanes:	7 lanes (4 upper, 3 lower)

Most Recent Parametric Data

- (p1) Parametric1 = 0.956726 Volts
- (p2) Parametric2 = 1.015015 Volts
- (p3) Parametric3 = 0.011292 Volts
- (p4) Parametric4 = 0.009766 Volts
- (p5) Parametric5 = 0.009766 Volts
- (p6) Parametric6 = 0.009766 Volts

Most Recent VParametric Data

- Min Wind Speed = 3.7 mph
- Avg Wind Speed = 12.652 mph
- Max Wind Speed = 40.3 mph
- Dir. Min Wind Speed = 121 de
- Dir. Avg Wind Speed = 307.76
- Dir. Max Wind Speed = 66 deg
- Air Pr. = 29.692 inHg
- Air Temp. = 23.996 F
- WS Internal Temp. = 24.276 F
- Humidity = 69.056 %RH
- Rain Accum. = 0 in
- Rain Duration = 20 sec
- Rain Intensity = 0 in/hr
- Rain Peak Intensity = 0 in/hr
- Hail Accum. = 0 hits/in2
- Hail Duration = 0 sec
- Hail Intensity = 0 hits/in2h
- Hail Peak Intensity = 0 hits/in2h
- Heating Temp. = 24.264 F
- Heating Voltage = 0 V
- Supply Voltage = 11.9 V
- Vref = 3.534 V
- TM2_temp = 0 deg C
- TM2_relativeHumidity = 0 % R
- TM2_3 = 0.0
- TM2_4 = 0.0
- TM2_5 = 0.0
- TM2 Battery = 0 V
- TM_temp = 46.2 deg F
- TM_relativeHumidity = 29.7 %

Figure 188. Screenshot. Web portal for secure remote data collection.

Phase II: Installation of the Corrosion Monitoring System in the Main Cable

Upon successful completion of the laboratory phase for testing the sensors, the selected setup of sensors, measuring temperature, relative humidity, and corrosion rate was installed on cable D of the Manhattan Bridge. Two 19.68-ft (6-m) panels on the Brooklyn side span were chosen along the cable between panel points 13 and 15 (see figure 189). In each of the two panels, the main cable was wedged at four groove positions along the circumference, and sensors were installed

inside the cable. The sensors were wired to a DAQ located at roadway level with a wireless modem which in turn transferred the data to a secured server to be made available to all stakeholders via a secured Web-based portal.

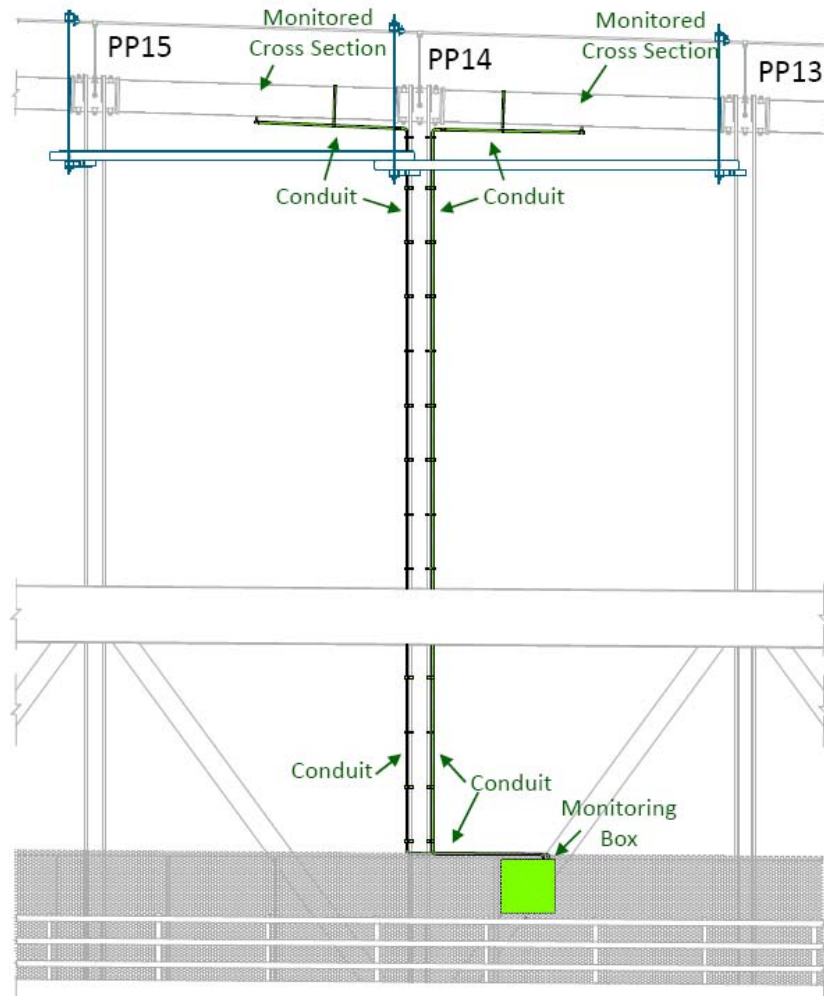


Figure 189. Illustration. Field installation location of sensor prototype on Manhattan Bridge north cable D.

Prior to installation, access to each panel point was required. Access was facilitated through the use of a suspended platform that was installed by NYCDOT maintenance personnel. The platform was suspended from three cable bands on the north cable between panel points 13 to 15 (see figure 190 and figure 191), with the top of the platform approximately 36 inches (914.4 mm) below the bottom of the main cable.



Figure 190. Photo. Suspended platform between panel points 13 and 15.



Figure 191. Photo. Walkway where the DAQ was installed.

After the platform was installed, the cable was unwrapped and wedged at four groove positions along the circumference, namely at the 3, 6, 9, and 12 o'clock positions (see figure 192).



Figure 192. Photo. Cable preparation by unwrapping and wedging.

Cable Inspection

The cable was inspected for its condition prior to installing the sensors, and the condition was documented so that a comparison could be made between the condition at the time of installation and at the end of the field testing upon sensor removal. This would have served as the basis for the assessment of the effects of the sensors on the condition of the cable wires over time. The internal wires were inspected by a cable expert and were found to be in good condition and covered with a grease-like coating. The surface wires exhibited corrosion levels 3 and 4 due to the wrapping wire condition, which was being replaced at the time of this system's installation as a part of a major rehabilitation project. No broken wires or any degradation of the zinc coating were found.

Sensor Installation

A total of 38 sensors (19 per panel) were installed within the 2 panels of the main cable on the Manhattan Bridge, as shown in figure 193. Each panel had eight temperature/humidity sensors, four LPR sensors, four BM sensors, and two CMAS.

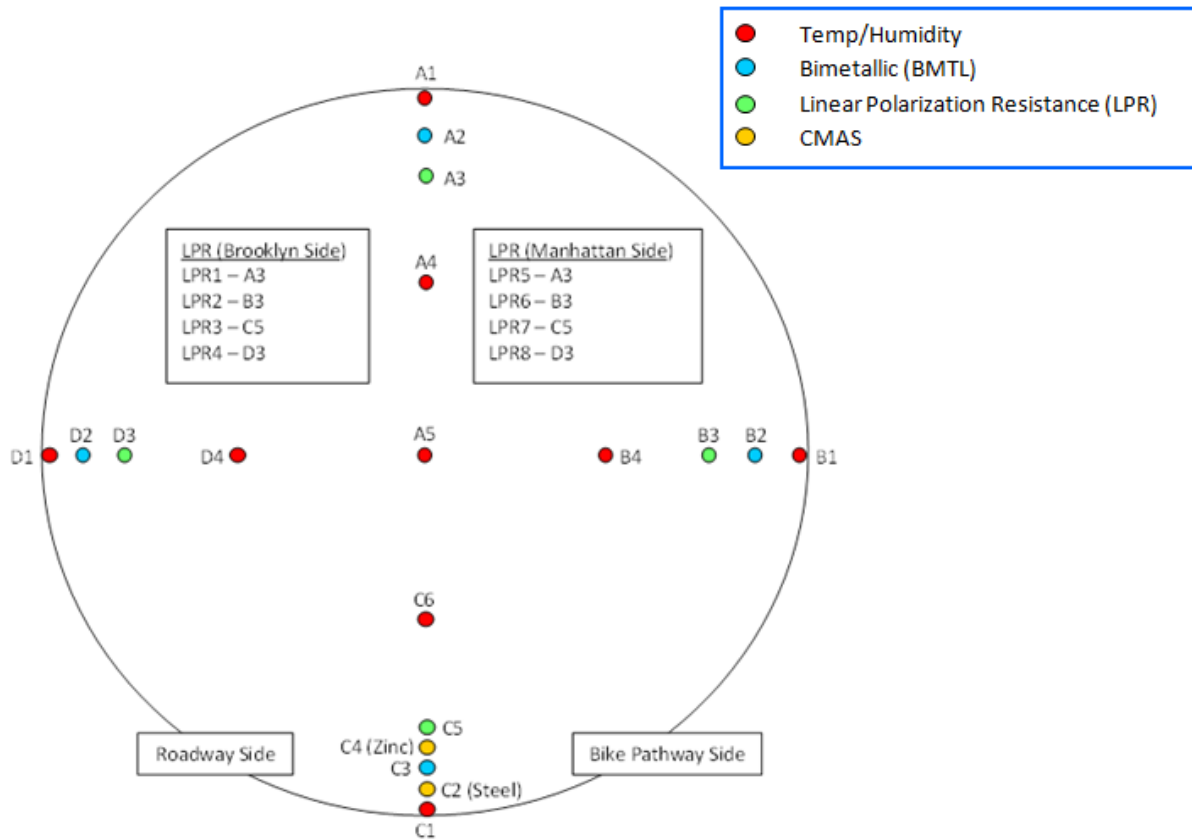


Figure 193. Illustration. Sensor distribution diagram within the cross section of the main cable (grooves A–D).

The sensors were assembled together (see figure 194) by placing them on a plastic strap that was then placed inside the cable (see figure 195). Each of the four locations contained at least one sensor of each type in order to look at the potential changes through the entire cross section of the cable (e.g., time of wetness, onset of corrosion, etc.). The sensors and wires for each section were protected from crushing through the use of polymer jackets and strapping. The wires from each section exited from the top, bottom, and sides of the main cable (see figure 195 and figure 196).

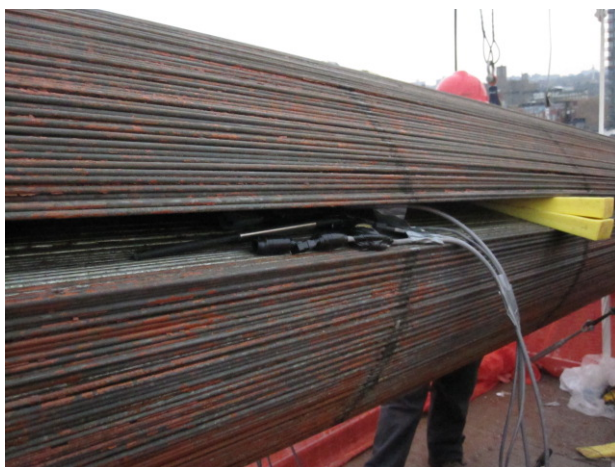


Figure 194. Photo. Sensor array used in each groove opening consisting of temperature/humidity sensors and LPR, CMAS, and BM corrosion sensors.



Figure 195. Photo. Set of sensors ready for installation.



Figure 196. Photo. Sensor lead wires exiting from the cable after installation.

Once the sensors were installed, the cable grooves were closed, and the cable was rewrapped with neoprene wrapping, leaving an exit port at the bottom of cable for the wires leading to the

data acquisition box at the sidewalk level (see figure 197 and figure 198). All sensor cables exiting the main cable were bundled, placed inside a conduit for protection, and pulled through a semi-rigid conduit from the platform location, through the platform deck, down the suspender rope, and then to the DAQ on the sidewalk level. For the LPR sensors, because of the short wiring length, the data collector box was located inside an enclosure right below the cable and then connected to the data acquisition box at the sidewalk level.



Figure 197. Photo. Cable temporary wrapping with neoprene and main conduit exiting at the bottom of cable leading to the main DAQ box at roadway level.



Figure 198. Photo. Final stage of the installation of the neoprene wrapping.

Prior to pulling the sensor cables from the platform, a NEMA-4 enclosure was installed along the sidewalk directly below the platform and panel points being monitored. Figure 199 through figure 201 show the installation of the DAQ enclosure for collection of data from all installed sensors. The DAQ was offset so that the enclosure did not extend past the vertical plane of the top railing or impede bicycle/pedestrian traffic on the pathway.



Figure 199. Photo. DAQ system/subsystem layout.



Figure 200. Photo. Installation of the central DAQ system.

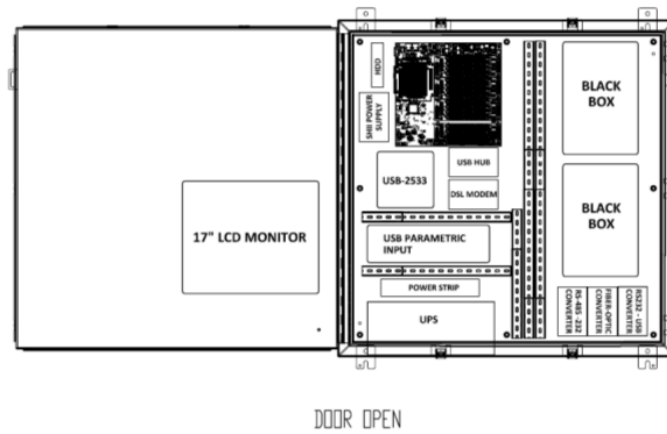


Figure 201. Illustration. Schematic representation of DAQ system.

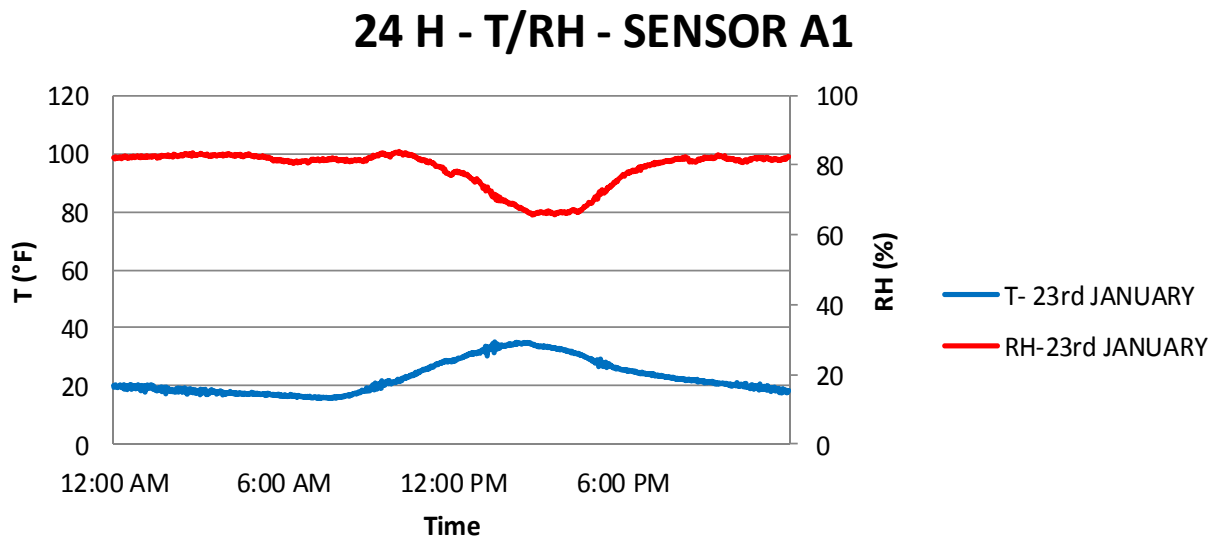
The DAQ housed all the components, subsystems, and hardware required for the collection of the data from the temperature, humidity, and corrosion sensors. The DAQ system included a main motherboard and central processing unit, subsystems for the BM and CMAS corrosion sensors (black boxes), RS485-232 converters, temperature/humidity parametric input board and converter (universal serial bus-2533), power supply, hard drive, monitor, uninterrupted power supply backup, and wireless cellular modem.

The installation of the sensors and systems was completed over a 2-week period. A total of 38 sensors (19 per panel) were distributed through the cross section of each panel. The collection of data lasted for almost 11 months, after which all the sensors and the DAQ were removed (October 18, 2011). All data were collected in real time and downloaded via cellular modem to central servers.

Data Collection and Analysis

The data collected by the 38 sensors provided a unique, real-time representation of the internal environment of the cable, which is an important key to understanding corrosion in suspension bridge cables and can help develop cost effective mitigation strategies.

In examining the temperature and relative humidity data inside the cable over a 24-h period, it was confirmed that there was a direct and inverse correlation between these two quantities (e.g., as the temperature rises the humidity level decreases, confirming the results from the laboratory phase). Figure 202 shows the recorded temperature and relative humidity recorded by sensor A1 located on the top portion of the cable cross section on January 23, 2011. As the temperature increased from 20 to about 38 °F (-6.67 to 3.33 °C) (around 3 p.m.), the relative humidity decreased from 100 to 80 percent.

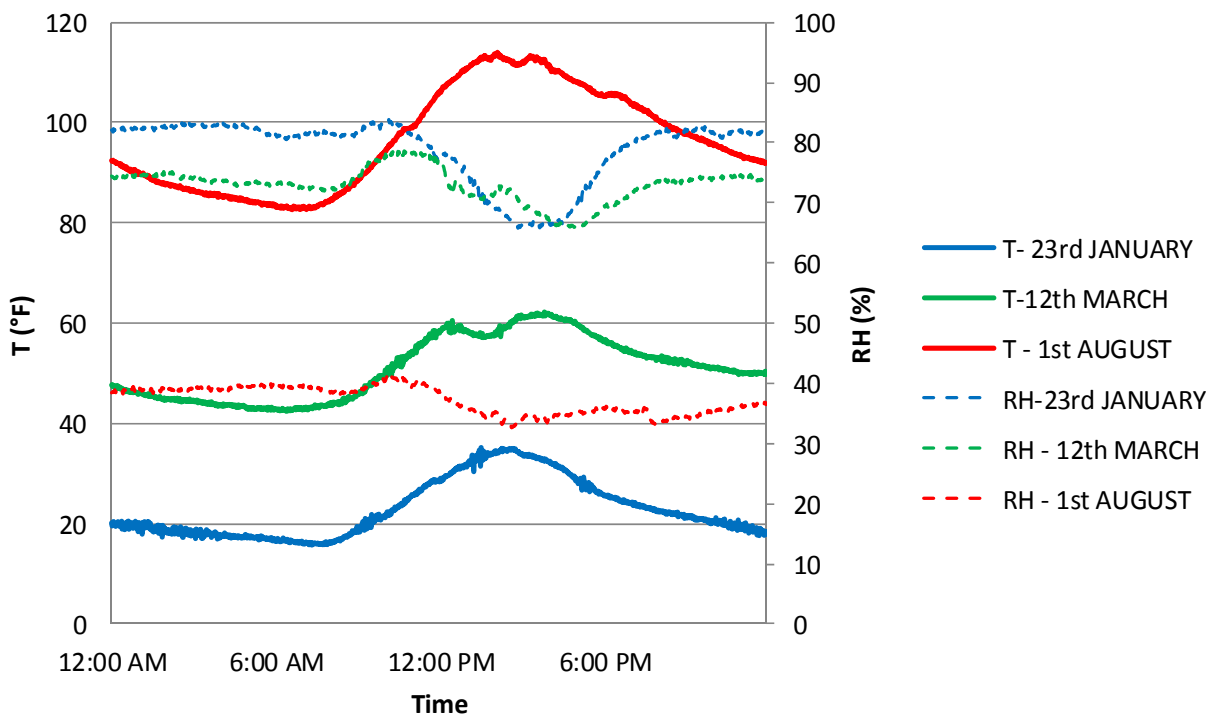


1 °C = (°F - 32)/1.8

Figure 202. Graph. Temperature and relative humidity over a 24-h period.

A similar inverse trend is shown in figure 203 where the daily variations of the temperature and relative humidity are plotted for 3 days at different times of the year (representing winter, spring, and summer). In August, as the temperature rose from 85 to 110 °F (29.44 to 43.33 °C) and reached a peak at 3 p.m. in the afternoon, the relative humidity decreased from 40 to 30 percent. In cooler months of the year (e.g., January and March), the temperature values were much lower (between 40 and 60 °F (4.44 and 15.56 °C) in March and 20 and 35 °F (-6.67 and 1.67 °C) in January), and the relative humidity values were much higher (between 65 and 75 percent in March and 65 and 90 percent in January). As shown in the laboratory phase of the experimental testing, the relative humidity values were affected by many different environmental parameters that were not necessarily synchronized with the sensor readings (e.g., rainfall during previous rain can affect the reading of a sensor a few days later).

24 H - T/RH - SENSOR A1



$$1\text{ }^{\circ}\text{C} = (\text{ }^{\circ}\text{F} - 32)/1.8$$

Figure 203. Graph. Temperature and relative humidity over a 24-h period showing variations from winter to summer.

In order to analyze the temperature and humidity distribution across the cable cross section between day and night and also between winter and summer, the maximum and minimum values of the temperature and relative humidity recorded during different days were plotted. Figure 204 shows an actual mapping of the maximum and minimum temperature and humidity readings taken from the all the sensors in the cross section of cable. These maps clearly show that the distribution of temperature and humidity as not uniform across the cable cross section and that the bottom and shaded side portions of cable were likely to retain higher levels of humidity than the upper portion. Moreover, the daytime exhibited higher temperatures and lower humidity. In

addition, when comparing the humidity levels between summer (August) and winter (January), the internal relative humidity level was higher in the winter than during the summer.

During the spring months when the temperature range was between 49 and 60 °F (9.44 and 15.56 °C) and the relative humidity was between 40 and 95 percent, the internal cable environment was the most conducive to corrosion, with high levels of humidity and with daily temperature cycles between day and night.

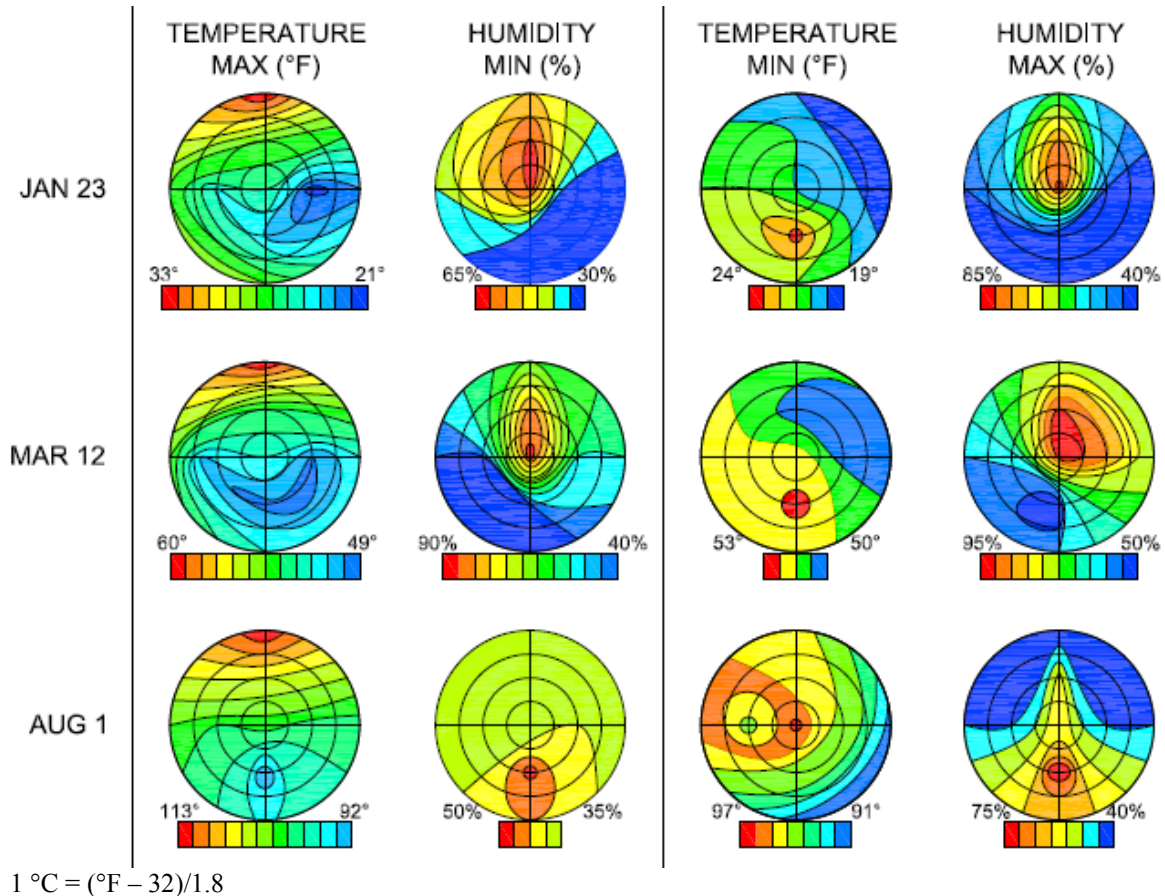
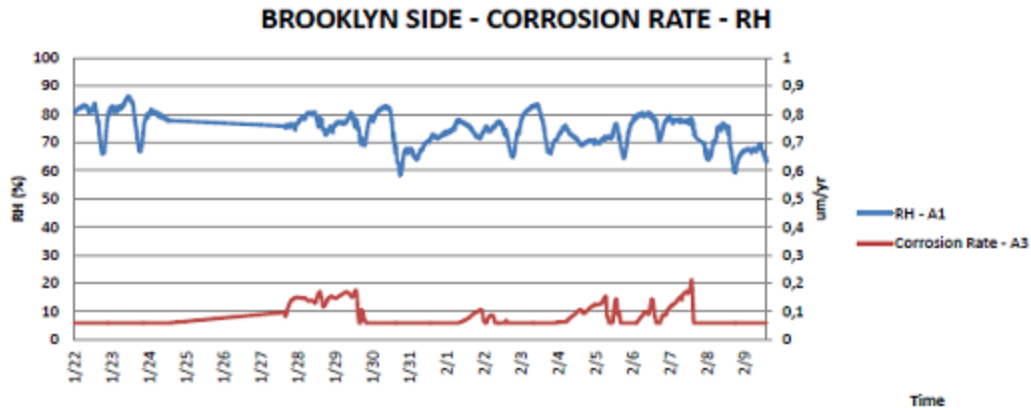


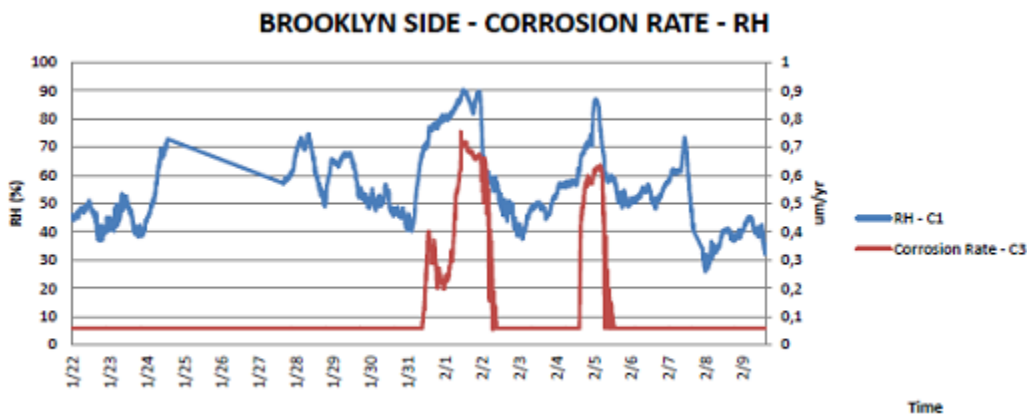
Figure 204. Illustration. Temperature and relative humidity relationship/distribution throughout the cable cross section during winter, spring, and summer.

In the figure, red represents the highest range value, while blue indicates the lowest range value. Additionally, the left column reflects daytime distribution, and the right column reflects nighttime distribution. With regard to the corrosion rate sensors (LPR, CMAS, and BM), all of the sensors provided some useful and consistent measurement of corrosion activity. For example, all sensors showed that no corrosion activity was detectable when the relative humidity was below 45 percent. The relation between relative humidity and corrosion rate is shown in figure 205 for the LPR sensor A3 and figure 206 for the BM sensor C3.



1 inch = 25,400 μm

Figure 205. Graph. Relative humidity versus corrosion rate measurement for LPR sensor.



1 inch = 25,400 μm

Figure 206. Graph. Relative humidity versus corrosion rate measurement for BM sensor.

An interesting event occurred between January 31 and February 3, 2011. During these 3 days, all the corrosion rate sensors installed in the Manhattan panel (between panel points 14 and 15) recorded a potential onset of corrosion activity. During these 3 days, there was a substantial snowfall followed by heavy rain. The BM corrosion rate sensor recorded a spike in both zinc and steel corrosion rates. The zinc sensor recorded an increase in the corrosion rate of approximately 0.0002 inch/year (5 $\mu\text{m}/\text{year}$), while the corresponding steel corrosion rate reached a value of 2.16×10^{-5} inch/year (0.55 $\mu\text{m}/\text{year}$) (see figure 207 and figure 208). Similarly, the LPR sensors recorded an increase in the corrosion rate of approximately 2.76×10^{-5} inch/year (0.7 $\mu\text{m}/\text{year}$) (see figure 209). Overall, it took approximately 24 h before the corrosion rate returned to normal (i.e., no corrosion) for all sensors. As an example, temperature, relative humidity, and corrosion rate data recorded on the bridge during the months of March and April are provided in appendix B.

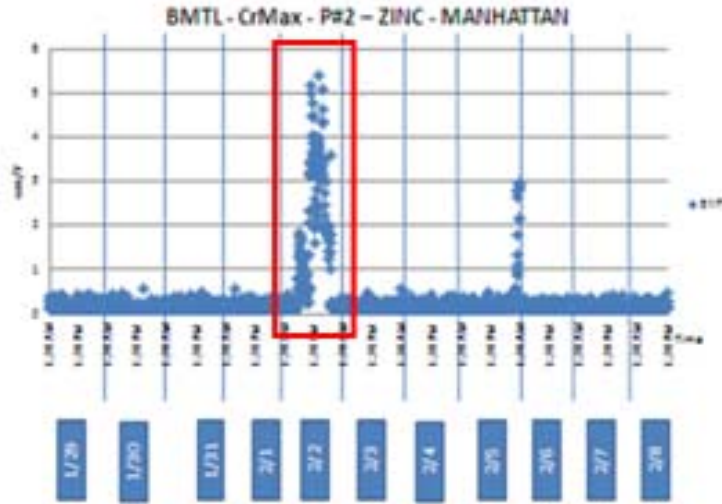


Figure 207. Graph. Increases in zinc corrosion recorded by BM sensor.

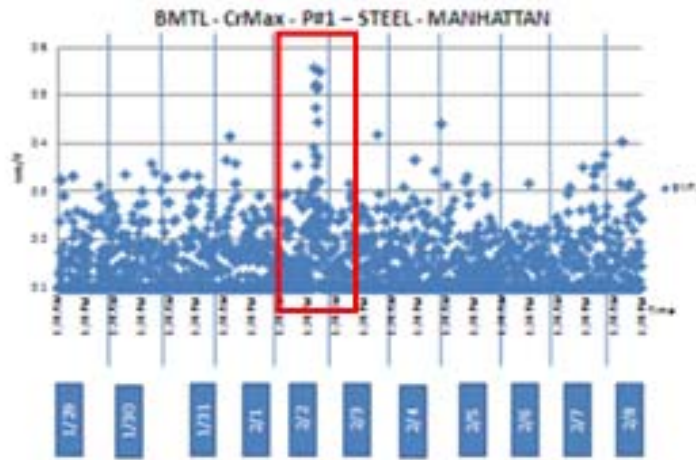
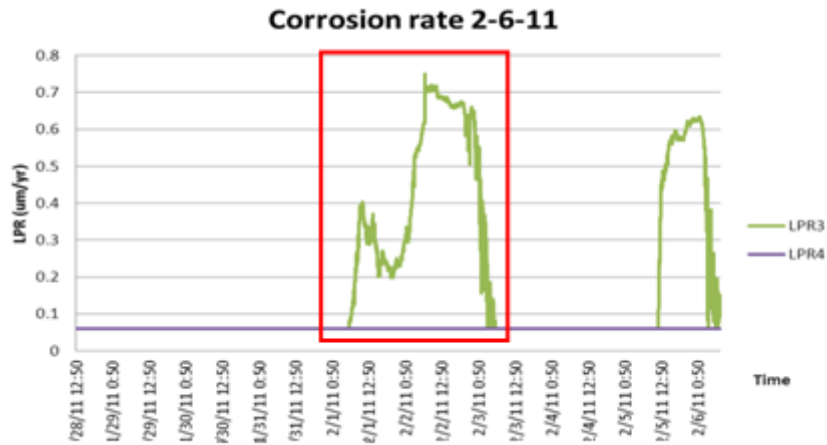


Figure 208. Graph. Increases in steel corrosion recorded by BM sensor.



1 inch = 25,400 μm

Figure 209. Graph. Increase in corrosion rate recorded by LPR sensors.

Following the measurement of what could be interpreted as an onset of corrosion activity, a visual inspection of the cable panels revealed that the neoprene wrapping used in these two panels was damaged due to construction activity (see figure 210). This sizeable opening might have been responsible for the penetration of water inside the cable.



Figure 210. Photo. Damaged neoprene wrapping due to construction activity on the bridge.

Decommissioning of the Cable Monitoring System

Upon completion of the 11-month monitoring, the cable wrapping was removed, and the cable was wedged open to retrieve the sensors, as shown in figure 211 and figure 212. The cable open groove was closely inspected for any damage due to contact with the sensors, but no damage was found (see figure 213). The cable was protected with temporary wrapping until the rehabilitation contractor began the permanent wrapping operation.



Figure 211. Photo. Decommissioning of the monitoring system by wedging the cable and pulling the sensors out.



Figure 212. Photo. Wires from sensors prior to removal.

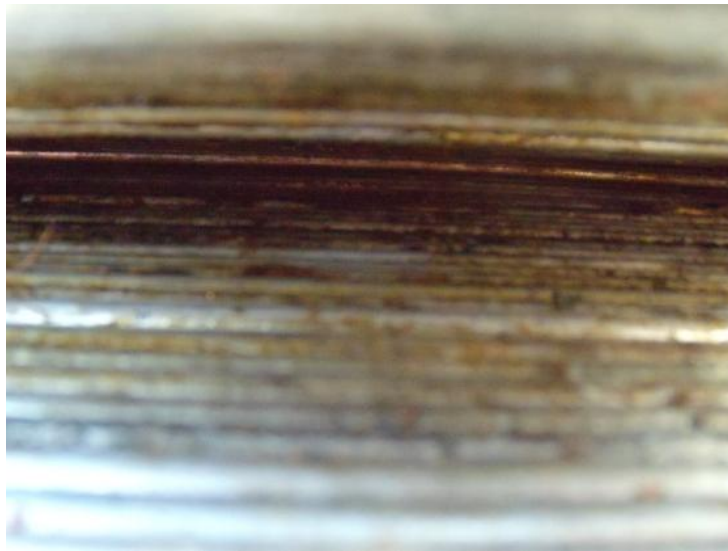


Figure 213. Photo. Close-up view of cable wires at the same location where the sensors were installed showing no damage to the main cable wire.

CHAPTER 9: CONCLUSIONS

The goal of this research project was to develop an integrated monitoring system that, using state-of-the-art sensing capabilities and NDE technologies, was capable of providing information about the conditions of high-strength steel wires inside a main cable of a suspension bridge.

Extensive experimental tests were conducted to test a variety of sensors and NDE technologies that could fit the specifics of field applications in real suspension bridges. The information provided by such a system can be useful in more reliably assessing the remaining service life and the current factor of safety of a main cable. Indirect sensing technologies are useful in monitoring environmental variables that can be related to corrosion and in detecting the onset of corrosion activity, serving as an early warning system. In addition, internal sensors can eventually be used for testing the reliability of a cable dehumidification system, in the case of pressure losses and leaks as well as dead zones along the cable, providing valuable information for estimating the optimum life-cycle cost of the dehumidification system in terms of operation and maintenance cost. The direct sensing system can provide a qualitative assessment of the cable condition along its entire length (e.g., number and location of broken wires) so that a detailed inspection of the main cable can be focused on the most critical segment of the cable.

The proposed sensor network system was successful in providing measurements of parameters such as temperature, relative humidity, and corrosion rate from the interior of a main cable. These parameters are essential for understanding the interior environment of a suspension bridge's main cable. It was the first time that an experiment of such a scale was attempted on a main cable. The construction of an environmental testing chamber permitted the testing of various environments affecting the temperature, relative humidity, and corrosion rate distributions within a full-scale mockup cable and provided a realistic test for the durability and reliability of the selected sensors. A corrosion rate analysis highlighted the clear differences in the dependency of the corrosion process on environmental variables like temperature and relative humidity. As expected, the selected sensors showed that increased levels of relative humidity resulted in increased levels of corrosion activity and that there is a strong linear dependence between the variability of the corrosion rate and temperature variations.

After extensive experimental tests, the selected sensors were integrated in a corrosion monitoring system that was installed on an in-service Manhattan Bridge cable. Field testing was used to determine the real-world functionality of the system and proved to be successful. The field pilot program was essential in validating the laboratory results and showed good correlation with the original assumptions.

The main conclusions of this research project are as follows:

- The selected sensor network system was successful in providing information on the interior environment of a suspension bridge's main cable, helping understanding the conditions in which main cables of suspension bridges operate.
- Tests performed on sensors focused on the accuracy of the measurements as well as on the capability of the sensor to survive in the interior of a suspension bridge's main cable.

The sensors selected in this study showed good reliability in all the testing phases, from the stand-alone sensor test in a small corrosion chamber to the insertion into a real main cable of a bridge.

- The construction of a cable mockup and of the surrounding environmental chamber allowed researchers to test the sensor system in conditions as close as possible to the in-service conditions, providing insight into the performance of the various types of sensors. In addition, the extensive testing of such a specimen allowed researchers to obtain a large amount of information on the various environments affecting the temperature, relative humidity, and corrosion rate distributions within a main cable.
- A detailed analysis of the data recorded during the laboratory phase highlighted the distinct differences in the dependency of the corrosion rate with environmental variables like temperature and relative humidity. Through monitoring, it was observed that increased levels of relative humidity resulted in increased levels of corrosion activity and that a strong linear correlation exists between the corrosion rate and the temperature.
- Field testing of the system on the Manhattan Bridge in the City of New York was used to determine the real-world functionality of the system and proved to be successful. The results from the field pilot test were essential in validating the laboratory results and showed good correlation with the original assumptions.
- During the field test, the sensor monitoring system was successful in detecting the onset of corrosion at one location, caused by a damaged protective wrapping. This showed that this system could also work as an early warning system for the safety of the cable.
- Some of the technologies for a direct sensing system showed great potential for future applications. Among those, the technology based on the main flux method performed well during the laboratory phase, even on the large cable mockup, and should be further investigated. The technology based on the combination of AE and MS showed great results and promise for small bundles of wires but suffered when dealing with relatively larger cables. It might be used at the anchorage site.
- The system can be commercially used on any suspension bridge cables and can be adapted with some modification to stay cables and possibly post-tensioning tendons.

In conclusion, this study demonstrated that it is possible to measure corrosion activity inside main cables of suspension bridges. The information provided by such a system can be used to make more reliable estimations of the safety factor and remaining service life of such important structural elements as well as to help bridge engineers in conducting more efficient and cost effective inspections. Because of the continuous advancements in sensor and NDT technologies, it is important to pay attention to any new developments that can help improve such a monitoring system.

APPENDIX A: CALIBRATION OF LPR SENSORS

CALIBRATION OF SENSORS

In order to obtain the bridge wire corrosion rate from LPR sensors, a relationship between corrosion rate and R_p readings from the sensors is needed. The corrosion rate is calculated from R_p and mass loss measurements on the corroding metal using the concept of equivalent weight and Faraday's Law. Equivalent weight (EW) is the amount of an element that reacts with 1 Faraday of charge, thus contributing to the corrosion and overall loss of material in the basic oxidation process for metals: $M \rightarrow M^{z+} + ze^-$. Here M indicates a metal atom, e indicates electron and z is the number of electrons lost per atom of metal. EW is calculated from the known atomic weight (AW) of the metal and z as follows:

$$EW = \frac{AW}{z}$$

Figure 214. Equation. Equivalent weight.

In order to relate the mass loss of metal to the current flow, Faraday's law is stated as follows:

$$Q = z \times F \times M$$

Figure 215. Equation. Relationship between the charge from the corrosion reaction with the number of lost electron and the moles of metal.

Where:

Q = Charge in Coulombs resulting from the reaction of corroding metal

F = Faraday's constant (i.e., 96,485.34 Coulombs/mole).

z = Number of electrons lost per atom of the metal.

M = Number of moles of metal reacting.

For the number of moles lost for the metal M , the amount of mass loss W can be calculated as follows:

$$W = M \times AW$$

Figure 216. Equation. Amount of mass loss.

Combining figure 214 through figure 216 and substituting for z and M , W can be related to charge Q as follows:

$$W = \frac{EW \times Q}{F}$$

Figure 217. Equation. Relationship between the amount of mass loss with the equivalent weight and the charge.

W can be converted to corrosion rate from the density and sampling area of the corroding metal using the basic identities as follows:

$$W = \rho \times V = \rho \times A \times T$$

Figure 218. Equation. Mass loss related to density of the material and volume of the lost material.

$$Q = I_{corr} \times t$$

Figure 219. Equation. Charge as the product of the corrosion current and time.

Where:

ρ = Density of metal.

V = Volume of corroding metal corresponding to the sampling area.

A = Sampling area.

T = Thickness of corrosion layer corresponding to the sampling area.

I_{corr} = Corrosion current.

t = Time in seconds.

From figure 219, the following can be obtained:

$$\rho \times A \times T = \frac{EW \times I_{corr} \times t}{F}$$

Figure 220. Equation. Mass loss from geometric considerations to the mass loss from equivalent weight and charge.

$$\frac{T}{t} = \frac{I_{corr} \times EW}{\rho \times A \times F}$$

Figure 221. Equation. Rate of change of thickness.

The rate of change of thickness $\left(\frac{T}{t}\right)$ is the corrosion rate (CR) of the metal as follows:

$$CR = \frac{I_{corr} \times K \times EW}{\rho \times A}$$

Figure 222. Equation. Corrosion rate of the metal.

Where K is a constant that accounts for Faraday's constant (F) in figure 221 and changes units of corrosion from seconds to years. I_{corr} can be substituted to yield the following:

$$CR = \frac{1}{R_p} \left(\frac{B \times K \times EW}{\rho \times A} \right)$$

Figure 223. Equation. Alternative expression of the corrosion rate.

$$CR = \frac{B'}{R_p}$$

Figure 224. Equation. Simplified expression of the corrosion rate.

Where B' is the overall proportionality constant in units mm-ohms/year. In order to determine B' , LPR sensors and ungalvanized bridge wires were tested together in various cyclic corrosion tests.

DETERMINATION OF B'

From the mass loss experiments with actual bridge wires, researchers determined the corrosion loss for each test. Both recorded R_p values and corrosion mass loss values were used to estimate the overall proportionality constant B' in figure 224.

The sampling frequency for R_p during the corrosion test was 1 recording/min. Hence, the estimated thickness loss induced by corrosion during a given minute ($C_{1\text{-min}}$) can be obtained by converting the corrosion rate CR in inches/year (mm/year) to inches/min (mm/min) and then multiplying times 1 min as follows:

$$C_{1\text{-min}} = CR \text{ (mm / year)} \times \frac{1 \text{ min}}{60 \text{ min/hr} \times 24 \text{ hr/day} \times 365 \text{ day/year}} = \frac{CR}{525,600} \text{ (mm)}$$

$$1 \text{ inch} = 25.4 \text{ mm}$$

Figure 225. Equation. Estimated thickness loss in 1 min.

Substituting for CR the expression presented in figure 224 leads to an expression for the thickness loss during a given minute as follows:

$$C_{1\text{-min}} = \frac{B'}{R_p} \times \frac{1}{525,600} \text{ (mm)}$$

$$1 \text{ inch} = 25.4 \text{ mm}$$

Figure 226. Equation. Alternative expression of the estimated thickness loss in 1 min.

Where R_p is obtained directly from the measurements. The total thickness loss for the duration of $3 \text{ (h)} \times 60 \text{ (min)} \times 48 \text{ (cycle)} = 8,640\text{-min}$ experiments (C_{Exp}) will then be expressed as follows:

$$C_{Exp} = \sum_{t=0}^{t=8640\text{min}} \frac{B'}{R_p(t)} \times \frac{1}{525,600} = \frac{B'}{525,600} \sum_{t=0}^{t=8640\text{min}} \frac{1}{R_p(t)} \text{ (mm)}$$

$$1 \text{ inch} = 25.4 \text{ mm}$$

Figure 227. Equation. Expression of the estimate of the total thickness loss.

Where the summation is intended for all the values recorded during the experiment. In this case, the proportionality constant B' can then be obtained from the following:

$$B' = \frac{C_{Exp} \times 525,600}{\sum_{t=0}^{t=8640 \text{ min}} \frac{1}{R_p(t)}} \quad \left(mm - ohms / year \right)$$

Figure 228. Equation. Proportionality constant as function of the thickness loss and of the polarization resistance.

As an example, the calculation of B' for the 0.006-inch (150- μm) LPR sensor used in experiment 1 is provided. In this experiment, only one 0.006-inch (150- μm) LPR sensor was placed in the chamber with the wires. Figure 229 shows the inverse of R_p readings for this sensor during the first eight cycles of experiment 1. Each data point on the plot corresponds to the inverse of R_p at a given instant in time and is proportional to the instantaneous corrosion rate value at that recording time, following the relation given by figure 226. The integration of this time series (multiplication of these values by the sampling interval (1 min) and summation of all these products) yields the denominator of figure 227.

The integrated area is shown for the first eight cycles of experiment 1 in figure 230. The area for the entire duration of the test (its integration) is 7.1020×10^{-3} min/ohms.

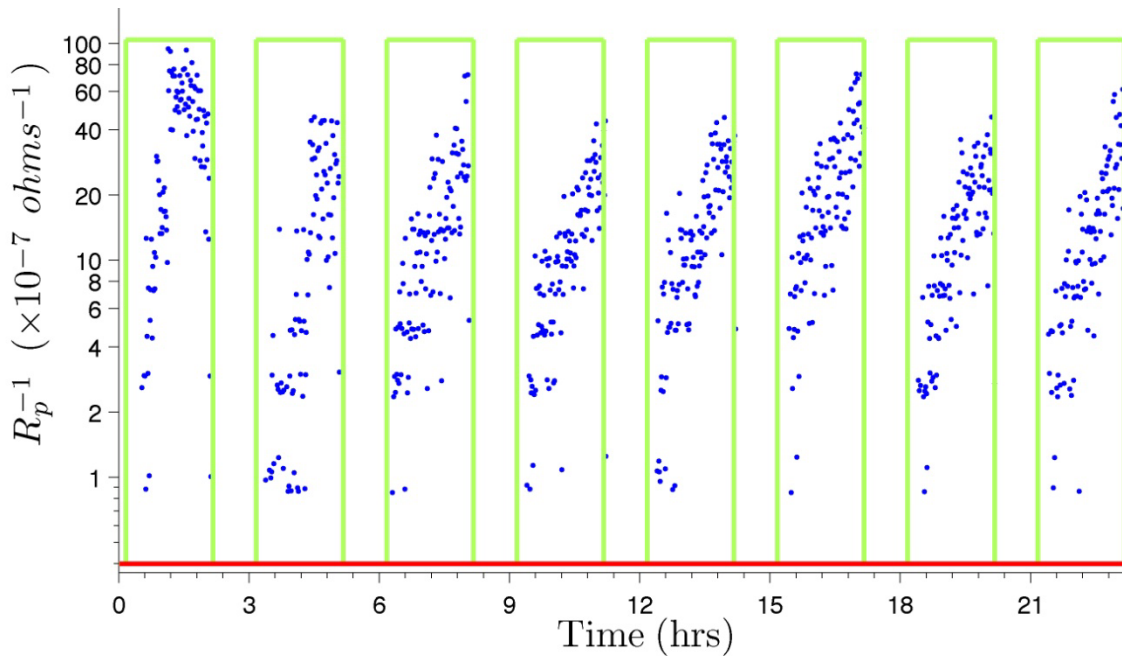


Figure 229. Graph. Inverse of R_p versus time.

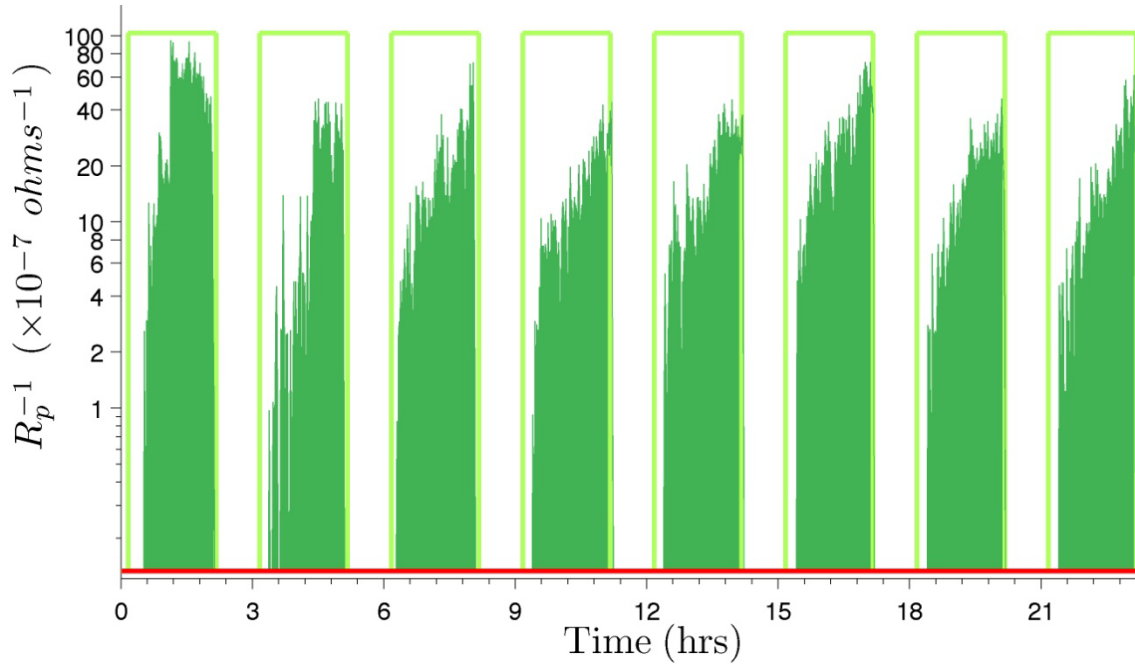


Figure 230. Graph. Integration of inverse of R_p .

The average thickness loss measured for the ten specimens tested in experiment 1 is 0.0006 inch (14.87 μm). This is obtained by measuring the wires before and after the experiment, as previously described. Overall proportionality constant B' for the sensor can then be calculated as follows:

$$B' = \frac{C_{Exp-1} \times 525,600}{\sum_{t=0}^{t=8640 \text{ min}} \frac{1}{R_p(t)}} = \frac{14.87 (\mu\text{m}) \times \frac{1(\text{mm})}{1000(\mu\text{m})} \times 525,600 (\text{min}/\text{year})}{7.1020 \times 10^{-3} (\text{min}/\text{ohms})}$$

$$= 1100491 \left(\frac{\text{mm-ohms}}{\text{year}} \right)$$

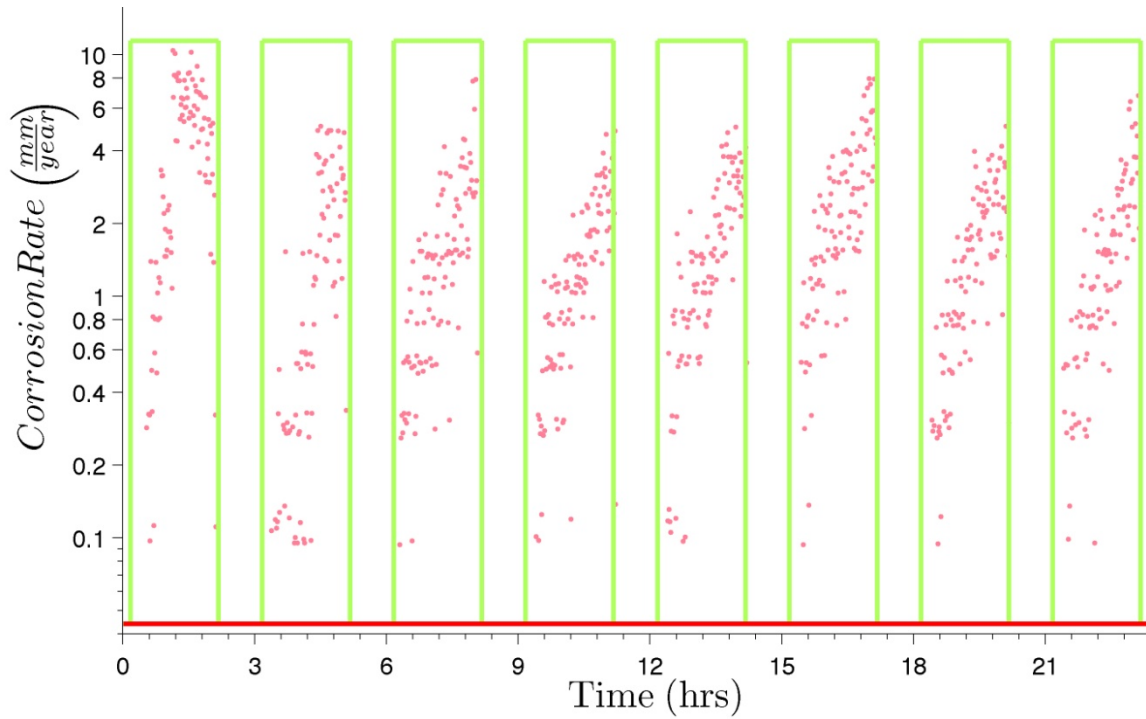
Figure 231. Equation. Estimation of constant of proportionality from experiment 1.

Where:

$$\sum_{t=0}^{t=8640 \text{ min}} \frac{1}{R_p(t)} = 7.1020 \times 10^{-3} (\text{min}/\text{ohms}).$$

$$C_{Exp-1} = 0.0006 \text{ inch (14.87 } \mu\text{m}).$$

Hence, when using measurements from the 0.006-inch (150- μm) LPR sensors, dividing this value of B' by R_p will provide an instantaneous measurement of the corrosion rate of the wire. Figure 232 displays the instantaneous corrosion rate values calculated using the overall proportionality constant B' .



1 inch = 25.4 mm

Figure 232. Graph. Instantaneous corrosion rates versus time.

APPENDIX B: SAMPLE DATA

This appendix provides temperature, relative humidity, and corrosion rate measurements recorded by the proposed monitoring system in the interior of one of the main cables of the Manhattan Bridge in the City of New York.

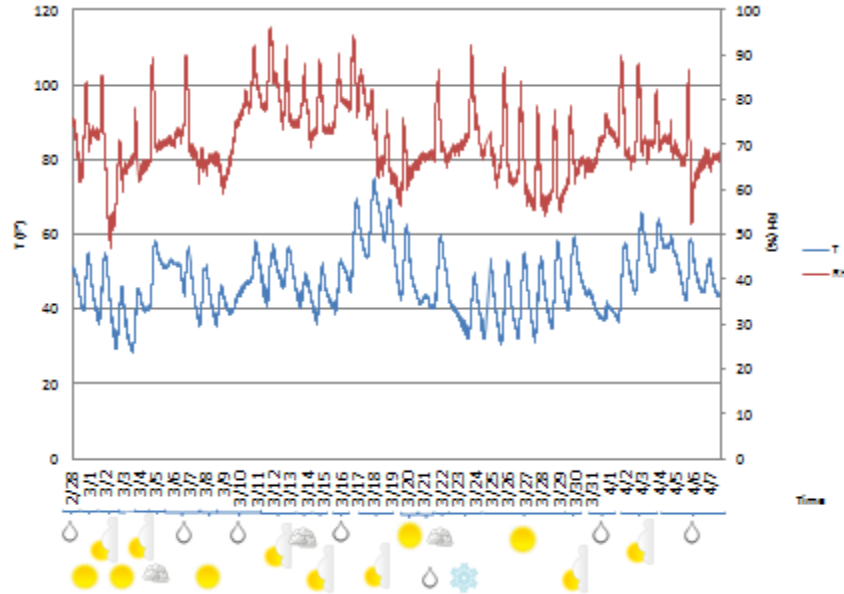


Figure 233. Graph. Temperature-relative humidity measurements for sensor A4 on Brooklyn side in March 2011.

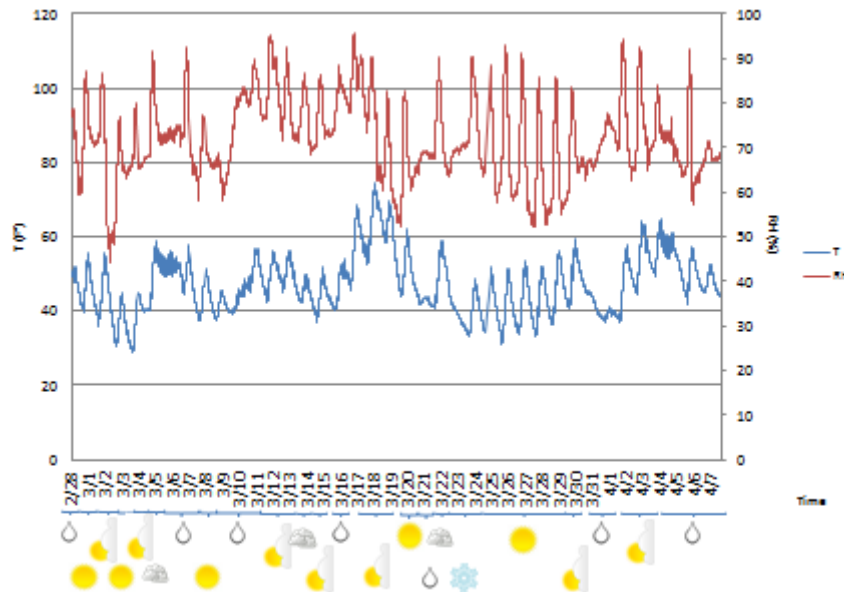


Figure 234. Graph. Temperature-relative humidity measurements for sensor A5 on Brooklyn side in March 2011.

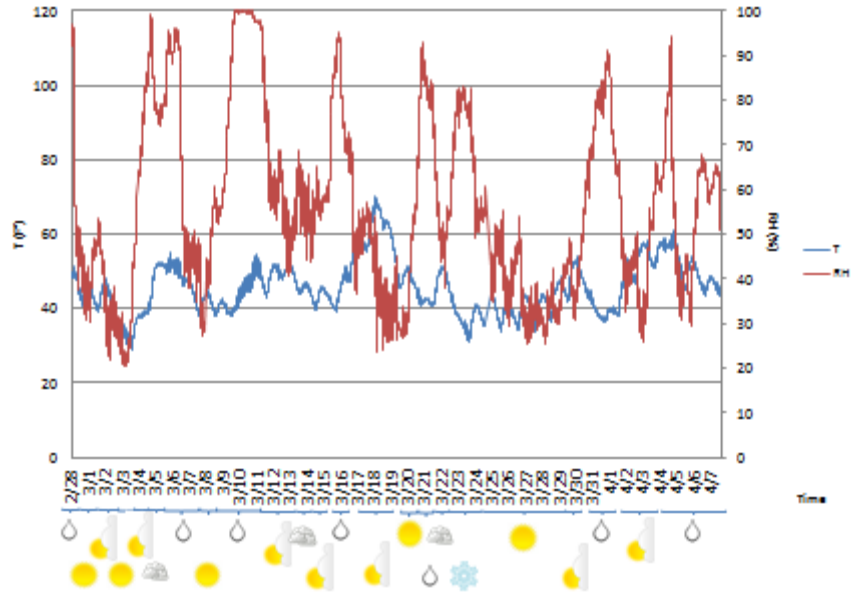


Figure 235. Graph. Temperature-relative humidity measurements for sensor B4 on Brooklyn side in March 2011.

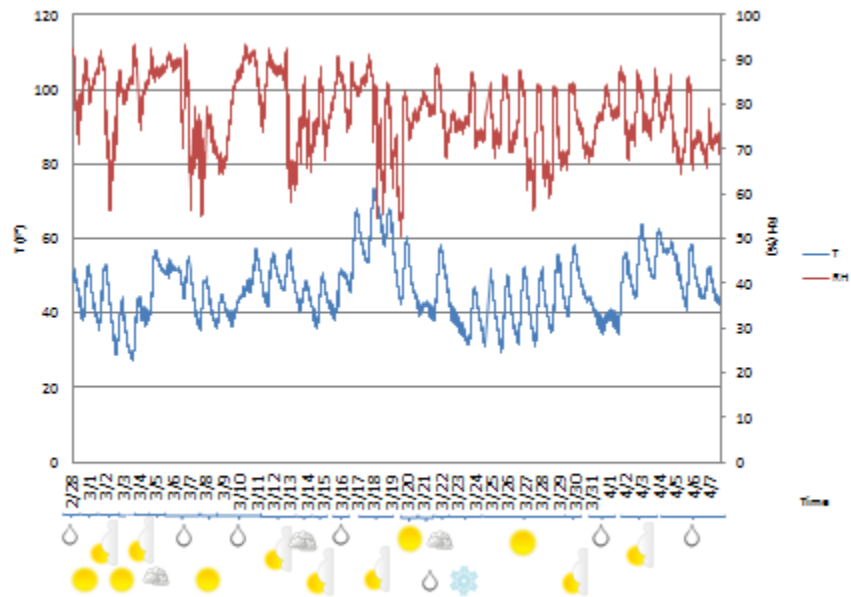


Figure 236. Graph. Temperature-relative humidity measurements for sensor A4 on Manhattan side in March 2011.

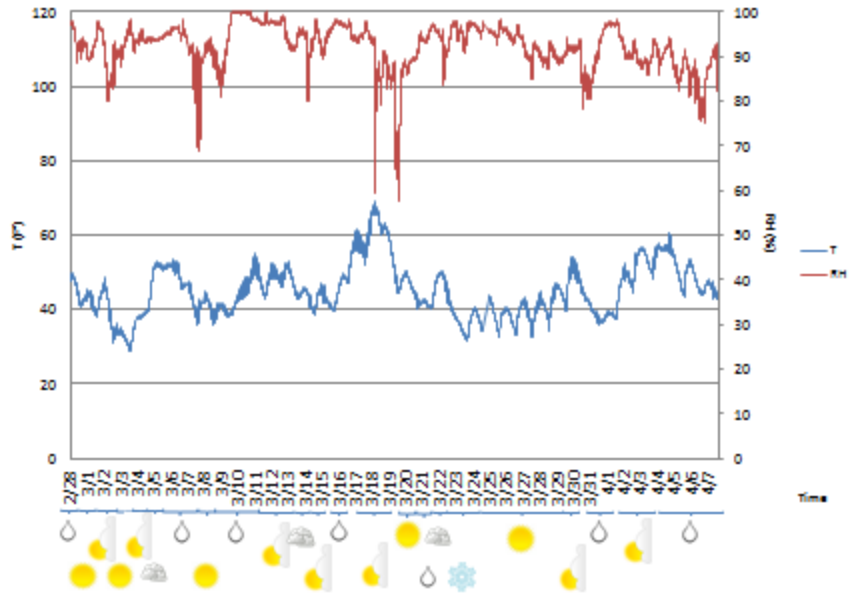


Figure 237. Graph. Temperature-relative humidity measurements for sensor B4 on Manhattan side in March 2011.

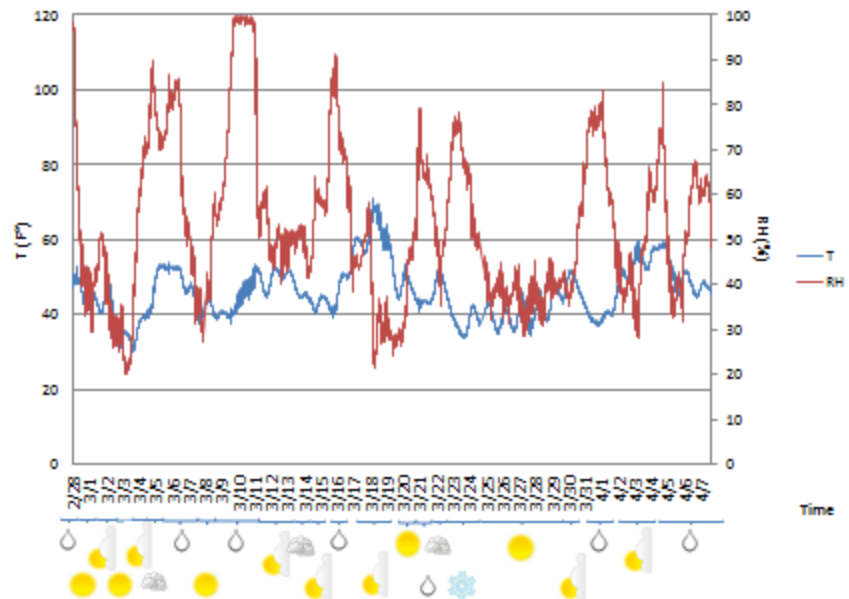


Figure 238. Graph. Temperature-relative humidity measurements for sensor C6 on Manhattan side in March 2011.

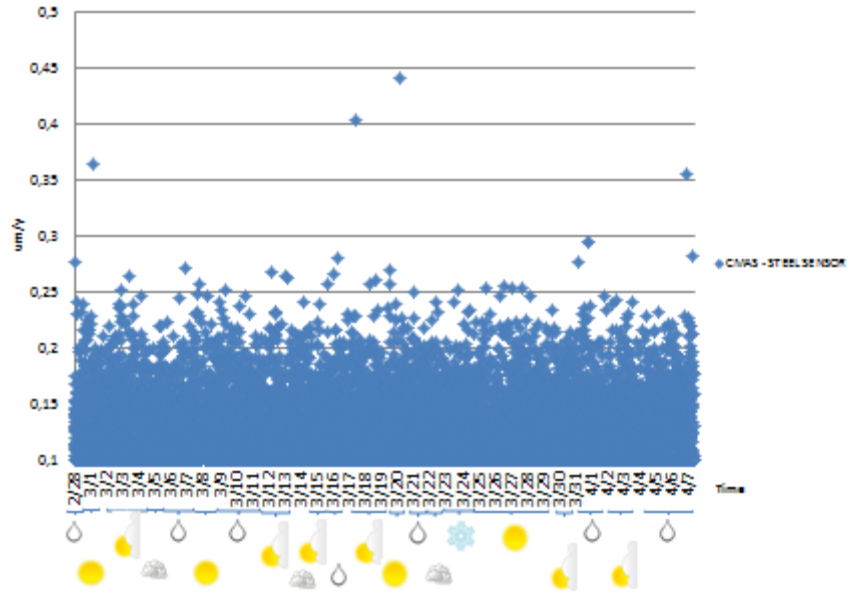


Figure 239. Graph. Corrosion rate measurements for CMAS CS sensor in March 2011.

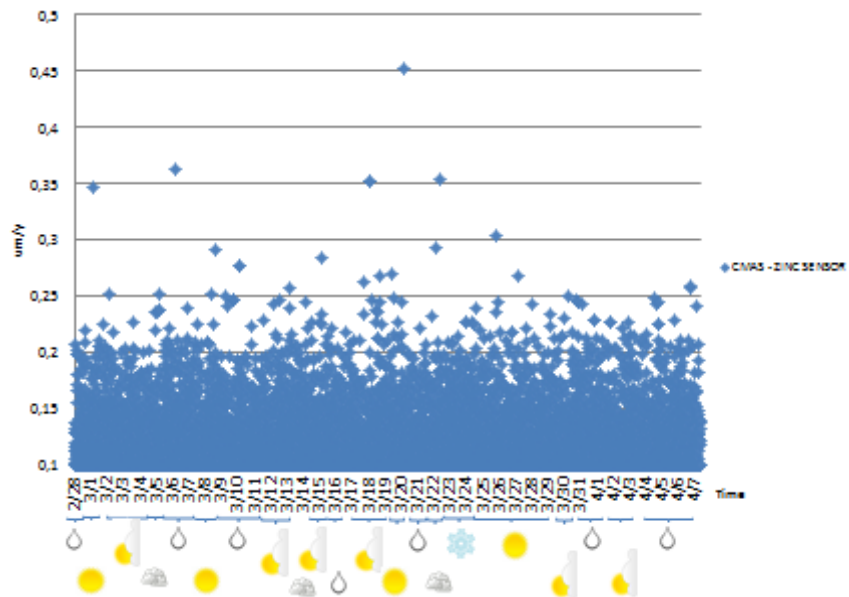


Figure 240. Graph. Corrosion rate measurements for CMAS Zn sensor in March 2011.

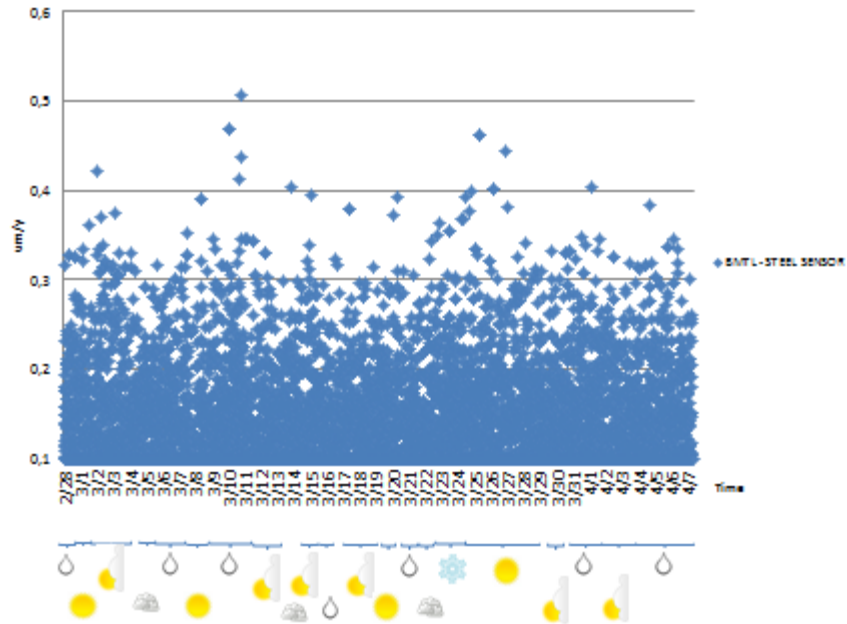


Figure 241. Graph. Corrosion rate measurements for BM CS sensor in March 2011.

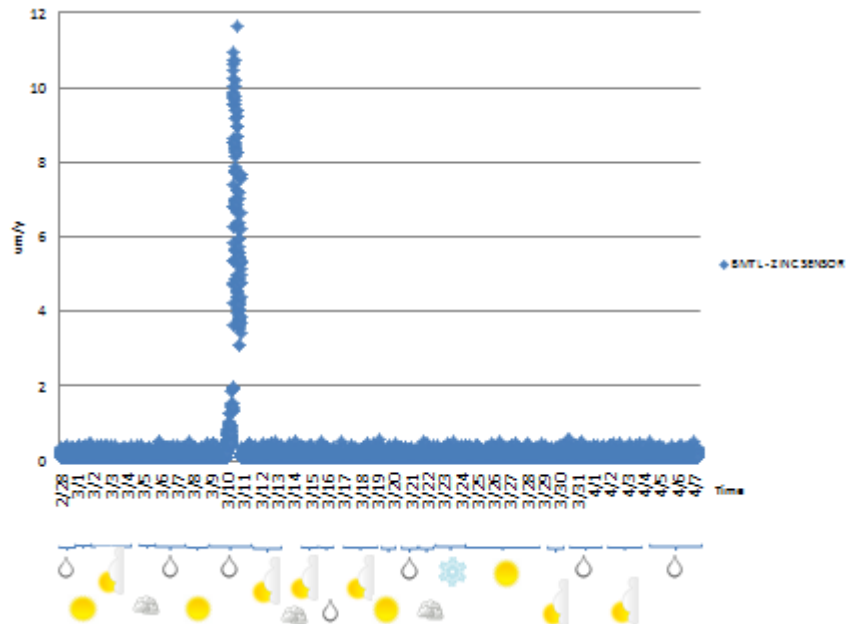


Figure 242. Graph. Corrosion rate measurements for BM Zn sensor in March 2011.

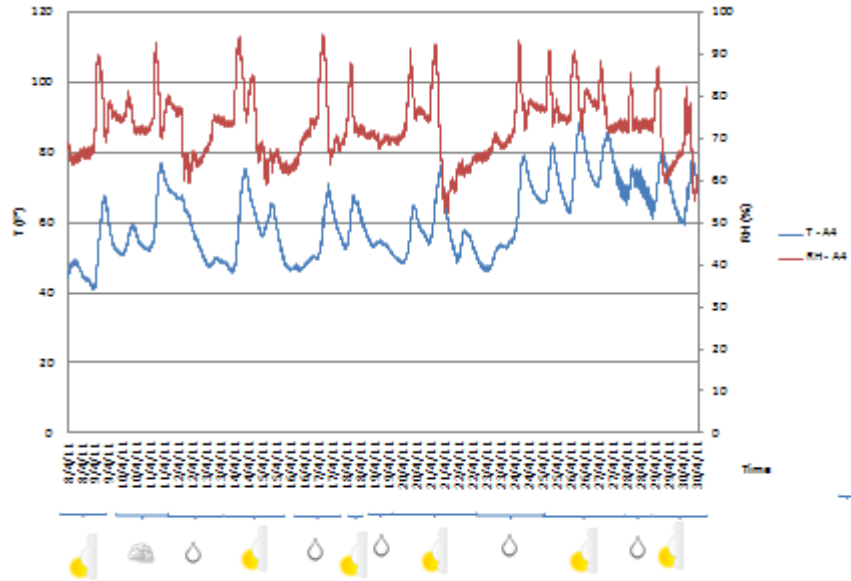


Figure 243. Graph. Temperature-relative humidity measurements for sensor A4 on Brooklyn side in April 2011.

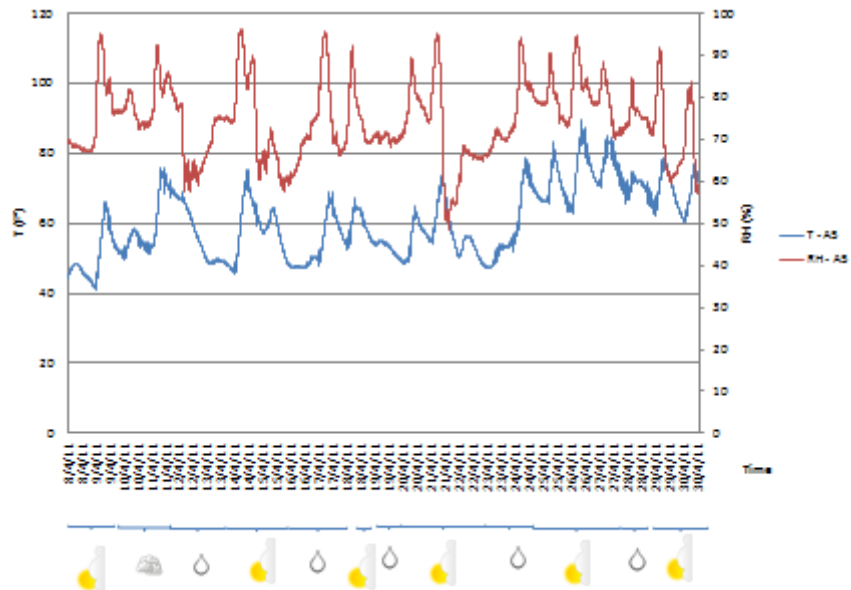


Figure 244. Graph. Temperature-relative humidity measurements for sensor A5 on Brooklyn side in April 2011.

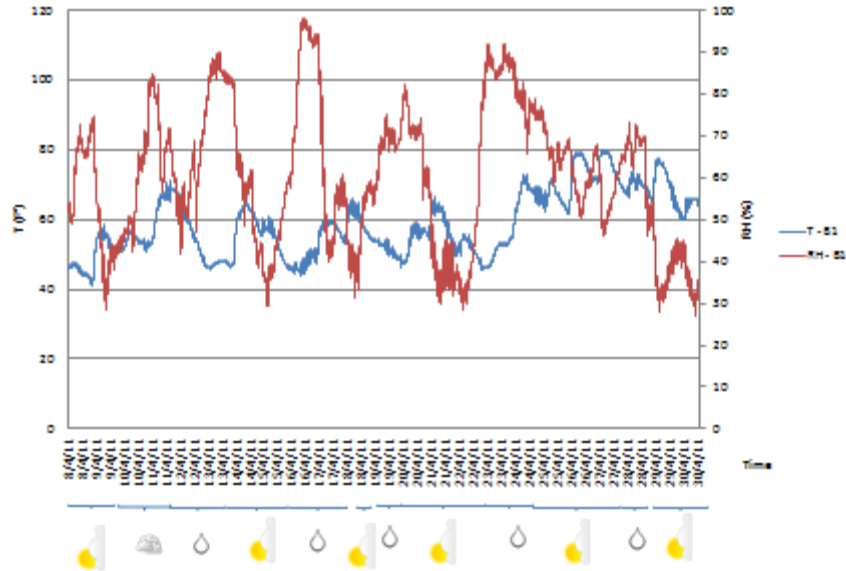


Figure 245. Graph. Temperature-relative humidity measurements for sensor B1 on Brooklyn side in April 2011.

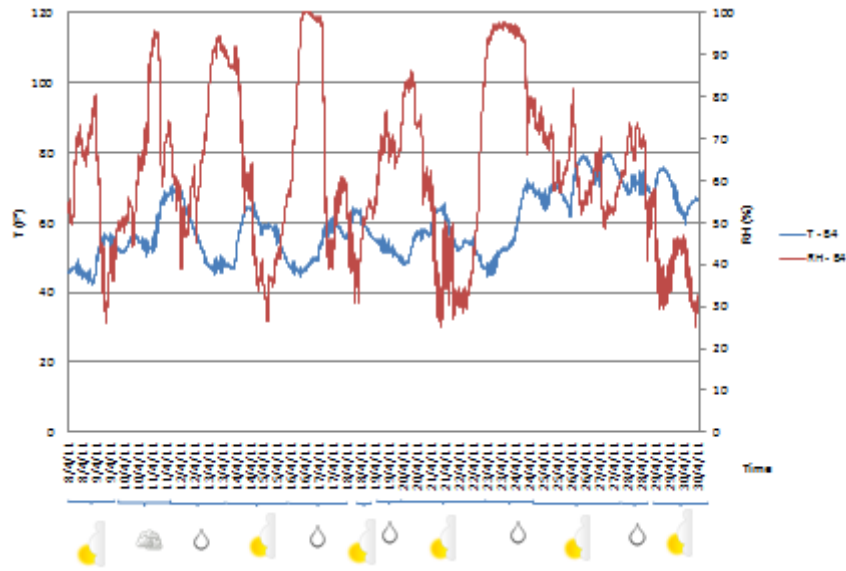


Figure 246. Graph. Temperature-relative humidity measurements for sensor B4 on Brooklyn side in April 2011.

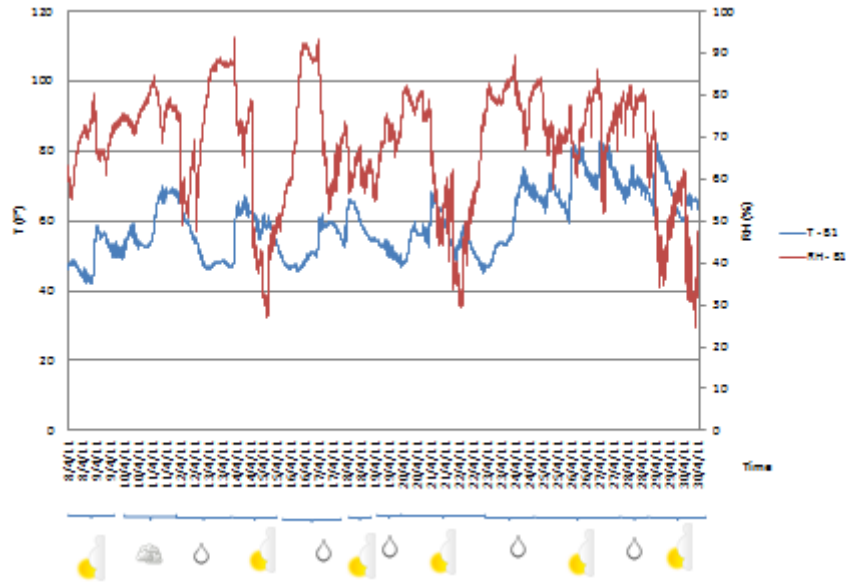


Figure 247. Graph. Temperature-relative humidity measurements for sensor B1 on Manhattan side in April 2011.

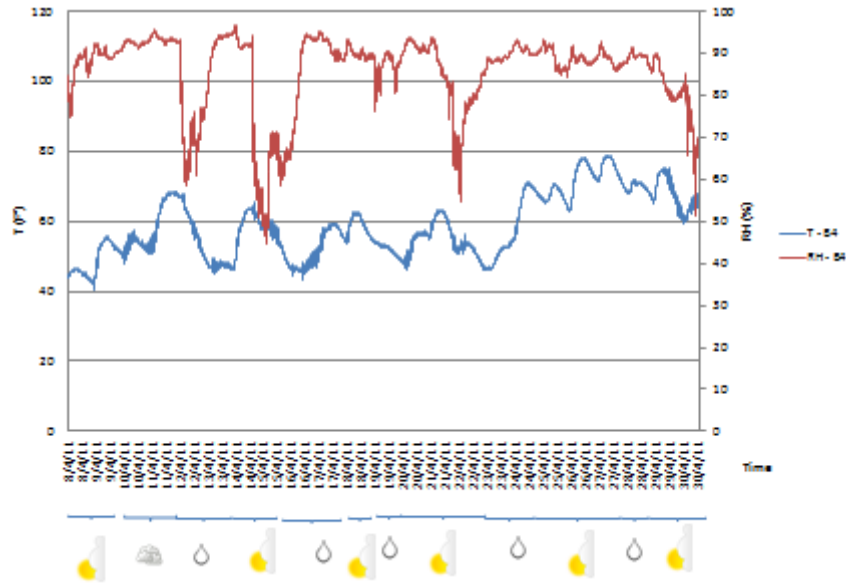


Figure 248. Graph. Temperature-relative humidity measurements for sensor B4 on Manhattan side in April 2011.

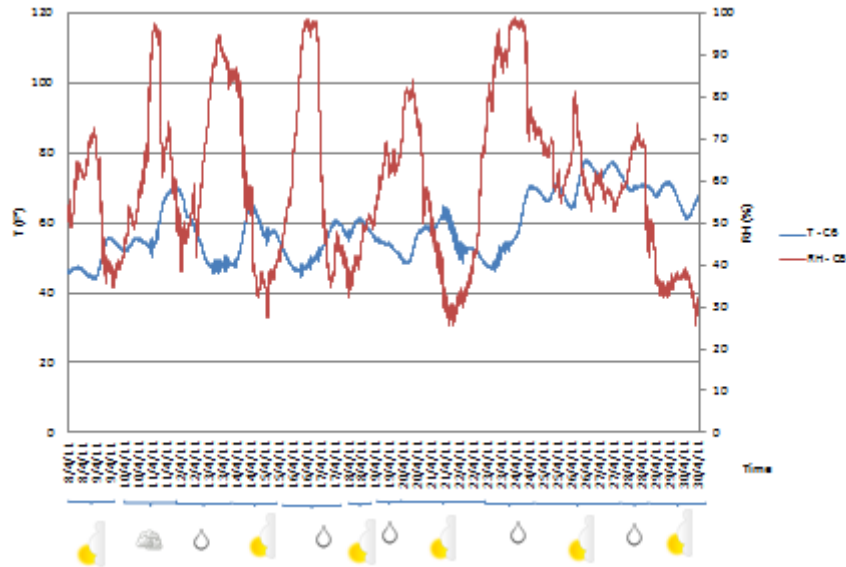


Figure 249. Graph. Temperature-relative humidity measurements for sensor C6 on Manhattan side in April 2011.

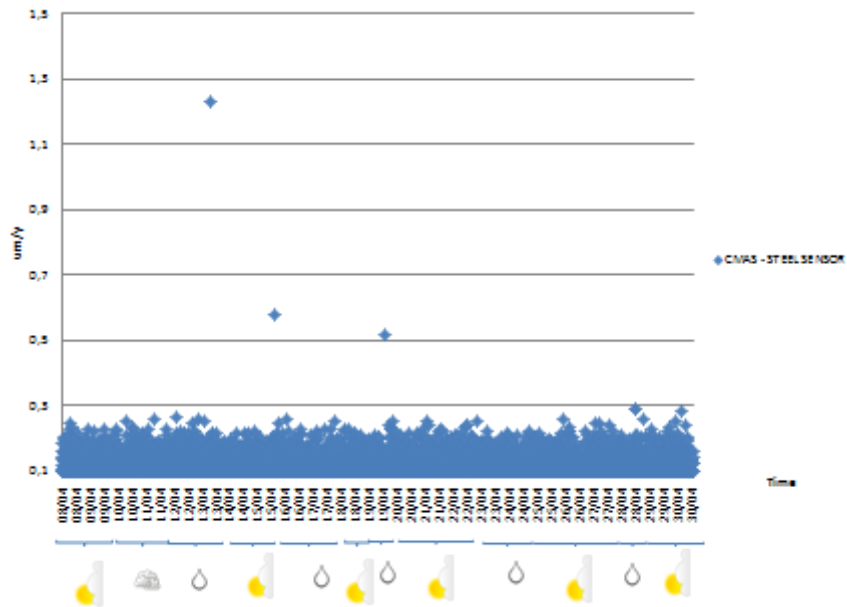


Figure 250. Graph. Corrosion rate measurements for CMAS CS sensor in April 2011.

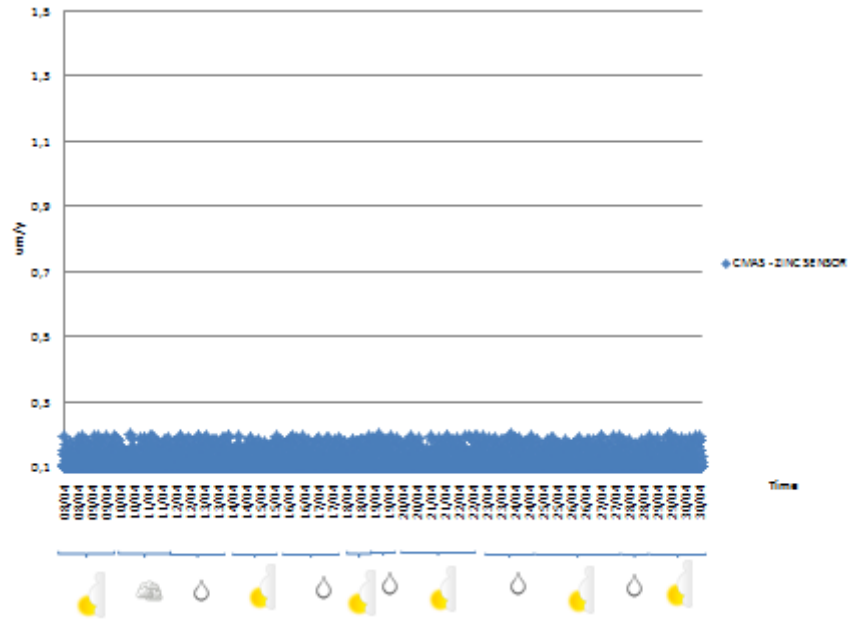


Figure 251. Graph. Corrosion rate measurements for CMAS Zn sensor in April 2011.

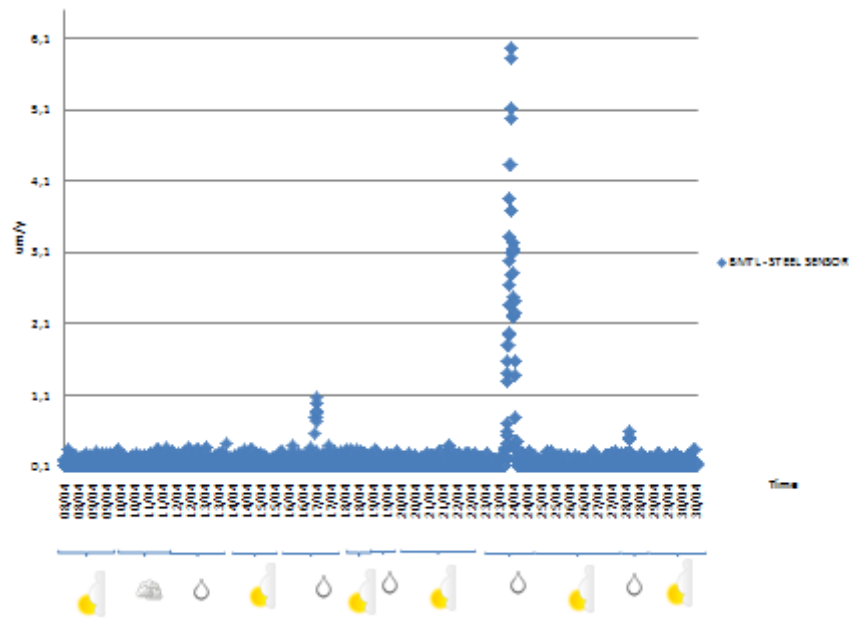


Figure 252. Graph. Corrosion rate measurements for BM CS sensor in April 2011.

REFERENCES

1. Mayrbaurl, R.M. and Camo, S. (2004). *NCHRP Report 534: Guidelines for Inspection and Strength Evaluation of Suspension Bridge Parallel Wire Cables*, National Cooperative Highway Research Program, Washington, DC.
2. Federal Highway Administration. (1986). *Inspection of Fracture-Critical Bridges*, Report No. FHWA-IP-86-26, U.S. Department of Transportation, Washington, DC.
3. Bieniek, M. and Betti, R. (1998). *Cable Conditions for New York City Bridges*, New York City Department of Transportation, New York, NY.
4. Cremer, N.D. (1989). *Prohesion Compared to Salt Spray and Outdoors: Cyclic Methods of Accelerated Testing*, Federation of Societies for Coatings Technology, Washington, DC.
5. Timmins, F.D. (1979). "Avoiding Paint Failures by Prohesion," *Journal of Oil and Colour Chemists Association*, 62(4), 131, Leicester, United Kingdom.
6. Haynes, G.S. (1995). *Corrosion Tests and Standards: Application and Interpretation*, 91–97, ASTM International, Conshohocken, PA.
7. Miyoshi, Y., Kitayama, M., Nishimura, K., and Naito, S. (1985). *Cosmetic Corrosion Mechanism of Zinc and Zinc Alloy Coated Steel Sheet for Automobiles*, SAE Technical Paper Series, SAE International, Washington, DC.
8. Standish, J.V., Whelan, G.W., and Roberts, T.R. (1983). "Corrosion Behavior of Galvanized and Cold Rolled Steels," *Proceedings of the Society of Automotive Engineers*, 1–12, Washington, DC.
9. Barton, S.C., Vermaas, G.W., Duby, P.F., West, A.C., and Betti, R. (2000). "Accelerated Corrosion and Embrittlement of High-Strength Bridge Wire," *Journal of Materials in Civil Engineering*, 12(1), 33–38.
10. Eiselstein, L.E. and Caligiuri, R.D. (1988). "Atmospheric Corrosion of the Suspension Cables on the Williamsburg Bridge," *ASTM Special Technical Publication*, 78–95, ASTM International, Conshohocken, PA.
11. Betti, R. (1996). "Environmental Deterioration Effects in Bridge Wires," *Recent Advances in Bridge Engineering: Proceedings of the U.S.-Europe Workshop on Bridge Engineering*, Barcelona, Spain.
12. Betti, R., West, A.C., Vermaas, G., and Cao, Y. (2005). "Corrosion and Embrittlement in High-Strength Wires of Suspension Bridge Cables," *Journal of Bridge Engineering*, 10(2), 151–162.
13. Cao, Y., Vermaas, G.W., Betti, R., West, A.C., and Duby, P.F. (2003). "Corrosion and Degradation of High-Strength Steel Bridge Wire," *Corrosion*, 59(6), 547–554.

14. Vermaas, G.W. (2001). *Corrosion and Embrittlement of High-Strength Steel Bridge Wires*, Thesis Dissertation, Columbia University, New York, NY.
15. Furuya, K., Kitagawa, M., Nakamura, S.-I., and Suzumura, K. (2000). "Corrosion Mechanism and Protection Methods for Suspension Bridge Cables," *Structural Engineering International: Journal of the International Association for Bridge and Structural Engineering*, 10(3), 189–193.
16. Nakamura, S. and Suzumura, K. (2005). "Corrosion Assessment of Bridge Cables," *Proceedings of the 5th International Conference on Bridge Management*, 28–36, Guildford, United Kingdom.
17. Nakamura, S.-I., Suzumura, K., and Tarui, T. (2004). "Mechanical Properties and Remaining Strength of Corroded Bridge Wires," *Structural Engineering International: Journal of the International Association for Bridge and Structural Engineering*, 14(1), 50–54.
18. Suzumura, K. and Nakamura, S.-I. (2004). "Environmental Factors Affecting Corrosion of Galvanized Steel Wires," *Journal of Materials in Civil Engineering*, 16(1), 1–7.
19. ASTM G85-11. (2011). "Standard Practice for Modified Salt Spray (Fog) Testing," *Book of Standards Volume 03.02*, ASTM International, Conshohocken, PA.
20. ASTM G1-03. (2011). "Standard Practice for Preparing, Cleaning, and Evaluating Corrosion Test Specimens," *Book of Standards Volume 03.02*, ASTM International, Conshohocken, PA.
21. Yang, L. and Sridhar, N. (2003). "Localized Corrosion Monitoring," *ASM Handbook Volume 13A—Corrosion: Fundamentals, Testing, and Protection*, ASM International, Materials Park, OH.
22. Klassen, R.D. and Roberge, P.R. (2008). "Zero Resistance Ammetry and Galvanic Sensors," *Techniques for Corrosion Monitoring*, Cambridge, England.

